NMR Studies of Enhanced Oil Recovery Core Floods and Core Analysis Protocols

Isabelle Bush

Selwyn College

This dissertation is submitted for the degree of Doctor of Philosophy

September 2018

Magnetic Resonance Research Centre

Department of Chemical Engineering and Biotechnology

University of Cambridge

Preface

This dissertation is the result of my own work and includes nothing which is the outcome of work done in collaboration with others, except as declared in the Preface and specified in the text.

It is not substantially the same as any that I have submitted, or, is being concurrently submitted for a degree or diploma or other qualification at the University of Cambridge or any other University or similar institution, except as declared in the Preface and specified in the text. I further state that no substantial part of my dissertation has already been submitted, or, is being concurrently submitted for any such degree, diploma or other qualification at the University of Cambridge or any other University or similar institution except as declared in the Preface and specified in the text.

The research presented herein was conducted at the Magnetic Resonance Research Centre, Department of Chemical Engineering and Biotechnology, University of Cambridge between October 2014 and September 2018. This thesis does not contain more than 65,000 words and 150 figures, including references, tables and equations.

20/09/2018

Isabelle Bush — Date

Acknowledgements

Firstly, I would like to thank my supervisor Prof. Lynn Gladden, for giving me the opportunity to study at the Magnetic Resonance Research Centre (MRRC), for her continued encouragement and guidance throughout the last few years, for helping to give me more confidence in my work, and for proofreading this thesis. I would also like to thank Dr Andy Sederman and Dr Mick Mantle for their time, help and invaluable advice and NMR expertise over the last few years. For financial support, I gratefully acknowledge Shell, The Cambridge Philosophical Society and my parents.

Thanks are also due to all those at the MRRC who have helped in this work. Particular thanks go to: Dr Nick Ramskill for his significant guidance throughout my first three years, from NMR, to core flooding and data acquisition; Dr Daan de Kort for his assistance in the acquisition and optimisation of the propagator experiments in Chapter 7; Kaspars Karlsons for his assistance and time in completing the final leg of the Amott-Harvey experiment in Chapter 8; and to Dr Tom Blythe and Dr Hilary Fabich for their support and considerable patience in explaining my many questions on NMR theory and pulse programming in the early days.

I am also indebted to several people at the Shell Technology Centre in Houston (STCH). I am particularly grateful to Dr Matthias Appel for the many useful discussions, for sharing his expertise on NMR within petrophysical applications, industry best-practice approaches for conducting experiments at reservoir-representative conditions, and core flooding system operation. I am also indebted to: Dr Stefan Hertel for his guidance in finalising the spatially-resolved relaxometry sequence at 2 MHz; to Kirk Smith for his help in constructing the MRRC core flooding system; to Dr Ben Anger for sending over rock core samples, EOR polymer samples and facilitating MIP measurements of core samples at STCH; and to Dr Justin Freeman and Dr XuDong Jing for useful discussions.

Thanks are also due to Zlatko Saracevic and Dr Simon Butler at the Department of Chemical Engineering for conducting MIP and rheometry measurements, respectively, and to Dr Thierry Guiheneuf at the Oxford Instruments Magnetic Resonance support team for sharing his expertise when running into the many programming issues on the 2 MHz.

Finally, I would like to thank my family and friends for their support throughout this time. To the many members of Selwyn MCR and housemates, past and present, for making me laugh, creating fun memories and keeping me going in stressful times. To my wonderful family, Mamma, Papa, Gianluca, Flavia and Nonna, for always being there, providing support, believing in me and pushing me. To Papa for sending over the oh-so-many OnePetro journal articles, upon request; to Mamma for encouraging me with her enthusiasm, always listening with real excitement, even to the most dire of thesis updates; and to Flavia for kindly accommodating me in the final fortnight of data acquisition! And lastly during the write-up phase – to Gianluca, Rachael and Xav for keeping me sane and making me smile.

A special mention must also go to London's many invigorating workspaces – the British Library, the National Arts Library at the V&A, the Library at the French Institute, the sofa, the Kensington, Hammersmith and Chiswick public libraries, with a short stint at the Bergen University Humanities Library. And the occasional Prêt-à-manger £1 coffee deal.

Abstract

With conventional oil reserves in decline, energy companies are increasingly turning to enhanced oil recovery (EOR) processes to extend the productive life of oilfield wells. Laboratory-scale core floods, in which one fluid displaces another from the pore space of a rock core, are widely used in petroleum research for oilfield evaluation and screening EOR processes. Achieving both macro- and pore-scale understandings of such fluid displacement processes is central to being able to optimise EOR strategies. Many of the mechanisms at play, however, are still poorly understood. In this thesis nuclear magnetic resonance (NMR) has been used for quantitatively, non-invasively and dynamically studying laboratory core floods at reservoir-representative conditions.

Spatially-resolved relaxation time measurements (L-T_1-T_2) have been applied to studying a special core analysis laboratory (SCAL) protocol, used for simulating reservoir oil saturations following initial oil migration (primary drainage) and characterising core samples (capillary pressure curves). Axial heterogeneities in pore filling processes were revealed. It was demonstrated that upon approaching irreducible water saturation, brine saturation was reduced to a continuous water-wetting film throughout the pore space; further hydrocarbon injection resulted in pore pressure rise and wetting film thinning.

L-T_1-T_2 techniques were also applied to a xanthan gum polymer-EOR flood in a sandstone core, providing a continuous measurement of core saturation and pore filling behaviours. A total recovery of 56.1% of the original oil in place (OOIP) was achieved, of which 4.9% was from xanthan. It was demonstrated that deposition of xanthan debris in small pores resulted in small-pore blocking, diverting brine to larger pores, enabling greater oil displacement therein.

L-T_1-T_2, spectral and pulsed field gradient (PFG) approaches were applied to a hydrolysed polyacrylamide (HPAM)-EOR flood in a sandstone core. A total recovery of 62.4% of OOIP was achieved, of which 4.3% was from HPAM. Continued brine injection following conventional recovery (waterflooding) and EOR procedures demonstrated most moveable fluid saturation pertained to brine, with a small fraction to hydrocarbon. Increases in residual oil ganglia size was demonstrated following HPAM-EOR, suggesting HPAM encourages ganglia coalescence, supporting the “oil thread/column stabilisation” mechanism proposed in the literature.

NMR relaxometry techniques used for assessing surface interaction strengths (T_1/T_2) were benchmarked against an industry-standard SCAL wettability measurement (Amott-Harvey) on a water-wet sandstone at magnetic field strengths comparable to reservoir well-logging tools (WLTs). At 2 MHz, T_1/T_2 was demonstrated to be weakly sensitive to the core wettability, although yielded wettability information at premature stages of the Amott-Harvey cycle. This suggests the potential for NMR to deliver faster wettability measurements, in SCAL applications or downhole WLT *in situ* reservoir characterisation.

Abbreviations and Nomenclature

Abbreviations

Symbol	Definition
1D	One-dimensional
2D	Two-dimensional
3D	Three-dimensional
ACC	Accumulator
AFM	Atomic force microscopy
AH	Amott-Harvey
AHFD	Amott-Harvey forced drainage stage
AHFI	Amott-Harvey forced imbibition stage
AHSD	Amott-Harvey spontaneous drainage stage
AHSI	Amott-Harvey spontaneous imbibition stage
AHWI	Amott-Harvey wettability index
APGSTE	Alternating pulsed gradient stimulated echo
BPR	Back pressure regulator
BVI	Bulk volume irreducible
CBW	Clay-bound water
CFS	Core flooding system
CPMG	Carl-Purcell-Meiboom-Gill
CT	(X-ray) computer tomography
CTFE	Chlorotrifluoroethylene
DI	Deionised (in context of laboratory purified deionised water)
DPR	Disproportionate permeability reduction
EDDYCM	Oxford Instruments pre-emphasis testing pulse sequence
EOR	Enhanced oil recovery
E&P	(Oil) exploration and production
F	In-line filter
FID	Free induction decay
FOF	Field of flow
FOV	Field of view
FT	Fourier transformation
FWHM	Full width at half maximum
GCV	Generalised cross validation
HDA	Hexadecylamine
HPAM	Hydrolysed polyacrylamide
I.D.	Inner diameter
LOC	Localisation regime
LSB	Low salinity brine
LSF	Low salinity flooding
L-T_1	Spatially-resolved T_1 plot
L-T_2	Spatially-resolved T_2 relaxometry sequence (or plot)
L-T_1-T_2	Spatially-resolved T_1-T_2 relaxometry sequence (or plot)
MAV	Motional averaging regime
MIP	Mercury intrusion porosimetry
MR	Magnetic resonance
MRI	Magnetic resonance imaging
MRRC	Magnetic Resonance Research Centre, University of Cambridge
NMR	Nuclear magnetic resonance
O.D.	Outer diameter
OE	Observed echo
OOIP	Original oil in place
PAM	Polyacrylamide
PEEK	Polyether ether ketone
PFD	Process flow diagram
PFG	Pulsed-field gradient
PGSE	Pulsed gradient spin echo

P&ID	Process and instrumentation diagram
PI	Pressure indicator
PIT	Pressure indicator transmitter
post-EOR	Rock core state, following EOR procedures
post-WF	Rock core state, following secondary waterflooding procedures
PSD	Pore size distribution
PTFE	Polytetrafluoroethylene
P.V.	Pore volume
PY	Pressure recorder (computer)
R	Reservoir
RARE	Rapid imaging with refocused echo
RCH	Rock core holder
RD	Rupture disc
r.f.	Radio-frequency
RF	Recovery factor
RINMR	NMR acquisition software on 2 MHz magnet system
RMS	Root-mean-square
SCA	Special core analysis
SCAL	Special core analysis laboratory
SE	Spin echo
SEM	Scanning electron microscopy
SNR	Signal-to-noise ratio
SP	Syringe pump
SPI	Single point imaging
ST	Short time regime
STCH	Shell Technology Centre Houston
STE	Stimulated echo
STP	Standard temperature and pressure conditions
T_1-IR	T_1 inversion recovery experiment
TMS	Tetramethyl silane
USBM	U.S. Bureau of Mines wettability test
V	Valve
WI	Wettability index
WLT	Well-logging tool

Nomenclature

Symbol	Definition	Units
A	Cross-sectional area of core face	m^2
$AHWI$	Amott-Harvey wettability index	-
$\mathbf{b}$	Data matrix in 1st-order Fredholm integral	-
$\mathbf{B}_0$	Polarising static external magnetic field	T
$\Delta\mathbf{B}_0$	Inhomogeneities of the static magnetic field	T
$\mathbf{B}_1$	Oscillating r.f. field	T
$b(t)$	Measured relaxation or diffusion signal (including noise)	-
c	Polymer concentration	wt%
c^*	Overlap concentration – polymer concentration at which coils touch	wt%
C_v	Flow coefficient	-
Ca	Capillary number	-
d	Average pore diameter	m
D	Self-diffusion coefficient	$m^2\ s^{-1}$
D_0	Free bulk liquid self-diffusion coefficient	$m^2\ s^{-1}$
$D_{\text{core-brine}}$	Self-diffusivity of brine in a brine-saturated rock core	$m^2\ s^{-1}$
D_{fluid}	Bulk liquid D of defined fluid, e.g. dodecane, brine, DI water, polymer	$m^2\ s^{-1}$
D_{LM}	Log-mean self-diffusion coefficients	$m^2\ s^{-1}$
d_{pore}	Pore throat size diameter	m
DC	Duty cycle	%
DC_{max}	Maximum allowable duty cycle	%
di/dt	Current switching rate	$A\ s^{-1}$
dS	Signal in a volume element of sample	-
DS	Number of dummy acquisition scans	-
dV	Volume element in sample	m^3
D_w	Bulk liquid water self-diffusivity	$m^2 s^{-1}$
$\mathbf{e}$	Experimental noise matrix in 1st-order Fredholm integral	-
$e(t)$	Noise in relaxation or diffusion measured signal	-
E	Energy level of nuclear spin states following application of $\mathbf{B}_0$	eV (J)
ΔE	Energy required to induce a transition between different nuclear spin states	eV (J)
$E(\mathbf{g}, \Delta)$	Ensemble echo spin amplitude (PFG measurements)	-
$\mathbf{f}$	Fitted distribution matrix of 1st-order Fredholm integral	-
$f(x)$	Distribution of time constant x on $\log_{10}$ scale in 1st-order Fredholm integral	-
f_e	Solution to 1st-order Fredholm integral, for a pure-noise dataset	-
FOF	Field of flow	m
$FOV_{phase,\ freq}$	Field of view in phase of frequency encoded directions, respectively	m
$FOV_{x,y,z}$	Field of view in the x, y and z directions, respectively	m
g	Subscript indicating gas phase	-
g	Gravitational acceleration	$m\ s^{-2}$
$\mathbf{g}$	PFG gradient pulse strength	$T\ m^{-1}$, $G\ cm^{-1}$
$\mathbf{G}$	Magnetic field gradient	$T\ m^{-1}$, $G\ cm^{-1}$
$\mathbf{G}_d$	Dephase read gradient	$T\ m^{-1}$, $G\ cm^{-1}$
g_{eff}	Effective gradient strength (external applied, plus internal gradients)	$T\ m^{-1}$, $G\ cm^{-1}$
G_{max}	Maximum gradient strength delivered by gradient coils	$T\ m^{-1}$, $G\ cm^{-1}$
$\mathbf{G}_r$	Rephase read gradient	$T\ m^{-1}$, $G\ cm^{-1}$
$\mathbf{G}_R$	Gradient strength in spatially-averaged direction	$T\ m^{-1}$, $G\ cm^{-1}$
$\mathbf{G}_{\text{slice}}$	Slice gradient	$T\ m^{-1}$, $G\ cm^{-1}$
G_x	Magnitude of gradient strength in x-direction	$T\ m^{-1}$, $G\ cm^{-1}$
G_y	Magnitude of gradient strength in y-direction	$T\ m^{-1}$, $G\ cm^{-1}$
G_z	Magnitude of gradient strength in z-direction	$T\ m^{-1}$, $G\ cm^{-1}$
h	Planck's constant = 6.63×10^{-37}	J s
$h(t)$	Noiseless signal with time	-
h_c	Height of capillary rise	m
HI	Hydrogen Index	-
HI_{fluid}	Bulk liquid HI of defined fluid, e.g. dodecane, brine, polymer, DI water	-
i	Imaginary unit	-
I	Nuclear spin quantum number	-
I_c	Current through gradient coils	A
$I_{c,\text{max}}$	Maximum current that can be supplied to the gradient coils	A

I_o	Oil-wetting index (within Amott-Harvey wettability index)	-
I_w	Water-wetting index (within Amott-Harvey wettability index)	-
j	Variable component or term	-
k	Absolute permeability	Da
k_0	Model kernel function in 1st-order Fredholm integral	-
$\mathbf{K}_0$	Kernel matrix in 1st-order Fredholm integral	-
$\mathbf{k}$	Reciprocal space vector	m^{-1}
$\Delta\mathbf{k}$	Increment in $\mathbf{k}$ space, reciprocal of *FOV*	m^{-1}
k_B	Boltzmann constant = 1.38×10^{-23}	m^2 kg s^{-2} K^{-1}
k_D	Diffusion exponent power in internal gradient correction	-
k_i	Effective permeability of phase i	Da
k_{ri}	Relative permeability of phase i	-
k_{rd}	Relative permeability of the displaced phase	-
k_{rD}	Relative permeability of the displacing phase	-
k_{ro}	Relative oil permeability	-
k_{rw}	Relative water permeability	-
$k_{x,max}$	Maximum $\mathbf{k}$-space x co-ordinate sampled	m^{-1}
$k_{y,max}$	Maximum $\mathbf{k}$-space y co-ordinate sampled	m^{-1}
l	Subscript indicating liquid phase	-
$\mathbf{L}$	Angular momentum	J s
l_e	RMS diffusion distance	m
l_g	Dephasing lengthscale from internal magnetic field gradients	m
l_s	Pore size	m
$\mathbf{L}_s$	Smoothing operator in Tikhonov regularisation	-
$\mathbf{M}$	Bulk magnetisation vector	A m^{-1}
$\mathbf{M}_0$	Net equilibrium magnetisation	A m^{-1}
M_0	Magnetisation amplitude recorded at time zero before attenuation	A m^{-1}
M_R	Mobility ratio	-
M_x	Magnetisation along x	A m^{-1}
$M_{x,y}$	Magnitude of transverse component of magnetisation	A m^{-1}
M_y	Magnetisation along y	A m^{-1}
M_z	Magnitude of longitudinal component of magnetisation	A m^{-1}
n	Number of nucleus 'jumps' in a given time, for random walk diffusion	-
N	Number of acquired complex points in read direction.	-
N_α	Number of spins in the low-energy α-state	-
N_β	Number of spins in the high-energy β-state	-
n_e	Number of echoes along the echo train at a particular point in time	-
N_{echoes}	Number of echoes in a CPMG train	-
N_{RARE}	RARE factor (number of times magnetisation refocused per excitation)	-
N_{VD}	Number of variable delay list values in T_1, T_1-T_2, or L-T_1-T_2 experiments	-
NS	Number of scans	-
$\mathbf{P}$	Spin angular momentum	J s (ħ)
ΔP_1	Pressure drop across the injection pump and CFS	psi, Pa
ΔP_2	Pressure drop across semi-permeable ceramic pressure disc	psi, Pa
∇P_i	Pressure gradient in adapted multiphase Darcy's equation	Pa
P_{cap}	Capillary pressure	psi, Pa
P_{inj}	Injection pressure	psi, Pa
P_{nw}	Pressure of non-wetting phase	psi, Pa
P_{pore}	Pore pressure	psi, Pa
$\bar{P}_s(\boldsymbol{r}, \Delta))$	Ensemble average propagator	-
P_w	Pressure of wetting phase	psi, Pa
PREYAn	Pre-emphasis gradient shape control amplitudes (RINMR parameter)	-
PREYKn	Pre-emphasis gradient shape control time constants (RINMR parameter)	S
PV_{inj}	Injected pore volumes of fluid	-
$\mathbf{q}$	$\mathbf{q}$-space wave vector	m^{-1}
Q	Volumetric flowrate	m^3 s^{-1}
q_i	Flux of phase 'i' in multiphase flow	m s^{-1}
Q_{inj}	Injection flowrate	ml min^{-1}
$\pm\mathbf{q}_{max}$	Maximum value of $\mathbf{q}$-space sampled	m^{-1}
r	Effective radius of oil/water interface	m
$\mathbf{r}$	Position vector of spin	-

$\Delta\mathbf{r}$	Displacement resolution of propagator measurements	m
$\mathbf{r}'$	Position vector of spin after an observation time	-
R	Displacement in 3D after *n* jumps in random walk diffusion model	m
$\mathbf{R}$	Net displacement of spin during an observation time	m
R_c	Gradient cable resistance	Ω
RD	Recycle delay time	s
s	Subscript indicating solid phase	-
$S(G)$	Echo amplitude signal in PFG experiments	-
$S(t)$	Free precession signal detected in transverse *x*-*y* plane	-
s_{diff}	1D axial root-mean-square displacement from unrestricted self-diffusion	m
s_{flow}	1D axial displacement from flow, in direction of applied flow	m
S_o	Oil phase saturation	-
S_p	Pore surface area	m^2
$s_{propagator\ (modal)}$	Propagator-observed modal displacements	m
S_w	Aqueous phase saturation	-
S_{wir}	Irreducible water saturation	-
SW	Sweep width	Hz
t	Time	s
T	Temperature	K, °C
$\mathbf{T}$	Torque	N m
T_1	Spin-lattice relaxation time constant	s
$T_{1,2}^{(bulk)}$	Bulk fluid T_1 or T_2	s
$T_{1,2}^{(surface)}$	Surface relaxation time components (where: $1/T_{1,2}^{(surface)} = \rho_{1,2} S_p/V_p$)	s
t_{180}	Duration of r.f. pulse required to achieve an excitation with 180° tip angle	s
$T_{1,fluid}$	Bulk liquid T_1 of defined fluid, e.g. dodecane, brine, polymer, DI water	s
$T_{1,LM}$	Log-mean T_1 of a T_1 distribution	s
T_2	Spin-spin relaxation time constant	s
T_2*	Spin-spin relaxation time due to inhomogeneities in the magnetic field	s
$T_2^{(diffusion)}$	T_2 relaxation attributed to diffusion under internal field gradients	s
$T_{2,fluid}$	Bulk liquid T_2 of defined fluid, e.g. dodecane, brine, polymer, DI water	s
$T_{2,LM}$	Log-mean T_2 of a T_2 distribution	s
t_{90}	Duration of r.f. pulse required to achieve an excitation with 90° tip angle	s
t_{ACQ}	Total acquisition time of a particular NMR experiment	s
$T^{(bulk)}$	Relaxation time of bulk liquid fluid, assuming $T_1^{(bulk)} \approx T_2^{(bulk)}$	s
t_d	Duration of dephase read gradient	s
t_{DW}	Dwell time, time between successive complex points acquired	s
t_E	Interecho time (time between two 180° pulses in a CPMG echo train)	s
t_{GS}	Half duration of slice encoding gradient	s
t_{GST}	Gradient stabilisation time	s
t_{homo}	Duration of homospoil gradient	s
t_p	Duration an r.f. pulse is applied for	s
t_r	Duration of rephase read gradient	s
T_{store}	Storage time in STE pulse sequence, T_1 processes occur, T_2 'freezes'	s
t_{vd}	Variable delay between te 180° and 90° pulses in a T_1-IR experiment	s
t_ε	Gradient ramp time	s
U_D	Reservoir interstitial velocity of displacing phase	ft day^{-1}, m s^{-1}
u_{int}	Average pore space linear interstitial flowrate	ft day^{-1}, m s^{-1}
V	Volume of fluid	m^3
V_{of}	Volume of produced oil during Amott-Harvey forced imbibition	ml
V_{os}	Volume of produced oil during Amott-Harvey spontaneous imbibition	ml
V_{wf}	Volume of produced water during Amott-Harvey forced drainage	ml
V_{ws}	Volume of produced water during Amott-Harvey spontaneous imbibition	ml
V_p	Pore volume	m^3
x y z	Laboratory coordinate frame	-
x' y' z'	Rotating coordinate frame of reference	-
$x_{1,2}$	General time constant in 1st-order Fredholm integral	-
YOFFSET	RINMR parameter for controlling DC-offset in Y-channel gradients	-
z	*z*-axis, defined along the horizontal bore of the 85 MHz magnet	-
Δz	Slice thickness (in selective slice excitation)	m
Z	z-Displacement after *n* jumps in random walk 1D diffusion model	m
α	Smoothing parameter controlling Tikhonov degree of smoothing	-

α_{eff}	Effective α, from averaged α_L at meaningful signal regions in FOV	-
α_L	Locally-optimised smoothing parameter	-
α_U	Universal α, from averaged α_{eff} of multiple L-T_1-T_2 datasets in a flood	-
γ	Gyromagnetic ratio	rad s^{-1} T^{-1}
γ_{lg}	Liquid-gas interface surface tension	N m^{-1}
$\dot{\gamma}_{max}$	Maximum shear rate at pore wall (assuming laminar, Newtonian flow)	s^{-1}
$\dot{\gamma}_{onset}$	Critical shear rate (property of HPAM EOR polymers)	s^{-1}
γ_{sg}	Solid-gas interface surface tension	N m^{-1}
γ_{sl}	Solid-liquid interface surface tension	N m^{-1}
γ_T	Interfacial tension	N m^{-1}
$\gamma_{o/w}$	Oil-water interfacial tension	N m^{-1}
γ	Surface tension	N m^{-1}
δ	Chemical shift	ppm
δ_G	PFG gradient pulse duration	s
Δ	Observation time	s
θ	Angle through which $\mathbf{M}_0$ is rotated upon application of $\mathbf{B}_1$ field	°
θ_c	Contact angle	°
$\boldsymbol{\mu}$	Magnetic moment of a nucleus	J T^{-1}
μ_{app}	Apparent viscosity	Pa s
μ_d	Viscosity of the displaced phase	Pa s
μ_D	Viscosity of the displacing phase	Pa s
μ_i	Viscosity of phase i	Pa s
μ_o	Viscosity of the oil phase	Pa s
μ_{signal}	Mean true signal intensity	-
μ_w	Viscosity of the aqueous phase	Pa s
ν	Nucleus resonance frequency	Hz
ν_0	Larmor frequency	Hz
ν_{TMS}	TMS reference frequency	Hz
ξ	Distance a nucleus 'jumps' in random-walk analogy of 1D diffusion	m
$\rho_{1,2}$	Surface relaxivities associated with T_1 and T_2 in porous materials	m s^{-1}
$\Delta\rho$	Density difference between reservoir fluid phases	kg m^{-3}
ρ_{fluid}	Mass density of specified fluid	kg m^{-3}
ρ_m	Mass density	g cm^{-3}
$\rho(\mathbf{r})$	Spin density as a function of position vector, $\mathbf{r}$	moles m^{-3}
σ_{noise}	Standard deviation of signal noise	-
τ	Half interecho time in spin echo sequences	s
τ_1	Time between 1st, 2nd 90° pulse, and 3rd 90° pulse, STE – in STE sequence	s
$\tau_{90\text{-}180}$	Time interval between the initial 90° and 180° pulse in a CPMG train	s
$\tau_{180\text{-}180}$	Interecho time, interval between 180° pulses in a CPMG train	s
τ_s	Mean time between jumps in random walk model of 1D diffusion	s
φ	Accrued phase of spins	rad
φ_p	Porosity	-
φ_r	Receiver phase	rad
$\Delta\chi$	Magnetic susceptibility differences	-
ω_0	Larmor frequency	rad s^{-1}
ω_1	Angular frequency of r.f. field $\mathbf{B}_1$	rad s^{-1}
ω_{ref}	Reference mixing frequency of non-resonant nuclei	rad s^{-1}
$\Delta\omega$	Offset frequency of signal	rad s^{-1}
$\Delta\omega_b$	Soft pulse bandwidth	rad s^{-1}

Contents

Chapter 1

Introduction

This Chapter introduces oil recovery processes and the methods used to study these processes in the laboratory, focusing on magnetic resonance (MR) approaches. The thesis aims and structure are also provided.

1.1 Enhanced Oil Recovery (EOR): an Overview

Hydrocarbons in the Earth's subsurface are contained within the pore space and fractures of reservoir rocks, typically sedimentary carbonate or sandstone formations. Extraction processes are classified as primary, secondary or enhanced oil recovery mechanisms. Primary recovery is the first extraction stage, resulting from natural reservoir pressure drives - illustrated in Fig. 1.1.

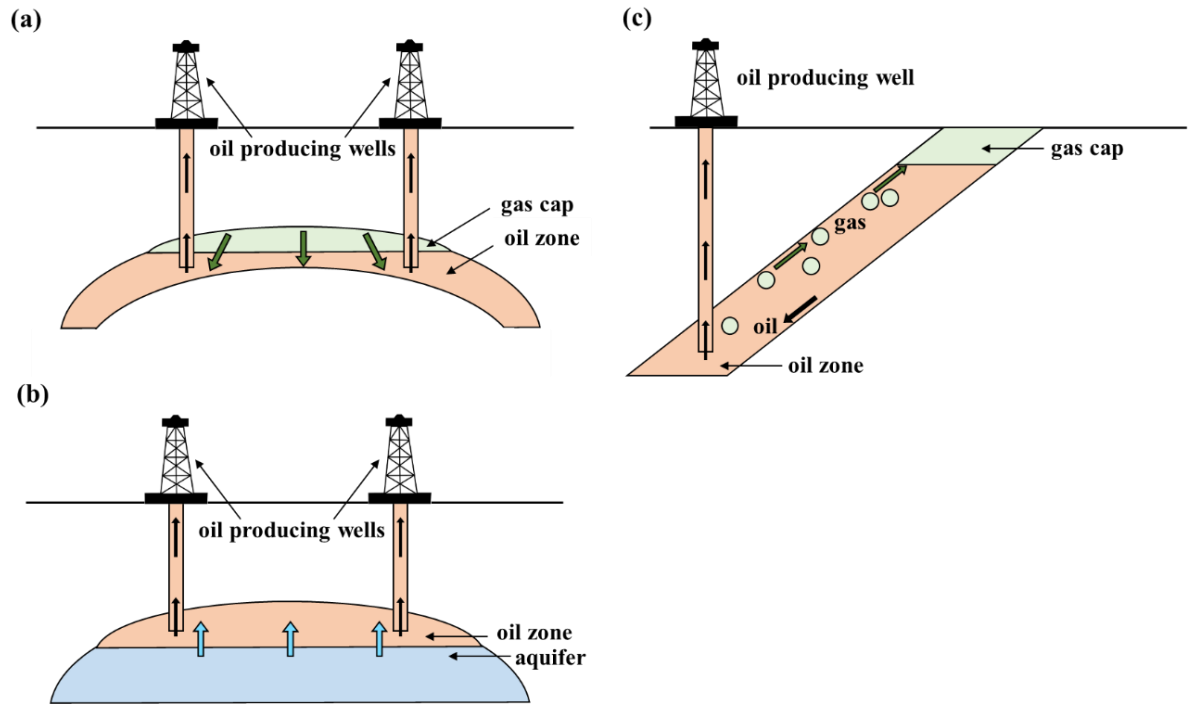

Figure 1.1. Illustrations of **(a)** gas cap expansion, **(b)** water drive, **(c)** gravity drainage primary recovery processes. Adapted from Clark (1969) and Cole (1969).

These promote hydrocarbon displacement from the reservoir towards the wellbore, and up to the surface. Density segregation is largely responsible, creating overpressures from expanding natural gas at the reservoir ceiling (gas cap expansion mechanism), and confining pressures from reservoir water movement towards the reservoir floor (water drive mechanism). Evolution of dissolved gas during reservoir pressure depletion is an additional contributing factor (gravity drainage mechanism). Once

these natural pressure drives are depleted, secondary recovery processes are employed. These mimic primary recovery by restoring reservoir pressure through waterflooding or gas injection.

EOR methods increase the mobility of trapped oil reserves that cannot be extracted *via* secondary processes. EOR techniques are categorised as miscible gas-, thermal-, and chemical-flooding methods. Gas flooding injects a gas miscible with the residual reservoir oil (typically N_2,CO_2 or light hydrocarbons) – the resulting zero oil-gas interfacial tension creates a single, mobile fluid. Thermal methods (such as *in situ* combustion or steam injection) heat crude oil within the formation. These reduce oil viscosity, vaporise oil components and reduce interfacial tension, thereby improving residual oil mobility. Chemical methods inject additives (primarily polymers and surfactants) to reservoir flooding waters. These alter the relative mobility of reservoir brine and oil – polymers increase the aqueous-phase viscosity, whilst surfactants reduce interfacial tensions (emulsifying the oil) and can alter rock wettability (the preferential attraction of either oil- or aqueous-phases to a rock surface) (North, 1985; Terry, 2001).

The reservoir recovery factor (RF) is the ratio of oil extracted to the original oil held in place (OOIP). The global average oilfield RF is approximately 30%, with significant amounts of oil not extracted. At present, most oil production (96.5%) originates from mature oilfields *via* primary or secondary recovery. EOR holds the potential to increase average oilfield RFs to between 50–70% (Muggeridge *et al.*, 2014).

The success of EOR mechanisms strongly depends on reservoir conditions: temperature, pressure, rock wettability, permeability and porosity, as well as the compositions of reservoir rock, brines and oil (Terry, 2001). EOR requires complex technologies, large capital investments, long lead times and carries large financial risks. There is thus considerable commercial drive to develop understandings and quantify how EOR mechanisms behave within reservoir environments.

1.2 Studying Oil Recovery Processes in the Laboratory

1.2.1 Core Analysis and Core Flooding

Reservoir simulation models are crucial for evaluating prospective and existing oil and gas reservoirs, enabling estimation of the reservoir OOIP, and the prediction of hydrocarbon production profiles. Reservoir engineers rely upon such models for optimising the economic extraction of hydrocarbons. These reservoir models draw upon a range of input data sources – seismic, wireline logging (well-logging data acquired at the reservoir well bore), drilling data, regional geology and core analysis. Whilst these primarily constitute remote measurements, core analysis procedures (both routine and special) provide direct measurements of reservoir rock properties.

Routine core analysis procedures are used to measure key reservoir parameters on “as-received” reservoir core samples, namely: pore structural information, absolute permeabilities and native

saturation conditions. Experiments are conducted on rock core samples (cylindrical plugs extracted from full-diameter borehole reservoir cores), with typical lengths of 7 cm and diameters in the range 2.5–3.8 cm, although larger plugs of several-metre length can also be studied. A wide variety of techniques are used, including X-ray computer tomography (CT) scans, electrical resistivity measurements and geomechanical tests.

Special core analysis laboratory (SCAL) procedures measure fundamental static and dynamic reservoir rock properties, typically involving two-phase flows at reservoir-representative conditions. These include measurements of capillary pressure curves (see Chapter 5), relative permeabilities, wettabilities (see Chapter 8), and core flooding experiments (McPhee *et al.*, 2015).

Core flooding experiments identify changes in core saturations following injection of oil-displacing fluids. Primarily, these fall under two objectives: oilfield evaluation and developing accurate models of recovery processes. Regarding the former, core flood data can provide critical information needed for deciding whether to develop a hydrocarbon reserve (Arora *et al*., 2010; Washburn and Madelin, 2010) and to screen and optimise EOR injectants for particular reservoir environments (Mitchell *et al*., 2012d). For the latter, core flood data is used for validating well-logging data interpretations (Mitchell *et al.*, 2012c) and to deepen understanding of fluid displacement processes (Brautaset *et al*., 2008; Yuechao *et al*., 2011).

1.2.2 Monitoring Core Floods: Putting MR on the Map

Dynamic monitoring of core floods and core internal fluid distributions has traditionally not been possible. Such systems were therefore treated as a "black-box", whereby only the volumes and compositions of recovered fluids could be determined (Yuechao *et al*., 2011).

These globally-averaged measurements cannot reveal local variations in fluid saturation, such as "oil banks" originating from EOR processes, or due to structural and surface wettability heterogeneities. Quantifying these saturation heterogeneities can be useful for reservoir characterisation or developing understandings in oil recovery processes. Furthermore, globally-averaged volumetric measurements over core samples do not yield recoveries representative of the behaviour in a reservoir, due to capillary end effects which can lead to higher wetting-phase saturations at the core outlet. Capillary end effects during core flooding can arise from the discontinuity of capillarity in the wetting phase at the core outlet (Archer and Wong, 1973; Enwere and Archer, 1992; Huang and Honarpour, 1996; Mitchell *et al*., 2012c,d).

The central regions of the core, however, are unaffected by capillary end effects and can yield quantitative information considered representative of reservoir conditions (Mitchell *et al*., 2012c, 2013d). Acquiring spatially-resolved information on the fluid distributions throughout the time-course of core floods is thus of considerable interest.

Today, numerous techniques can be used for studying laboratory core floods, from surface-sensitive techniques on the millimetre-nanometre scale, such as atomic force microscopy (AFM) (Hassenkam *et al.*, 2011, 2012) and scanning electron microscopy (SEM) (Fogden, 2012), to imaging techniques capable of revealing spatial heterogeneities in saturation on the pore-to-core scale – the most widely used techniques being X-ray CT (Kumar *et al.*, 2009; Andrianov *et al.* 2012; Haugen *et al.*, 2014; Youssef *et al.*, 2014) and magnetic resonance imaging (MRI), (Fernø *et al.*, 2007; Aspenes *et al.*, 2008; Brautaset *et al.*, 2008; Ersland *et al.*, 2009, 2010a,b; Suekane *et al.*, 2009; Romero-Zerón *et al.*, 2009, 2010; Loahardjo *et al.*, 2010; Wang *et al.*, 2010; Washburn and Madelin, 2010; Liu *et al.*, 2011; Yuechao *et al.*, 2011; Mitchell *et al*., 2012b,c,d, 2013d; Song *et al.*, 2013).

Both MR and CT techniques can non-destructively image multiphase fluid systems in porous media, although the origin of image contrast associated with these approaches are different (Vinegar, 1986). Whilst X-ray CT delivers higher spatial resolution than MRI (micrometre, rather than sub-millimetre scale), MR offers a broader range of non-invasive contrast mechanisms, being chemically-sensitive (spectra, resonant spin nuclei), and motion-sensitive (diffusion, velocity) (Gladden, 1994). Further, its existing applications in special core analysis (porosity, permeability and pore size distribution characterisation (Gallegos *et al*., 1987; Davies and Packer, 1990; Davies *et al*., 1991), surface interaction and wettability measurements (Mitchell *et al.*, 2009b) and oilfield well-logging activities (Freedman, 2006)) make using MR for studying laboratory core floods a natural choice. Numerous nuclear magnetic resonance (NMR) and MRI techniques have been applied to studying petrophysical systems and core floods in the laboratory – further discussed in Chapter 2.

1.3 Scope of this Thesis

The aims of the work reported in this thesis were to use NMR to non-invasively, quantitatively and dynamically study EOR core floods and standard SCAL procedures at reservoir-representative conditions, to: (i) deepen understanding of core- and pore-level oil recovery mechanisms; and (ii) assess standard SCAL procedures for sample characterisation, with a view to benchmarking these against alternative NMR approaches.

This thesis is structured as follows:

Chapter 1 introduces EOR, SCAL procedures, laboratory core floods, and the application of NMR to these systems.

Chapter 2 describes the basic principles of NMR and MRI, introducing MR techniques applied to petrophysical systems.

Chapter 3 presents the implementation, development and validation of spatially-resolved relaxation time sequences (L-T_1-T_2 and L-T_2) on 85 MHz and 2 MHz magnet systems.

Chapter 4 presents the core flooding system (CFS) used for achieving reservoir-representative conditions in core flooding experiments.

Chapter 5 monitors a primary drainage capillary pressure flood, *via* the semi-permeable ceramic disc method, using L-T_1-T_2.

Chapter 6 monitors a xanthan gum polymer-EOR flood using L-T_1-T_2.

Chapter 7 monitors a hydrolysed polyacrylamide (HPAM) polymer-EOR flood using spectral, L-T_1-T_2, pulsed-field gradient (PFG) diffusion, and PFG T_2-propagator measurements.

Chapter 8 benchmarks an industry-standard SCAL Amott-Harvey wettability measurement on a water-wet core, against an NMR technique for probing surface interaction strengths.

Chapter 9 summarises the conclusions of this thesis and suggests possible future research areas.

Chapter 2

NMR Theory and its Applications to Petrophysical Systems

This chapter introduces the basic principles of NMR and MRI, followed by an overview of MR techniques used in petrophysical systems. More detailed explanations can be found in the literature (Fukushima and Roeder, 1981; Callaghan, 1991; Gladden, 1994; Mantle and Sederman, 2003).

2.1 Basic Principles of NMR

2.1.1 Introduction

2.1.1.1 Nuclear Spin and the Zeeman Effect

All elemental particles possess a fundamental quantum mechanical property called spin, quantified by the spin quantum number, I. Individual protons and neutrons have I = ½. For an atomic nucleus, I depends on its number of unpaired protons and neutrons. The net spin of NMR-active nuclei generates a spin angular momentum, **P**. For an isolated nucleus, **P** takes discrete values quantised by:

$$\mathbf{P} = \frac{h}{2\pi}[I(I+1)]^2 , \tag{2.1}$$

where h is Planck's constant. I can be integral or half-integral. Nuclei are only NMR-active if $I \neq 0$ – the most commonly studied nuclei, ^{13}C and ^{1}H, have I = ½.

For non-zero spin nuclei, **P** creates a magnetic field with an associated magnetic moment, **μ**, related by γ, the gyromagnetic ratio (a property of the nucleus):

$$\boldsymbol{\mu} = \gamma \mathbf{P} . \tag{2.2}$$

The ^{1}H nucleus has the highest known γ, of 2.675×10^{8} rad T^{-1} s^{-1}. All data in this thesis was acquired probing the ^{1}H nucleus.

In the absence of an external magnetic field, magnetic moments of individual nuclei are randomly oriented (degenerate) and the net moment across all nuclei, $\mathbf{M}_0$, is zero. By applying a static external magnetic field in the z-direction, $\mathbf{B}_0$, nuclear spins align with $\mathbf{B}_0$, adopting one of their $2I+1$ energy level states (between $-I$ and $+I$, in I = ½ increments). This lifting of degeneracy is known as the "Zeeman effect". The energy of each state, resulting from the interaction between a nuclear dipole moment and magnetic field is:

$$E = -\boldsymbol{\mu} \cdot \mathbf{B}_0 . \tag{2.3}$$

Transition between states can occur through photon absorption or emission, quantised by:

$$\Delta E = h\nu = \left|\gamma \frac{h}{2\pi} \Delta I \mathbf{B}_0\right| = \gamma \frac{h}{2\pi} \mathbf{B}_0 \,, \tag{2.4}$$

where ν is the nucleus resonance frequency.

For ^{1}H, two possible energy states occur – the lower energy α-state, with spins aligned with $\mathbf{B}_0$, and the higher energy β-state with spins not aligned with $\mathbf{B}_0$. Figure 2.1 presents a Zeeman diagram for ^{1}H.

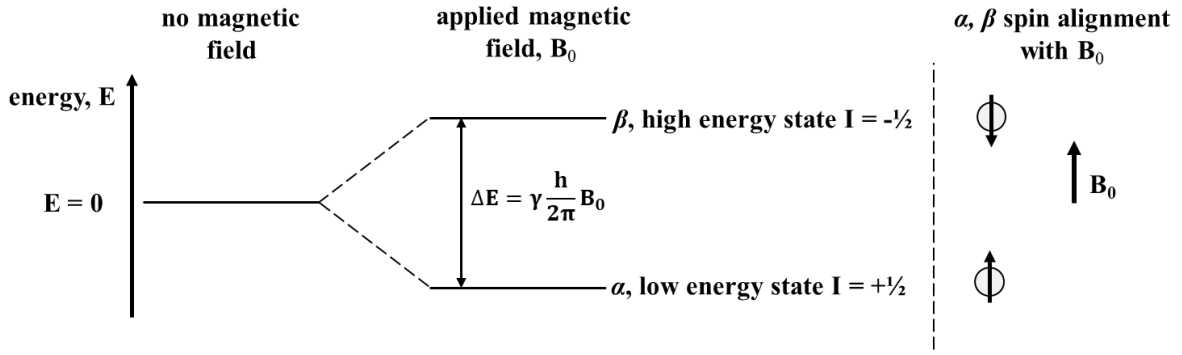

Figure 2.1. A Zeeman energy level diagram for a ^{1}H nucleus in the presence of an external magnetic field, $\mathbf{B}_0$.

Equation 2.4 defines the nucleus Larmor frequency (υ_0, ω_0) – the frequency that magnetisation precesses about $\mathbf{B}_0$.

$$\upsilon_0 = \frac{\gamma \mathbf{B}_0}{2\pi} \text{ [Hz]} \quad \text{or} \quad \omega_0 = \gamma \mathbf{B}_0 \text{ [rad s}^{-1}\text{]} \,. \tag{2.5}$$

2.1.1.2 The Bloch Vector Model

On applying $\mathbf{B}_0$, relative populations of spins in each energy state are governed by the Boltzmann distribution:

$$\frac{N_\beta}{N_\alpha} = \exp\left(-\frac{\Delta E}{k_B T}\right). \tag{2.6}$$

N_β and N_α are the number of spins in β- and α-states, k_B is the Boltzmann constant (1.38×10^{-23} J K^{-1}), T is absolute temperature. A surplus of spins exist in the lower energy α-state. These can be visualised as a series of magnetic moments randomly distributed around a precessional cone.

Summation of individual spin magnetic moments, $\boldsymbol{\mu}$, yields a net macroscopic magnetisation, $\mathbf{M}_0$ (the bulk magnetisation vector). $\mathbf{M}_0$ is parallel to $\mathbf{B}_0$, with zero net magnetisation in x-y. This approach to visualising net magnetisation is termed the Bloch vector model, illustrated in Fig. 2.2.

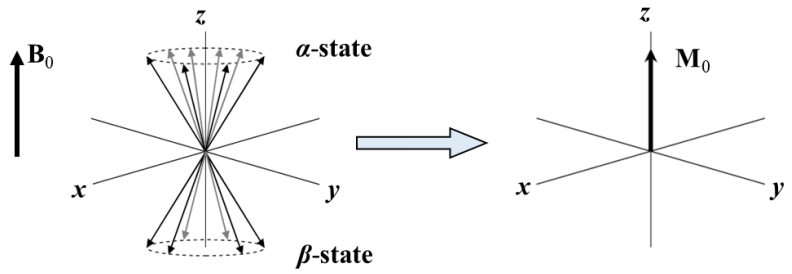

Figure 2.2. Illustration of the Bloch vector model.

As a summation over a large spin ensemble, $\mathbf{M}_0$ can be described in classical terms, where $\boldsymbol{\mu}$ is described as a vector relating torque, $\mathbf{T}$, to $\mathbf{B}_0$:

$$\mathbf{T} = \boldsymbol{\mu} \times \mathbf{B_0} \,. \tag{2.7}$$

From classical descriptions, torque is related to angular momentum, $\mathbf{L}$ and time, t:

$$\mathbf{T} = \frac{\mathrm{d}\mathbf{L}}{\mathrm{d}t} \tag{2.8}$$

Equivalently, considering spin angular momentum, $\mathbf{P}$,

$$\frac{\mathrm{d}\mathbf{P}}{\mathrm{d}t} = \boldsymbol{\mu} \times \mathbf{B_0} \,. \tag{2.9}$$

Substituting Eq. 2.2 into Eq. 2.9 and considering net magnetic moment, $\mathbf{M}_0$ is described by:

$$\frac{\mathrm{d}\mathbf{M_0}}{\mathrm{d}t} = \mathbf{M_0} \times \gamma \mathbf{B_0} \,. \tag{2.10}$$

The solution to Eq. 2.10 corresponds to magnetisation precessing about $\mathbf{B}_0$ at ω_0, as in Eq. 2.5.

2.1.2 The NMR Experiment

Physically, an NMR system consists of a magnet (superconducting, or permanent), generating a magnetic field. A probe containing a radio-frequency (r.f.) coil is held within the magnet bore. The sample desired to be measured is loaded into the probe. During an NMR experiment the r.f. coil both produces pulses which excite nuclear spins in the sample, and it collects their resultant decaying signal. The magnet is controlled by a computer and console, which together transmit pulses and receive signals. 'Shimming' coils are used to fine-tune additional magnetic fields to $\mathbf{B}_0$, to ensure a homogeneous field is 'felt' by the sample. Additional magnetic field gradient coils can be used to supply locally-varying magnetic field strengths, for imaging applications. The following sections explain in further detail how signal is detected in a laboratory NMR experiment.

2.1.2.1 Spin Excitation and the Rotating Frame of Reference

Pulsed-NMR techniques provide energy for spin state transitions by applying an additional, oscillating radio-frequency (r.f.) field, $\mathbf{B}_1$ – using a sinusoidal r.f. current in the transmitter coil (an "r.f. pulse").

By Faraday's law of induction, this induces a magnetic field of amplitude B_1, which rotates with angular frequency ω_1, disrupting $\mathbf{M}_0$ from equilibrium. NMR experiments measure the evolution of bulk magnetisation $\mathbf{M}$ following an r.f. pulse in the transverse *x*-*y* plane. $\mathbf{B}_1$ must therefore oscillate in resonance with $\mathbf{B}_0$, so that $\mathbf{B}_1$ tips $\mathbf{M}$ into *x*-*y*, where $\mathbf{M}$ simultaneously precesses about both $\mathbf{B}_0$ at ω_0, and $\mathbf{B}_1$ at ω_1.

For simplicity, convention denotes a rotating reference frame, axes: *x′*, *y′*, *z′*. This rotates with angular frequency ω_0 about *z* in the laboratory frame. $\mathbf{B}_1$ thus appears static, such that $\mathbf{M}$ simply precesses about $\mathbf{B}_1$ in the rotating frame, illustrated in Fig. 2.3.

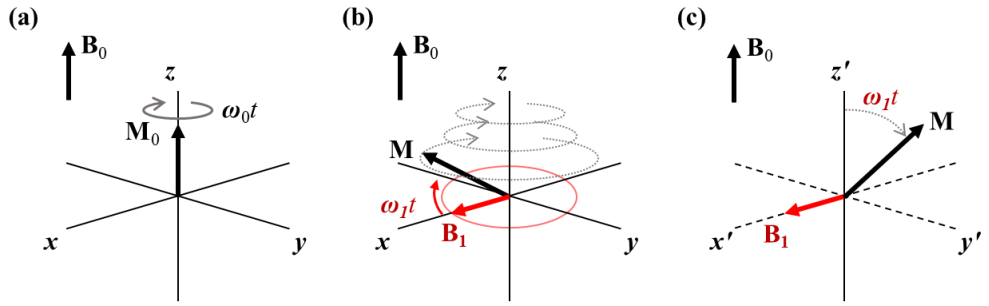

Figure 2.3. Illustration of Bloch vector model and rotating frame of reference: **(a)** equilibrium net magnetisation, $\mathbf{M}_0$ precessing about $\mathbf{B}_0$ at ω_0, **(b)** and **(c)** $\mathbf{M}$ precessing about $\mathbf{B}_0$ and $\mathbf{B}_1$ due to additional RF field, $\mathbf{B}_1$. (b) is in the laboratory frame of reference, (c) in the rotating frame of reference.

On applying $\mathbf{B}_1$, $\mathbf{M}_0$ rotates in *y′z′* by angle θ, depending upon r.f. pulse duration t_p, and $\mathbf{B}_1$ magnitude:

$$\theta = \omega_1 t_p = \gamma \mathbf{B}_1 t_p \,. \tag{2.11}$$

For example, a 90° pulse rotates $\mathbf{M}_0$ into *x′y′*. Subsequent decay of transverse magnetisation occurs, until $\mathbf{M}_0$ lies along *z*, *z′*. For a 90° pulse-acquire experiment, transverse signal $M_{x,y}$ decays in an exponential manner:

$$M_{x,y}(t) = M_0 e^{iw_0 t} \,. \tag{2.12}$$

2.1.2.2 Signal Detection

Laboratory spectrometers have receivers in *x*-*y* detecting $M_{x,y}$, longitudinal magnetisation is not detected. $M_{x,y}$ decay induces an oscillating r.f. current at ω_0, and a free precession signal $S(t)$ in the receiver coils directly proportional to $M_{x,y}(t)$ – termed a 'free induction decay' (FID). As $\mathbf{M}$ precesses about $\mathbf{B}_0$, it is detected by heterodyning (frequency converting) signal using two reference signals $\pi/2$ out of phase with each other. This allows two transverse signal components ('real', 'imaginary') to be separately sampled (quadrature detection):

$$M_{x,y}(t) = M_x(t) + iM_y(t) \,. \tag{2.13}$$

Only the offset frequency from ω_0 is considered, $\Delta\omega = \omega_0 - \omega_{ref}$, such that:

$$S(t) \propto M_0 e^{i\varphi_r} e^{i\Delta w t}, \tag{2.14}$$

where φ_r is the receiver phase. Acquired signal is digitally sampled over a frequency range termed the sweepwidth, *SW*. The time between complex digitised points is the dwell time, t_{DW}, where $t_{DW} = 1/SW$. Following Nyquist-Shannon sampling theory, *SW* must be at least twice the maximum frequency in a sample. The phase corrected Fourier transformation (FT) of $S(t)$ yields peaks at sample resonant frequencies – an NMR spectrum. Figure 2.4 presents a schematic of an FID and resultant spectrum.

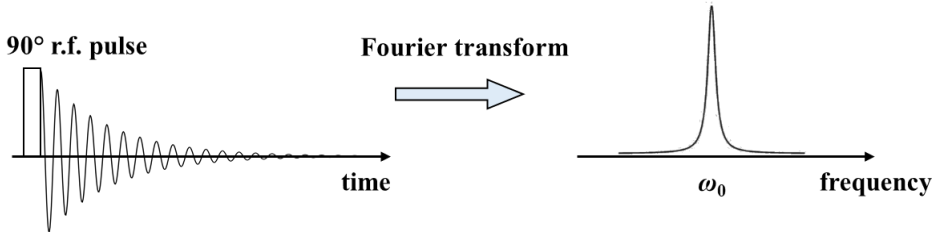

Figure 2.4. Schematic of **(a)** free induction decay (FID) at a single frequency, and **(b)** resultant NMR spectrum after Fourier transformation.

This capacity for detecting changes in $M_{x,y}$ forms the basis of all pulsed-NMR experiments. As $S(t)$ is directly proportional to $M(t)$, in turn proportional to the number of spins in a sample, NMR is volumetrically quantitative. NMR sensitivity improves with decreasing temperature and increasing sample volume, gyromagnetic ratio and field strength (Eqs. 2.5, 2.6).

NMR signal is affected by fluctuations from thermal motion, background electrical interferences and imperfections in electronic components – signal noise. Signal noise has a Gaussian distribution about the true sample signal. The signal-to-noise ratio (SNR) is defined by mean true signal intensity, μ_{signal}, and the standard deviation of noise, σ_{noise}:

$$SNR = \frac{\mu_{\text{signal}}}{\sigma_{\text{noise}}}. \tag{2.15}$$

SNR improves by repeating acquisitions multiple times (true signal magnitude is directly proportional to number of experimental scans, NS, whereas noise scales with $\sqrt{NS}$). Between successive scans, a recycle delay *RD* is used, allowing for full relaxation to $\mathbf{M}_0$. R.f. pulse and receiver phases can be incremented between successive scans (termed phase cycling) – used to remove signal artefacts.

2.1.2.3 Chemical Sensitivity

Spectral chemical sensitivity results from resonance frequency differences for nuclei in different environments, due to differing chemical bonds. Neighbouring electrons shield nuclei, altering local magnetic fields and resulting in signal oscillating at an offset frequency $\Delta\omega$. More shielded nuclei experience a lower magnetic field, thus a smaller resonance frequency (and vice versa). Chemical shift, δ, is defined relative to a reference molecule, usually tetramethyl silane (TMS), in parts per million (ppm):

$$\delta = \frac{v - v_{\mathrm{TMS}}}{v_{\mathrm{TMS}}} \times 10^6 \,, \tag{2.16}$$

where v_{TMS} is the TMS resonance frequency, v is the resonance frequency of the nucleus of interest. These chemical shifts lead to different NMR spectral peaks, giving a signature for sample molecular structure. Spectral resolution depends on spectral linewidths and the overlap between them.

2.1.3 Nuclear Spin Relaxation

Following $\mathbf{B}_1$ application, a nuclear spin system has excess energy, containing non-equilibrium spin distributions with transverse and longitudinal magnetisations. Excited spins undergo relaxation processes where excess energy is redistributed to the surrounding system. Relaxation processes require a random local magnetic field, fluctuating at a frequency where nuclear spins interact with it as an energy sink, for example, as provided by molecular tumblings in a liquid.

Two relaxation mechanisms are commonly studied: spin-lattice and spin-spin. The time constants describing both processes can characterise a system, as they are influenced by sample composition, phase, motion and microscopic structure.

2.1.3.1 Spin-Lattice Relaxation

Spin-lattice relaxation describes the recovery of longitudinal magnetisation $M_z(t)$ to equilibrium through energy exchange with surrounding molecules, the "lattice". Assuming exponential behaviour, this is defined by:

$$\frac{\mathrm{d}M_z}{\mathrm{d}t} = -\frac{(M_z - M_0)}{T_1} \,, \tag{2.17}$$

where T_1 is the spin-lattice relaxation time constant.

T_1 is typically measured using the inversion recovery pulse sequence, where $\mathbf{M}_0$ is first inverted using a 180° r.f. pulse to $-\mathbf{M}_0$. A 90° r.f. pulse is applied after a time t_{vd}, returning magnetisation into *x-y*, enabling its detection. The experiment is repeated for a series of t_{vd}. Figure 2.5 illustrates the sequence, the signal development with time, and corresponding spin isochromats (averaged spin aggregate macroscopic models).

Assuming initial conditions $M_z(t = 0) = -1$, the solution of Eq. 2.17 is:

$$M_z(t) = M_0 \left[1 - 2\exp\left(-\frac{t}{T_1}\right)\right]. \tag{2.18}$$

Equilibrium in M_z is usually established after $t = 5 \times T_1$. This provides a guideline for the optimal *RD* between signal averaging scans.

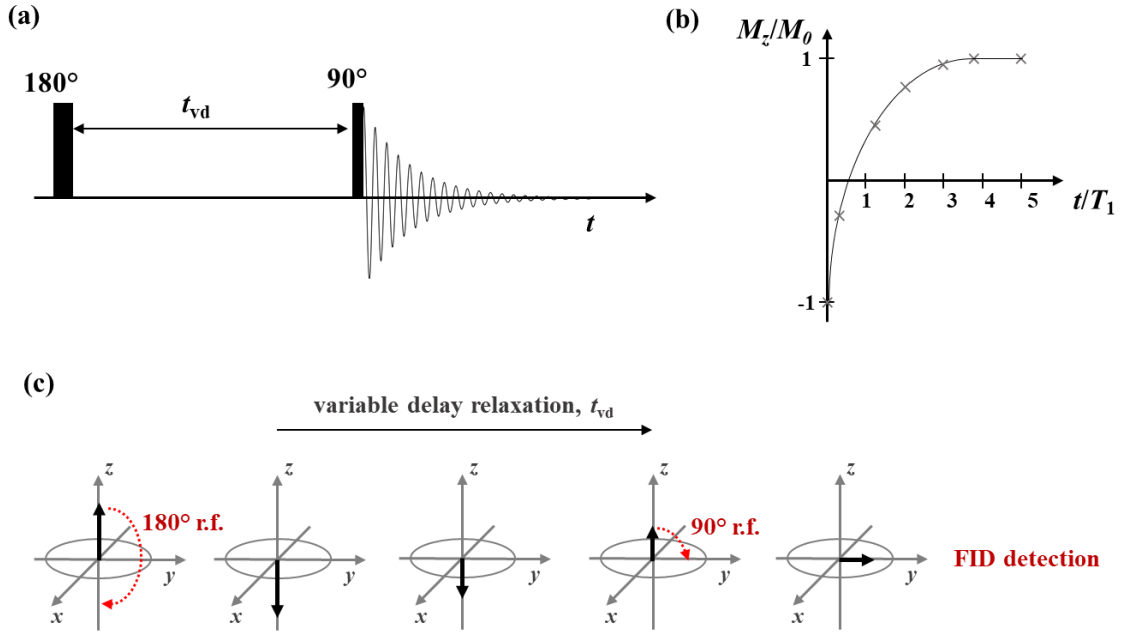

Figure 2.5 T_1 inversion recovery pulse sequence **(a)** sequence timing diagram, **(b)** illustration of detected signal development with time, **(c)** spin isochromats.

2.1.3.2 Spin-Spin Relaxation

The spin-spin relaxation time constant, T_2, describes transverse $M_{x,y}$ relaxation *via* interactions with other nuclear spins ("spin-spin" energy exchange). The T_2* time constant characterises $M_{x,y}$ relaxation from magnetic field inhomogeneities, defined by:

$$\frac{1}{T_2{}^*} \approx \frac{1}{T_2} + \gamma \Delta \mathbf{B}_0 \,, \tag{2.19}$$

where $\Delta\mathbf{B}_0$ is the magnetic field variation.

T_2* is reversible, whereas T_2 is irreversible. T_2 is often measured using the Carr-Purcell-Meiboom-Gill (CPMG) (Carr and Purcell, 1954; Meiboom and Gill, 1958) spin-echo (SE) sequence, presented in Fig. 2.6.

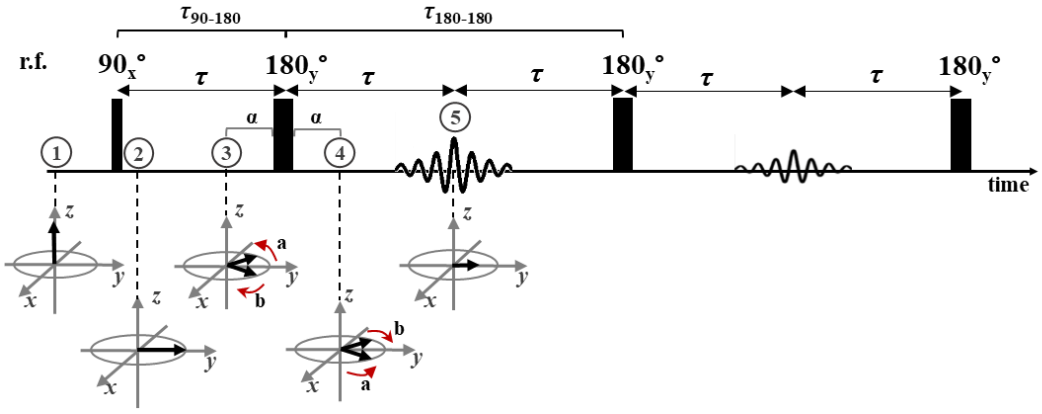

Figure 2.6. CPMG spin-echo sequence with corresponding spin isochromats. A train of 180° pulses are repeated (truncated here for clarity) such that the full T_2 decay process can be monitored.

A 90° r.f. pulse disturbs net magnetisation into the transverse plane. The reversibility of T_2* dephasing is then exploited using a train of 180° refocusing pulses, forming "spin echoes", and $M_{x,y}$ decay is monitored with time. The refocusing 180_y° pulses are 90° out of phase to the 90_x° excitation r.f. pulse. The time between the first 90° and 180° pulse, $\tau_{90\text{-}180}$, must equal half the interecho time, $\tau_{180\text{-}180}$. These criteria are termed the CPMG condition. If not satisfied, destructive echo interferences and a more rapid decay occur, impacting the accuracy of T_2 values extracted. Using short interecho times significantly reduces molecular diffusion effects, and thus their contribution to signal losses. In a CPMG experiment, a full FID is acquired for a series of variable echo loop counts. Assuming exponential behaviour, T_2 recovery is defined by:

$$\frac{\mathrm{d}M_{\mathrm{xy}}}{\mathrm{d}t} = -\frac{M_{\mathrm{xy}}}{T_2}. \tag{2.20}$$

Its solution is given by:

$$M_{\mathrm{x,y}}(t) = M_{\mathrm{x,y}}(0)\exp\left(-\frac{t}{T_2}\right), \tag{2.21}$$

where $M_{x,y}(0)$ is the initial magnitude of transverse magnetisation. A one-shot CPMG experiment follows the same structure as Fig. 2.6, although one complex point is acquired at every echo along the train. T_2* can be measured from the full width at maximum height (FWHM) of an NMR spectrum, following a pulse-acquire experiment:

$$T_2{}^* = \frac{1}{\pi\, FWHM}. \tag{2.22}$$

2.1.3.3 Stimulated Spin Echoes

The stimulated echo (STE) sequence (Fig. 2.7) offers another approach for measuring T_2.

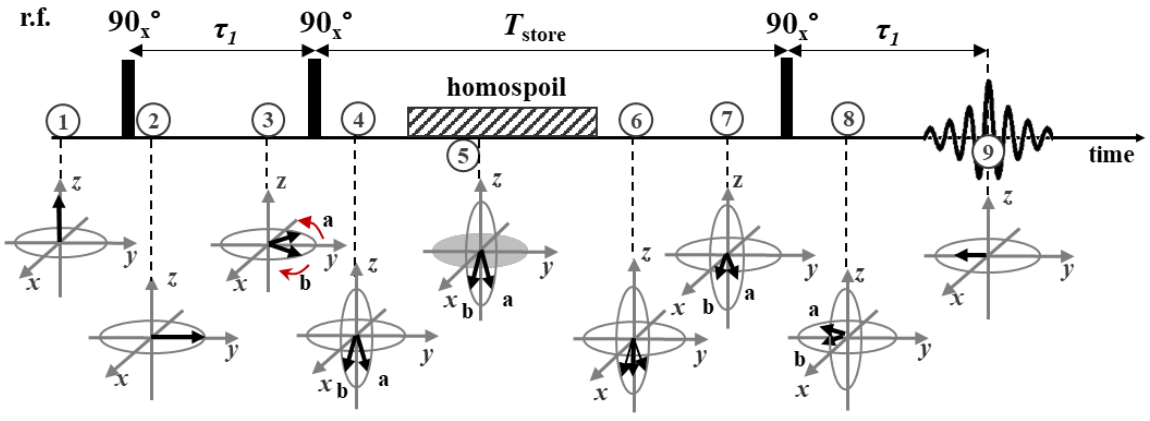

Figure 2.7. Timing diagram of the simulated echo (STE) sequence, with corresponding spin isochromats.

Following an initial 90° r.f. excitation, two further 90° pulses are used; T_2, T_2* and T_1 processes subsequently occur. The initial 90° pulse disturbs net magnetisation into the transverse plane, after which spins undergo T_2* relaxation. At time τ_1 after initial excitation, a second 90° pulse is applied. This

projects magnetisation into the $z'x'$ plane, where T_2 and T_2* processes 'freeze', and T_1 relaxation ensues for time T_{store}. The final 90° pulse returns magnetisation into the transverse plane, creating an echo – the stimulated echo. A homospoil magnetic field gradient is applied after the second 90° pulse, rapidly dephasing any residual transverse magnetisation.

The STE sequence is useful for systems with long T_1 but short T_2 and for studying diffusive motion, enabling transverse signal detection over longer time periods.

2.2 Basic Principles of MRI

2.2.1 Introduction

2.2.1.1 Magnetic Field Gradients and k-space

MRI delivers spatial resolution to NMR techniques. This is encoded into NMR acquisitions by spatially varying the applied magnetic field, achieved by applying an additional magnetic field gradient, **G**, to $\mathbf{B}_0$ such that the Larmor frequency varies spatially:

$$\omega(\boldsymbol{r}) = \gamma \mathbf{B}_0 + \gamma \mathbf{G} \cdot \mathbf{r}\,, \tag{2.23}$$

where **r** is the spin position vector.

A volume element dV at position **r** with spin density $\rho(\mathbf{r})$, contains $\rho(\mathbf{r})$ dV spins. Neglecting relaxation, the total signal within the volume element, dS, is given by:

$$\mathrm{d}S(\mathbf{G}, t) \propto \rho(\mathbf{r})\mathrm{d}V \exp[\mathrm{i}\omega(\mathbf{r})t]. \tag{2.24}$$

Combining Eqs. 2.23 and 2.24, and neglecting the $\mathbf{B}_0$ term (assuming the system is on resonance in the rotating frame), $S(t)$ is:

$$S(t) = \iiint \rho(\mathbf{r}) \exp[\mathrm{i}\gamma \mathbf{G} \cdot \mathbf{r}t]\, \mathrm{d}\mathbf{r}\,. \tag{2.25}$$

To simplify this relationship, the **k**-space vector (units of m^{-1}) is introduced:

$$\mathbf{k} = \frac{\gamma \mathbf{G} t}{2\pi}. \tag{2.26}$$

Substituting Eq. 2.26 into Eq. 2.25 highlights the Fourier relationship between time domain signal and spatial spin density (Eq. 2.27). Its inverse yields the Fourier conjugate (Eq. 2.28), from which spin density in real space, $\rho(\mathbf{r})$, is obtained.

$$S(\mathbf{k}) = \iiint \rho(\mathbf{r}) \exp[\mathrm{i}2\pi \mathbf{k} \cdot \mathbf{r}]\, \mathrm{d}\mathbf{r}, \tag{2.27}$$

$$\rho(\mathbf{r}) = \iiint S(\mathbf{k}) \exp[-\mathrm{i}2\pi \mathbf{k} \cdot \mathbf{r}]\, \mathrm{d}\mathbf{k}\,. \tag{2.28}$$

k-space can be traversed by either varying **G** (phase-encoding), or the gradient duration, t (frequency-encoding).

2.2.1.2 Traversing k-space

The progression (sampling pattern) through **k**-space is often illustrated using a **k**-space raster – a two-dimensional (2D) example is illustrated in Fig. 2.8b, for the 2D spin-warp imaging sequence in Fig. 2.8a (Edelstein *et al.*, 1980).

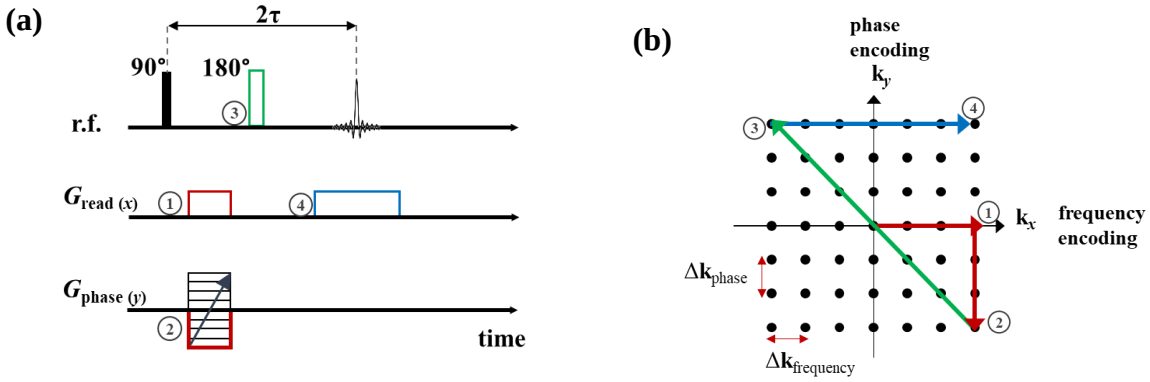

Figure 2.8. (**a**) 2D spin-warp MRI sequence. (**b**) **k**-space raster describing traversal through **k**-space for the sequence. A 90° excitation pulse rotates net magnetisation into the transverse plane. A dephasing frequency-encoding and a phase-encoding gradient are applied. (1,2). Application of a 180° pulse inverts the spin position through the centre of **k**-space (3). A rephasing readout gradient is applied (4), traversing a line of k-space, during which the signal is acquired.

The initial readout gradient (dephase gradient, $\mathbf{G}_d$) determines the extent **k**-space is sampled. Following a 180° pulse, a readout gradient (rephase gradient, $\mathbf{G}_r$) is used to traverse **k**-space until the desired **k**-space (defined by $\mathbf{G}_d$) is met. Signal is acquired during $\mathbf{G}_r$. For $\mathbf{G}_r$ to sample the **k**-space region set by $\mathbf{G}_d$, Eq. 2.29 must be satisfied:

$$\mathbf{G}_r t_r = 2\,\mathbf{G}_d t_d\,, \tag{2.29}$$

where t_r, t_d are rephase and dephase gradient durations. This is an example of frequency-encoded sampling. In contrast, **k**-space data can be acquired using phase-encoding sampling, such as single-point-imaging (SPI) techniques. Frequency-encoding facilitates more rapid data acquisition, as practically, the gradient coil hardware is not subjected to repeated ramping of field gradients (which carry associated delays).

2.2.1.3 Imaging Field of View

The spatial window in which a sample is imaged, the Field of View (*FOV*) (in units of m) is inversely proportional to the **k**-space increment, Δ**k**. For frequency and phase-encoded directions it is given by:

$$\text{(a)}\quad FOV_{\text{freq}} = \frac{1}{\Delta k} = \frac{2\pi}{\gamma \mathbf{G} \Delta t} \qquad \text{and} \qquad \text{(b)}\quad FOV_{\text{phase}} = \frac{1}{\Delta k} = \frac{2\pi}{\gamma \Delta \mathbf{G} t}\,. \tag{2.30}$$

2.2.1.4 Slice Selection

Prior discussions assumed r.f. pulses affect all spins uniformly. This can be achieved with a "hard" r.f. pulse, of high-power and short duration (thus, wide bandwidth $\Delta\omega_b$). MRI slice selection excites only a chosen sample region by selectively exciting a narrow frequency range. This is achieved by simultaneously applying a "soft" r.f. pulse (low-power, long duration with narrow bandwidth, $\Delta\omega_b$), to

an applied magnetic field gradient (slice gradient, $\mathbf{G}_{slice}$). Gaussian- or sinc-shaped ($\sin(x)/x$) pulses are typically used as the soft pulses.The soft pulse excites a narrow range of frequencies, whilst spin resonance frequencies along the gradient direction are spread out by $\mathbf{G}_{slice}$. Only spins resonating within the r.f. pulse bandwidth are excited (illustrated in Fig. 2.9).

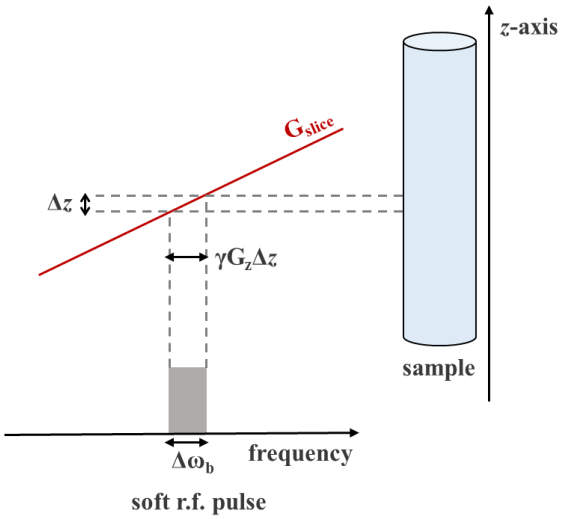

Figure 2.9. Slice selection by simultaneous application of a magnetic field gradient and a soft, narrow bandwidth r.f. pulse. Only spins that resonate within the bandwidth of the r.f. pulse, and thus slice, are observed.

The thickness of the excited slice is given by:

$$\Delta z = \frac{\Delta\omega_b}{\gamma G_{\text{slice}}}. \tag{2.31}$$

However, $\mathbf{G}_{slice}$ also acts as an image-encoding gradient, dephasing transverse magnetisation. To counteract this, dephased magnetisation must be rephased following the slice selective pulse. For a 90° soft pulse, magnetisation is assumed to reach the transverse plane halfway through the pulse. Thus, only the gradient in the second half of the soft pulse must be accounted for. This change in **k** is typically compensated for by applying a slice refocusing gradient of equal magnitude, half duration, and opposite direction to $\mathbf{G}_{slice}$ (see Fig. 2.10a). For a 180° soft pulse (Fig. 2.10b), a refocusing slice gradient is not usually needed, as any dephasing in the first half of the slice gradient is balanced by refocusing from the 180° inversion.

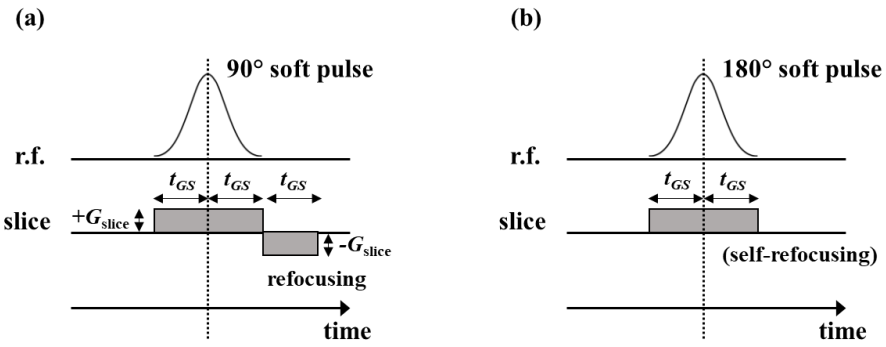

Figure 2.10. Refocusing gradient pulses used following the soft pulse during slice selection procedures, for **(a)** 90° soft pulse, **(b)** 180° soft pulse.

2.2.2 RARE Imaging

This section introduces the Rapid Acquisition with Relaxation Enhancement (RARE) imaging technique, used in Chapters 5 and 8. RARE (Hennig *et al.*, 1986) is a rapid, fully-sampled **k**-space, multidimensional imaging approach. Figure 2.11 shows a pulse sequence diagram for a 2D RARE acquisition.

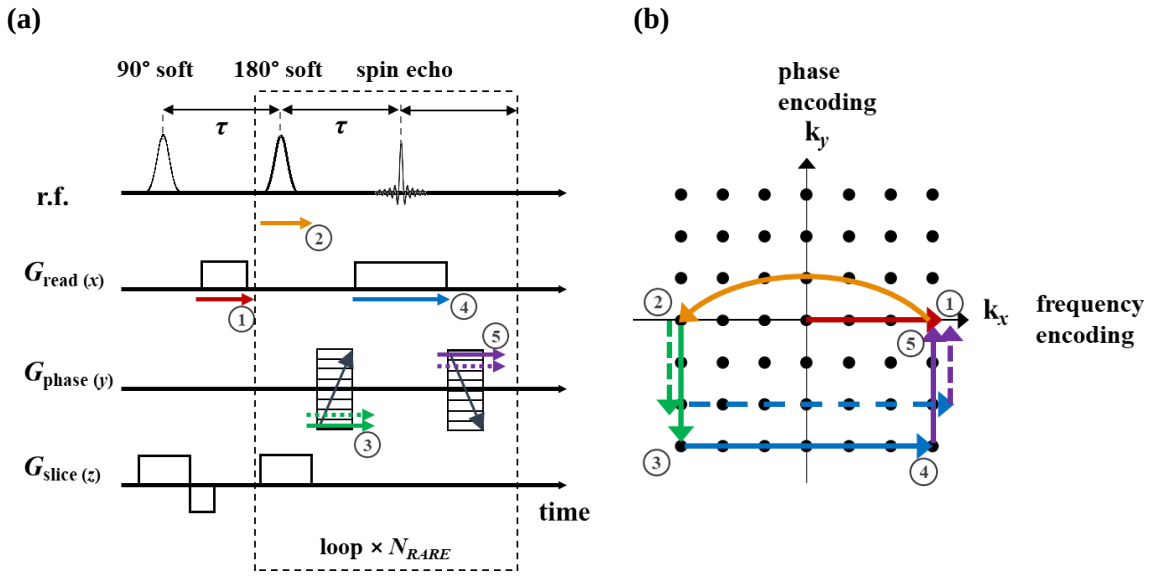

Figure 2.11. (a) 2D-RARE pulse sequence diagram; **(b)** corresponding 2D **k**-space raster, illustrating traversal through **k**-space within 2D-RARE sequence.

Following 90° soft pulse excitation, a dephasing frequency-encoding gradient is applied such that magnetisation lies at coordinates ($+k_{x,max}$, 0) in the 2D **k**-space raster. A 180° refocusing pulse inverts phase to ($-k_{x,max}$, 0). Next, the first phase-encoding gradient shifts magnetisation to ($-k_{x,max}$,k_{y1}). Simultaneously applying a frequency-encoding gradient, while digitally sampling the signal, allows a complete line of **k**-space to be acquired and results in a final magnetisation of ($+k_{x,max}$, k_{y1}). A second phase-encoding gradient (equal magnitude, opposite direction to the first) returns magnetisation to ($+k_{x,max}$,0). By incrementing phase-encoding gradients within each 180° r.f. pulse loop, multiple lines of

k-space are sampled with each initial excitation. The increment in applied phase gradient, ΔG_{phase}, is fixed, so that $\Delta\mathbf{k}$ and FOV_y are constant. The number of times magnetisation is refocused with 180° pulses, per each single excitation, is the RARE factor N_{RARE} (usually, 1–64). In 2D-RARE, slice gradients are applied perpendicular to the read and phase gradients. In three-dimensional (3D) RARE, a second phase-encoding gradient is used instead of slice gradients.

2.3 Pulsed-Field Gradient (PFG) NMR

2.3.1 PFG-NMR for Labelling Molecular Motion

PFG-NMR is an approach for measuring molecular motion (Stejskal and Tanner, 1965; Tanner, 1970), in which paired gradient pulses detect nuclear spin positional changes. As in Eq. 2.23, magnetic field gradients encode spatial position using locally-varying Larmor frequencies. By removing base Larmor frequency dependency (at $\mathbf{B}_0$), appropriate when considering signal heterodyning (section 2.1.2.2), the accrued phase of spins, φ, varies with position:

$$\varphi(\mathbf{r}) = \gamma\delta_G\mathbf{G}\cdot\mathbf{r} \tag{2.32}$$

where δ_G is gradient pulse duration. At time t after a first gradient pulse, gradient effects can be reversed with a second gradient pulse. If during t no molecular motion occurs, accrued phase of nuclear spins should fully rewind. If molecular motion occurs, a net phase shift is instead accrued:

$$\varphi(\mathbf{r}) = \gamma\delta_G\mathbf{G}\cdot(\mathbf{r}-\mathbf{r}')\,. \tag{2.33}$$

PFG-NMR uses this concept to detect both coherent (flow) and incoherent (diffusive) processes. This section focuses on PFG-NMR techniques for probing diffusion.

Signal attenuation from diffusion, under magnetic field gradients, can be modelled using a random walk analogy – where diffusion consists of discrete jumps, and motion is resolved in one dimension (along the applied gradient in z). For a nucleus jumping a displacement ξ (along z) at each step, with mean time τ_s between jumps, the displacement, Z, after n jumps at $t = n\tau_s$ is:

$$Z(n\tau_s) = \sum_{i=1}^{n}\xi a_i \tag{2.34}$$

where a_i is a random number equal to ±1.

The self-diffusion coefficient in one dimension, D, is:

$$D = {\xi^2}\Big/{2\tau_s}\,, \tag{2.35}$$

such that mean square displacement after t is:

$$\overline{Z^2(t)} = \overline{Z^2(n\tau_s)} = \sum_{i=1}^{n} \xi^2 \overline{a_i{}^2} = n\xi^2 = 2n\tau_s D = 2Dt \tag{2.36}$$

and for three dimensions:

$$\overline{R^2(t)} = 6Dt\,. \tag{2.37}$$

Following Eqs. 2.23, 2.32, the cumulative phase accrued during such a random-walk process after time *t* is:

$$\varphi(t) = \gamma \mathbf{B_0} n\tau_s + \sum_{m=1}^{n} \gamma \mathbf{G} \tau_s \sum_{i=1}^{m} \xi a_i\,. \tag{2.38}$$

The first term in Eq. 2.38 denotes constant average Larmor precession (not of interest and henceforth ignored), the second term is the phase deviation, $\Delta\varphi$, across the spin ensemble.

By assuming a Gaussian distribution of phase deviations (appropriate for a large sum of randomly varying quantities, by 'central limit theorem'), mean phase shift is:

$$\overline{\exp(\imath\Delta\varphi)} = \exp\left(-\frac{\overline{\Delta\varphi^2}}{2}\right) = \exp(-\tfrac{1}{3}\gamma^2 G^2 D t^3). \tag{2.39}$$

This t^3 dependency is characteristic of self-diffusion under a steady gradient. For a PFG experiment with two gradient pulses (duration δ_G), separated by observation time Δ, echo amplitude attenuation, S, is given by the Stejskal-Tanner equation:

$$S(G)/S(0) = \exp\left(-\gamma^2 G^2 {\delta_G}^2 D \left(\Delta - {\delta_G}/{3}\right)\right). \tag{2.40}$$

Equation 2.40 is used to calculate self-diffusivities from PFG-NMR experiments.

2.3.2 PFG Techniques

The pulsed-gradient spin echo (PGSE) sequence (Fig. 2.12) is the most basic PFG technique. Following initial 90° excitation, two magnetic field gradient pulses are applied either side of a refocusing 180° r.f. pulse (separated by observation time, Δ). If motion occurs during Δ, a net phase offset is accrued, resulting in signal attenuation (Eq. 2.40).

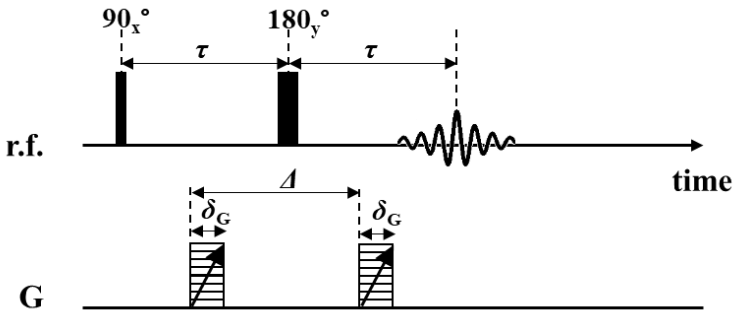

Figure 2.12. PGSE pulse sequence.

The accuracy of PFG-NMR measurements relies upon a homogeneous $\mathbf{B}_0$. For heterogeneous samples, such as fluid-imbibed porous materials, magnetic susceptibility contrast within a sample results in local magnetic field gradients. The alternating pulsed-gradient stimulated echo (APGSTE) sequence (Fig. 2.13), minimises such internal gradients. Developed by Cotts *et al.* (1989), it consists of a stimulated echo, a homospoil gradient, and paired gradient pulses of equal magnitude and opposite directions. Using a stimulated echo is advantageous for systems where $T_2 \ll T_1$ (common to porous media).

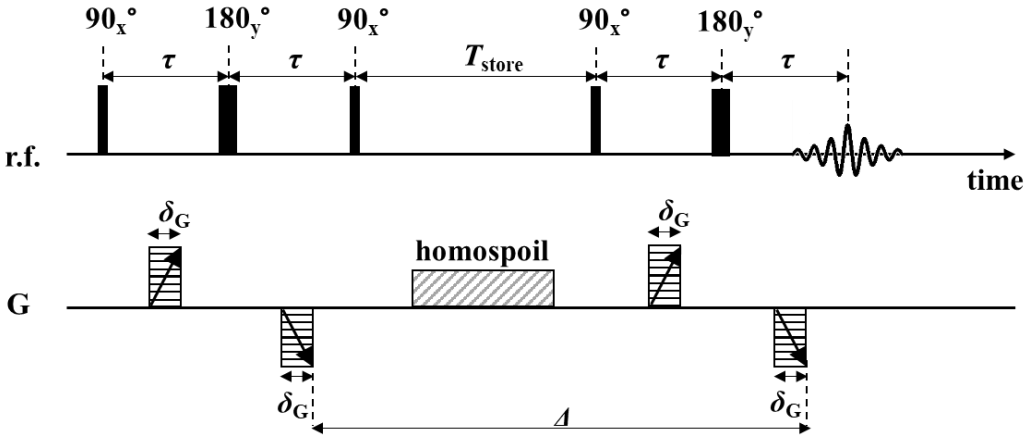

Figure 2.13. APGSTE pulse sequence.

Pulsed gradients, instead of continuous gradients, facilitate retention of chemical shift information and for entire sample volumes to be probed.

2.4 NMR in Petrophysical Systems

This section discusses NMR applications to petrophysical systems, including: magnetic field strengths; core floods; saturation quantification; pore structure, wettability and emulsion characterisation; and the challenges of internal field gradients.

2.4.1 Magnetic Field Strengths

NMR has been applied to reservoir well-logging tools (WLTs) since 1978, using permanent magnets with pulsed r.f. fields. The downhole requirement for permanent magnets limits WLTs to low magnetic fields, typically 50 mT, such that only ^{1}H NMR provides sufficient signal (high gyromagnetic ratio, abundant ^{1}H nuclei in reservoir fluids) (Kleinberg, 2001; Kleinberg and Jackson, 2001).

Ferromagnetic impurities, paramagnetic impurities and magnetic susceptibility contrasts at solid/fluid interfaces induce internal magnetic field gradients. These are common to fluid-imbibed rock samples (from iron-rich chlorite clays, or other magnetic materials in rocks) (Hürlimann, 1998). In laboratory core flooding mechanistic studies, clean outcrop cores (low impurity concentrations) are often used as reservoir rock analogues, to minimise internal gradients.

Internal gradients present several challenges. Very short T_2* values are induced (Eq. 2.19), resulting in increased signal attenuation, decreased SNR (Baldwin and King, 1998; Mitchell *et al.*, 2013c) and broad resonant frequencies (Eq. 2.5) giving broad spectral linewidths and limited chemical resolution. Internal gradients also increase diffusive attenuation, influencing diffusion-sensitive T_2 measurements.

To minimise internal gradients, low-field laboratory systems (0.4 – 3T) (Mitchell *et al.*, 2013c) are often used. This enables comparison with oilfield NMR well-logging tools, however limits SNR and chemical resolution, due to reduced offset frequencies between nuclei in different chemical environments. Internal gradient corrections can be applied post-processing – see section 2.4.6.

2.4.2 MR Techniques in Core Flood Monitoring

Most early MRI core flood studies acquired 2D images of rock core cross sections at varying timepoints in a flood, using primarily spin-echo imaging sequences (Baldwin and Yamanashi, 1988, 1991; Majors *et al.*, 1990; Enwere and Archer, 1992; Kim *et al.*, 1992; Williams *et al.*, 1991, 1994), among other MRI approaches (Rothwell and Vinegar, 1985; Blackband *et al.*, 1986).

Whilst many authors continued using these sequences (Baraka-Lokmane *et al.*, 2001; Baldwin *et al*. 2009; Ersland *et al.*, 2010a,b; Washburn and Madelin, 2010; Liu *et al.*, 2011; Song *et al.*, 2013), other MRI techniques are now also used. For example, SPI approaches (Chen *et al*., 2003; Romero-Zerón *et al*., 2009, 2010; Yuechao *et al.*, 2011); axially-resolved T_2 (Majors *et al.*, 1997; Beyea *et al.*, 2000; Li *et al.*, 2009; Petrov *et al.*, 2011; Mitchell *et al.*, 2012c, 2013d); and rapid, undersampled 3D-imaging, with compressed-sensing RARE (Ramksill *et al.*, 2016, 2018), enabling dynamic 3D core flood monitoring. PFG propagator measurements have been used for quantifying fluid mobility changes (Johns *et al.*, 2003; Colbourne *et al.*, 2016), and 2D T_1-T_2 and D-T_2 techniques for quantitative saturation monitoring (Mitchell *et al*., 2012a,b,c, 2013a,c).

2.4.3 Volumetric Quantification using Hydrogen Indices

NMR signal is proportional to nuclear spin density. Fluid-specific signal volumetric quantification (thus, saturation) can be quantified using the hydrogen index, *HI*, defined at standard temperature and pressure (STP) conditions:

$$HI = \frac{\text{quantity of } {}^1\text{H in sample}}{\text{quantity of } {}^1\text{H in pure water at STP}}. \tag{2.41}$$

HI are measured by calibrating NMR signal intensity responses for known sample volumes, against that of water, at the conditions of interest:

$$HI = \frac{\left(M_{0,\text{fluid}}/V_{\text{fluid}}\right)_{\text{conditions of interest}}}{\left(M_{0,\text{H}_2\text{O}}/V_{\text{H}_2\text{O}}\right)_{\text{conditions of interest}}}, \tag{2.42}$$

where M_0 is initial signal intensity, V is fluid volume. M_0 is determined by extrapolating FID or CPMG responses to zero time (Appel, 2004; Schön, 2011).

Alkane *HI* can be predicted, as a function of mass density ρ_m (in g cm^{-3}), by the Gaymard and Poupon (1968) correlation (Eq. 2.43). Zhang *et al.* (1998) demonstrated good agreement for pure hydrocarbons at ambient conditions:

$$HI = 9\rho_m[0.15 + 0.2(0.9 - \rho_m)^2] . \quad (2.43)$$

2.4.4 Relaxation Time Measurements for Probing Petrophysical Systems

The following sections introduce how relaxation times can characterise pore size distributions and surface interaction strengths. Mathematical regularisation methods for obtaining relaxation time distributions for multicomponent datasets are also discussed.

2.4.4.1 Pore Size Distributions from Relaxation Time Distributions

For liquids in porous media, the resultant T_1 and T_2 distributions are related to pore size distributions (Gallegos *et al.*, 1987; Davies and Packer, 1990; Davies *et al.*, 1991) by:

$$\frac{1}{T_1} = \frac{1}{T_1^{(\text{bulk})}} + \rho_1 \frac{S_p}{V_p} \quad (2.44)$$

$$\frac{1}{T_2} = \frac{1}{T_2^{(\text{bulk})}} + \rho_2 \frac{S_p}{V_p} + \frac{1}{T_2^{(\text{diffusion})}} \quad (2.45)$$

where $T_{1,2}$ indicates measured T_1 or T_2, $T_{1,2}^{(\text{bulk})}$ indicates bulk fluid T_1 or T_2, $\rho_{1,2}$ are surface relaxivity terms associated with T_1 or T_2, S_p/V_p is the pore space surface-to-volume ratio and $T_2^{(\text{diffusion})}$ is T_2 relaxation attributed to diffusion under internal field gradients. These relationships are applicable provided spins on the pore surface exchange with bulk pore liquid spins on the experiment timescale – fast-diffusion (surface-limited) regime (Brownstein and Tarr, 1987). In rocks, surface-limited regimes are expected, as relaxation times are temperature-independent (for 25-175 °C) and are thus not in the slow-diffusion (diffusion-limited) regime (Latour *et al.*, 1992; Kleinberg, 1994).

Differences in $T_{1,2}$ and $T_{1,2}^{(\text{bulk})}$ result from enhanced relaxation of fluids confined within porous materials, from molecules colliding with pore walls. Typically, $T_{1,2}^{(\text{bulk})} >> T_{1,2}$ such that the bulk term is negligible and observed $T_{1,2}$ distributions yield pore size distributions.

2.4.4.2 Surface Interaction Strengths from T_1/T_2

Recent developments have shown that T_1/T_2 indicates surface interaction strengths and adsorption energies, where higher ratios imply higher interaction strengths (McDonald *et al.*, 2005; Mitchell *et al.*, 2009b; D'Agostino *et al.*, 2014). This has been applied to rock wettability characterisation (Mitchell *et al.*, 2013a) and competitive adsorption in catalysis (Weber *et al.*, 2009).

Reduced T_1 and T_2 times occur in porous media, from molecular mobility changes when molecules adsorb onto solid surfaces (Liu *et al.*, 1991). In bulk liquids molecular tumblings are fast and isotropic, so $T_1 \approx T_2$, $T_1/T_2 \approx 1$. In porous media, T_2 molecular tumblings are slow and anisotropic, where T_2 is

additionally influenced by surface diffusion (Weber *et al.*, 2010; Mitchell *et al.*, 2013a). T_2 is thus more affected than T_1, with $T_2 < T_1$ and $T_1/T_2 > 1$ (McDonald *et al.*, 2005).

Although T_1 and T_2 are influenced by surface interactions, their dependence on S_p/V_p means that, alone, they cannot compare surface interactions for materials of differing pore sizes and geometries. However, T_1/T_2 is independent of S_p/V_p, facilitating such comparisons, as can be demonstrated from Eqs. 2.44, 2.45. Negating diffusive influences on T_2, a general expression for T_1 and T_2 is:

$$\frac{1}{T_{1,2}} = \frac{1}{T_{1,2}^{(\text{surface})}} + \frac{1}{T^{(\text{bulk})}}, \tag{2.46}$$

where $T_{1,2}^{(\text{surface})}$ indicates surface relaxation time components (where: $1/T_{1,2}^{(\text{surface})} = \rho_{1,2} S_p/V_p$) and $T^{(\text{bulk})}$ is the relaxation time of bulk liquid fluid, assuming $T_1^{(\text{bulk})} \approx T_2^{(\text{bulk})}$. Using Eq. 2.46 to compute T_1/T_2 gives:

$$\frac{T_1}{T_2} = \frac{T_1^{(\text{surface})}\left(T_2^{(\text{surface})} + T^{(\text{bulk})}\right)}{T_2^{(\text{surface})}\left(T_1^{(\text{surface})} + T^{(\text{bulk})}\right)}. \tag{2.47}$$

Generally, for porous media $T_{1,2}^{(\text{surface})} \ll T^{(\text{bulk})}$, such that:

$$\frac{T_1}{T_2} \approx \frac{T_1^{(\text{surface})}}{T_2^{(\text{surface})}} = \frac{\rho_2}{\rho_1}. \tag{2.48}$$

This condition is limited by bulk relaxation times, and pore sizes (influencing signal proportions from surface-interacting spin nuclei, or nuclei in pore centres) (Mitchell and Fordham, 2014; Valori *et al.*, 2017). Further, $\rho_{1,2}$ depend on spin resonance frequency, and thus $\mathbf{B}_0$. With increasing field strength, ρ_1/ρ_2 decreases, whilst ρ_2/ρ_1 increases – delivering a T_1/T_2 ratio of increased sensitivity (Godefroy *et al.*, 2001; Mitchell and Fordham, 2014).

A particularly useful method for measuring T_1, T_2 and T_1/T_2 is the 2D T_1-T_2 measurement (English *et al.*, 1991; Song *et al.*, 2002; Song *et al.*, 2010). These datasets provide information on the correlation of both relaxation time distributions and can provide signal contrast between different fluids, based upon relaxation time differences. In addition, the correlation corrects for relaxation effects, enabling for recovery of true NMR signal intensity (hence spin populations and fluid volumes). A pulse sequence diagram is presented in Fig. 2.14.

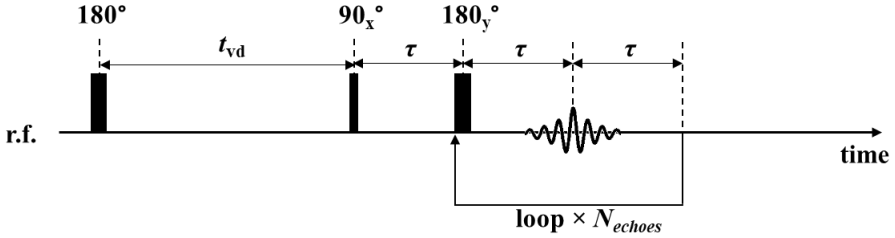

Figure 2.14. 2D T_1-T_2 inversion recovery preconditioned CPMG pulse sequence. N_{echoes} denotes the number of echoes in the CPMG train.

2.4.4.3 1D and 2D Inversion Processing of Relaxation Time Measurements

The following outlines processing methods by which one-dimensional (1D) T_1, T_2, D and 2D T_1-T_2 distributions can be extracted from NMR relaxation and diffusion datasets. The numerical methods described are those within the Magnetic Resonance Research Centre (MRRC) in-house code. Further details can be found in the literature (Mitchell *et al.*, 2012a; 2013c).

NMR relaxation and diffusion data can be described by the first-order Fredholm integral, with general form in 1D:

$$\frac{h(t)}{h(0)} = \int_0^\infty k_0(x,t) f(x)\ d(\log_{10} x) \tag{2.49}$$

where $h(t)/h(0)$ is normalised, noiseless signal with time, k_0 is the model kernel function describing signal attenuation, x is the time constant (that is, T_1, T_2, D) and $f(x)$ is the distribution of x on the $\log_{10}$ scale.

Equivalently, for a 2D NMR correlation, the general form becomes:

$$\frac{h(t_1,t_2)}{h(0,0)} = \iint_0^\infty k_0(x_1,t_1,x_2,t_2) f(x_1,x_2)\ d(\log_{10} x_1) d(\log_{10} x_2) \tag{2.50}$$

where subscripts 1,2 denote direct and indirect experimental dimensions respectively – for example, for 2D T_1-T_2 (Fig. 2.14): T_2 is direct, T_1 is indirect.

In reality, measured signal $b(t)$ is composed of "noiseless" signal $h(t)$ and noise $e(t)$:

$$b(t) = h(t) + e(t)\ . \tag{2.51}$$

For NMR relaxation and diffusion, the kernel has general form:

$$k_0(x,t) = exp\left(-t/x\right). \tag{2.52}$$

Equations 2.49, 2.50 are challenging inverse problems to solve and numerical methods are required. Using matrix notation, the Fredholm integral is expressed as:

$$\mathbf{b} = \mathbf{K_0 f} + \mathbf{e} \tag{2.53}$$

where $\mathbf{b}$ is the data matrix, $\mathbf{K}_0$ is the kernel matrix, $\mathbf{f}$ is the desired fitted distribution and $\mathbf{e}$ is experimental noise.

Numerically, the solution to Eq. 2.53 is given by the minimisation:

$$\hat{\mathbf{f}} = \text{argmin}_{\mathbf{f}\geq 0} \|\mathbf{b} - \mathbf{K_0 f}\|^2 \tag{2.54}$$

where ||…|| is the Euclidean norm. The inversion in Eq. 2.54 can however lead to non-physical solutions, as $\mathbf{K}_0$ is ill-conditioned. The problem can be constrained by limiting $\hat{\mathbf{f}}$ to be non-negative, bounded by limiting values of x and a smooth distribution.

Tikhonov regularisation (Wilson, 1992; Venkaramanan *et al.*, 2002) delivers a smoothed solution by introducing a penalty function that suppresses solutions with non-physical fluctuations. Following Tikhonov regularisation inversion approaches, Eq. 2.54 becomes:

$$\hat{\mathbf{f}} = \text{argmin}_{\mathbf{f} \geq 0}(\|\mathbf{b} - \mathbf{K_0}\mathbf{f}\|^2 + \alpha\|\mathbf{L}_s\mathbf{f}\|^2). \quad (2.55)$$

The term $\alpha\|\mathbf{L}_s\mathbf{f}\|^2$ is the penalty function, where $\mathbf{L}_s$ is the operator representing the smoothing criterion and α is the smoothing parameter controlling the degree of smoothing. α can be optimised using a variety of methods – in the MRRC code, General Cross Validation (GCV) is used (Wahba, 1977). The resulting solutions (1D or 2D correlated probability distributions of diffusivities or relaxation times) are corrected for diffusion and relaxation time effects and are thus volumetrically quantitative.

2.4.5 Restricted Diffusion PFG for Structural and Emulsion Characterisation

PFG-NMR techniques detect phase shifts from spin motion during an experimental observation time, Δ. For unrestricted systems, this measures molecular self-diffusivities. If diffusion occurs, spin nuclei move such that a refocusing gradient cannot refocus accrued phase differences, resulting in signal attenuation.

If spin nuclei are restricted by a boundary (such as a pore wall, or an enclosing emulsion droplet "wall"), restricted diffusion effects can occur. Provided Δ is sufficiently large such that spins can diffuse without being limited by this boundary, PFG-NMR will probe sample self-diffusivity. If Δ is less than the time required for spins to diffuse and collide with this boundary, spins are limited to diffusing a fixed distance, undergoing multiple collisions with the enclosing boundary – termed restricted diffusion (Johns and Hollingsworth, 2007).

Restricted diffusion PFG-NMR can characterise internal porous structures and emulsions, typically in a size range 5-100 μm (Barrie, 2000). For example, Mitra *et al.* (1993) and Hürlimann *et al.* (1994) demonstrated that rock S_p/V_p can be estimated from D, obtained through PFG-NMR measurements as a function of Δ. For emulsion sizing, acquiring PFG-NMR experiments at variable Δ can detect onsets of restricted diffusion. Numerous authors have derived mathematical expressions to model the influence of droplet size on PFG signal attenuation (Johns and Hollingsworth, 2007).

2.4.6 Internal Field Gradients

Internal magnetic field gradients are common to rocks in NMR systems (section 2.4.1). The total magnetic field variation across a pore is given by $\Delta\chi\mathbf{B}_0$, where $\Delta\chi$ reflects magnetic susceptibility differences. Thus, strongest internal gradients are observed in smaller pores, weakest internal gradients in larger pores. For weak internal gradients, maximum effective internal gradients can be estimated from spectral line broadening when a liquid is imbibed in porous material, relative to a bulk liquid response.

Although T_1 is unaffected, observed T_2 relaxations contain multiple components due to contributions from surface relaxation and diffusion in the presence of internal gradients. Internal gradient corrections

can be applied in post-processing to negate these effects on T_2. The following section outlines the internal gradient correction – further details are found in the literature (Mitchell *et al.*, 2010a,b; 2013c).

As spins diffuse through internal gradients, enhanced signal attenuation occurs. The influence of internal gradients is determined by three lengthscales: pore size l_s, bulk liquid root-mean-square (RMS) diffusion distance l_e, and dephasing lengthscale from internal gradients l_g, where l_e, l_g are:

$$l_e = \sqrt{D_0 t_E} \tag{2.56}$$

$$l_g = \left(\frac{D_0}{\gamma g_{eff}}\right)^{\frac{1}{3}}. \tag{2.57}$$

D_0 is the free bulk liquid diffusion coefficient, t_E is CPMG interecho time, g_{eff} is effective gradient strength. The relative scaling of these lengthscales determines how observed diffusion tends towards one of three asymptotic limiting regimes, the motional averaging (MAV), short time (ST) and localisation (LOC) regimes.

The MAV regime applies when $l_s \ll l_g$, l_e, where signal attenuation varies with l_s^4 and t_E. This is not expected in well-connected pore networks. The ST regime applies when $l_e \ll l_g$, l_s, equivalent to free diffusion, where surface relaxation varies with t_E and diffusive attenuation varies with t_E^3. In this regime, diffusive and surface relaxation contributions can be deconvolved. The LOC regime applies when $l_g \ll l_e$, l_s, with signal attenuation varying with t_E – such conditions result in rapid signal loss and is thus not expected in pores. Beyond these three asymptotic regimes, magnetisation decay is governed by a diffusion exponent varying with t^{k_D}, where $1 < k_D < 3$, and a surface relaxation time varying with t_E.

Surface relaxation and diffusive internal gradient components can be separated within this pre-asymptotic regime. To determine internal gradient contributions to observed T_2, a CPMG experiment is acquired with varying interecho times. To obtain a 2D distribution of T_2-g_{eff}, the variable-interecho CPMG dataset is fitted using the first-order Fredholm integral (section 2.4.4.3). The kernel function for diffusive decay is described assuming a pre-asymtotic regime, where k_D is identified from when normalised CPMG magnetisation (acquired at variable interecho times), collapses onto a smooth continuous line when plotted against t^{k_D}.

Once the g_{eff}-T_2 2D distribution is known, g_{eff} is obtained by projecting the 2D distribution onto the g_{eff} axis. Its influence can subsequently be removed from other CPMG-based experiments, by incorporating g_{eff} into inversions of measured T_2 decays.

Chapter 3

Implementation and Validation of Spatially-Resolved NMR Relaxometry Sequences

3.1 Introduction

This chapter introduces spatially-resolved T_2 (L-T_2) and spatially-resolved T_1-T_2 (L-T_1-T_2) sequences used in subsequent chapters. The methodologies for implementation and validation at different field strengths (85 MHz and 2 MHz) are discussed, together with data processing techniques.

Spatially-resolved measurements are invaluable to core flood monitoring, due to localised heterogeneities in core properties and fluid distributions (section 1.2.2). Combined with the pore structural, wettability and chemical contrast information (section 2.4.4) provided by NMR relaxometry, L-T_2 and L-T_1-T_2 measurements deliver a powerful toolkit for probing fluid displacement mechanisms in core flooding experiments

Prior work with L-T_2 and L-T_1-T_2 sequences has been conducted using both frequency-encoded (Majors *et al.*, 1997; Chen *et al.*, 2010; Mitchell *et al.*, 2013c) and phase-encoded methods (Li *et al.*, 2009; Chen *et al.*, 2010; Petrov *et al.*, 2011; Mitchell *et al.*, 2013d). Phase-encoding approaches provide more robust measurements for short-T_2 samples (Mitchell *et al.*, 2013d), however acquisition times are slower. In this thesis, the higher temporal resolution offered by frequency-encoding is exploited, enabling dynamic monitoring of displacement processes in systems with moderately-long T_2 characteristics (typical to rock cores).

Figure 3.1 displays timing diagrams for the L-T_2 and L-T_1-T_2 sequences implemented at 85 MHz and 2 MHz. Spatial-T_2 information can be extracted from L-T_2 sequences by Fourier transforming each spin echo, obtaining decaying axial profiles with time. By fitting a multicomponent T_2 decay (using 1D regularisation, section 2.4.4.3) to each pixel position along relaxing axial profiles, an axial T_2-map is produced. The L-T_1-T_2 sequence has a preconditioning 180° inversion pulse prior to the L-T_2 train, akin to the 2D T_1-T_2 inversion recovery sequence.

At 85 MHz, a non-continuous imaging gradient was applied; at 2 MHz, a continuous gradient was used. The non-continuous gradient approach is more favourable: it does not introduce slice-selection risks, has smaller gradient duty cycles, and does not magnify imperfect 180° pulse effects at outer sample regions (the latter arising from simultaneous r.f. pulse and gradient applications, where axially-variant fields would influence optimal r.f. durations for achieving a desired tip angle from $\mathbf{B}_0$, Eq. 2.11). Whilst possible at 85 MHz, the non-continuous approach was not possible at 2 MHz due to long gradient stabilisation times. Sequence implementation and validation approaches at each field strength are discussed in sections 3.2 and 3.3.

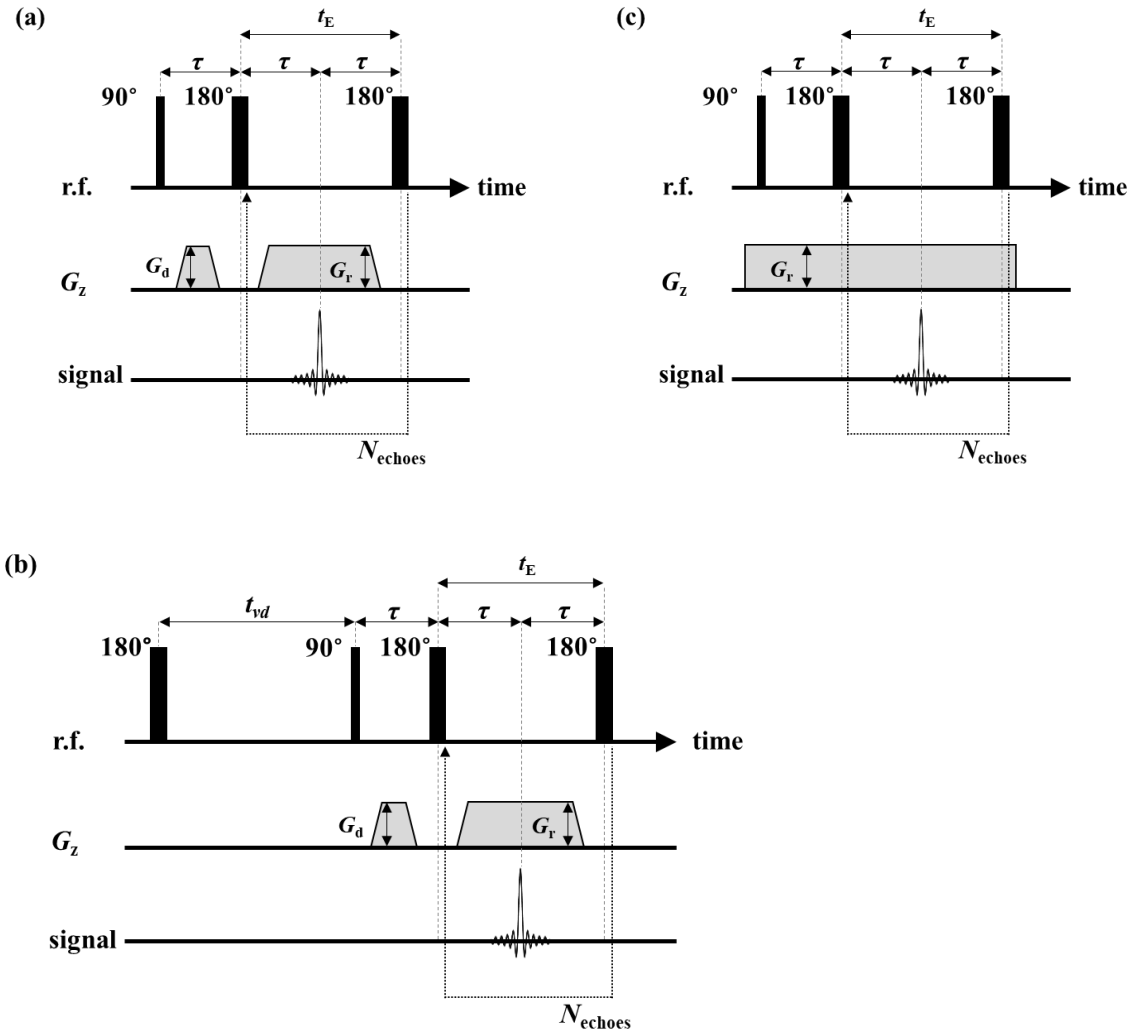

Figure 3.1. Timing diagrams of frequency-encoded, spatially-resolved NMR relaxometry sequences implemented on 85 MHz and 2 MHz systems: **(a)** L-T_2, 85 MHz; **(b)** L-T_1-T_2, 85 MHz; **(c)** L-T_2, 2 MHz. All sequences consist of a CPMG train, combined with a frequency-encoding gradient for 1D spatial resolution. $\boldsymbol{\tau}$ is half interecho time; 180° and 90° are r.f. pulse tip angles; G_d and G_r denote dephase and rephase gradients; N_{echoes} denotes number of echoes; t_{vd} is variable delay time between the preconditioning 180° r.f. pulse and L-T_2 train.

3.2 Implementation and Validation at 85 MHz

This section details the implementation (section 3.2.1) and validation (section 3.2.2) of L-T_2 and L-T_1-T_2 sequences at 85 MHz.

3.2.1 Implementation Approach

Multiecho frequency-encoded sequences are sensitive to echo interferences within the echo train, and imbalanced dephase and rephase imaging gradients (Williams *et al.*, 1999). A non-centred spin echo propagates through a CPMG train, resulting in echo splitting, echo interference and following Fourier transformation, yields non-physical axial profiles. Similarly, imbalanced gradients (resulting from not satisfying Eq. 2.29) incur echo interferences and yield non-physical axial profiles. In both cases, non-

physical axial profiles along spin echo trains are manifested with inaccurate relaxation characteristics in the resultant axial-T_1 and -T_2 maps. Accordingly, it is essential that both spin and gradient echoes are preserved between successive 180° pulses.

The L-T_2 sequence structure was first optimised before including the preconditioning inversion pulse for L-T_1-T_2. Firstly, spin echo timings were tested to ensure consistent echo occurrence midway between refocusing 180° r.f. pulses (validated through split echo acquisitions). Secondly, gradient strengths were optimised to ensure identical progression through **k**-space for each echo. These stages are further discussed in sections 3.2.1.2 and 3.2.1.3.

3.2.1.1 Materials and NMR Hardware

Sequence implementation was conducted using a doped deionised water (DI) phantom, in a 160 mm × 10 mm flat-bottomed glass NMR tube. This was selected as a cylindrical liquid-filled tube has a uniform, flat-top 1D profile, illustrated in Fig. 3.2. Thus, any non-physical discrepancies in Fourier-transformed spin echoes, compared to the expected flat-top profile, would indicate presence of spin or gradient echo interferences in the pulse sequence.

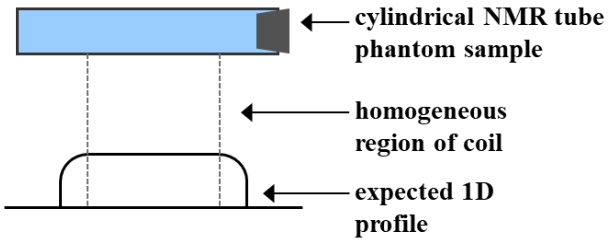

Figure 3.2. Schematic of expected 1D axial profile for a cylindrical liquid-filled NMR tube.

The phantom was prepared using gadolinium(III) chloride hexahydrate crystalline aggregates (99.9 %, Alfa Aesar) and DI obtained from a laboratory purification system (ELGA, DV25, Pure Lab Option), to a concentration of 1.075 ± 0.001 g $GdCl_3$/litre deionised water. All DI water used for every study within this thesis was obtained from this purification system.

All NMR experiments in section 3.2 were conducted at room temperature (20 ± 1 °C) in a 2 T (85 MHz for ^{1}H nuclei) horizontal bore superconducting magnet, controlled by a Bruker AV spectrometer. A 63 mm inner diameter (I.D.) r.f. birdcage coil, tuned to 85.2 MHz was used for excitation and signal detection. Spatial resolution along the coil axis (z) was achieved with a magnetic field gradient, capable of maximum gradient strength G_{max} = 10.7 G cm^{-1}.

3.2.1.2 Spin Echo Timing Preservation in Multiecho Sequences

This section outlines the methods used for verifying that L-T_2 spin echoes are preserved between successive 180° pulses. This stage was conducted without imaging gradients, to remove any influence of imaging gradients on echo position. To accurately determine the location of spin echo centres, sharp echoes were required. This was achieved by deshimming and disrupting the magnetic field homogeneity, to reduce sample T_2* (Eq. 2.19), resulting in rapid signal decay and thus sharper echoes.

Whilst section 2.1.3 presented spin (SE) and stimulated echoes (STE) as independent processes, due to imperfect 180° pulses certain spins will experience 90° pulses (Norris *et al.*, 1992). Provided the CPMG condition (section 2.1.3.2) is satisfied, STEs and SEs will coincide and interfere constructively, illustrated in Fig. 3.3.

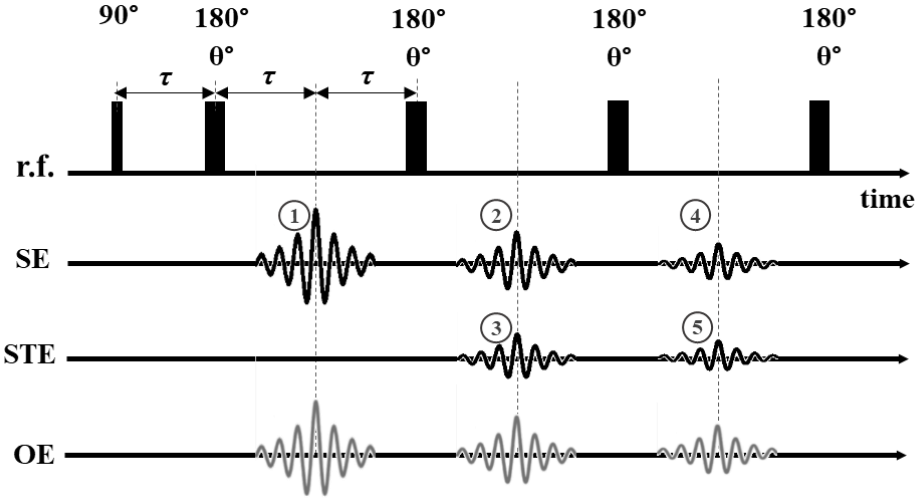

Figure 3.3. SE and STE formation from a train of 180° and 90° pulses. STEs result from imperfect 180° pulses. OE denotes experimentally observed echoes, resulting from constructive interference of SEs and STEs. SEs form following the first 90° and subsequent refocusing from repeated 180° pulses. STE (3) forms from the first 90°, and first two 180° pulses. STE (5) forms from the stimulated echo of SE (1) about the second and third 180° pulses.

By doubling the echo acquisition window (such that $\tau_{180\text{-}180} = 4\tau_{90\text{-}180}$), spin and stimulated echoes can be separated – termed split echo acquisition (Fig. 3.4). If the CPMG condition is not fulfilled, additional echoes located at unexpected positions within the 4τ window, together with destructive interferences, appear (Fukushima and Roeder, 1981; Callaghan, 1991; Norris *et al.*, 1992; Chen, 2010).

This acquisition protocol can be used for testing whether a multi-spin echo sequence satisfies the CPMG condition. Figure 3.5a presents raw NMR signal for a split echo acquisition recorded using: $\tau = 3362$ µs, $N_{\text{echoes}} = 8$, $t_{\text{DW}} = 10$ µs and number of complex points, $N = 1024$. For clarity, only the first four echoes are presented. Echo maxima locations, reported as fractional positions within the 4τ inter-180° pulse period, are presented in Fig. 3.5b.

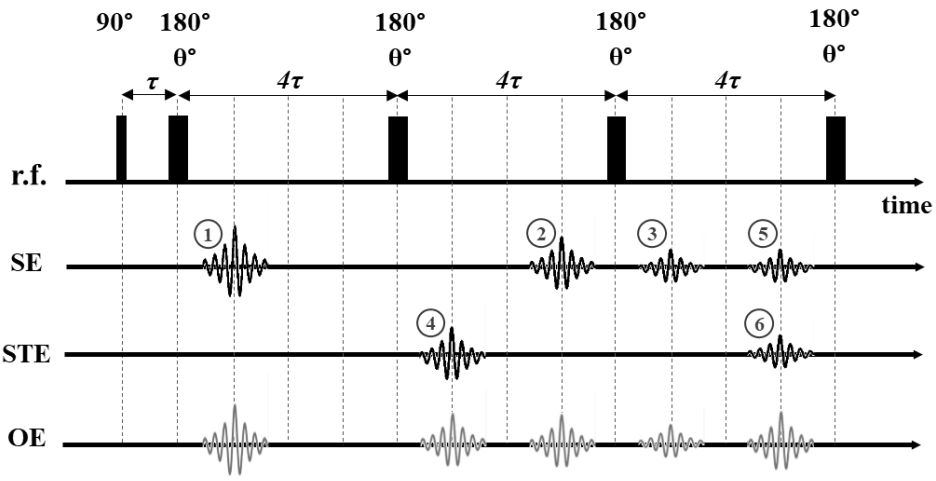

Figure 3.4. Spin echo train sequence under split echo acquisition, where interecho spacing between 180° pulses is four times greater than that between the first 90° and 180° pulse, τ. OE denotes experimentally-observed echoes, from SE and STE interferences. Echo (1) is the primary SE formed from the 90° and first 180° pulse. (2) and (3) are subsequent SEs through 180° spin echo refocusing of echo (1). Echo (4) is the first STE, produced from the first 90°, and first two (imperfect) 180° pulses. (5) is the SE of STE (4) about the third (imperfect) 180° pulse. (6) is the STE of the SE (1) about the second two (imperfect) 180° pulses.

Figure 3.5 demonstrates that the L-T_2 timing structure satisfied the CPMG condition, such that STEs and SEs constructively interfere, as in Fig. 3.4, without additional echoes from destructive interferences. Accordingly, observed echoes consistently occur at locations τ and 3τ within the 4τ period.

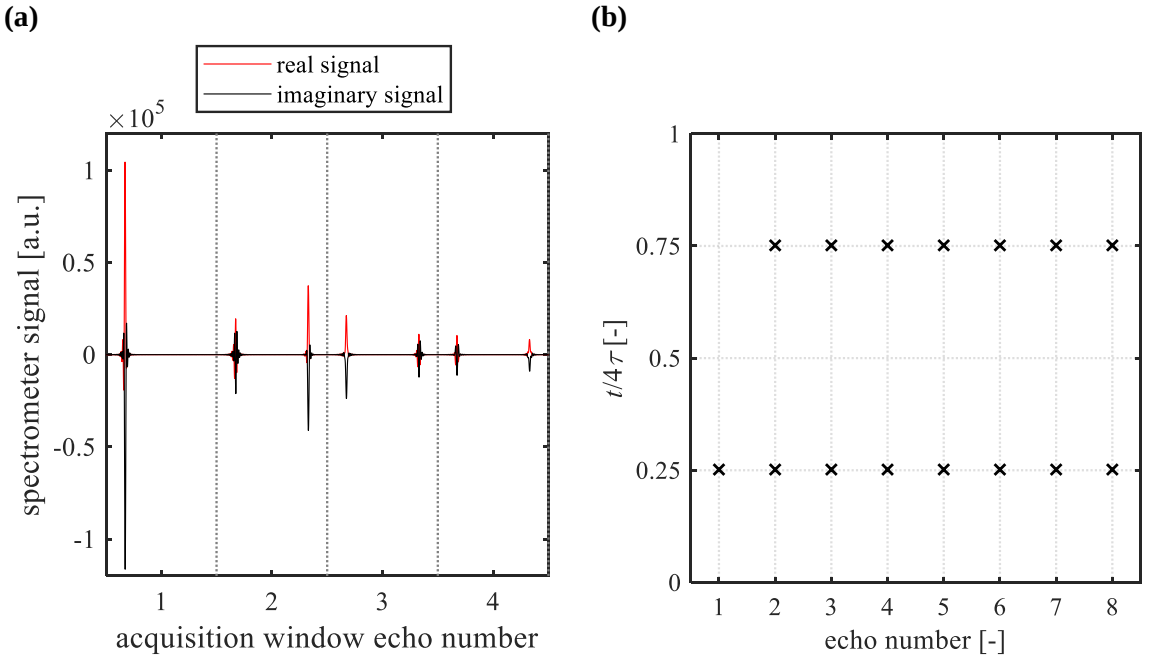

Figure 3.5. (a) Raw NMR signal from the L-T_2 sequence, acquired without imaging gradients, with a deshimmed system and under split echo acquisition. Only the first four echoes are presented. The acquisition windows were centred within each 4τ inter-180° period, collecting signal for a period less than 4τ. **(b)** Locations of the observed echo maxima are denoted as fractional time positions within the full 4τ period, $t/4\tau$.

3.2.1.3 Calibration of Frequency Encoded Imaging Gradient Strengths

L-T_2 imaging gradients were designed to be as stable as possible: (i) to allow for gradient rise times in gradient coil activation and deactivation (Callaghan, 1991), gradient durations were increased beyond that required for data sampling, and the acquisition window centred within this; (ii) ramped gradients were used for increasing stability of gradient switching, reflected in Fig. 3.1a. To test the gradients: the rephase gradient required for the desired *FOV* was applied, (Eq. 2.30); next, the theoretically-defined dephase gradient required to symmetrically traverse **k**-space at each echo was calculated (Eq. 2.29).

The theoretically-calculated dephase gradients did not preserve the gradient echo, resulting in echo interferences and non-physical profiles along the echo train (see Fig. 3.6a). The first echo profile is an accurate representation of the phantom profile (no echo interferences, physically meaningful profile) whilst the following echoes experience echo interferences, resulting in non-physical profiles. Gradient optimisation was subsequently conducted, by calibrating dephase gradient strengths to obtain flat, physically-representative profiles throughout the train – demonstrated in Fig. 3.6b.

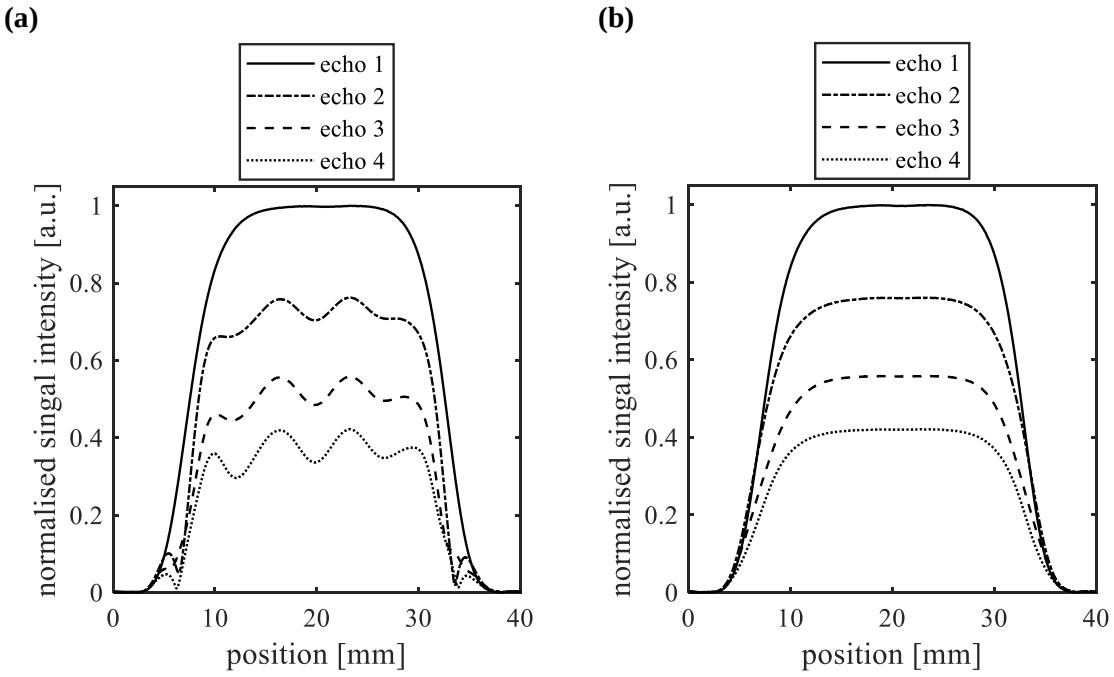

Figure 3.6. Profiles from the first four echoes in the L-T_2 echo train of a $GdCl_3.6H_2O$-doped DI water phantom in a cylindrical NMR tube. **(a)** L-T_2 with theoretically-calculated dephase gradient strengths. **(b)** L-T_2 with calibrated dephase gradient strength. Both (a) and (b) were acquired with 512 complex data points, 8 T_2 echoes, 2τ = 6.6 ms, sweep width 100,000 Hz, RD = 1.5s and FOV = 40 mm.

It is interesting to note the sequence sensitivity to gradient strengths. In Fig. 3.6a, theoretical dephase and rephase gradients were used: G_d = 0.04110 $G_{max,}$ and G_r = 0.04020G_{max}. Post-G_d calibration (Fig. 3.6b), G_d = 0.04065G_{max}, G_r was unchanged. This is a 0.045% change from the maximum gradient strength and highlights the importance for manual dephase gradient calibration, supplementary to initial theoretical calculations.

3.2.2 Validation, Calibration and Sensitivity Testing of L-T_2 and L-T_1-T_2

L-T_2 and L-T_1-T_2 sequences were validated by testing that:

- extracted relaxation times, T_1 and T_2, were accurate relative to measurements using standard spatially-unresolved techniques;
- a volumetrically-quantitative measurement was produced;
- T_2 measurements were dominated by relaxation, not diffusion from imaging gradients.

This section describes the methods and results of the above validation tests.

3.2.2.1 Materials and NMR Experiments

To test the accuracy of extracted volumes and relaxation times from L-T_2 and L-T_1-T_2 sequences, a phantom was required with axially-varying relaxation times, where fluid volumes in each region were known. Accordingly, six vials filled with near-equal volumes of water were used. Three vials (A–C) contained 1.35 ± 0.02 mM $GdCl_3.6H_2O$-doped DI, three vials (D–F) contained undoped DI. This produced two solutions with T_1, T_2 values on the order of tens of milliseconds for the doped solution, and seconds for the undoped solution – see section 3.2.2.4. This sample selection was made to emulate expected T_1, T_2 ranges in rock samples – from 30 ms (water bound clays in sandstones (Coates *et al.*, 2001)) to orders of seconds (bulk liquid fluids in large pores). This allowed for the sequence sensitivity to systems studied within this thesis to be assessed. The vials were aligned such that three distinct relaxation time regions existed, illustrated in Fig. 3.7. Table 3.1 reports the fluid mass in each vial A-F. Solutions were prepared using $GdCl_3.6H_2O$ crystalline aggregates (99.9 %, Alfa Aesar) and DI water.

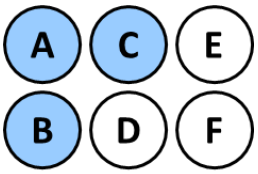

Figure 3.7. Phantom sample used for validating L-T_2 and L-T_1-T_2 sequences - consisting of six vials, with vials A–C having relaxation times two orders of magnitude smaller than those for vials D–F.

Table 3.1. Mass of fluid in vials A-F, reported to ± 0.001 g.

Vial	Contents	Mass [g]
A	$GdCl_3.6H_2O$-doped DI H_2O	8.416
B	$GdCl_3.6H_2O$-doped DI H_2O	8.392
C	$GdCl_3.6H_2O$-doped DI H_2O	8.471
D	DI H_2O	8.323
E	DI H_2O	8.341
F	DI H_2O	8.424

Hard r.f. pulse durations of t_{90} = 22.1 μs and t_{180} = 44.2 μs, equivalent to 90° and 180° tip angles, were used for all NMR experiments. Reference relaxation time measurements of the individual solutions were first measured using three repeats of standard, spatially-unresolved inversion recovery (T_1-IR) and one-shot CPMG experiments. For the undoped solution, T_1-IR measurements were acquired with a 16-point variable delay list in the range t_{vd} = 2 ms to t_{vd} = 22 s, and with RD = 22 s. For the doped solution, T_1-IR experiments were acquired with 16 variable delays in the range t_{vd} = 2 ms to t_{vd} = 1 s, and RD = 1 s. For both samples t_{DW} = 25 μs, NS = 8 were used. Reference one-shot CPMG experiments were acquired with t_E = 6 ms, t_{DW} = 25 μs, RD = 15 s and NS = 8 for the undoped solution; and with t_E = 1 ms, t_{DW} = 25 μs, RD = 1 s and NS = 8 for the doped solution.

2D T_1-T_2 measurements were acquired with an eight-point variable delay list from t_{vd} = 4 ms to t_{vd} = 15 s, with t_E = 5 ms, RD = 15 s and NS = 16. L-T_2 measurements were acquired with t_E = 5 ms, RD = 6 s, NS = 8, and with 128 pixels for FOV = 100 mm, giving slice resolution 0.78 mm pixel^{-1}. Likewise, L-T_1-T_2 measurements were acquired with the same t_E, numbers of pixels and slice resolution. Eight t_{vd} values in the range t_{vd} = 4 ms to t_{vd} = 15 s were employed, with RD = 15 s, and NS = 16. For L-T_2 and L-T_1-T_2, imaging gradients were applied along the length of the rectangular vial arrangement.

3.2.2.2 Data Processing Methodologies

Data processing of L-T_2 and L-T_1-T_2 datasets were conducted by first Fourier transforming each echo within the train. For L-T_2, these were stacked to form a 2D matrix consisting of decaying axial profiles, creating a T_2 decay at each pixel in the FOV. For L-T_1-T_2, this was repeated for each variable delay, t_{vd}, in the T_1 dimension, to produce N_{VD} 2D position-T_2 decay matrices, where N_{VD} is the number of t_{vd} values.

For both sequences, a zeroth-order phase correction was next applied to maximise the real component in the complex, Fourier transformed profiles. As phase accrued varies with position, an independently-optimised phase correction was applied at each axial position. At each position, the optimal phase correction was determined using the first profile. This was subsequently applied along the echo train. For L-T_1-T_2, the locally-optimised phase corrections were determined using spatial-T_2 datasets obtained at the maximum t_{vd} (i.e. maximum signal intensity echo trains), and subsequently applied across all variable delay time datasets. Next, each localised T_2 and T_1-T_2 decay datasets along the axis were individually inverted to yield spatially-resolved T_2 and T_1-T_2 correlation datasets, using the methodology below.

Each localised T_2 and T_1-T_2 dataset were processed by following the inversion and regularisation methods discussed in section 2.4.4.3. To facilitate justifiable comparisons between relaxation time distributions at different axial positions, it was necessary to regularise each spatial T_2 and T_1-T_2 dataset using a fixed smoothing parameter α, denoted the effective smoothing parameter, α_{eff}. For both L-T_2 and L-T_1-T_2, α_{eff} was optimised firstly by independently regularising each localised T_2, or T_1-T_2 dataset (at each pixel within the L-T_2 and L-T_1-T_2 datasets), giving a locally-optimised alpha, α_L. α_{eff} was obtained

by averaging all α_L, only considering regions in the FOV pertaining to the sample. Excluding the no-sample regions prevented α_{eff} from being weighted by noisy signals (illustrated in Fig. 3.8).

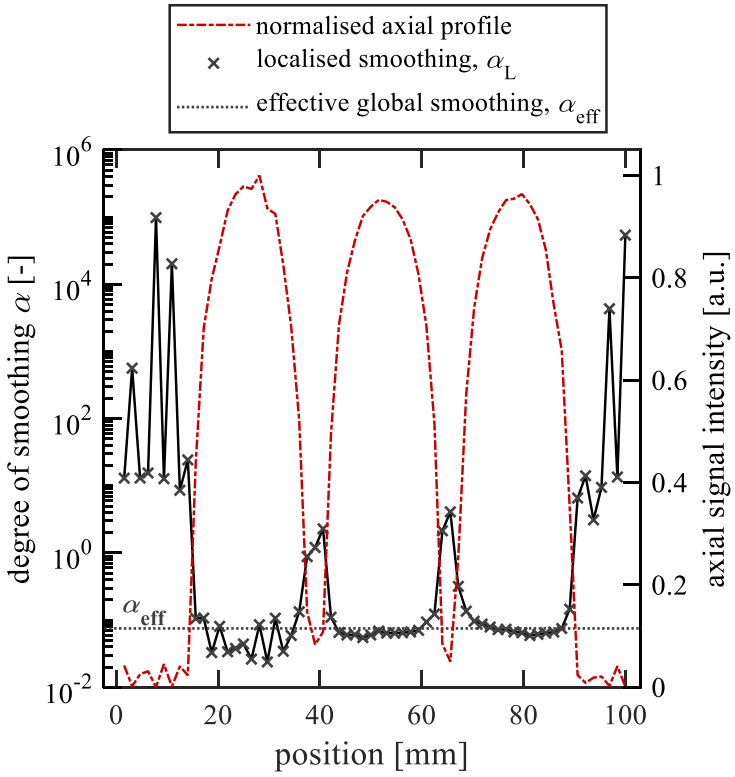

Figure 3.8. Comparison of locally-optimised, α_L and effective global smoothing parameter, α_{eff} obtained for the L-T_1-T_2 dataset on a phantom sample (illustrated in Fig. 3.7). The normalised axial intensity profile is also shown to illustrate the variation in α_L with respect to axial NMR signal.

Figure 3.8 illustrates how at noisy signal regions (outer regions of the FOV, boundaries between glass vials) α_L can be orders of magnitude greater than those optimised for the high signal intensity regions in which liquid sample resides.

3.2.2.3 Quantifying Errors in Fitted Intensities and Relaxation Time Values from Data Processing Methods

The sensitivity of relaxation time measurements from L-T_2 and L-T_1-T_2, were determined from the resolution of the fitted solution. As in Mitchell *et al.* (2012a), resolutions were obtained from the bandwidth of the fitted logarithmic-scale T_1 and T_2 axes:

$$\Delta \log_{10} T_{1,2} = \frac{bandwidth\ in\ \log_{10}(T_{1,2}) fitted\ axis}{number\ of\ fitted\ T_{1,2}\ components} \quad . \tag{3.1}$$

The uncertainty in fitted intensities were determined by considering what the solution to the inverse problem would be, if measured signal only comprised of noise, $e(t)$, with standard deviation σ, (Rezghi and Hosseini, 2009). Following Eq. 2.55, section 2.4.4.3, if input NMR signal only comprised of noise, the solution to Eq. 2.55 would be given by (Calvetti *et al.*, 1999; Rezghi and Hosseini, 2009):

$$f_{\mathrm{e}} = (K^{\mathrm{T}}K + \alpha I)^{-1}K^{\mathrm{T}}e \tag{3.2}$$

where I is the identity matrix, f_{e} denotes the optimal solution to the Fredholm integral for an input consisting only of noise – i.e., allowing the effect of pure noise on the regularised solution to be determined. From Eq. 3.2, it is possible to define $C = (K^T K + \alpha I)^{-1}K^T$, for which the individual rows in C are $\underline{c_i}$, and hence the error vector is comprised of i entries,

$$\underline{f_{e,i}} = \underline{c_i}\,\underline{e}\,. \tag{3.3}$$

Further, as each entry in $\underline{e}$ is individually distributed, the standard deviation of each $i^{\text{-th}}$ entry is given by $\|\underline{c_i}\|\sigma_{\mathrm{noise}}$, such that the overall error vector is given by (Reci, 2016):

$$\underline{f_e} = \sigma_{\mathrm{noise}}\begin{bmatrix} \|\underline{c}_1\| \\ \|c_2\| \\ \vdots \\ \|\underline{c}_m\| \end{bmatrix} \tag{3.4}$$

Physically, $e(t)$ can be obtained from NMR signal, by assuming signal noise has a Gaussian distribution, with mean $\mu_{\mathrm{signal}} = 0$, for which variance is estimated from the SNR (defined in Eq. 2.15), by:

$$SNR = \frac{b(0,0)}{\sigma_{\mathrm{noise}}} \tag{3.5}$$

where σ_{noise} is measured from the standard deviation of trailing imaginary datapoints.

3.2.2.4 Sequence Validation: Characterising Relaxation Times and Populations

To assess the accuracy of relaxation times measured from the implemented spatially-resolved relaxometry sequences, time constants obtained from L-T_2 and L-T_1-T_2 experiments on individual fluid samples were compared with those from standard, spatially-unresolved measurements (T_1-IR and one-shot CPMG).

Reference measurements on single-component fluid samples were processed using standard Bloch fits (Eqs. 2.18, 2.21) and 1D regularisation protocols for obtaining T_1 and T_2 distributions. This dual-pronged approach enabled unambiguous assignment of inaccuracies in L-T_1-T_2 and L-T_2-obtained relaxation time constants — expected to originate either from the pulse sequence, or from uncertainties associated with regularisation fittings. Likewise, 2D spatially-unresolved T_1-T_2 distributions were acquired on the multicomponent phantom sample (Fig. 3.7). The accuracy of sample populations derived from L-T_2 and L-T_1-T_2 measurements, identified from relaxation weighting-corrected intensities, was determined through comparison with information obtained from gravimetric sample preparation (Table 3.1).

Single component Bloch fits on reference T_1-IR and one-shot CPMG measurements of individual solutions yielded: $T_1 = 58.52 \pm 0.09$ ms, $T_2 = 49.31 \pm 0.01$ ms for the doped solution; $T_1 = 2.66 \pm 0.01$ s, $T_2 = 1.85 \pm 0.01$ s for the undoped solution. The data and fitted Bloch solutions are presented in Figs. 3.9a-b – both demonstrating excellent fits. 1D regularisation procedures resulted in relaxation time distributions with sharp peaks (expected for pure, bulk liquids), with log-mean relaxation times of: $T_{1,\mathrm{LM}}$

= 54.50 ± 4.30 ms, $T_{2,LM}$ = 49.25 ± 2.92 ms for the doped solution; $T_{1,LM}$ = 2.67 ± 0.17 s, $T_{2,LM}$ = 1.85 ± 0.11 s for the undoped solution (presented in Figs. 3.9c-d).

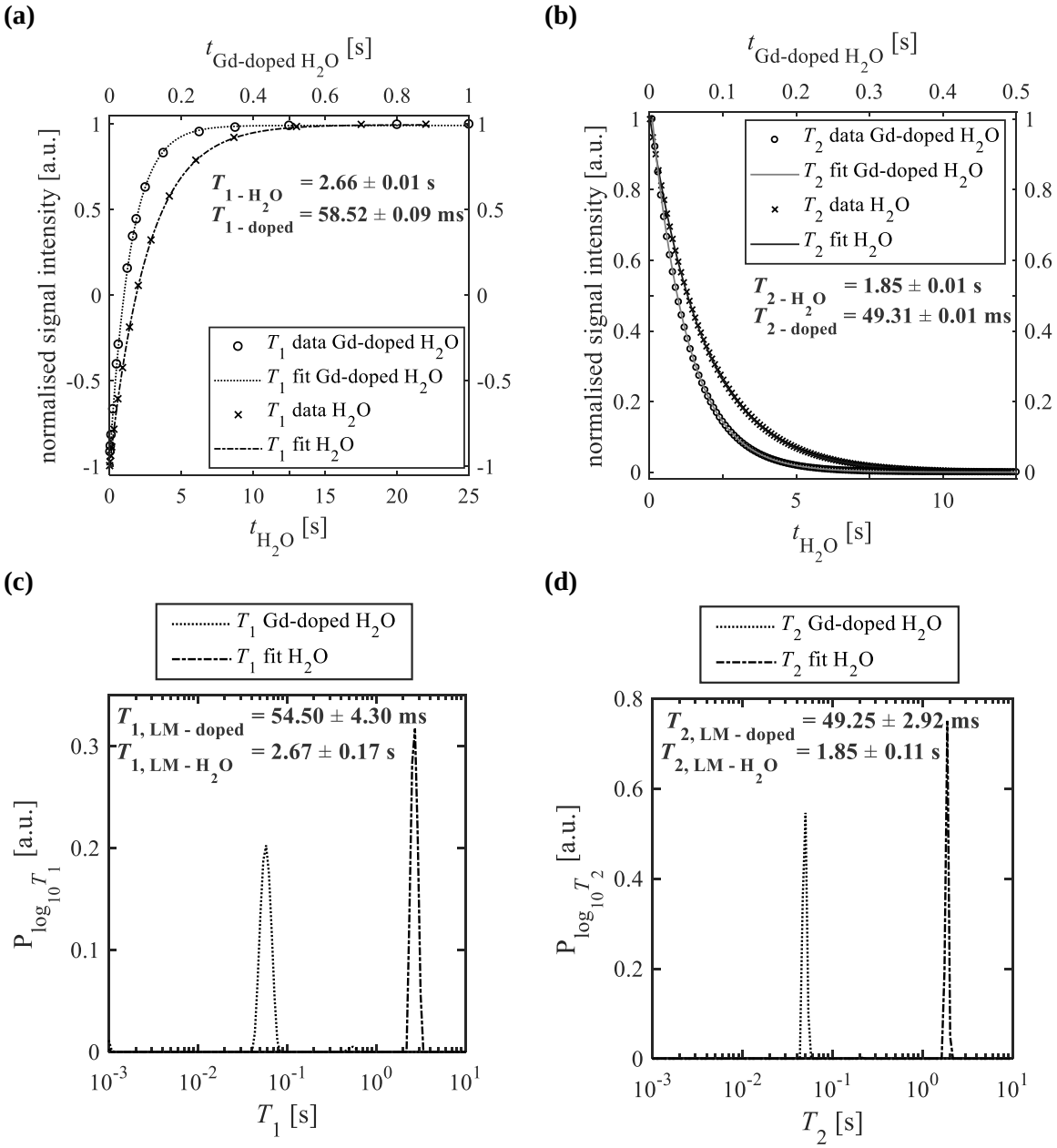

Figure 3.9. Reference spatially-unresolved T_1-IR and one-shot CPMG measurements applied to individual samples of gadolinium chloride-doped DI water and undoped DI water. **(a)** T_1-IR processed with Bloch fit, **(b)** one-shot T_2 processed with Bloch fit, **(c)** T_1-IR processed with 1D regularisation, **(d)** one-shot T_2 processed with 1D regularisation. Experimental data and fits are shown superimposed for both samples. In (a) and (b), the time axes for the decay of undoped water signal is on the bottom, that for the doped sample is on the top.

The spatially-unresolved 2D T_1-T_2 correlation for the multicomponent phantom produced bimodal relaxation time distributions, constituting log-mean relaxation times: $T_{1,LM}$ = 52.76 ± 4.10 ms, $T_{2,LM}$ = 51.35 ± 3.55 ms for the fast-relaxing peak; $T_{1,\,LM}$ = 2.71 ± 0.18 s, $T_{2,\,LM}$ = 2.01 ± 0.12 s for the slow-relaxing peak. The 2D correlation plot, together with its projected T_1 and T_2 distributions, is presented

in Fig. 3.12a, demonstrating two clear regions of signal intensity. This will be discussed later, in conjunction with the L-T_1-T_2 results.

Qualitatively, the capability of L-T_2 and L-T_1-T_2 to spatially-resolve relaxation times is demonstrated in Figs. 3.10a and 3.11, in which axial-T_1 and -T_2 maps of the phantom sample are presented for both sequences. Considering Fig. 3.10a (obtained from L-T_2) the axial-T_2 map reveals three relaxation time regions. A high intensity, fast-relaxing T_2 region to the left, a high intensity slow-relaxing T_2 region to the right, and a two-component T_2 region in the centre – each component at lower intensity than the comparatively high-intensity single component regions, located at either end of the sample. These observations correspond with the expected response, considering the phantom arrangement (see Fig. 3.7).

Figure 3.10b presents the relaxation weighting-corrected signal intensity profile, achieved by summing the L-T_2 map along the spatial dimension. This demonstrates that approximately uniform fluid volumes are located along the sample axis, as expected. Its comparison with the standard, non-relaxation-weighting-corrected profile highlights the advantage of the volumetrically quantitative nature of such spatially-resolved relaxometry measurements.

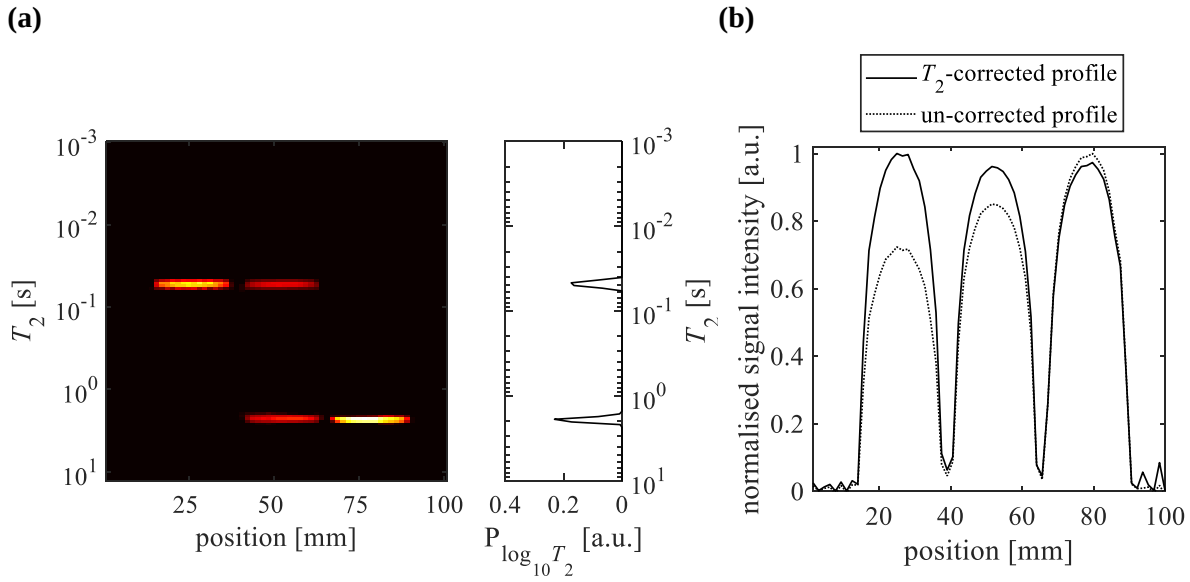

Figure 3.10. L-T_2 measurement of the phantom A-F. **(a)** Axial-T_2 map with its projected global T_2 distribution presented in the satellite plot. **(b)** Comparison of axial profiles obtained from a standard 1D imaging method (un-corrected profile), and the T_2-corrected profile (through summation of the population distributions in the L-T_2 map).

A similar qualitative demonstration in the axial trends of relaxation time constants and intensities is presented in Fig. 3.11 for the L-T_1-T_2 sequence. Figure 3.11a presents three localised 2D T_1-T_2 correlations, each obtained from the pixel centrally-located within the three axial pot regions; Figs. 3.11b and c present the axial T_1 and T_2 maps.

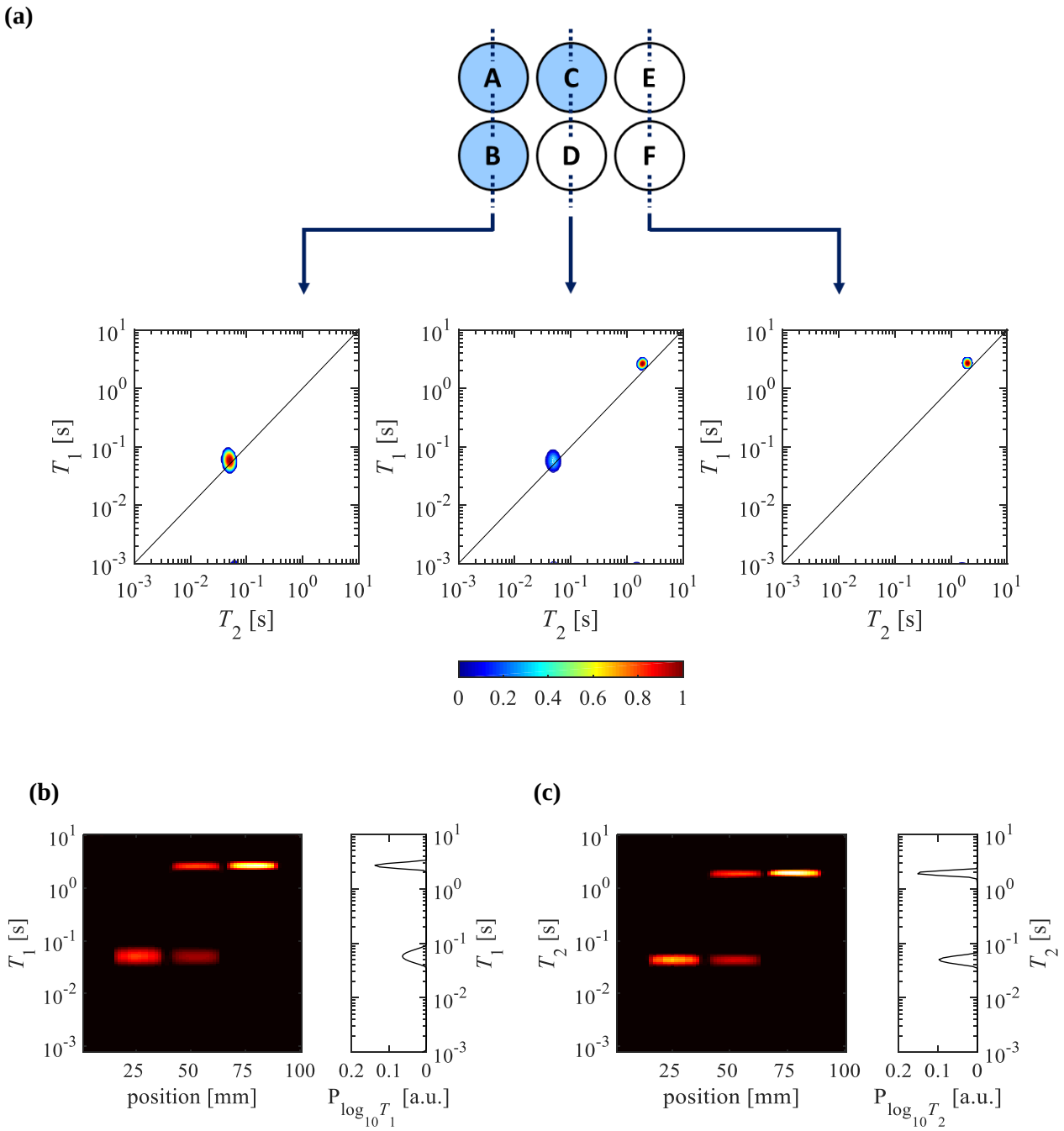

Figure 3.11. L-T_1-T_2 measurement of the phantom A-F. **(a)** 2D T_1-T_2 correlation plots, extracted from three axial positions located at the centre of each of the three pot regions: from left to right centred at 25.00 mm, 51.56 mm and 78.13 mm within the 100 mm FOV, with slice resolution 1.56 mm. A colourbar denoting the intensity scaling is also presented. **(b)** Axial-T_1 map, together with its global projected T_1 distribution. **(c)** Axial-T_2 map, together with its global projected T_2 distribution.

Furthermore, a comparison between L-T_1-T_2 and spatially-unresolved relaxation time measurements can be made through summation of the total L-T_1-T_2 signal along the sample axis. This produces a global L-T_1-T_2 measurement, equivalent to a conventional, spatially-unresolved T_1-T_2 measurement. This comparison is shown presented in Fig. 3.12, which demonstrates that the two techniques are in very good agreement.

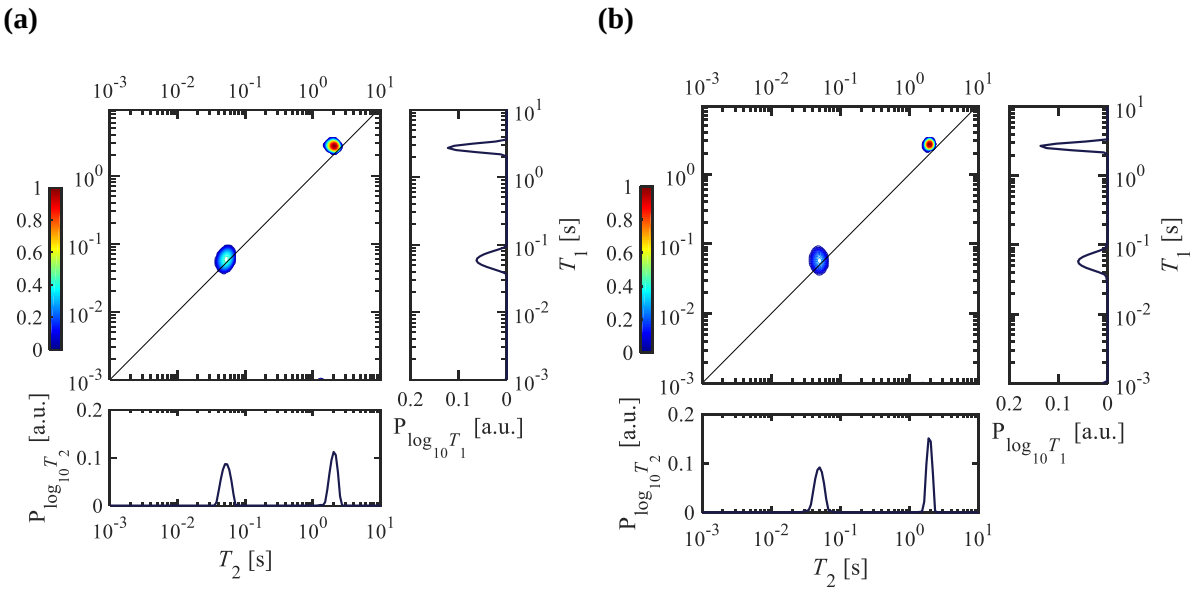

Figure 3.12 Comparison of 2D T_1-T_2 correlation plot of phantom sample A-F, acquired using two measurement techniques: **(a)** spatially-unresolved T_1-T_2, **(b)** spatially-resolved L-T_1-T_2, with axial correlations summed over all regions of the axis to achieve a global sample T_1-T_2 measurement. For both (a) and (b) 1D T_1 and T_2 distributions, obtained through projection of the 2D T_1-T_2 correlation along the appropriate axis, are shown presented in the satellite plots.

Quantifying the accuracy of the L-T_2 and L-T_1-T_2 relaxation time measurements, their log-mean relaxation times (compared to those obtained from standard spatially-unresolved techniques) are presented in Table 3.2. Table 3.2 demonstrates that the sequences yield relaxation times that are, within measurement uncertainty, in excellent agreement with conventional spatially-unresolved relaxation time measurements. The following observations can be made:

i. considering single fluid systems, measurement sensitivities reported for the inversion fits are worse than those from Bloch single component fits;
ii. the fast-relaxing component displays a shortened T_2 when measured using L-T_2, relative to other methods.

With reference to observation i., this behaviour is expected. Bloch fits were applied to systems known to exhibit single component relaxation times (single composition, bulk liquid samples). In contrast, regularisation fits were working to fit a distribution to this single component system. While sharp peaks are observed in the distributions, the spread inherent to fitting over a range of values introduces a greater fitting error, relative to the Bloch fits.

Table 3.2 A comparison of T_1 and T_2 values extracted for the phantom sample. Conventional T_2 one-shot and T_1-IR measurements are reported for single component systems, the conventional T_1-T_2 and spatially-resolved L-T_2 and L-T_1-T_2 results are reported for the dual component phantom. 'Global' refers to the summation of all spatially-resolved values within one measurement, akin to a spatially-unresolved technique. 'Bloch' refers to values extracted following single-component Bloch fits. '1D Reg' refers to values extracted following 1D regularisation methods. For the spatially-resolved measurements, labels 'left', 'centre', 'right', refer to the summation of relaxation behaviours within the three distinct sample regions, where: 'left' denotes the far-left position in Figs. 3.7, 3.10 and 3.11. Log-mean values are reported for the distributions fitted by regularisation methods. Error quantification follows the methods discussed in section 3.2.2.3.

	T_1		T_2	
	fast-relaxing component [ms]	slow-relaxing component [s]	fast-relaxing component [ms]	slow-relaxing component [s]
reference measurements on single component systems				
T_2 one-shot (Bloch)	–	–	49.31 ± 0.01	1.85 ± 0.01
T_2 one-shot (1D Reg)	–	–	49.25 ± 2.92	1.85 ± 0.11
T_1-IR (Bloch)	58.52 ± 0.09	2.66 ± 0.01	–	–
T_1-IR (1D Reg)	54.50 ± 4.30	2.67 ± 0.17	–	–
measurements on dual-component phantom sample				
L-T_2 (global)	–	–	40.39 ± 2.94	1.91 ± 0.12
L-T_2 (left)	–	–	44.03 ± 2.94	–
L-T_2 (centre)	–	–	43.88 ± 2.94	1.87 ± 0.12
L-T_2 (right)	–	–	–	1.93 ± 0.12
T_1-T_2	52.76 ± 4.10	2.71 ± 0.18	51.35 ± 3.55	2.01 ± 0.12
L-T_1-T_2 (global)	51.03 ± 4.46	2.63 ± 0.17	48.00 ± 8.18	1.93 ± 0.12
L-T_1-T_2 (left)	54.54 ± 4.34	–	48.77 ± 8.18	–
L-T_1-T_2 (centre)	50.99 ± 4.39	2.63 ± 0.16	49.06 ± 3.55	1.89 ± 0.12
L-T_1-T_2 (right)	–	2.70 ± 0.17	–	1.95 ± 0.12

Considering observation ii., this behaviour could be attributed to diffusive processes under the application of imaging gradients, for which shortening of T_2 (and not T_1) values would be expected. If however this were the case, one would expect greater reductions in the slow-relaxing T_2 component than the fast-relaxing component (see Eq. 2.45), for which diffusion processes would have a greater timeframe over which to have an effect.

To quantify the accuracy of population measurements extracted from L-T_2 and L-T_1-T_2, global and localised relaxation-corrected intensities measured for the phantom were compared against known gravimetric measurements (detailed in Table 3.1). The following three criteria were tested:

i. global population of fast- and slow-relaxing components;

ii. relative populations of fast- and slow-relaxing components in the phantom central region (the only dual component region);

iii. relative total populations within each of the three regions along the axis.

The results are presented in Table 3.3. Uncertainties reported for gravimetric values result from the propagation of error in the measurement sensitivity. Uncertainties reported for L-T_2 and L-T_1-T_2 result from cumulative errors introduced through random errors, the SNR and the error in the regularised fitted intensities – the latter, defined in section 3.2.2.3. As chemical compositions of both solutions were near-identical, their respective *HI*, and thus relaxation-weighting corrected intensities, were assumed comparable.

Table 3.3 Population measurements obtained using L-T_2 and L-T_1-T_2, compared with known gravimetric values.

(i) Global populations of fast- and slow-relaxing component [%]		
	fast component	slow component
gravimetric	50.190 ± 0.004	49.810 ± 0.004
L-T_2	49.72 ± 0.47	50.28 ± 0.47
L-T_1-T_2	49.75 ± 0.60	50.25 ± 0.47
(ii) Relative populations of fast- and slow-relaxing component in central region [%]		
	fast component	slow component
gravimetric	50.441 ± 0.007	49.559 ± 0.007
L-T_2	48.24 ± 0.06	51.76 ± 0.06
L-T_1-T_2	48.45 ± 0.59	51.55 ± 0.35

(iii) Relative populations of the three distinct axial regions [%]			
	left region	central region	right region
gravimetric	33.371 ± 0.003	33.344 ± 0.003	33.285 ± 0.003
L-T_2	33.65 ± 0.02	33.21 ± 0.06	33.14 ± 0.01
L-T_1-T_2	33.56 ± 0.51	33.15 ± 0.72	32.29 ± 0.52

The results presented in Table 3.3 demonstrate that both spatially-resolved sequences yield sample population measurements that match very closely with the populations known from the gravimetric data. Considering population criteria tests *i.* and *ii.*, with respect to gravimetric measurements, the slow-relaxing component population is consistently overestimated, and the fast-relaxing component population is underestimated. The exact cause of these differences is unknown, although this could be attributed to the relatively large echo time used (t_E = 5 ms), compared to the fast-relaxing T_2 component (T_2 = 49.31 ± 0.01 ms). This would result in poorer sampling of the T_2 relaxation of the fast-relaxing T_2 component, relative to the slow-relaxing T_2 component. This could lead to a poorer fit, an underestimation of initial magnetisation and thus population of the fast-relaxing T_2 component. This is consistent with log-mean values reported in Table 3.2 which show a reduction in T_2 obtained from spatially-resolved sequences for the fast-relaxing T_2 component. As spatial information is encoded

within the frequency domain, large echo times are often required, highlighting a limitation of the technique.

Considering the population criteria test number *iii*, there are not any significant local variations, confirming uniformity in the linearity of magnetic field strength applied within the experimental coil set-up. For the intended applications within this thesis, T_2 components in rock cores typically vary within the range 30 ms, to orders of seconds. While these validation tests have demonstrated that the L-T_2 and L-T_1-T_2 techniques can distinguish such values of T_2, minor errors in the value of T_2 and sample populations extracted for the fast-relaxing T_2 component can exist.

3.2.2.5 Sensitivity Testing: Influence of Diffusive Processes on Relaxation

Application of imaging gradients can result in shortening of T_2 relaxation processes due to diffusive attenuation (Callaghan, 1991). Quantifying the extent to which this introduces errors to the T_2 measurements obtained from spatially-resolved relaxometry techniques is important, critically: to what extent is the L-T_2 measurement affected by differing ranges of diffusivity values; and do the errors incurred significantly blur T_2 values such that T_2-contrast is no longer sufficient for distinguishing different species?

The signal attenuation due to both T_2 and diffusion in the presence of pulsed linear field gradients is described by

$$M_{xy}(t) = M_{t=0} exp\left(-\frac{t}{T_2} - n_e D\gamma^2 G^2 \delta^2 \left(\Delta - \frac{\delta}{3}\right)\right) , \tag{3.6}$$

where $M_{t=0}$ is the transverse magnetisation at t = 0, n_e is number of echoes along the echo train at a particular point in time (equivalent to $n_e = t/2\tau$), D is fluid diffusivity, γ is gyromagnetic ratio, G is effective imaging gradient strength in z, δ is gradient pulse duration and Δ is time between successive gradient pulses, here equivalent to 2τ, the interecho spacing (Callaghan, 1991).

The effect of diffusive attenuation on the L-T_2 measurement was tested by incorporating Eq. 3.6 into the model kernel function, within the T_2 inversion. Using the L-T_2 dataset acquired on the phantom A-F, for which the non-diffusion-corrected solution was presented in Fig. 3.10a and Table 3.2, the inversion calculation was repeated for a series of D values, in the range 10^{-12} – 10^{-7} m^2 s^{-1}. These bounds exceed the conditions exhibited in typical liquid-phase core flooding experiments, including the systems within this thesis. For physical context, these bounds lie close to the self-diffusion coefficients under ambient conditions of crude oil in porous rock (order of 10^{-11} m^2 s^{-1}, Mitchell *et al.* (2012c)) and gaseous, unconfined methane (order of 10^{-5} m^2 s^{-1}, Winn (1950)).

Each calculation used a fixed D. A literature value of D_w = 2.3 × 10^{-9} m^2 s^{-1} for bulk water at 25 °C (Mills, 1973) was selected as the ground-truth. Accordingly, Table 3.4 presents the log-mean T_2 values extracted for short- and fast-relaxing T_2 populations for a range of self-diffusivities. Whilst for liquid-saturated porous media a single value of D is unrealistic, here, the goal was to conduct a sensitivity

analysis to identify the limiting D values for which the accuracy of the T_2 measurement would be compromised, if such diffusive effects were not corrected. A single-component diffusivity correction was thus deemed sufficient.

Table 3.4 Log-mean T_2 of the fast- and slow-relaxing components of phantom A-F, globally-averaged from the L-T_2 measurement. The L-T_2 inversion is processed with a T_2 model kernel function incorporating single-component diffusion effects under linear imaging gradients. The influence of diffusive processes over a range of diffusivities is presented, denoted as multiples of the self-diffusivity of water at 20 °C, $D_w = 2.299 \times 10^{-9}$ m^2 s^{-1}. Errors in the T_2 measurements are quoted based on the resolution of the T_2 inversion fitted axis.

Self-diffusivity [×D_w]	Fast component [ms]	Slow component [s]
0	48.1 ± 2.9	1.91 ± 0.12
0.001	48.1 ± 2.9	1.91 ± 0.12
1	48.1 ± 2.9	1.91 ± 0.12
10	48.1 ± 2.9	1.97 ± 0.12
100	48.5 ± 2.9	2.78 ± 0.17

Table 3.4 demonstrates that, compared to the case in which no diffusion correction is applied ($0D_w$), the T_2 component extracted is only affected for $D > 10D_w$, for which the greatest sensitivity is observed in the slow-relaxing component. As D exceeds this value, the extracted T_2 values increase. This is expected – at higher T_2, relaxation decay is slower, so diffusion effects would have a greater influence than in the rapid spin-spin relaxation regimes. Here, the tests were only conducted for the L-T_2 sequence as diffusive attenuation does not alter T_1 processes. The results from these sensitivity tests can thus be directly translated to the L-T_1-T_2 sequence.

The systems explored within this thesis (brines and synthetic oils as bulk liquids and imbibed within porous outcrop rocks) typically have diffusion coefficients in the range 10^{-11} to 10^{-9} m^2 s^{-1}and T_2 values in the range of tens of milliseconds to seconds. Herein, studies at 85 MHz (Chapters 5-7) have been conducted with L-T_2 and L-T_1-T_2 sequences using similar experimental parameters (FOV, gradient strengths and interecho times) as the L-T_2 dataset screened in Table 3.4. It can thus be concluded that for such systems, the influence of diffusion under the imaging gradients present in the L-T_2 sequence does not significantly impact the accuracy of the T_2 values extracted. It is important to note that in porous media, internal gradients are often present, due to magnetic susceptibility contrasts. System-dependent, this can be corrected for during post-processing (see section 2.4.6).

3.3 Implementation and Validation at 2 MHz

3.3.1 Implementation Approach

At 2 MHz, implementation of the L-T_2 sequence initially followed the same approach as at 85 MHz – consisting of a pulse sequence design as in Fig. 3.1a, implemented through echo timing preservation and gradient calibration. Subsequent difficulties with gradient interferences at 2 MHz led to the development of a continuous gradient approach. This section details the methods and results at all stages of sequence development – in particular, focusing on the optimisation of the gradient stabilisation time and gradient pre-emphasis within the latter continuous imaging gradient approach.

3.3.1.1 Materials and NMR Hardware

All NMR experiments described in section 3.3 were conducted at 35 ± 0.1 °C in a 51 mT (2.18 MHz for ^{1}H nuclei) vertical bore permanent magnet (Oxford Instruments Geospec 2-75 Rock Core Analyser), controlled by a DRX HX spectrometer and RINMR software. A 29 mm I.D. r.f. probe was used for excitation and signal detection. Spatial resolution along the vertical axis (y) was achieved using a magnetic field gradient, capable of a maximum gradient strength, G_{max}, of 35.1 G cm^{-1}, along the y-direction.

As discussed in section 3.2.1.2, sharp echoes are required to accurately determine the location of echo centres. At 2 MHz, significant deshimming and disruption of magnetic field homogeneity is not possible, as the system uses factory-calibrated mechanical shims which cannot be readily altered. Accordingly, for split echo acquisition tests (Fig. 3.4), sharp echoes were achieved using a sample with short T_2* – a 1″ diameter, 1.5″ long Berea sandstone core (Kocurek Industries, Houston, USA) imbibed in DI. Unless stated otherwise, all gradient calibration and optimisation tests were conducted on phantom samples of $GdCl_3$-doped DI, held within a flat-bottomed NMR tube of diameter 29 mm. Gadolinium concentrations and fluid volume within each phantom are specified for each result presented in section 3.3.1.3. $GdCl_3$ crystalline aggregates (99.9%, Alfa Aesar) were used.

3.3.1.2 Spin Echo Timing Preservation

To achieve sharp echoes, a short-T_2* sample was used (see section 3.3.1.1). In addition, the 'YOFFSET' RINMR parameter, used to control the amount of DC-offset on the signal input to Y-channel gradient amplifiers, was altered to provide additional disruption to magnetic field homogeneity. The DC-offset is defined as the mean amplitude of a periodic waveform in the time domain. Although capable of varying between +1 to -1 (equivalent to gradient amplifier outputs set to maximum), a value of YOFFSET = 0.005 was temporarily applied, altered from the original factory-calibrated value of YOFFSET = -0.00018311. This value (an upper limit to prevent damage to the gradient amplifiers and gradient coil) was selected based upon guidance from Oxford Instruments Magnetic Resonance.

Using split echo acquisition, the L-T_2 sequence structure was tested to ensure the CPMG condition was satisfied along the echo train. As shown for the 85 MHz L-T_2 sequence (Fig. 3.5), the echo maxima

location for the L-T_2 sequence at 2 MHz under split echo acquisition is presented in Fig. 3.15. The test dataset was acquired using: τ = 4 ms; N_{echoes} = 32; t_{DW} = 8 µs and N = 1064.

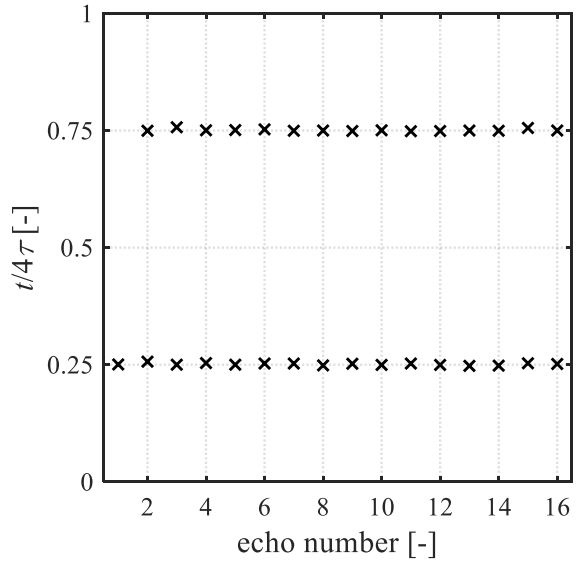

Figure 3.15. Locations of the observed echo maxima during split echo acquisition of the L-T_2 sequence at 2 MHz. Echo locations are denoted as fractional time positions within the full 4τ period, t/4τ.

Small fluctuations in signal maxima locations about the expected locations (τ/4τ and 3τ/4τ) are observed in Fig. 3.15. These are not periodic, and are random, associated to the lower SNR achievable at 2 MHz, rather than at 85 MHz. Figure 3.15 demonstrates that the timing loop structure of the L-T_2 sequence at 2 MHz satisfied the CPMG condition, such that STEs and SEs constructively interfered, as in Fig. 3.4.

3.3.1.3 Frequency Encoding Gradient Optimisation

An approach identical to that conducted at 85 MHz was initially attempted for gradient optimisation. Unfortunately, it was not possible to achieve gradient echoes which produced physically-representative profiles along the L-T_2 echo train. This occurred both for theoretically-calculated and subsequent iteratively-optimised dephase gradients, following the methods in section 3.2.1.3. Figure 3.16 presents the profiles along the L-T_2 echo train for theoretically-calculated (Fig. 3.16a) and iteratively-optimised dephase gradient strengths (Fig. 3.16b), measured on a cylindrical $GdCl_3$-DI water phantom sample (described in section 3.3.1.1, with fluid height 33 ± 1 mm (total volume 22 ± 0.7 ml), concentration 1.090 ± 0.001 g $GdCl_3$/litre DI, with measured T_1 = 12.6 ± 0.1 ms, T_2 = 12.6 ± 0.1 ms). For the iteratively-calibrated dataset, the applied gradient was incremented to its limit of sensitivity (± 0.001 G cm^{-1}).

Figure 3.16 demonstrates that despite taking the system to its gradient sensitivity limit, it was not possible to remove all gradient interferences. This was believed to result from asymmetries in the applied gradients, in turn leading to inconsistent traversing through **k**-space for each echo, and thus interferences giving non-physical profiles. Such asymmetries could result from distorted gradient shapes, instead of the expected rectangular pulses. Calibration experiments were subsequently conducted, to optimise the

system pre-emphasis, for compensation against eddy currents; and to identify the minimum gradient rise times.

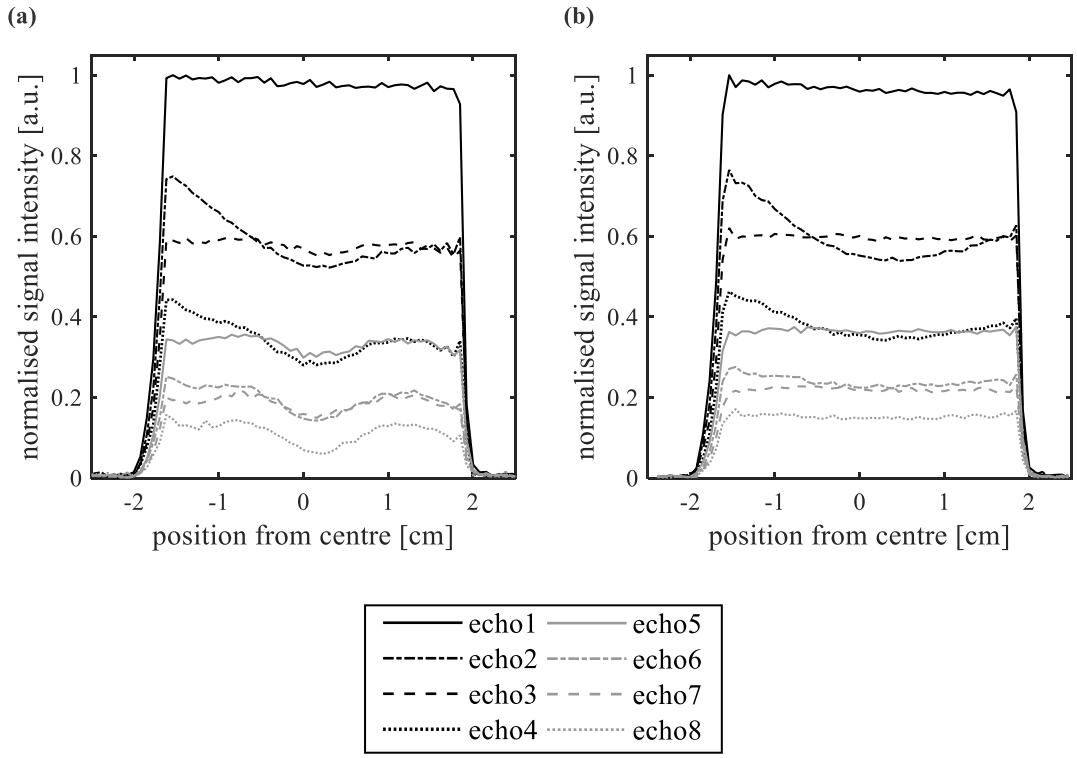

Figure 3.16. Profiles from the first eight echoes in the L-T_2 echo train of a $GdCl_3.6H_2O$-doped DI water phantom in a cylindrical NMR tube. **(a)** L-T_2 with theoretically-calculated dephase gradient strengths. **(b)** L-T_2 with iteratively-optimised dephase gradient strengths. Both (a) and (b) were acquired with N = 64, n = 64, 2τ = 3 ms, sweep width 50,000 Hz, RD = 0.3 s and FOV = 5.1 cm (pixel resolution, 0.8 mm). (a) was acquired with $G_{dephase}$ at 7.32% of G_{max}, (b) was acquired with $G_{dephase}$ at 7.49% of G_{max}.

Gradient pulses result in rapidly changing magnetic fields – these fields interact with surrounding metal within a magnet system, inducing eddy currents *via* Faraday induction. In turn, eddy currents possess associated magnetic fields which distort gradient profiles around a sample. These currents can persist for tens of milliseconds after the gradient pulse has been switched off, and their magnitude is proportional to the current switch rate (di/dt), as per Faraday's law – hence their effects are greatest in fast imaging sequences with rapid gradient pulsing, or in multiecho imaging sequences with short echo times. To compensate for eddy currents, 'pre-emphasis' techniques are commonly used. These involve deliberately overdriving applied current at the leading and tailing ends of a gradient pulse (Callaghan, 1991) – illustrated in Fig. 3.17.

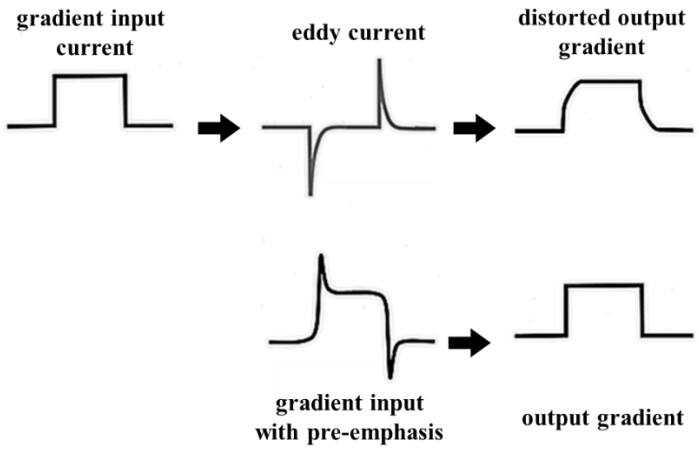

Figure 3.17. Schematic of pre-emphasis gradient pulse shaping for eddy current compensation. Adapted from Dehner and Kessler (2005).

Optimisation of pre-emphasis currents is usually conducted by iteratively adjusting additional gradient current amplitudes and time constants, that are convoluted with the input current, until eddy current effects are minimised (Terpstra *et al.*, 1998). In the 2 MHz system, digital pre-emphasis for gradient shape control is controlled with four time constants (PREYKn) and amplitudes (PREYAn) in the y-gradient channel (where n = 1-4). These define the decays of the superimposed compensatory waveforms. PREYAn are defined by constants varying from 0 to 1, PREYKn range from 4 μs to 100 s. An in-built Oxford Instruments pre-emphasis testing EDDYCM pulse sequence (illustrated in Fig. 3.18) and analysis package was used.

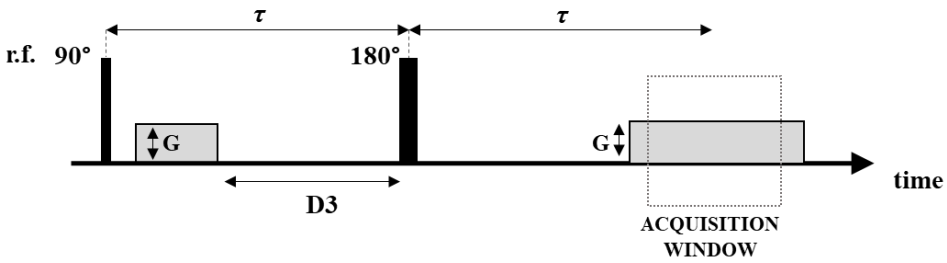

Figure 3.18. Timing diagram of the Oxford Instruments EDDYCM sequence for pre-emphasis parameter testing and optimisation. The gradient pulse tested is applied immediately after the first 90° r.f. pulse. A variable delay 'D3' is incremented to identify the extent of eddy current effects.

The EDDYCM sequence consists of a spin echo, where the gradient pulse shape to be optimised immediately follows the initial 90° r.f. pulse. Subsequently, a variable delay 'D3' is applied. This is incremented from a maximum (where eddy currents are not expected, on the order of milliseconds) to a minimal (where eddy currents are present, on the order of tens-hundreds of microseconds). An in-built analysis tool subsequently identifies the location of echo maximum signal intensity within the acquisition window, at each value of D3. The extent of eddy currents can be determined from the minimum D3 beyond which no further change in echo location occurs.

With supervision from Oxford Instruments Magnetic Resonance, factory-set pre-emphasis parameters were tested and further optimised using this protocol. Figure 3.19 presents the echo positions with variable D3 for the original factory-set and newly-optimised pre-emphasis parameters, acquired on a cylindrical $GdCl_3$-DI phantom (described in section 3.3.1.1, with fluid height 39 ± 1 mm, total volume 26 ± 0.7 ml, concentration 0.061 ± 0.001 g $GdCl_3$ /litre DI, with measured T_1 = 175.1 ± 0.2 ms, T_2 = 174.6 ± 0.3 ms). The following NMR experimental parameters were used: a gradient pulse of duration 1.2 ms, gradient strength 0.49G_{max}, τ = 50 ms, *NS* = 32, dummy scans, *DS* = 4, *N* = 2048 and *RD* = 1 s.

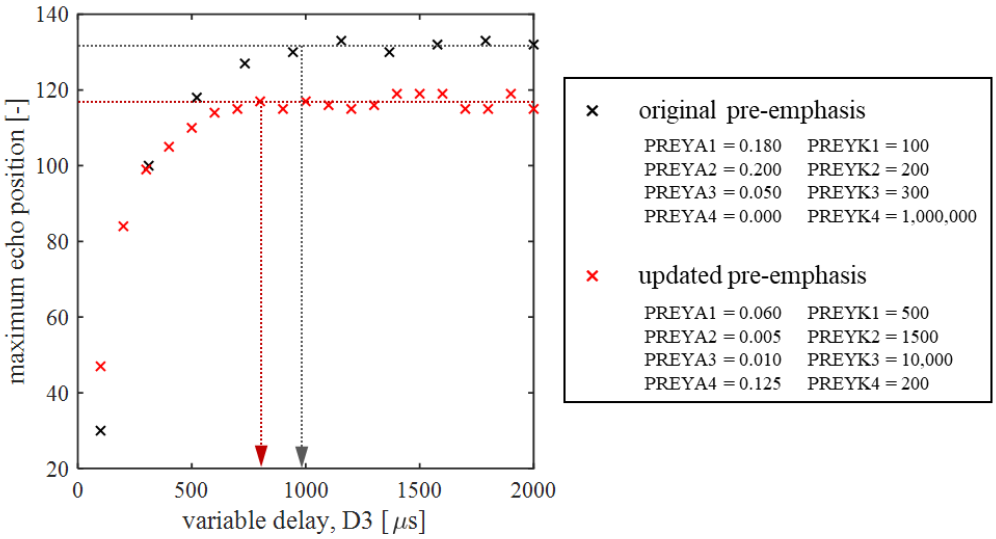

Figure 3.19. Maximal echo position with variable pre-180° delay, D3, for the original factory-set pre-emphasis and newly optimised pre-emphasis parameters. The dashed lines indicate the minimum D3 for which no change in the echo position, within signal noise fluctuations, is detected.

The earlier equilibration in maximal echo position (Fig. 3.19) demonstrates that optimisation of system pre-emphasis parameters resulted in a reduction in gradient eddy current effects. In addition, it highlights that a minimum gradient stabilisation time of ~800 μs should be used. This suggested that a minimum total delay of 1.6 ms per interecho pulse period would be required to deliver imaging gradients with eddy currents that do not present interference issues along the L-T_2 echo train. Combining this delay with the typical acquisition period required for obtaining an axial core profile at sub-millimetre resolution, this would result in a minimum interecho time of ~3 ms, leading to signal information loss at the short relaxation times common to rock cores. This sequence limitation is undesirable and so the final iteration of the L-T_2 sequence at 2 MHz was developed using a constant gradient approach, depicted in Fig. 3.1c. Figure 3.20 presents profiles obtained from the first eight echoes in the constant gradient L-T_2 train, acquired on a cylindrical $GdCl_3$-DI water phantom sample (described in section 3.3.1.1, with fluid height 39 ± 1 mm, total volume 26 ± 0.7 ml, concentration 0.101 ± 0.001 g $GdCl_3$ /litre DI, with measured T_1 = 120.5 ± 0.1 ms, T_2 = 119.6 ± 0.1 ms).

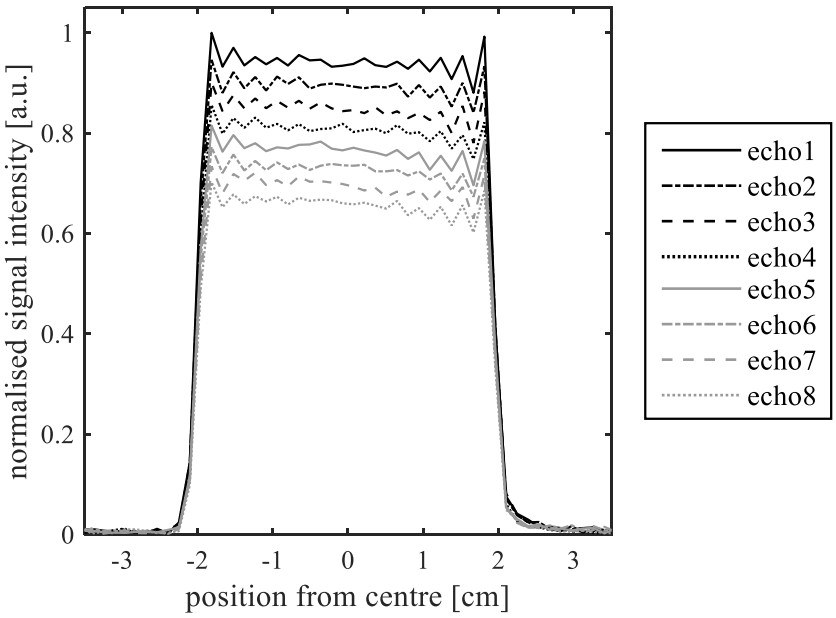

Figure 3.20. Profiles from the first eight echoes in the L-T_2 echo train of a 39 phantom in a cylindrical NMR tube. Dataset acquired with N = 64, NS = 4, n = 180, τ = 1.5 ms, SW = 50,000 Hz, RD = 5 s and FOV = 9.1 cm (pixel resolution of 1.5 mm).

Figure 3.20 demonstrates that L-T_2 with continuous imaging gradients does not display gradient echo interferences, unlike in Fig. 3.16. Quantitative validation of the sequence is discussed in section 3.3.2.

It is important to note there are limitations to the continuous gradient approach, primarily the risk of slice selection, and high gradient duty cycles. Considering first slice selection: under an applied magnetic field gradient, spins within a sample exhibit a spread in Larmor frequencies, along the applied gradient direction. Simultaneous application of an r.f. pulse results in slice selection, whereby only spins within a specific layer of sample are excited (section 2.2.1.4). The continuous gradient approach in L-T_2 thus introduces the risk of slice selection – here, an undesirable effect. Whether selective excitation takes place within a certain imaging FOV, is dependent upon the r.f. pulse bandwidth and applied gradient strength: (i) only spins with a resonance frequency within the r.f. pulse bandwidth will be excited; and (ii) a larger gradient strength imparts a greater range in Larmor frequencies along the desired axis of the sample. Therefore, the sensitivity to selective slice excitation increases with r.f. pulses of narrower bandwidths, and/or larger magnetic field gradient strengths. Verification of whether selective slice excitation would occur in the L-T_2 sequence was conducted using a back-of-the-envelope calculation – by comparing the expected bandwidth of the r.f. pulse applied, with the expected range in Larmor frequencies across a typical sample measured (Callaghan, 1991).

For hard, non-selective r.f. pulses, bandwidths are on the order of t_p^{-1} (t_p is pulse duration). For the 29 mm probe, typical 180° r.f. pulse durations are ~10 μs, giving a bandwidth of 100 kHz. Considering the expected range of Larmor frequencies along the sample axis, it follows from Eq. 2.23, that along the length of the sample, the change in local Larmor frequency would be given by:

$$\Delta\omega = \omega(\boldsymbol{r}_2) - \omega(\boldsymbol{r}_1) = \gamma(\boldsymbol{G}\cdot\boldsymbol{r}_2 - \boldsymbol{G}\cdot\boldsymbol{r}_1) = \gamma\boldsymbol{G}\cdot\Delta\boldsymbol{r} \tag{3.7}$$

i.e. for the samples in this thesis expected to be tested (core lengths of 1.5″ (~4 cm), maximum system gradient strength, G_{max} = 36.1 G cm^{-1}) a maximum imaging gradient up to 16.3% of G_{max} could be used before the range in Larmor frequencies approached the 100 kHz bandwidth. In reality, for the desired FOV, typical gradients strengths of 3% G_{max} were required, giving $\Delta\omega \approx 18$ kHz – considerably less than the r.f. pulse bandwidth and therefore not presenting a slice selection issue.

Secondly, MRI experiments operated with long-duration or high-power gradients pose the risk of high duty cycles. This is undesirable as the combination of high currents and high duty cycles can cause gradient coil heating, in turn affecting resonance frequencies or even damaging equipment hardware. For the constant-gradient L-T_2 experiment, the duty cycle, DC, is defined as the fraction of time over which the gradients are applied per single experiment scan:

$$DC = \frac{2N_{\text{echoes}}\tau}{(2N_{\text{echoes}}\tau + RD)}. \tag{3.8}$$

In practice, a burst of strong gradient pulses with a high duty cycle in the short term is often acceptable, provided the recycle delay is long enough such that the overall duty cycle is low. For potentially high-duty cycle experiments, it is important that the maximum allowable duty cycle is determined. These can be calculated as gradient duties are a function of the capacity of the gradient amplifier power supply for sustaining large loads, and the ability of the gradient coil to dissipate heat (Fishbein *et al.*, 2005). For the 2 MHz, the maximum current, $I_{c,max}$, that can be supplied to the gradient coils is 160 A (occurring at the system maximum gradient strength, 35.1 G cm^{-1}), the resistance of the gradient cables at maximum operating temperature (35 °C) is 1.2 Ω, and the gradient power limit is 140 W (based upon the heat dissipation achievable from the magnet chiller) – all Oxford Instruments factory-reported values. For an applied gradient strength, G, the maximum allowable gradient duty cycle for the L-T_2 experiment can be calculated as follows. First, the current, I_c, through the gradient coils is determined by:

$$I_c = \left(\frac{G}{G_{\max}}\right) I_{c,\max}. \tag{3.9}$$

The maximum duty cycle allowable would be equivalent to the rate of heat dissipation provided by the chiller,

$$DC_{\max} = \frac{140\ W}{{I_c}^2 R_c} \tag{3.10}$$

where R_c is the gradient cable resistance. The appropriate recycle delay for a given set of experimental parameters can then be determined.

3.3.2 Validation Approach

The accuracy of the T_2 and volumetric measurements obtained from the L-T_2 sequence at 2 MHz, was tested and validated using the same approach as at 85 MHz (section 3.2.2). This section describes the samples used and presents the validation test results. The same processing and error quantification methods, as in sections 3.2.2.2 and 3.2.2.3, were used.

3.3.2.1 Materials and NMR Experiments

As in section 3.2.2, a phantom sample was required with axially-varying relaxation times, in which the fluid volumes of each relaxation time were known.

The phantom consisted of two solutions – sample A at 0.061 ± 0.001 g $GdCl_3$/litre DI, sample B at 0.024 ± 0.001 g $GdCl_3$/litre DI. Both were prepared using $GdCl_3$ crystalline aggregates (99.9%, Alfa Aesar) and DI water. Each solution was loaded into a separate cylindrical flat-bottomed NMR tube, of 8.4 mm outer diameter (O.D.). Each NMR tube contained a near-same fluid volume – as determined by mass (sample A: 1.733 ± 0.001 g, sample B: 1.738 ± 0.001 g). Initial calibrations of the relaxation times of each solution were conducted on the two vials independently. Subsequently, the two tubes were aligned with a vertical offset, such that three differing relaxation time regions occurred along the vertical axis. The NMR tubes were then firmly taped together in this alignment, with NMR-silent PTFE tape. Their arrangement is illustrated in Fig. 3.21.

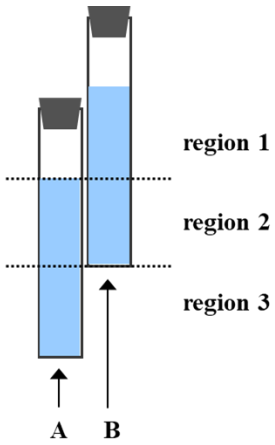

Figure 3.21. Phantom sample used for validating L-T_2 at 2 MHz, consisting of two NMR tubes filled with solutions of differing relaxation time properties. Their vertical offset gives axially-varying relaxation time characteristics, along which the imaging gradients of the L-T_2 sequence were applied.

Hard r.f. pulse durations of t_{90} = 4.55 μs and t_{180} = 9.1 μs were used for all NMR experiments. Reference relaxation time measurements of the individual solutions were conducted using spatially-unresolved T_1-IR and one-shot CPMG. For sample A, T_1-IR were acquired with a 16-point t_{vd} list in the range t_{vd} = 1 ms to 3.2 s and RD = 3.2 s. For sample B, a 16-point t_{vd} list in the range t_{vd} = 1 ms to 5 s, and RD = 5 s was used. For both, signal was acquired with t_{DW} = 20 μs and NS = 16. Reference one-shot CPMG experiments were acquired using t_E = 1.5 ms, t_{DW} = 20 μs, N_{echoes} = 512, RD = 3.5 s and NS = 16 for sample A; and t_E = 1.5 ms, t_{DW} = 20 μs, N_{echoes} = 2048, RD = 5 s and NS = 16 for sample B.

Spatially-unresolved one-shot T_2 CPMG measurements were conducted on the combined phantom using the same parameters as for the T_2 measurement of sample B alone. Spatially-resolved L-T_2 measurements on the combined phantom were acquired with t_E = 2.5 ms, N_{echoes} = 512, RD = 15 s, NS = 512, and with 64 pixels over FOV = 56 mm, giving a slice resolution 0.88 mm pixel^{-1}.

3.3.2.2 Sequence Validation: Characterising Relaxation Times and Populations

Reference relaxation time measurements for individual samples yielded: T_1 = 210.6 ± 0.6 ms, T_2 = 210.2 ± 0.8 ms for sample A; T_1 = 585.8 ± 1.7 ms, T_2 = 575.8 ± 2.2 ms for sample B (using single component Bloch fits). Application of 1D T_1 and T_2 regularisation procedures gave log-mean relaxation times: $T_{1,LM}$ = 212 ± 14 ms, $T_{2,LM}$ = 209 ± 14 ms for sample A; $T_{1,LM}$ = 591 ± 46 ms, $T_{2,LM}$ = 566 ± 43 ms for sample B. As discussed in section 3.2.2.4, the sensitivity of relaxation times obtained from regularisation methods is based on the local resolution of the relaxation time fitting axis of each T_1, T_2 peak, in turn largely affected by dataset SNR. Similarly, spatially-unresolved T_2 measurements on the combined phantom produced a bimodal T_2 distribution with log-mean $T_{2,LM}$ = 211 ± 14 ms and $T_{2,LM}$ = 540 ± 36 ms for the two peaks, obtained through 1D regularisation. The T_2 distribution obtained is presented in Fig. 3.22.

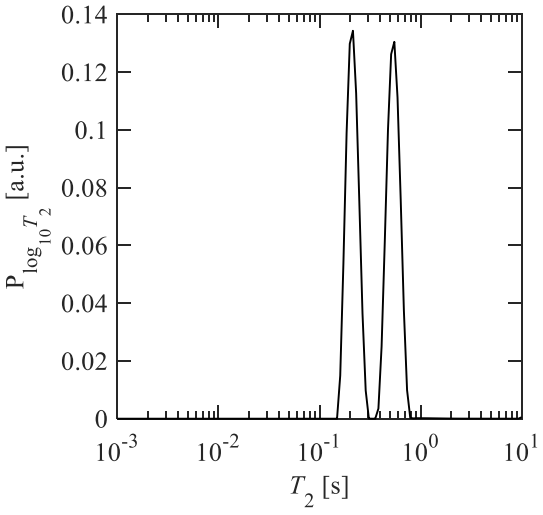

Figure 3.22. Reference 1D T_2 distribution measured from spatially-unresolved T_2-CPMG acquisitions of the phantom sample, illustrated in Fig. 3.21.

The measured T_2 on the single fluid samples can be used to benchmark the accuracy of extracted relaxation times from L-T_2. T_2 values obtained through 1D regularisation of T_2-CPMG measurements, on both individual samples and the combined phantom, enable errors in the L-T_2 relaxation times (resulting from either the regularisation fitting or from sequence limitations) to be distinguished.

Qualitatively, the capability for L-T_2 to spatially resolve relaxation time differences is demonstrated in Fig. 3.23 – an axial-T_2 map of the phantom (Fig. 3.23a) and its relaxation-weighting-corrected axial profile (Fig. 3.23b) are presented. The axial-T_2 map (Fig. 3.23a) highlights three regions of relaxation time behaviour: a fast-relaxing T_2 region at the bottom, a two-component (fast- and slow-relaxing) T_2

region in the centre, and a slow-relaxing T_2 region at the top. These observations correspond with the expected behaviour for the phantom arrangement, shown in Fig. 3.21. Considering Fig. 3.23b, three differing signal intensity regions are apparent, in which the central region has approximately double the signal intensity of the upper and lower regions. This is expected, considering the NMR tube overlap – a pixel in the central region would hold double the fluid volume compared to a pixel within the single NMR tube regions.

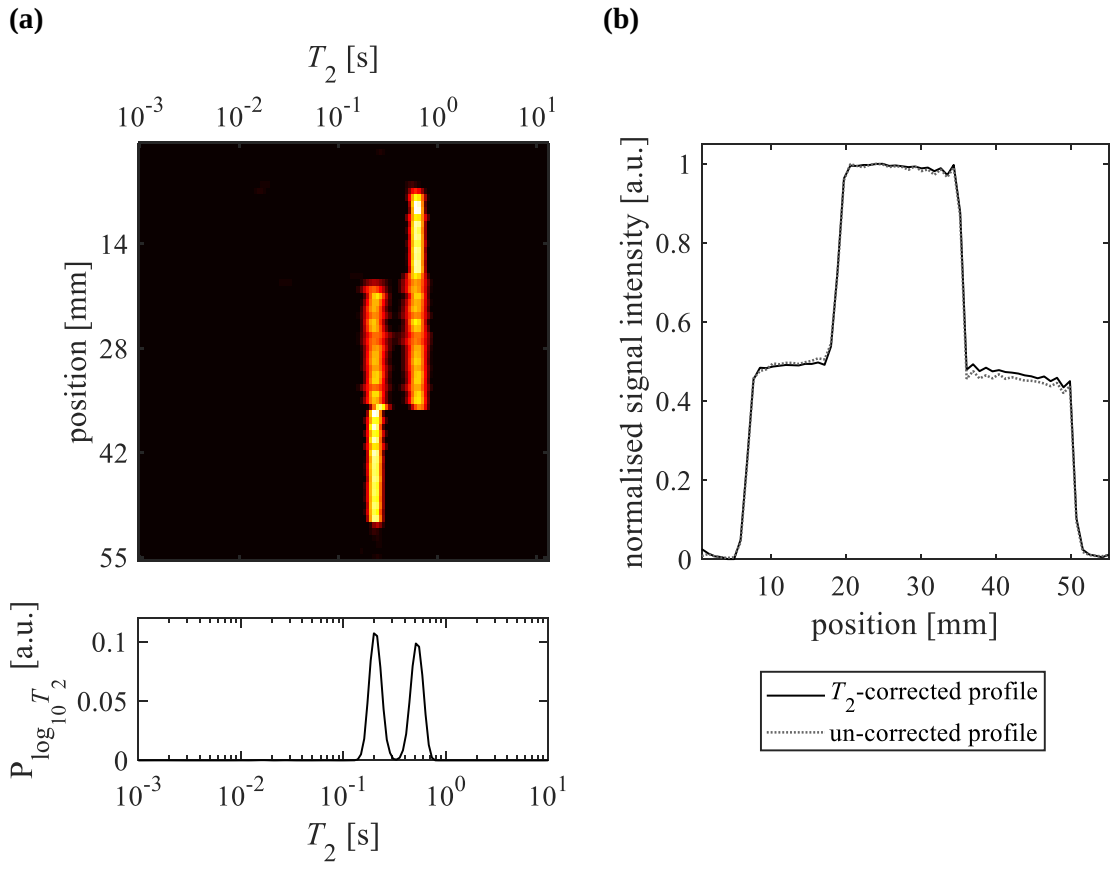

Figure 3.23. *L*-T_2 measurement of the phantom sample (illustrated in Fig. 3.21). **(a)** Axial-T_2 map, with its projected global T_2 distribution in the satellite plot. **(b)** Comparison of axial profiles obtained through standard 1D imaging techniques (un-corrected profile) and the T_2-corrected profile, obtained through summation of the population distributions in the *L*-T_2 map.

Fig. 3.23b highlights the volumetrically quantitative advantages of spatially-resolved relaxometry measurements. Here, the difference in profile intensities is not as stark as in Fig. 3.10b, as the phantom used at 2 MHz contained solutions with much closer T_2 values in order of magnitude than those at 85 MHz.

To quantify the accuracy of *L*-T_2 relaxation time measurements, log-mean T_2 values are compared with those from standard, spatially-unresolved techniques – presented in Table 3.5. Therein, the reported uncertainty is based upon the bandwidth of fitted logarithmic T_2 axes. T_2 measurements from *L*-T_2 are documented for both the overall global sample and each segmented region of the phantom.

Table 3.5 T_2 measurements on the phantom sample, comparing L-T_2 with conventional T_2 one-shot techniques, reported for both the single solutions and the dual-component phantom. 'Global' refers to the summation of all spatially-resolved values within one measurement. 'Bloch' refers to the single component Bloch T_2 model fits and '1D Reg' refers to processing the datasets using 1D inversion and regularisation protocols. The spatial locations bottom, centre, top refer to the three regions in the phantom.

		T_2	
		fast-relaxing component [ms]	slow-relaxing component [s]
individual solutions	T_2 one-shot (Bloch)	210.2 ± 0.8	578.8 ± 2.2
	T_2 one-shot (1D Reg)	210 ± 13	575 ± 35
phantom sample	T_2 one-shot (1D Reg)	209 ± 15	538 ± 35
	L-T_2 (global)	203 ± 14	521 ± 34
	L-T_2 (bottom)	205 ± 13	
	L-T_2 (centre)	207 ± 14	520 ± 34
	L-T_2 (top)	–	525 ± 33

Table 3.5 demonstrates that the L-T_2 sequence at 2 MHz yields T_2 relaxation times that are, within experimental and fitting errors, in good agreement with conventional T_2 measurement protocols. The following observations are drawn:

i. for individual solutions, measurement sensitivities are worse for the regularisation fits than for Bloch fits;
ii. the L-T_2 technique shortens T_2 measurements, relative to the T_2 one-shot measurement.

The behaviour in observation i. is expected, as explained in section 3.2.2.4. The behaviour in observation ii. is most apparent for the slow-relaxing component, for which a 9 % reduction in measured T_2 is observed. For the fast-relaxing component, only a 2% reduction in T_2 is observed. As stated in section 3.2.2.4, this can be attributed to diffusion under imaging gradients, for which the greatest T_2 reductions would be expected in the slow-relaxing component (Eq. 2.45), as diffusive processes would have a greater timeframe in which to have an effect. Furthermore, the T_2 reduction presented in Table 3.5 is both greater than the uncertainty of the T_2 measurement and is more pronounced than that observed at 85 MHz. This suggests that the L-T_2 developed at 2 MHz is more susceptible to diffusive effects than that at 85 MHz. This could be attributed to the continuous imaging gradient at 2 MHz. A discussion on the influence and sensitivities to diffusive processes is presented in section 3.3.2.3.

To quantify the volumetric nature of the L-T_2 technique, gravimetrically- and L-T_2-measured sample populations were compared, by testing:

i. global populations of fast- and slow-relaxing components;
ii. relative populations of fast- and slow-relaxing component in the phantom central region (the only dual-component region).

The results are presented in Table 3.6. The *L*-T_2 population was obtained from relaxation-weighting-corrected profiles. As the chemical compositions of solutions A and B were near-identical, their respective *HI*, and thus relaxation-weighting corrected intensities, were assumed comparable. Gravimetric populations were determined from: mass measurements obtained during sample preparation (see section 3.3.2.1) for criteria (i); and NMR tube I.D. for the cross-over central region for criteria (ii). Gravimetric uncertainties result from error propagation of the measurement sensitivity, and the tolerances of the NMR tube I.D.; *L*-T_2 uncertainties result from random errors, SNR, and regularisation fitting intensity errors – the latter, defined in section 3.2.2.3.

Table 3.6 Population measurements obtained using *L*-T_2, compared with known gravimetric values.

(i) Global populations of fast- and slow-relaxing component [%]		
	fast component	slow component
gravimetric	49.92 ± 0.06	50.08 ± 0.06
L-T_2	51.6 ± 0.3	48.4 ± 0.3
(ii) Relative populations of fast- and slow-relaxing component in central region [%]		
	fast component	slow component
gravimetric	50.0 ± 0.1	50.0 ± 0.1
L-T_2	49.1 ± 0.2	50.9 ± 0.2

The results presented in Table 3.6 demonstrate that the *L*-T_2 sequence at 2 MHz yields population measurements that very closely match with gravimetrically-obtained measurements. The greater differences in the extracted populations, compared to those at 85 MHz, are believed to result from reduced SNR in the measurements at 2 MHz.

3.3.2.3 Sensitivity Testing: Influence of Diffusive Processes on Relaxation

As discussed in section 3.2.2.6, imaging gradients can result in enhanced T_2 relaxation decay processes due to diffusive attenuation. The signal attenuation of a CPMG echo train in the presence of a continuous linear field gradient (as in the *L*-T_2 sequence developed at 2 MHz) is described by Eq. 3.11 (Callaghan, 1991)

$$M_{xy}(t) = M_{t=0} exp\left(-\frac{t}{T_2} - \frac{1}{3} D\gamma^2 G^2 \tau^2 t\right), \tag{3.11}$$

where $M_{xy}(t)$ is the transverse magnetisation at time t from initial excitation, $M_{t=0}$ is the transverse magnetisation at t = 0 from initial excitation, τ is half-interecho time, D is fluid diffusivity, γ is gyromagnetic ratio and G is effective imaging gradient strength.

The effect of such diffusive attenuations on the continuous gradient *L*-T_2 sequence at 2 MHz was explored, by incorporating Eq. 3.11 into the model kernel of the T_2 inversion. This was tested using the *L*-T_2 dataset acquired on the phantom, for which non-diffusion-corrected solutions were first presented

in Figs. 3.22, 3.23 and Table 3.5. The same sensitivity testing approach as employed at 85 MHz (section 3.2.2.6) was used. Here, a literature value of $D_w = 2.919 \times 10^{-9}$ m^2 s^{-1} for bulk water at 35 °C (Mills, 1973) was assumed. Table 3.6 presents the log-mean T_2 values for the fast- and slow-relaxing T_2 populations of the calibration phantom, obtained for D in the range 10^{-12} m^2 s^{-1} to 10^{-7} m^2 s^{-1}.

Table 3.6 Log-mean T_2 values of the fast- and slow-relaxing components of the phantom calibration sample, obtained from the globally-averaged T_2 distribution from an L-T_2 measurement. The L-T_2 dataset was inverted using a model kernel function that incorporates both T_2 relaxation and the single-component diffusion effects under continuous linear imaging gradients. The influence of diffusive processes is tested for a range of D values, expressed as multiples of D_w at 35 °C, $D_w = 2.919 \times 10^{-9}$ m^2 s^{-1}. Errors in the T_2 measurements are quoted based on the resolution of the T_2 regularisation fitted axis.

Self-diffusivity [×D_w]	Fast component [ms]	Slow component [ms]
0	204 ± 14	526 ± 36
0.001	204 ± 14	526 ± 36
1	204 ± 14	527 ± 36
10	206 ± 14	541 ± 36
100	228 ± 16	722 ± 53

Table 3.6 demonstrates that compared to the case in which no diffusion correction is applied (0D), the accuracy of the T_2 component extracted is only affected for diffusion coefficients at and above an order of magnitude of 10D, for which the greatest sensitivity is observed in the slow-relaxing component. As stated in section 3.2.2.6, the sample systems explored in this thesis typically have diffusivities and T_2 values akin to the D and T_2 ranges tested using the L-T_2 dataset in Table 3.6. It is thus concluded that for such systems, diffusion under imaging gradients does not significantly impact the accuracy of the relaxation parameters extracted from the L-T_2 sequence at 2 MHz.

3.4 Conclusions

Spatially-resolved frequency-encoded relaxometry sequences were implemented on both 85 MHz and 2 MHz magnet systems. A pulsed-gradient and a continuous gradient approach were used, respectively. These sequences were qualitatively tested by confirming a lack of spin echo and gradient echo interferences throughout the multiecho train. The first was achieved by validating that under split-echo acquisition the stimulated and spin echoes occur at fixed positions within the echo train, as expected by theoretical predictions. The second was achieved by confirming that axial profiles obtained through Fourier transforming each echo along the multiecho train, were physically-representative of the sample.

Quantitatively, the techniques were validated by comparing the relaxation time values extracted from the sequences relative to those obtained from accepted spatially-unresolved techniques. Tests were conducted on dual-component phantom samples with relaxation time constants similar, in magnitude, to those observed in fluid-imbibed rock cores. The phantom samples were prepared with axial variations

in their relaxation times, with gravimetrically-measured fluid volumes. Across both magnet systems, excellent agreement was achieved between the extracted relaxation times and populations from the spatially-resolved sequences and those from standard techniques.

Finally, the influence of diffusive processes on T_2 relaxation under linear imaging gradients was explored. A model for single-component diffusive attenuation was incorporated into the T_2 inversion kernel function and tested at varying orders of magnitude of diffusion. For the range of diffusivities and T_2 values typical to oils and brines within rock core systems, and the typical imaging gradient strengths used within the work conducted in this thesis, diffusive attenuation resulting from imaging gradients does not have any significant impact on the T_2 relaxation constants extracted.

Chapter 4

Simulating Reservoir Conditions in a Laboratory

4.1 Introduction

This chapter details the techniques and equipment that enabled experiments to be conducted at reservoir-representative conditions. This includes: (i) details on core sample preparation approaches; (ii) the MRRC core flooding system (CFS).

Considering (i), industry-standard special core analysis (SCA) approaches recommend using 'restored state' cores. These consist of reservoir (or outcrop) cores, cleaned to water-wet conditions, and then taken to irreducible water saturation (S_{wir}) by simulating reservoir hydrocarbon migration. Subsequently, the core is aged at reservoir temperatures and pressures to achieve restored-reservoir wettabilities. Hydrocarbon migration involves movement of hydrocarbons from a source rock, towards a reservoir formation in which accumulation can occur. Prior to hydrocarbon migration, reservoir rock is usually brine-saturated. S_{wir} is the water saturation at which no further brine can be displaced from a core during forced hydrocarbon injection into an initially water-saturated core – that is, the maximum achievable hydrocarbon saturation, prior to oil extraction processes. Specifically, this chapter discusses core cleaning methods.

Considering (ii), a CFS facilitates controlled fluid injections into core samples, at reservoir-representative pressure and temperature conditions. This chapter details the MRRC-custom-built NMR-compatible CFS, for conducting SCAL core flooding experiments. The MRRC CFS was designed by Dr Nick Ramskill, Dr Andy Sederman, Dr Mick Mantle (MRRC) and Dr Matthias Appel (Shell Technology Centre, Houston (STCH)), based upon existing STCH CFS designs. The MRRC CFS was built and commissioned by Dr Nick Ramskill, myself (MRRC) and Mr Kirk Smith (STCH) between August 2015 and March 2016.

4.2 Core Cleaning

This section details core cleaning methods for achieving initial water-wetting conditions, *via* hot-solvent Soxhlet extraction.

Although numerous SCA methods exist for core cleaning (centrifuge flushing, gas-driven solvent extraction, liquefied-gas extraction, cold solvent extraction, solvent flush cleaning), hot-solvent extraction is considered industry-standard – it is low-cost, rapid, and requires minimal operator supervision. It is however considered a harsh method, involving high-temperature reflux cycles that can cause water removal and damage certain clay minerals. Less-intrusive techniques, such as solvent flush

cleaning, can be better-suited to delicate samples (McPhee *et al.*, 2015). Soxhlet-extraction was used for all cores within this work.

4.2.1 Soxhlet Extraction

The Soxhlet extractor was originally designed to extract oils from solid materials (Soxhlet, 1879), involving a reflux system, in which a solvent is repeatedly condensed over the chosen sample. Solvents are selected such that the component desired to be extracted has limited solubility within the solvent. Figure 4.1 presents a schematic of Soxhlet extraction equipment.

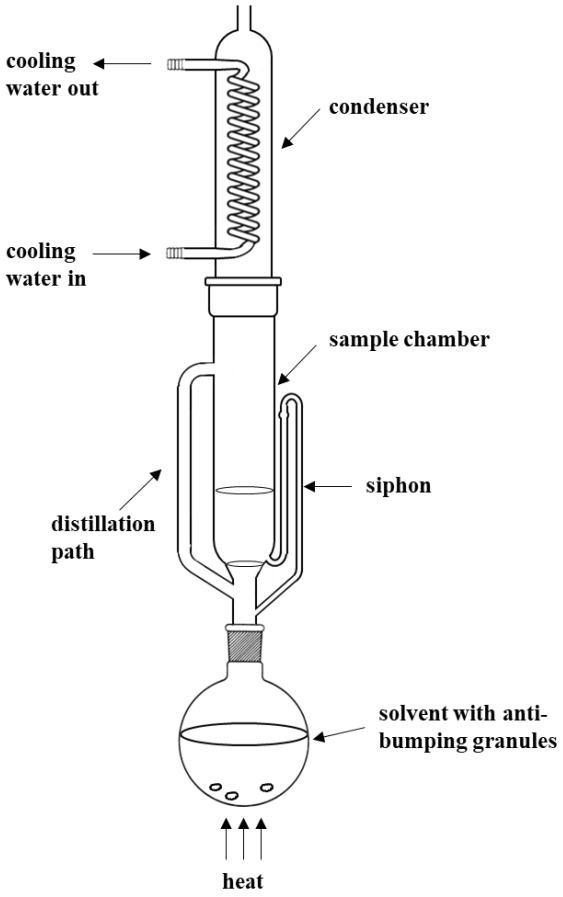

Figure 4.1. Schematic of the hot-solvent Soxhlet extraction apparatus.

The sample to be 'cleaned' is loaded into the sample chamber, beneath which a round-bottomed flask is connected, part-filled with solvent and a few anti-bumping granules. Above the sample chamber, a condenser unit circulated with chilled water is attached. As the flask is heated, solvent evaporates once its boiling point is surpassed. Solvent vapours travel through the distillation path, entering at the top of the sample chamber. Vapours continue to rise into the condenser, before condensing and dripping into the sample chamber. As the process continues, hot condensed solvent fills the chamber, submerging the samples, diffusing into material pores and leaching out impurities. Once the solvent level reaches the top of the siphon, condensed solvent (and extracted impurities) reflux and drain through the siphon, into the round-bottomed flask.

This process continues repeatedly and can be left unattended. Solvent discolouration can occur, due to leached organic components from core samples. The operator should frequently check the solvent for discolouration – replacing the solvent if this occurs. This criterion can be used to identify the endpoint of cleaning. For rock cleaning, a series of solvents are used to leach out different components in rocks (hydrocarbons, water, salts). The completion of each cleaning stage can be checked by testing cores under UV lighting for oil fluorescence, and testing effluent solvents with 10% silver nitrate solution, for presence of salt chloride ions. The entire process can take from several days to weeks. Solvents used have variable water solubilities, with boiling points in the range ~56 °C (acetone) to ~140 °C (xylene). Further details on commonly-used solvents are given in McPhee *et al.* (2015).

4.2.1.1 Materials and Chemicals

Soxhlet cleaning of all cores in this thesis was conducted with toluene (≥ 99.3%, Sigma Aldrich), chloroform (≥ 99.8%, Sigma Aldrich) and methanol (≥ 99.6%, Sigma Aldrich). Silver nitrate solution, prepared with $AgNO_3$ (≥ 99%, Sigma Aldrich) and DI water, was used to test for chloride ions.

4.2.1.2 Cleaning Protocol

The protocol for Soxhlet core cleaning was conducted as follows:

1. 650 ml solvent was loaded into the 1000 ml round-bottomed flask, together with 5-10 anti-bumping granules;
2. after loading cores into the sample chamber and assembling the Soxhlet extractor, the round bottomed flask and neck, distillation path and siphon tube were wrapped in several layers of aluminium foil (to minimise heat losses);
3. cooling water and the heating mantle were switched on, and the solvent brought to a slow boil;
4. each solvent stage was run continuously for at least 48 h (solvent was replaced if discolouration occurred);
5. the solvent stages (boiling points denoted in parentheses) were conducted as follows: firstly toluene (111 °C), secondly a 3.5:1 chloroform/methanol azeotrope (54 °C), thirdly methanol (65 °C). These extract water, hydrocarbons and salts, respectively;
6. following the methanol stage, a few drops of 10% $AgNO_3$ solution were added to 5 ml of the methanol solvent effluent to check for presence of chloride ions. If needed, the solvent was replaced with fresh methanol and the stage repeated;
7. cleaned cores were dried in a laboratory oven at 95 °C for 24 h.

4.3 The MRRC CFS

This section presents the process flow diagrams (PFDs) and process and instrumentation diagrams (P&IDs) for the MRRC CFS. An overview of the CFS is presented – including overall design criteria and PFD of the full system. Subsequently the independent injection and confining loops within the system are considered in turn, providing details on operational protocols and equipment sensitivities.

Finally, the rock core holder (RCH) cells used for core flooding experiments within the 85 MHz and 2 MHz magnet systems are discussed.

4.3.1 CFS Overview

The purpose of the CFS is to safely inject fluids into rock cores at reservoir-representative conditions, simultaneously monitoring any physical changes in injection conditions and NMR responses of the core sample signal. Accordingly, CFS design requirements are to:

- mimic reservoir-representative conditions:
    - inject fluids at reservoir-representative flowrates;
    - switch between injection of several process fluids (hydrocarbons/brines/EOR injectants), with minimal disruption and no introduction of air to the system;
    - flow through the RCH in both up-flow and down-flow directions (simulating different directional flows in a reservoir);
    - maintain pressures and temperatures consistent with typical reservoir conditions;
    - control outflow pressure conditions (by maintaining a back-pressure);
- maintain safe operating conditions:
    - CFS, RCH and all equipment should fail safely;
    - construction materials should withstand pressure, temperature and chemical conditions presented by process fluids;
- enable monitoring of core flooding events:
    - all materials entering the magnet, not pertaining to the core, should be NMR-silent;
    - capacity for recording pressure and temperature changes;
    - injection lines should have minimal dead volumes, to reduce uncertainties in external volumetric quantification of produced and injected volumes to the core.

A PFD of the overall CFS is presented in Fig. 4.2.

The CFS is comprised of two flow loops – an injection and confining loop, as highlighted in Fig. 4.2. The injection loop controls injection of pore fluids into the core. The confining loop provides reservoir environmental conditions – heating, and an overburden pressure around the core. The latter simulates stresses and loads present below the Earth's surface, due to the weight of material above a section of reservoir rock.

The injection loop (MRRC-built) consists of an injection pump, three fluid accumulators, and a backpressure regulator valve in the RCH effluent line. The injection pump (Quizix QX-20K dual syringe pump, Chandler Engineering, Oklahoma, USA) pumps DI from a reservoir, in turn driving three 1 litre capacity floating-piston accumulators (FPA 1000-10 Hast, Vinci Technologies, France). The accumulators hold the process fluids (hydrocarbon/brine/EOR injectant) and a valve manifold (see section 4.3.2) controls which accumulator is driven by the pump. The flow direction through the RCH

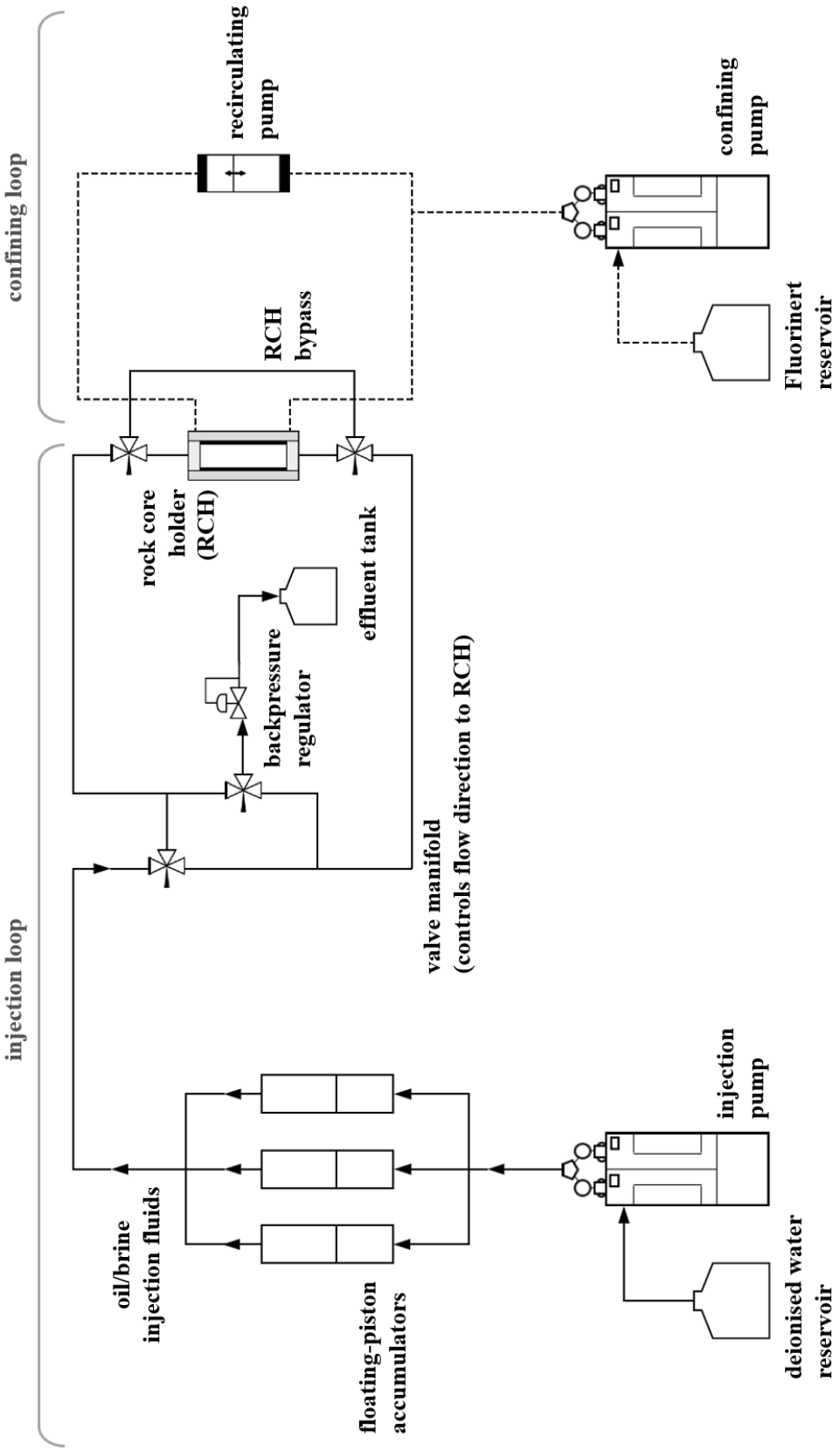

Figure 4.2. PFD of the overall CFS, including the injection and confining loops.

is subsequently controlled by a further valve manifold, which facilitates flow in either up/down directions. In both cases, effluent flows through a backpressure regulator valve downstream (Tescom 26-1700 Series low-flow C_v = 0.02, Emerson, UK), and into a collection reservoir. If desired, the RCH can be bypassed using a bypass flow loop. The CFS-RCH connection is not permanent and is interchangeable. For both the 85 MHz and 2 MHz, two differing, custom-built RCHs are used, as further discussed in section 4.3.5.

The confining loop (Core Laboratories, Texas, USA) consists of a syringe pump (Isco 100 DM, Core Laboratories) which feeds a confining fluid into the RCH – within a cavity wall surrounding, but not contacting, the core. Fluorinert FC-43 (Acota, UK), an NMR-silent material, is used as the confining fluid. The syringe pump sets the desired overburden pressure, and an additional recirculating pump (Recirculation HS Pump, Core Laboratories) heats and recirculates Fluorinert around the core.

The CFS is designed to operate up to 10,000 psi (~69 MPa) and 100 °C. All equipment components are rated at or beyond these conditions. Further, all CFS equipment must withstand the harsh chemical conditions presented by typical EOR process fluids – including high salinity brines and crude oils with acidic or sulphur compounds. Accordingly, all CFS wetted materials are in stainless steel 316, (or Hastelloy for the accumulators) and the seals within the pump, RCH and valves are of: Viton/Teflon/PTFE/Buna-N/CTFE. All tubing, valves (needle valves) and connectors were supplied by Staffordshire Hydraulics, all connections were made using Swagelok or Taper Seal high pressure fittings. Dead volumes in the CFS are minimised by using the minimum diameter tubing possible for the required pressure rating (0.06 ″ (1.5 mm) I.D., 1/8 ″ (3.2 mm) O.D.). Rupture disc (pressure relief) safety devices are installed throughout the CFS – details shown in Figs. 4.3 and 4.4. A series of pressure indicators and transistors (the latter with data logging capacities) are installed on both injection and confining loops – details presented in sections 4.3.2, 4.3.3. Additional start-up injection, drainage ports and purging lines are located throughout the CFS, enabling drainage and filling of isolated regions of the CFS – presented in Figs. 4.3, 4.4.

4.3.2 CFS Injection Loop

This section presents the injection loop P&ID (Fig. 4.3), providing further details on: injection loop operating procedures (accumulator filling, controlling RCH flow direction); sensitivities of injection loop equipment; and additional operational notes.

4.3.2.1 Injection Loop Operation: Accumulator Filling

This section outlines the protocol for filling accumulator vessels, nomenclature as in Fig. 4.3. The protocol is here described for filling ACC-01, an equivalent process is used for ACC-02 and ACC-03.

1. isolate ACC-01 from SP-01 and downstream lines by closing all V-01 and V-02 ports;

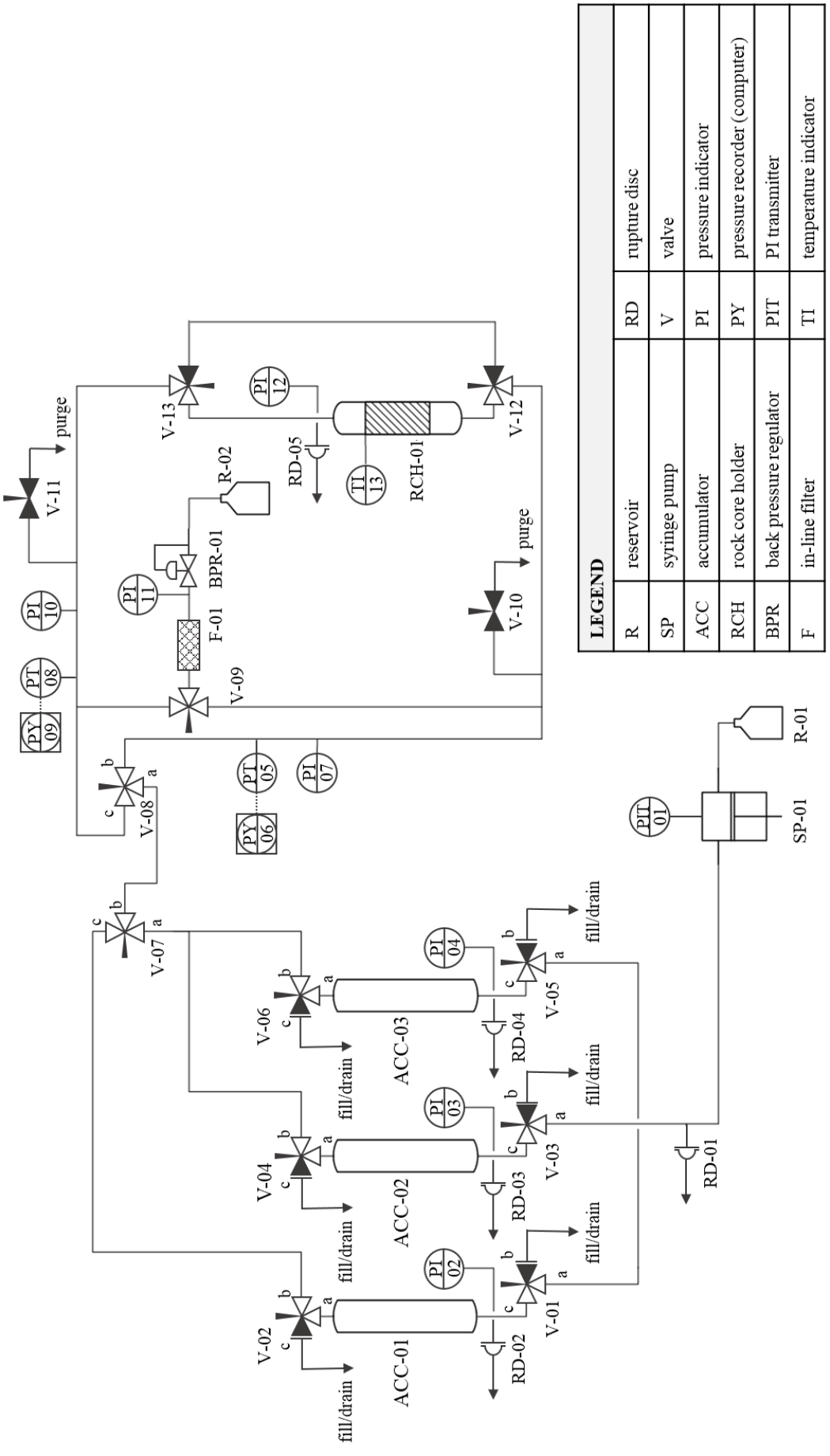

Figure 4.3. P&ID of the CFS injection loop.

2. connect laboratory compressed air source (closed) at V-02c, connect a drain line to drain port V-01b;
3. open V-02c and V-01b (maintaining all other ports in V-01 and V-02 shut) and using compressed air, apply a pressure of ~30-40 psi (~207-276 kPa) to the floating piston to drain all DI water beneath the piston in ACC-01;
4. close V-02c and V-01b, detach the drain line at V-01b and compressed air line at V-02c;
5. connect a vacuum pump (RV3, Edwards) at V-02c using a three-way valve (connecting to the pump, and a feedline in a reservoir containing the desired fluid to fill ACC-01);
6. open V-02c (maintaining all other V-01 and V-02 ports shut), and open the three-way valve towards the pump and apply a vacuum;
7. close the three-way valve at the pump, stop the vacuum pump and open the three-way valve to the reservoir – ACC-01 will start to fill with this reservoir fluid;
8. once no further change in reservoir fluid level occurs, remove the feedline from the reservoir and open to air (bringing ACC-01 to atmospheric pressure), then close V-02c;
9. detach the filling lines from V-02c;
10. open V-01a, V-01c, connect a drain line to V-02c, open V-02c, and use SP-01 to drive the floating piston and purge any air at the top of ACC-01 through V-02c.

4.3.2.2 Injection Loop Operation: Controlling Flow Direction through the RCH

This section outlines the protocol for placing the RCH in both downflow and upflow directions (nomenclature as in Fig. 4.3):

1. adjust valve manifolds to achieve flow from the desired accumulator (V-01 to V-06), and accordingly open either V-07a or V-07c;
2. open V-07b and V-08a;
3. for downflow through the core and exiting via BPR-01: open V-08c, V-13b, V-13c, V-12c, V-12a, V-09a, V-09b (maintaining all other valve ports closed);
4. for upflow through the core and exiting via BPR-01: open V-08b, V-12a, V-12c, V-13c, V-13b, V-09c, V-09b (maintaining all other valve ports closed);
5. under downflow conditions, PY-06 and PY-09 record the core downstream and upstream pressures, respectively (vice versa for upflow conditions).

4.3.2.3 Injection Loop Equipment Sensitivities

This section outlines sensitivities of key equipment within the injection loop, including: SP-01 (and PIT-01), PT-07, PT-09 and F-01 (nomenclature as in Fig. 4.3).

The syringe pump, SP-01 (Quizix QX-20K) is rated to 20,000 psi (~138 MPa), with in-built Sensata pressure transducers of sensitivity 1.6 psi (~11 kPa). SP-01 provides flowrates up to 7 ml min^{-1}, with flow sensitivity 0.00015 ml min^{-1}. All delivered pressures, flowrates and produced volumes can be logged using Quizix PumpWorks software, at a minimum datalogging frequency of 1 s. Pressure

transducers PT-07 and PT-09 (Heise Digital Precision Model DXD, Ashcroft, UK) are rated to 10,000 psi (~69 MPa), with sensitivity 2 psi (~14 kPa), update frequency 15 ms. Datalogging is possible using Heise DXD software.

The in-line filter F-1 (Staffordshire Hydraulics, UK) was retrospectively installed and commissioned in August 2017 following repeated long-term failure of BPR-01. The latter resulted from accumulation of rock particulates in the BPR valve seat. A mesh filter of size 40 µm was selected, based upon recommendations from the BPR manufacturers, also in accordance with typical sandstone grain particulate sizes.

4.3.2.4 Injection Loop Additional Operational Notes

Although the CFS is rated for operation up to 10,000 psi (~69 MPa), the RCHs currently in use at the MRRC are not designed for such pressures (see section 4.3.5). Thus, it is important to note that appropriate rupture discs (RD-01 to RD-05) should be selected based upon the RCH in operation. Following CFS commissioning at 10,000 psi, the original 10,000 psi rupture discs were exchanged for those rated to lower pressures, appropriate to the RCHs in use. If experiments at higher pressures are to be conducted, these should be exchanged for appropriately rated safety devices.

4.3.3 CFS Confining Loop

The confining loop was purchased from Core Laboratories. As proprietary data, their design and P&ID cannot be reproduced. A simplified PFD is presented in Fig. 4.4

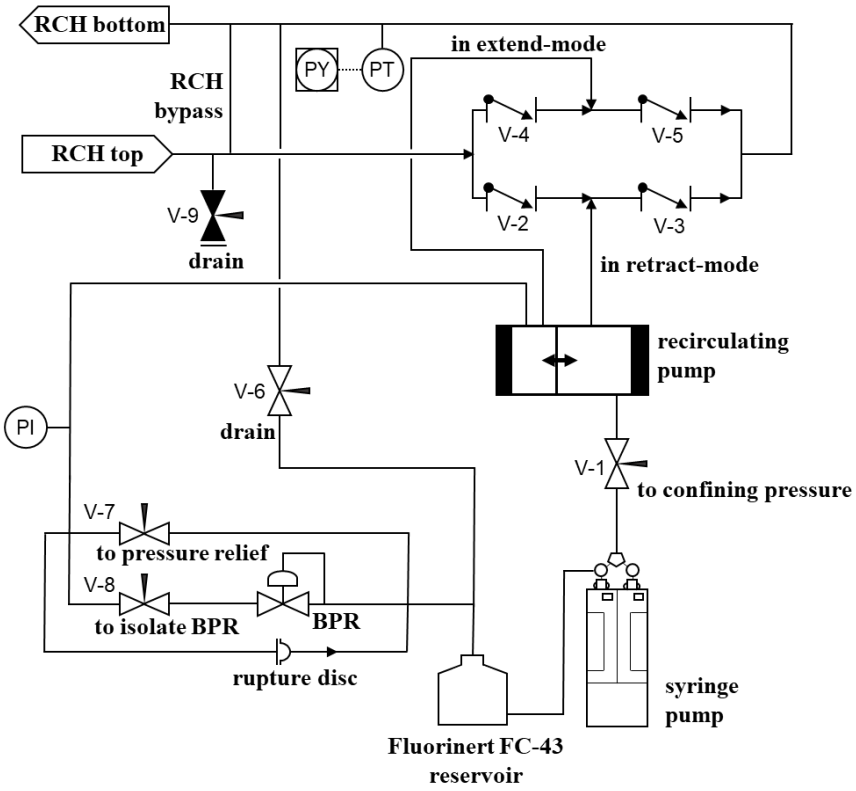

Figure 4.4. Simplified PFD of the Core Laboratories confining loop system.

Recirculation of confining fluid is unidirectional (top-to-bottom of the RCH), regardless of whether the recirculating pump is in extension or retraction. This is facilitated by a series of non-return valves (see Fig. 4.4). The following sections outline the operating procedures for filling the confining loop, and the sensitivities of confining loop equipment.

4.3.3.1 Confining Loop Operation: Filling the Confining Loop

This section outlines the protocol for filling the confining loop, nomenclature as in Fig. 4.4. The protocol is described for filling the loop and RCH, when connected to the Oxford Instruments RCH overburden cell.

1. connect the Fluorinert reservoir outlet to the syringe pump inlet, and the confining loop inlet/outlet ports to the RCH;
2. close valve ports to the RCH and open the confining system bypass – enables filling, air-purging and leak-testing of the confining loop, isolated from the RCH;
3. open V-1, V-6, V-7 and V-8 and operate the syringe pump in constant pressure mode at a low pressure (100 psi (~689 kPa)) to pump fluid into the confining loop, until Fluorinert begins to drain back into the reservoir – i.e. the confining loop is liquid-filled;
4. ensure the isolated confining loop has no leaks and all air has been purged – the pump should maintain set pressure at a zero flowrate;
5. close V-6, V-7, V-8 and the RCH bypass loop, open the valve port towards the RCH bottom and open the RCH bleed valve, V-9 – enables filling the RCH overburden pressure annulus;
6. operate the syringe pump in constant pressure (at low pressures, ~100 psi (~689 kPa)) until all air is purged through V-9 (including air in the RCH anulus);
7. close V-9, close the RCH bypass, open both confining loop ports at the RCH top and bottom;
8. verify all air is purged from the system – the syringe pump should maintain set pressure at zero flowrate;
9. pressure test the full system, to ensure adjustable connections at the RCH ports have been made safely;
10. switch on the recirculation pump, complete several extension/retraction cycles and periodically open V-9 to purge any entrained air.

4.3.3.2 Confining Loop Equipment Sensitivities

This section outlines the sensitivities of key equipment within the confining loop, including the Isco syringe pump and pressure transducer.

The Isco syringe pump has an operating pressure range up to 10,000 psi (~69 MPa), providing flowrates up to 30 ml min^{-1}, with sensitivity 0.00001 ml min^{-1}. The pressure transducer (PT-PY, Fig. 4.4) is a Heise Digital Precision Model DXD (Ashcroft, UK) with pressure-ratings, sensitivities and data-logging capabilities equivalent to the pressure transducers in the CFS injection loop (see section 4.3.2.3).

4.3.4 CFS Commissioning and Testing

The full CFS underwent a complete and rigorous HAZOP analysis covering all potential hazards, safety issues and risk situations that could occur in operation, including: over or under-pressure; high or low temperature; high, low or no flow conditions; leaks; and incorrectly positioned valves.

Upon completion of the CFS construction, the CFS underwent pressure and leak-testing, to ensure all components and connections satisfied the design pressure rating. Injection and confining loops were tested separately – the former with deionised water, the latter with Fluorinert.

In both cases, all lines were filled with their respective process fluids and all air purged to ensure a hard system. Pressure and leak tests were conducted by operating the syringe pumps in each flow loop in constant pressure mode and incrementally increasing pressure, up to 10,000 psi (~69 MPa) – at each pressure step, the pump was required to hold set pressure at zero flow. If not possible, this indicated presence of a leak. The leak would be subsequently identified, the system depressurised, the responsible connection re-tightened and the system re-tested. This procedure was iterated until all connections within the CFS were able to reach 10,000 psi (~69 MPa), leak-free. This procedure should be followed when any changes are made to permanent connections within the CFS.

4.3.5 Connection of CFS to Different NMR Magnet Systems

All experiments reported within this thesis were carried out at 85 MHz or 2 MHz – for both magnets, custom-built RCHs tailored to each NMR system were used. This section details the RCH designs for use at 85 MHz and 2 MHz, together with associated operational procedures.

4.3.5.1 CFS RCH at 85 MHz

At 85 MHz, a low-pressure RCH designed by ErgoTech (Conwy, UK) was used – a schematic is presented in Fig. 4.5.

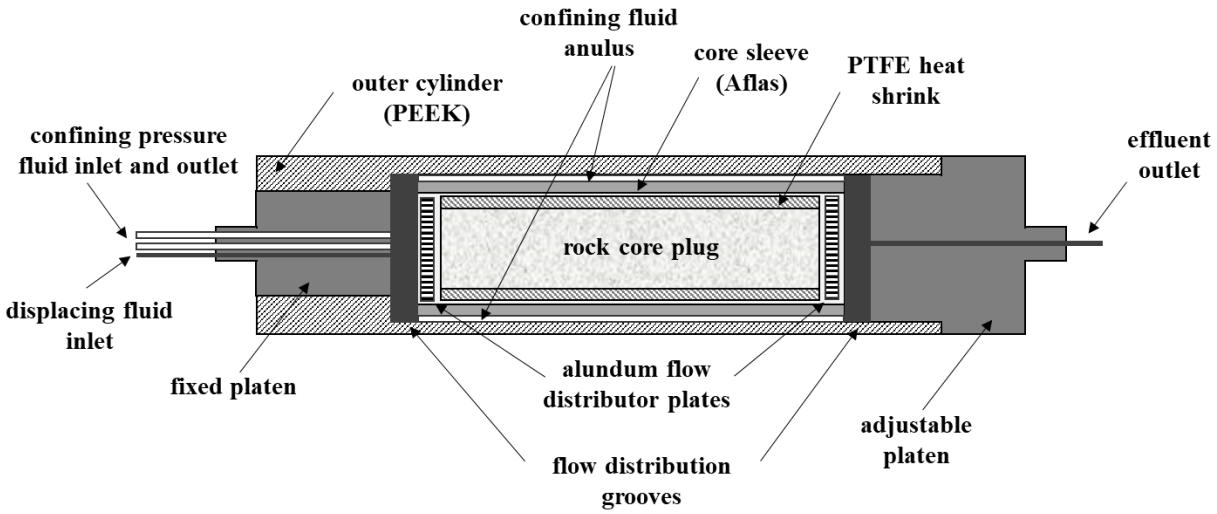

Figure 4.5. Schematic of the ErgoTech RCH (Conwy, UK), for use in the 85 MHz magnet.

The ErgoTech RCH is rated to 750 psi (~5 MPa) and room temperature conditions, and is designed for holding 1.5″ (38.1 mm) diameter cores, with lengths in the range 60-70 mm. With a 59.5 ± 0.1 mm O.D., the RCH is designed for use in both 61 mm and 63 mm I.D. r.f. probes.

The RCH consists of an outer cylinder, sealed with two end platens, and four ports for fluid injection. A core sample is held within the RCH centre, separated from the cylinder walls by an Aflas (fluoroelastomer) sleeve. Between the Aflas sleeve and cylinder wall, an anulus exists for the confining fluid. The confining fluid is recirculated into the anulus through two ports located at the core inlet face; the injection fluid has inlet and outlet ports at either end of the RCH. Flow distribution grooves on the inner faces of the end platens promote even distribution of injected fluids to the core. The end platens (one fixed, one adjustable) enable samples of variable length to be held within the RCH. Alundum flow distributor discs are inserted at the core inlet and outlet, further promoting uniform distribution of injected fluids. Prior to insertion in the RCH and Aflas sleeve, the core is encased in a single layer of polytetrafluoroethylene (PTFE) heat-shrink tubing. This prevents pore fluids from contacting the oil-wetting Aflas sleeve, which can result in (non-reservoir-representative) preferential oil flow pathways at the core-Aflas interface.

The RCH is entirely constructed of NMR-silent, non-metallic and non-magnetic materials (polyether ether ketone (PEEK) cylinder, PEEK tubing and connection ports, Aflas and PTFE core sleeves, and Fluorinert FC-43 confining fluid). Fluorinert and PTFE are both ^{1}H-free, whilst Aflas and PEEK have very short T_2* times. The materials are thus 'invisible' in ^{1}H-NMR experiments, such that only signal from the core is detected.

Although connection of the 85 MHz RCH to the CFS confining loop (Fig. 4.4) is possible, for all core floods reported in this thesis at 85 MHz, a separate low-pressure confining loop pumping system (suited to the ErgoTech pressure limits) was used – a Gilson 207 HPLC pump (Gilson Inc., USA), together with a backpressure regulator (Idex Health and Science, USA) to maintain fixed confining pressure conditions of 290 ± 25 psig (~ 2 ± 0.2 MPaG). All injection fluids were delivered using the CFS injection loop (Fig. 4.3).

It is important to note that there are multiple options for connecting the ErgoTech RCH to the CFS injection loop. For the work conducted in Chapter 5, the Ergotech injection feed line was connected at V-02c, with pressure datalogging taken from PIT-01 on SP-01 (nomenclature as in Fig. 4.3). For the work conducted in Chapters 6 and 7, the Ergotech injection feed line was connected to both V-12c and V-13c (nomenclature as in Fig. 4.3). The two ports facilitated smooth transitions between injecting different fluids in the polymer-brineflood EOR protocols. Connection of both feedlines to the RCH was facilitated through an additional Y-piece, wherein each flow-path was controlled by an independent ball valve. Datalogging of pressure conditions was taken from both PIT-01 and either PIT-02 or PIT-03 (the latter two dependent upon the pore fluid injected, and from which accumulator the fluid originated).

4.3.5.2 CFS RCH at 2 MHz

At 2 MHz a high-pressure RCH (Oxford Instruments, UK) in-built within an NMR probe was used. This was designed to connect directly to the CFS injection loop (V-12c and V-13c, Fig. 4.3), and the CFS confining loop (indicators 'RCH top' and 'RCH bottom', Fig. 4.4). A schematic of the Oxford Instruments RCH is presented in Fig. 4.6.

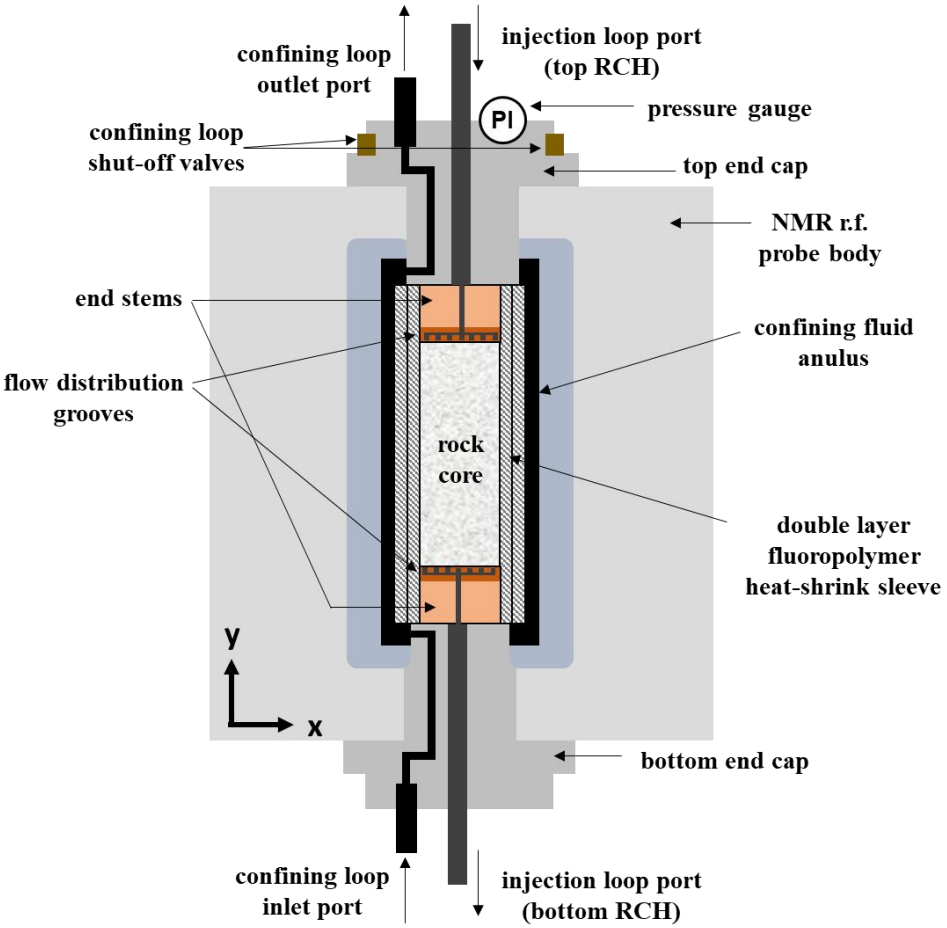

Figure 4.6. Schematic of the 2 MHz RCH (Oxford Instruments, UK), here illustrated with flow configuration from top-to-bottom in the injection loop.

The Oxford Instruments RCH is rated to 5000 psi (~34 MPa) and 100 °C, and designed for holding 1″ (25.4 mm) diameter cores, with lengths in the range 1″-2″ (25.4-50.8 mm). The RCH consists of an inner compartment holding the core and injection fluids, surrounded by the confining fluid anulus – the two regions are separated by a double layer sleeve of fluoropolymer heat-shrink tubing (Geoshrink, Adtech, UK). The injection compartment is sealed with two end stems – each consisting of a PEEK endplate with flow distribution grooves (in contact with the core sample faces), and an injection loop feed line (connecting the CFS injection loop to the core). The position of the end stems within the RCH borehole is adjustable from both directions, allowing for cores of variable length. The confining fluid anulus connects to the CFS confining loop, with additional shut-off valves and a pressure indicator gauge located at the top of the RCH probe. The RCH is supported and fixed in-place within the r.f. probe

body using two end caps at either end of the probe. The end stem injection lines and end caps are made of 316 stainless steel, although these do not fall within the active imaging region of the magnet. All RCH materials held within the active region of the coil are constructed of NMR-silent materials (PEEK end plates, fluoropolymer core sleeves and Fluorinert confining fluid).

4.3.5.3 CFS Dead Volume Calibration at 2 MHz

For the RCH system at 2 MHz, all connections within the RCH and to the CFS are rated to 5000 psi, (~34 MPa) and thus consist of the same stainless steel 1/8″ (3.2 mm) high pressure tubing used throughout the CFS. This results in a considerable dead volume in the connections from the CFS outlets to the RCH (V-13c-to-RCH top, V-12c-to-RCH bottom), with no opportunity for purging beyond V-13a or V-12b. It was thus necessary to quantify the dead volumes of these connecting lines. This was important for quantifying fluids injected into a core sample during core flooding fluid switchovers.

Dead volume calibration in both cases (top-RCH and bottom-RCH feedlines) was conducted as follows. The connection lines from the RCH to the CFS were detached and filled with an oil-phase fluid. Using a syringe, an aqueous-phase fluid was then injected and flushed through the lines until no further oil was produced. All effluent was collected in a measuring cylinder and the produced oil was recorded, giving a measure of the connection line dead volume. This procedure was repeated three times, fully cleaning the lines with compressed air between each repeat cycle. These calibration measurements produced dead volumes of 4.8 ± 0.2 ml (V-13c-to-RCH top) and 5.2 ± 0.2 ml (V-12c-to-RCH bottom).

Chapter 5

Insights to the Primary Drainage Mechanism in a Sandstone Core from Spatially-Resolved NMR Relaxometry

5.1 Introduction

Laboratory core floods are widely used in petroleum research for oilfield evaluation and EOR screening. Within this, primary drainage floods are critical to both reservoir characterisation and preparing cores to reservoir-representative conditions (for use in oil recovery screening experiments). Primary drainage consists of a non-wetting fluid displacing wetting fluid within a porous material, initially fully-saturated in the wetting phase. Conducting primary drainage floods as a capillary pressure measurement is useful for reservoir characterisation. These can be used for evaluating reservoir rock quality (capacity for hydrocarbon storage, distribution and flow), pore throat size distributions, wetting characteristics, and predicting reservoir saturation with depth – all fundamental input parameters in reservoir modelling. In the context of sample preparation, primary drainage floods mimic oil migration into an initially water-wet reservoir formation (introduced in section 4.1).

This chapter builds upon the L-T_1-T_2 sequence development in Chapter 3. The sequence is herein used to quantitatively and dynamically monitor the primary drainage of dodecane into a brine-saturated Bentheimer core. The aim is to use spatially-resolved T_1-T_2 correlation maps to provide localised quantitative saturations of each of the hydrocarbon and water phases, as well as qualitative trends in surface wetting and pore filling mechanisms within the core.

5.1.1 Putting Primary Drainage Capillary Pressure Curve Measurements into Context

Reservoir capillary pressure, P_{cap}, is defined as the pressure difference between wetting and non-wetting phases,

$$P_{\mathrm{cap}} = P_{\mathrm{nw}} - P_{\mathrm{w}} \tag{5.1}$$

where P_{nw} and P_w are the pressures of non-wetting and wetting phases, respectively.

In a reservoir formation (for simplicity, modelled as a cylindrical capillary tube), capillary pressure conditions with reservoir depth can be thought of as the buoyancy pressure difference between reservoir oil and water phases (Eq. 5.2), and from the interfacial tensions at the phase boundary (Eq. 5.3):

$$P_{\mathrm{cap}} = \Delta\rho g h_{\mathrm{c}} \tag{5.2}$$

where $\Delta\rho$ is the density difference between fluid phases, g is gravitational acceleration and h_c is the height of capillary rise; and

$$P_{cap} = \frac{2\gamma_T cos\theta_c}{r} \tag{5.3}$$

where γ_T is interfacial tension, θ_c is fluid contact angle on the tube wall and r is the effective radius of the oil/water interface. Reservoir capillary pressure is thus dependent upon wettability, pore structure, and hydrostatic pressure (i.e. reservoir depth) – illustrated in Fig. 5.1, for a water-wet reservoir.

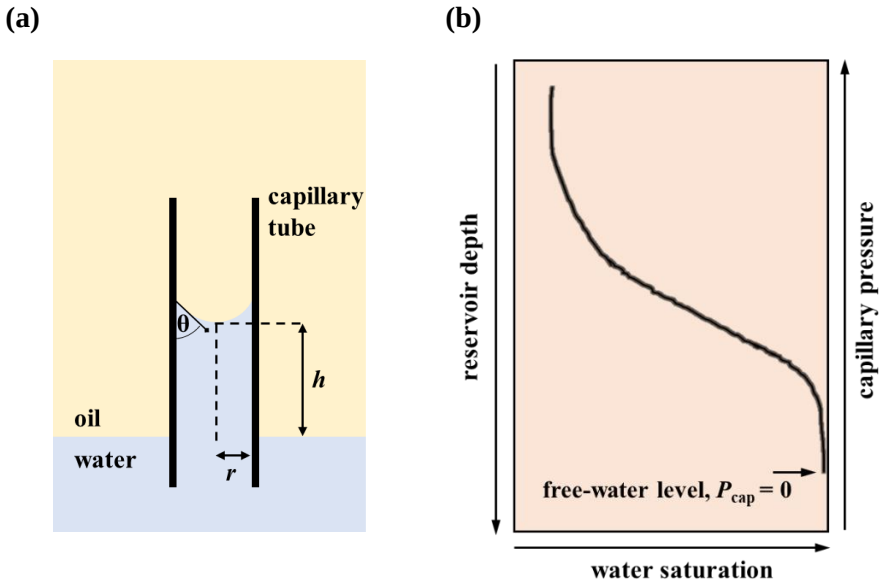

Figure 5.1. Illustration of relationship between capillary pressure, reservoir depth and saturation for a water-wet reservoir, (a) modelled as a capillary tube, (b) visualised in the context of a reservoir. Adapted from Abdallah *et al.* (2007).

Fig. 5.1 and Eqs. 5.1-5.3 highlight that reservoirs exhibit varying saturation profiles with depth (and pore structure). Generally, this results in higher oil saturations at the top of a reservoir, transitioning to higher water saturations at the bottom, until the free-water level is reached (Abdallah *et al.*, 2007). The free-water level is the highest point in a reservoir at which hydrocarbon and water phase pressures are equivalent – that is, $P_{cap} = 0$. Located at the bottom of a hydrocarbon column, the free-water level also marks the point below which a reservoir only produces water. These saturation-depth characteristics are largely governed by reservoir capillary pressure and wettability profiles; as such, it is clear why capillary pressure curve measurements are considered critical for modelling reservoir performance.

Reservoir capillary pressure curves are obtained from primary drainage flooding experiments. As non-wetting fluid is injected, pores and throats of lowest capillary pressure fill first, such that overall, capillary pressure increases as progressively smaller pores are filled – in turn, requiring greater injection pore pressures to achieve. For most reservoirs, water preferentially wets the reservoir rock surface rather than oil – that is, oil is the non-wetting phase and water is the wetting phase. This is thought to occur since for most reservoirs, the original rock depositional environment is believed to have been water-

filled. For oil-water systems, the lowest wetting-phase saturation achievable, for the maximum capillary pressure conditions attainable, is the irreducible water saturation S_{wir} (McPhee *et al.*, 2015).

Achieving a pore-scale understanding of such fluid displacement processes is central to optimising reservoir characterisation, oilfield evaluation and EOR strategies. By nature, the associated measurements are challenging to attain, limited by the complexity of fluid environments present in rocks – dynamic, multicomponent and multiphase, within highly tortuous, three-dimensional pore structures. As a result, to date, macroscopic measurements have most commonly been used to monitor the evolution of such core flooding displacements. Traditional capillary pressure curve measurement methods include: the porous-plate technique (McCullough *et al.*, 1994); mercury injection (Purcell, 1949) and the centrifuge method (Hassler and Brunner, 1945; Slobod *et al.*, 1951). Their relative strengths and weaknesses have been discussed by many authors (Gray *et al.*, 1992; Newsham *et al.*, 2004; Roland *et al.*, 2013; McPhee *et al.*, 2015). Whilst much expertise exists in the acquisition and interpretation of capillary curve data, any molecular scale understanding of the displacement process is, inevitably, indirect.

5.1.2 Probing Pore Filling Mechanisms of Primary Drainage

Direct experimental evidence of primary drainage pore filling mechanisms is essential for validating assumptions made in reservoir pore-scale models, such as the widely-successful pore-network modelling approach (Dullien, 1992; Blunt, 2001; Blunt *et al.*¸ 2002; Blunt *et al.*, 2013). Prior studies have predominantly used model systems that allow optical access: glass beads and particle packings (Harris and Morrow, 1964; Dullien *et al.*, 1986), particle-packed columns (Haines, 1930; Smith, 1933), model porous media (Datta *et al.*, 2014) and glass capillaries or micromodels (Lenormand *et al.*¸1983; Dullien *et al.*, 1986). Experiments using rock samples have typically involved techniques that are destructive (Yadav *et al.*, 1985; Dullien *et al.*, 1986) or invasive, through addition of dopants or tracers (Salter and Mohanty, 1982; Berg *et al.*, 2013).

Various authors have focused on investigating the pore-level events underpinning oil transport during primary drainage, such as snap-off events (see section 6.1.4.1) (Datta *et al.*, 2014) and Haines jumps (Berg *et al.*, 2013). Haines jumps are abrupt increases in interfacial velocity, that result from pore-scale instabilities when a nonwetting fluid displaces a wetting fluid in a pore; these are accompanied by a sudden drop in capillary pressure. The behaviour of the original wetting phase, particularly as the perceived limit of irreducible water saturation is approached, has also been of significant research interest (Haines, 1930; Smith, 1933; Morrow, 1970; Dullien *et al.*, 1986). Both physical processes are important input parameters in pore-level modelling, as discussed by Jerauld and Salter (1990) and Al-Gharbi and Blunt (2005). In addition, recent developments in attaining pore-scale measurements have also been made whereby X-ray microtomography has been used to directly measure the contact angle between immiscible fluids in rock cores at the pore scale, at reservoir-representative conditions (Andrew *et al.*, 2014; Alhammadi *et al.*, 2018). Whilst X-ray microtomography can directly image rock core

fluids at the pore-scale, MRI techniques yield images at the mm-to-core scale. Pore-scale information can be inferred from NMR techniques through relaxation time and PFG approaches.

Considering the concept of irreducible water saturation, several works have demonstrated that as oil continues to be injected and as S_{wir} is approached, the wetting fluid maintains a wetting layer on the pore surface (Morrow, 1970; Dullien *et al.*, 1986; Yadav *et al.*, 1987). Early work using smooth glass beads suggested that S_{wir} takes a fixed value for a particular system, due to trapping of the wetting fluid as hydraulically isolated pendular rings (Morrow, 1970). This was later shown not to be the case in rock samples (Dullien *et al.*, 1986). Dullien and coworkers (1986) used glass micromodels to demonstrate that S_{wir} continues to decrease during primary drainage with increasing capillary pressure, *via* a leakage mechanism. This was facilitated through the hydraulic continuity provided from surface roughness (such as microgrooves in pore walls, pore wedges, edges and corners).

Whilst pore-scale understandings of primary drainage have been pieced together from an assortment of independent techniques, to date, no *in situ* continuous measurement of a primary drainage capillary pressure curve in a rock core sample at representative reservoir conditions has yet been conducted.

NMR relaxation time measurements are well-established in characterising pore size distributions and the extent to which different chemical species, within a porous matrix, preferentially interact with the internal pore surface (see section 2.4.4). In this chapter, the L-T_1-T_2 sequence is used to continuously and non-invasively monitor the development of S_{wir} in a brine-saturated Bentheimer sandstone core *via* primary drainage of dodecane. Spatial resolution is applied in only one dimension along the length of the core, in the direction of superficial flow. Simultaneous tracking of the pressure development with changing water saturation, S_w, produced a capillary pressure curve measurement.

The aim of this work is to use the concurrent measurement of capillary pressure and spatially-resolved T_1-T_2 to directly relate pore-scale events to macroscopic changes in the rock core, as observed in the capillary pressure curve. In particular, spatial resolution of the T_1/T_2 characteristic allows changes in the surface wetting phase to be tracked along the core.

5.2 Materials and Methods

5.2.1 Materials

This section outlines the various sample materials and chemicals used in the experiment, together with the equipment set-up used in the core flood.

5.2.1.1 Materials and Chemicals

A Soxhlet-cleaned outcrop Bentheimer sandstone core (provided by STCH), of diameter 37.53 ± 0.09 mm, and length 60.39 ± 0.48 mm, was used as a reservoir-representative rock system. Soxhlet-cleaning methods were used (see section 4.2.1). The pore size distribution was unimodal, with log-mean pore size and variance 26 μm and 22 μm respectively, as determined by mercury intrusion porosimetry (MIP).

The core pore volume (P.V.) was measured as 15.23 ± 0.02 ml by gravimetric analysis, corresponding to a porosity, φ_p = 22.26 ± 0.01%. The clean core was vacuum dried for 6 h and vacuum saturated in synthetic brine for over 12 h. Low salinity, benign synthetic brine was prepared using sodium chloride (99%, Sigma Aldrich) and deionised water to a concentration of 30.0 ± 0.1 g NaCl litre^{-1}. Dodecane (99%, Acros Organics) was used as the hydrocarbon phase.

5.2.1.2 Core Flooding System

The core flood was conducted using the MRRC CFS, with the arrangement shown in Fig. 4.2, section 4.3.5.1. Following brine saturation, the core and a semi-permeable ceramic disc were, together, enclosed in a layer of PTFE heat-shrink tubing (Adtech Polymer Engineering, UK) and loaded into an Aflas sleeve. The ceramic disc (ELE International) was rated to 15 bar (218 psi, 1.5 MPa), with effective pore size 0.16 µm. The Aflas sleeve and PTFE-enclosed core and disc assembly were loaded into a PEEK RCH flow cell (ErgoTech, Conwy, UK), following the procedure outlined in section 4.3.5.1. The ceramic disc was loaded at the core outlet and was required for achieving S_{wir} by the continuous injection method; simultaneous pressure measurement yielded a capillary pressure curve measurement.

Injection pressure was monitored using the CFS injection pump in-built Sensata pressure transducers (0-20,000 psi (~0-138 MPa) range, ± 1.6 psi (~11 kPa) sensitivity). A confining pressure of 290 ± 25 psig (~2 ± 0.2 MPaG) was applied externally to the core. RCH outlet lines were open to atmospheric conditions. A simplified diagram of the CFS used in this experiment is presented in Fig. 5.2.

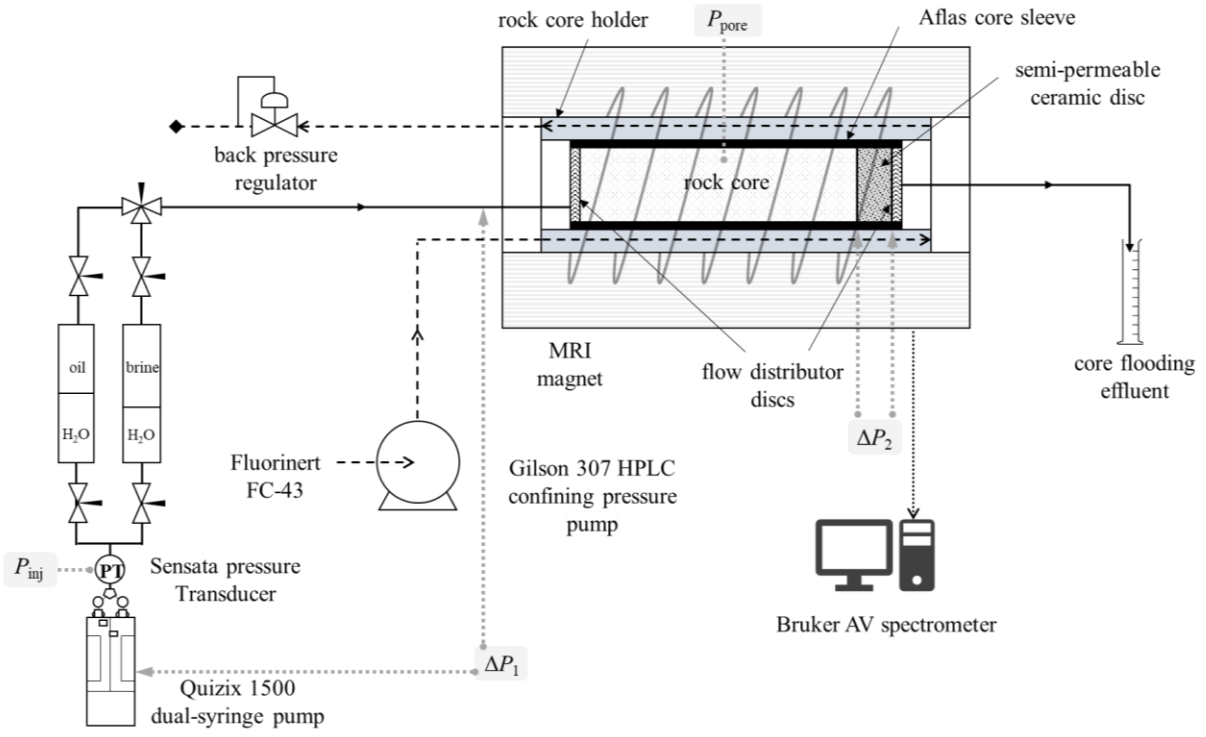

Figure 5.2. Schematic of the CFS set-up. ΔP_1 and ΔP_2 refer to the pressure drops across the (i) pump and CFS, and (ii) ceramic disc, respectively. P_{inj} and P_{pore} are the injection and pore pressures.

Prior to connecting the injection loop to the RCH, the confining loop was filled, purged of air, and both pressure and leak tested externally to the magnet. Subsequently, the injection loop was connected to the RCH and leak tested externally to the magnet. Synthetic brine was injected at 0.055 ml min^{-1} (equivalent to 1 ft day^{-1} linear, interstitial flow velocity) for 2 P.V., to ensure uniform saturation through the core and the removal of any air bubbles within the RCH and core holder assembly.

5.2.2 Methods

This section outlines the various methodologies employed within the experiment, including core flooding protocols, NMR measurement techniques, *HI* calibrations (for volumetric signal quantification) and data processing methodologies.

5.2.2.1 Core Flooding Protocol

Primary drainage of the core to S_{wir} was achieved by continuously injecting dodecane at a fixed injection flow rate, Q_{inj} = 0.016 ml min^{-1} (equivalent to a linear interstitial flow rate, u_{int} = 0.29 ft day^{-1}). This procedure follows a protocol for continuous injection primary drainage capillary pressure measurement, as used by de Waal *et al.* (1989), Zeelenberg and Schipper (1991), Gray *et al.* (1992) and Kokkedee and Boutkan (1995).

For flow in porous media, both viscous and capillary forces will exist. To justify the assumption that continuous injection protocols operate at equilibrium conditions, it is necessary to select a flow rate under which viscous pressure drops are minimised and capillary forces dominate (Huang and Honarpour, 1996; Plug and Bruining, 2007). Under the operating conditions used in this study (0.016 ml min^{-1}, equivalent to 0.06 P.V. h^{-1}), flow regimes fall within the acceptable bounds of continuous injection protocols for capillary pressure measurements (Plug and Bruining, 2007), provide a capillary number (Eq. 6.2, the ratio of capillary to viscous forces) of $Ca = 2.6 \times 10^{-7}$ and a pressure drop across the core on the order of 10 Pa. These, together with the criterion that capillary-dominated flow occurs when $Ca < 10^{-5}$ (Jerauld and Salter, 1990), allow the assumption that flow is dominated by capillary rather than viscous forces.

Pressure drops across the pump and CFS (ΔP_1), as well as the ceramic disc (ΔP_2), were independently measured – denoted in Fig. 5.2. These were subsequently subtracted from the recorded in-flood pump injection pressure, to determine pore pressure, P_{pore}. All effluent liquids were collected in measuring cylinders, facilitating comparison of measured core saturations from NMR-recorded saturations and external volumetric measurements.

The above primary drainage protocol was continued until the injection pressure tended towards an asymptote and approached the ceramic disc pressure limit. A total volume of 0.83 P.V. of dodecane was injected and the total volume of expelled brine collected in the effluent measuring cylinders was determined to be 12.70 ± 0.35 ml.

5.2.2.2 NMR Protocol for Monitoring the Primary Drainage Flood

All NMR experiments were conducted at room temperature (20 ± 1 °C) in a 2 T (85 MHz for ^{1}H nuclei) horizontal bore superconducting magnet, controlled by a Bruker AV spectrometer. A 63 mm inner diameter r.f. birdcage coil, tuned to 85.2 MHz was used for excitation and signal detection. Spatial resolution along the direction of superficial flow (z) was achieved using a magnetic field gradient, capable of a maximum gradient strength 10.7 G cm^{-1}, along the z-direction.

The primary drainage flood was continuously monitored using spatially-resolved L-T_1-T_2 measurements acquired in immediate succession. In addition, a series of reference measurements were acquired both prior to and at the end of the flood. These reference experiments were conducted under no-flow conditions and included:

(i) spatially-unresolved measurement of T_2 (one-shot CPMG);

(ii) spatially-unresolved measurement of the contribution of internal magnetic field gradients to T_2 relaxation times (variable inter-echo time one-shot CPMG);

(iii) a high spatial resolution (0.31 mm pixel^{-1} × 0.39 mm pixel^{-1} × 0.39 mm pixel^{-1}) 3D MRI image (RARE);

(iv) a spatially-resolved T_2 map, averaged in the plane perpendicular to the superficial flow with spatial resolution along the length of the core (L-T_2);

(v) a spatially-resolved T_1-T_2 map, averaged in the plane perpendicular to the superficial flow with spatial resolution along the length of the core (L-T_1-T_2).

Experiment (i) provided a global, spatially-unresolved measurement over the entire core sample. Experiment (ii) was acquired to determine the sample internal gradient effects, facilitating an internal gradient correction in the T_2-dimension of T_2, L-T_2 and L-T_1-T_2 measurements. Experiment (iii) was acquired to verify that the core was uniformly saturated and that no air bubbles had entered the core during flooding procedures. Experiment (iv) was acquired to obtain a spatially-resolved pore size distribution of the brine-saturated core. Experiment (v) was acquired to obtain reference spatially-resolved T_1-T_2 measurements at saturation endpoints, without pixel blurring effects from flow effects.

5.2.2.3 NMR Experimental Parameters

Hard r.f. pulse durations of t_{90} = 22.1 μs and t_{180} = 44.2 μs were used for all NMR experiments.

One-shot CPMG experiments (Kleinberg and Horsfield, 1990) were acquired using t_E = 3.6 ms, RD = 5 s, NS = 8, resulting in a total acquisition time, t_{ACQ} = 2 min per T_2 experiment. Variable inter-echo time one-shot CPMG experiments (T_2-g) (Mitchell *et al.*, 2010a) were acquired with t_E in the range 750 μs to 8 ms, RD = 6 s and NS = 16, resulting in t_{ACQ} = 30 min.

High resolution RARE images were acquired with Gaussian-shaped 90° excitation and 180° refocusing r.f. pulses of duration 512 μs and power levels 27 dB and 21 dB, respectively. An imaging FOV of 83 mm × 50 mm × 50 mm for a corresponding data matrix size of 256 × 128 × 128 pixels was used in the

z, *x*, and *y* directions, respectively. This produced a 3D imaging resolution of 0.31 mm pixel^{-1} × 0.39 mm pixel^{-1} × 0.39 mm pixel^{-1}. Echo times of 4.69 ms and a RARE factor of 8, resulted in a total imaging time of 14 h.

The L-T_2 and L-T_1-T_2 pulse sequences used in this experimental study are shown in Figs. 3.1a and 3.1b, respectively. L-T_2 measurements were acquired at t_E = 3.6 ms and using 128 pixels with FOV = 82 mm, giving a slice resolution of 0.64 mm pixel^{-1}. A recycle delay of 5 s with 16 scans were used, resulting in t_{ACQ} less than two minutes. L-T_1-T_2 measurements were acquired with the same inter-echo time, numbers of pixels and slice resolution. Sixteen different t_{vd} values in the range t_{vd} = 1 ms to t_{vd} = 6 s were employed. Using RD = 6 s, together with NS = 16 scans, resulted in t_{ACQ} = 47 min per L-T_1-T_2 experiment. Given u_{int} = 0.3 ft day^{-1} and considering only displacement in one axial (z) direction, it is expected that pore fluids would have displaced 3 mm during each acquisition time, resulting in some pixel blurring of the T_1-T_2 correlations extracted per 0.64 mm slice. A total of sixteen L-T_1-T_2 measurements were acquired during the flooding process, together with two reference measurements, at no-flow, acquired before and after primary drainage. The total flooding time during which NMR measurements were continuously acquired was ~12.5 h. The total experimental time (including magnet set-up, pulse and sequence optimisation and end-point reference experiments) was ~4 days.

5.2.2.4 Data Processing – Spatially-Resolved Relaxometry Measurements.

Data processing of the L-T_1-T_2 datasets was conducted as described in section 3.2.2.2. To deconvolve internal field gradient effects, an internal gradient correction was applied. Through using the reference T_2-g experimental datasets recorded at S_w = 1, prior to the start of the drainage process, internal gradient corrections were applied across all L-T_1-T_2 datasets (Mitchell *et al.*, 2010a; Mitchell *et al.*, 2013b). The resulting correlations consist of probability distributions of T_1 and T_2 relaxation time constants corrected for relaxation time effects — and are thus volumetrically quantitative.

To facilitate justifiable comparisons between T_1-T_2 correlations acquired at (i) different spatial locations within the core, and (ii) different time points in the flooding process, it was necessary to regularise each T_1-T_2 dataset using a single value of smoothing parameter α. Here, this universally fixed value of α is denoted the universal smoothing parameter, α_U. Optimisation of α_U was conducted in three stages:

1) each axially-resolved T_1-T_2 dataset (existing within a single L-T_1-T_2 measurement) was first independently regularised, to obtain a locally-optimised alpha value, denoted α_L

2) an effective alpha for each L-T_1-T_2 measurement (acquired at a unique time point in the flooding experiment) was obtained by averaging locally-optimised α_L values and considering only the signal regions of the FOV pertaining to the core – this effective alpha is denoted α_{eff}

3) finally, the universal alpha, α_U, was determined by calculating the average of all values of α_{eff}, acquired across all time points throughout the flooding experiment.

To obtain volumetrically quantitative measurements of saturation, NMR signal intensity was scaled using hydrogen indices. Quantification of fluid *HI* is further discussed in section 5.2.2.5.

5.2.2.5 Species-Specific Volumetric Quantification of NMR Signal *via* Hydrogen Index Calibration

Volumetric quantification of NMR signal for different fluid species can be achieved through calibration of their respective Hydrogen Indices (see section 2.4.3). Experimentally, these can be determined from the linear gradient which describes the directly proportional relationship of NMR signal intensity against liquid volume; the *HI* of the desired fluid is the ratio of this gradient to the equivalent gradient value obtained for water. To obtain volumetrically-quantitative measurements of core saturations during the primary drainage flood, the *HI* for brine and dodecane were calibrated against deionised water. These were measured using both L-T_2 and L-T_1-T_2 sequences and benchmarked against the standard NMR spectrum pulse-acquire sequence.

It is well-documented that with increasing salt concentration, receiver efficiency and SNR are reduced (Mo *et al.*, 2009; Takeda *et al.*, 2011). This results in longer 90° pulse lengths and, in the extremes, can lead to dephasing and sample heating, together with the associated lengthening of duty cycles; in NaCl brine, such behaviours are reported to occur above 200 mM concentrations. Given that the brine concentrations used for all core floods within this thesis are above this threshold (30 g l^{-1} NaCl brine, equivalent to ~513 mM), it was necessary to identify for the typical liquid volumes encountered in 1.5″ rock cores whether such ionic effects would present any issues.

Typical liquid volumes in a 1.5″ diameter by 60 mm length core (the sample sizes that can be measured in the MRRC RCH at 85 MHz – see section 4.3.5.1) were assumed to range up to 18 ml, based on the typical reservoir source rock porosities which lie between 5-25 % (Tiab and Donaldson, 2016). Accordingly, signal intensities for the three fluids (brine, dodecane, DI water) were recorded for volumes in the range 0 to 21 ml. The results for the L-T_2, L-T_1-T_2 and spectral sequences are presented in Figs. 5.3 a-c. The measurement error bars are too small to be shown in Fig. 5.3, although the fluid volumes were gravimetrically measured to a sensitivity of 0.001 g, and NMR signal intensities were recorded with a sensitivity of 0.4 %.

The signal intensities measured for the L-T_2, L-T_1-T_2 and spectral sequences are directly proportional to the sample fluid volumes; the goodness of fit described by the coefficient of determination, R^2, was greater than 0.99 for all NMR sequences and for the three fluids tested. From these calibration experiments, the hydrogen indices attained from the L-T_2 sequence yielded a dodecane *HI* of 1.01 ± 0.01, compared to a theoretical value of 1.04; and the *HI* of 30,000 ppm NaCl brine of 0.95 ± 0.01, compared to a reported value of 0.975 (Kleinberg and Vinegar, 1996).

Hydrogen indices attained from L-T_1-T_2 measurements yielded a dodecane *HI* of 1.02 ± 0.01 and an *HI* of 30,000 ppm NaCl brine of 0.94 ± 0.01. For reference, the hydrogen indices attained from NMR spectra yielded a dodecane *HI* of 1.02 ± 0.01 and a brine *HI* of 0.96 ± 0.01. For brine, *HI* was quantified

using sample volumes up to 12.5 ml (observed in Fig. 5.3). This was due to the influence of brine salinities on the receiver efficiency at greater fluid volumes.

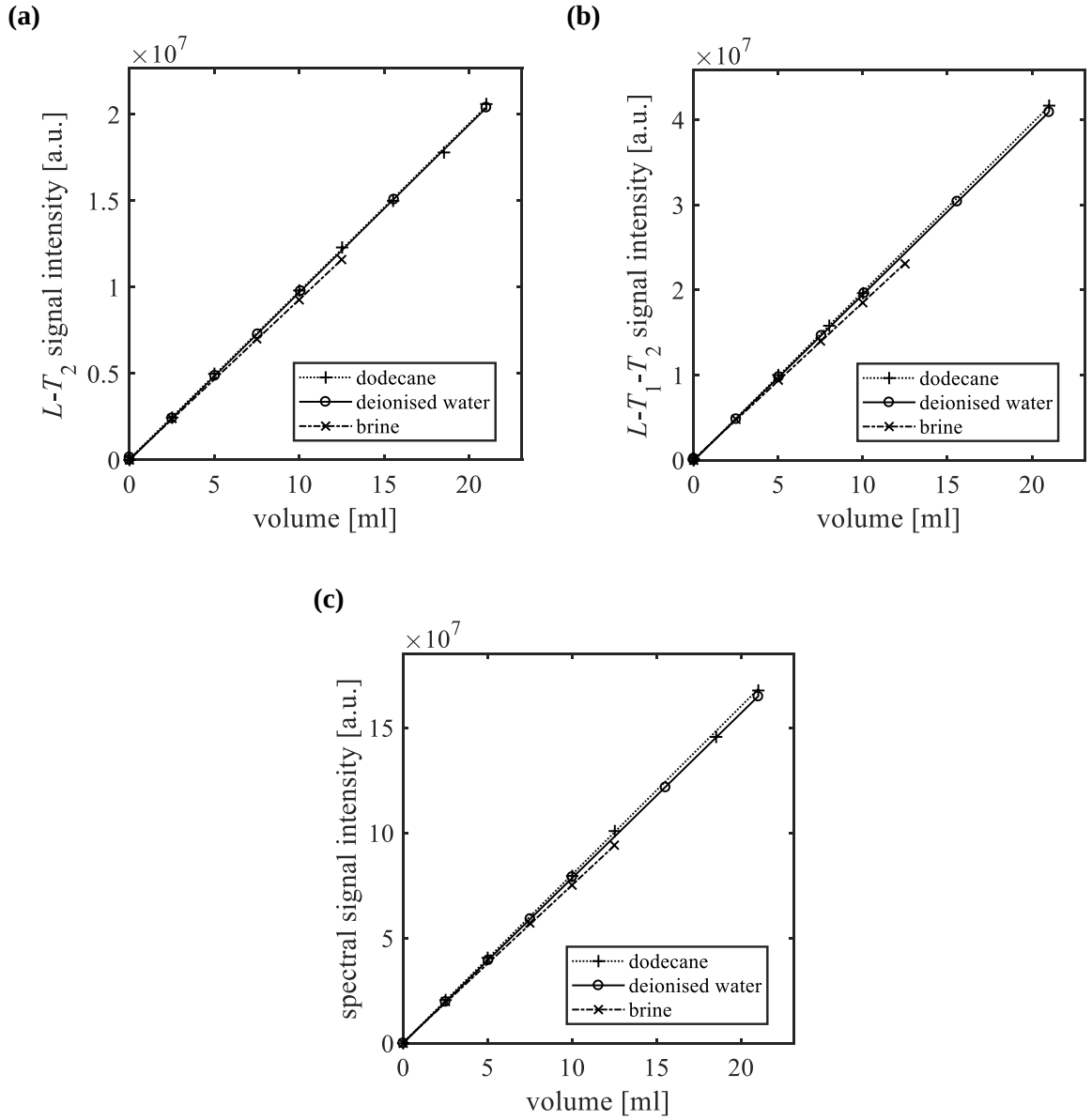

Figure 5.3 Calibration plots of signal intensity against fluid volume, for determination of fluid *HI*, for dodecane and 30 g l^{-1} NaCl brine, compared against deionised water. **(a)** L-T_2 sequence, **(b)** L-T_1-T_2 sequence, **(c)** spectral sequence. In all cases (a)-(c), error bars for both gravimetric sample volumes and NMR signal intensities have not been included, as they are too small to see.

The influence of brine salinity on the receiver efficiency is presented in Fig. 5.4. Figure 5.4a shows the variation in the optimal 90° pulse length with increasing fluid volume for 30 g l^{-1} brine, dodecane and deionised water. Although for dodecane and deionised water, slight fluctuations in the optimal pulse length are observed (within a range of ± 0.5 µs), the range in optimal pulse lengths for brine is considerably larger (± 2.5 µs). For brine, a sharp increase in optimal pulse length is observed at and beyond 12.5 ml, beyond which the range in optimal pulse length exceeds the ± 0.5 µs value observed for dodecane and deionised water.

Figure 5.4b presents the normalised signal intensity responses for increasing brine fluid volumes (using L-T_2, L-T_1-T_2 and NMR spectra). The expected linear relationships (normalised), obtained from the brine *HI* calibrations in Fig. 5.3, are overlaid. This highlights the deviation of brine signal intensity from the expected linearity at increasing brine fluid volumes. Figure 5.4b thus demonstrates a similar trend as observed in Fig. 5.4a – beyond a brine volume of 12.5 ml, a reduction in the receiver efficiency occurs. This is likely to result from greater numbers of salt ions at greater fluid volumes.

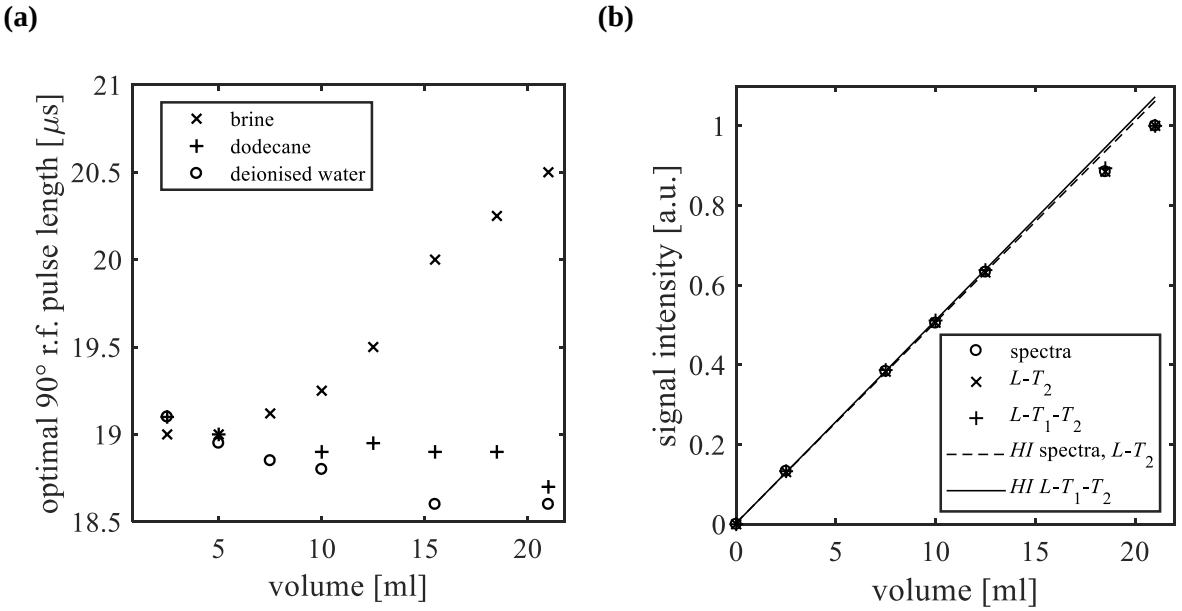

Figure 5.4 (a) Optimal 90° r.f. pulse calibrations for varying fluid volumes of brine, dodecane and deionised water. **(b)** Normalised signal intensity responses for increasing brine fluid volumes, measured using L-T_2, L-T_1-T_2 and NMR spectra. Normalised expected linear relationships obtained from prior *HI* calibrations (from Fig. 5.3) are also shown. Error bars for both the gravimetric sample volumes and NMR signal intensities have not been included, as they are too small to see. The *HI* trendline for the spectra and L-T_2 measurements overlap.

From the calibration experiments presented in Fig. 5.4, it was concluded that the influence of brine salinity on receiver efficiency is, on this 85 MHz magnet system, observed beyond fluid volumes of ~12.5 ml, for the 30,000 ppm NaCl brine sample tested herein. Thus, in the context of core flooding experiments, accurately identifying core saturation conditions can be conducted using the Hydrogen Index calibrations presented in Fig. 5.3, provided the total pore volume of brine does not exceed this volume. Care should be taken at higher brine volumes, as the *HI* calibrations in Fig. 5.3 may no longer be valid. In the context of the Bentheimer sandstone core sample tested in this study, this is equivalent to 82% of the P.V. – i.e., NMR saturation measurements based upon *HI* calibrations are expected to lose accuracy above core brine saturations of $S_w = 0.82$.

5.2.2.6 Rock Core Structural Characterisation

NMR-structural characterisation of the core sample at a fully-brine saturated state ($S_w = 1$) was conducted prior to commencement of the primary drainage flood. Figure 5.5 shows 2D slice sections

within a 3D high resolution RARE image. These images confirm that the core was uniformly saturated, did not contain trapped air, and displayed a homogeneous texture.

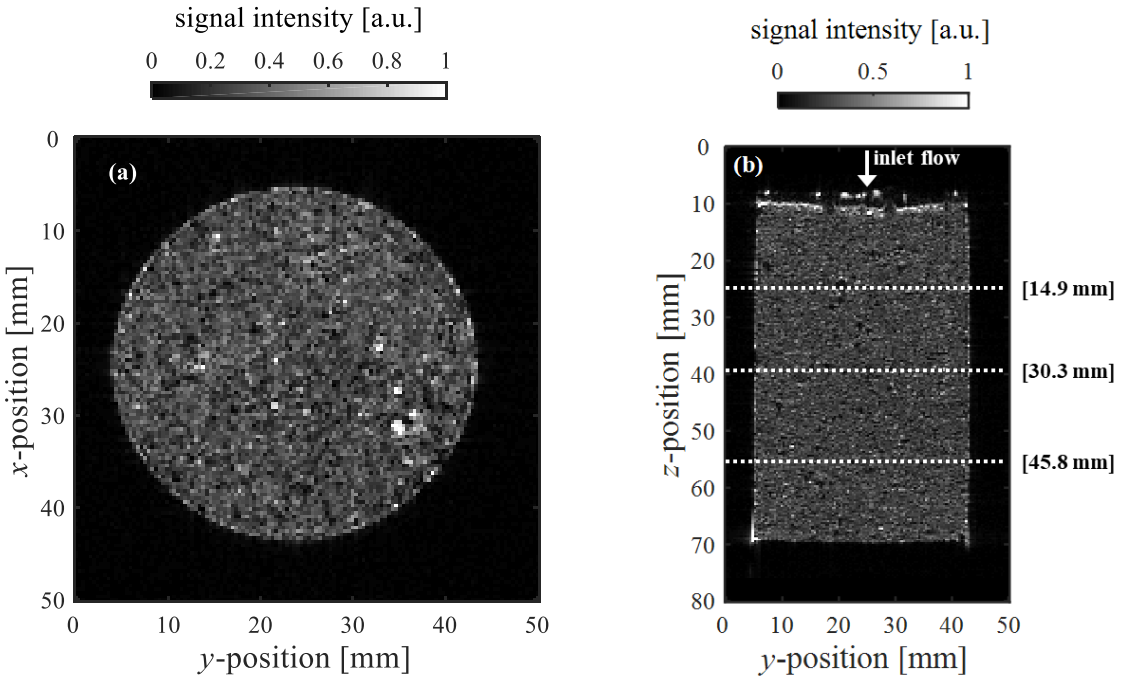

Figure 5.5. Reference saturation maps of the brine-saturated Bentheimer core at S_w = 1, prior to primary drainage, extracted from 3D fully-sampled RARE images. The intensity scale has been normalised relative to its maximum intensity pixel and is proportional to the local brine content in the rock, and thus its porosity. Fig. **(a)** is taken from the central slice in the *x*-*y* plane. Fig. **(b)** is taken from the central transverse slice in the *z*-*y* plane. The arrow indicates the inlet face during the primary drainage flood. The dashed white lines mark the locations within the core from the inlet face, from which the three axial T_1-T_2 slices in the L-T_1-T_2 datasets shown in Fig. 5.9 are taken.

While MIP and NMR T_2 both provided global, spatially-averaged information on the Bentheimer pore structure, L-T_2 distributions were recorded to obtain axially-resolved pore size distribution maps, with a view to identifying any spatial heterogeneities in the core microstructure. To extract pore throat size distributions (PSDs) from the reference T_2 measurements at S_w = 1, a measure of ρ_2 was required (see Eq. 2.45). Following the method of Coates *et al.*, (2001) an effective surface relaxivity was determined by benchmarking the global, spatially-unresolved T_2 distribution against the MIP-PSD, as shown in Fig. 5.6. The difference between the integral area of the T_2 distribution, relative to the MIP-PSD, was minimised and accordingly the optimal effective T_2 surface relaxivity parameter for the Bentheimer core was found to be 27.2 μm s^{-1}. This is comparable with ρ_2 values for sandstones reported elsewhere in the literature, shown to range between 14.3–51.2 μm s^{-1} (Slijkerman and Hofman, 1998; Mitchell and Fordham, 2014) and more specifically for Bentheimer sandstones, quoted as 8 μm s^{-1} (Holland *et al.*, 2013) and 13.73 μm s^{-1} (Slijkerman and Hofman, 1998).

An MIP pore throat size distribution is obtained from a mercury intrusion experiment, in which mercury (a non-wetting fluid) is injected into a porous material. As mercury is non-wetting, it does not automatically penetrate pores by capillary action; instead, mercury must be forced into progressively

smaller pores by applying an external pressure. A mercury porosimeter quantifies the incremental volumes of mercury injected, with increasing applied pressure. When a cylindrical pore dimensions are assumed, the pore throat diameters (d_{pore}) being intruded can be obtained from the applied pressure, P, using the expression, $d_{\text{pore}} = -4\gamma\cos\theta_c/P$, where γ is the surface tension of mercury and θ_c is the mercury contact angle. This provides a measurement of an 'apparent pore diameter' (ASTM Standard D4404-84, 1998).

Both the T_2 and MIP datasets in Fig. 5.6 show a largely unimodal pore throat size distribution; the NMR-PSD, however, has an additional low population peak ~3 μm. This disparity between NMR- and MIP-PSDs in Bentheimer sandstones has previously been observed, where it was attributed to water molecules bound to chlorite minerals (Mitchell and Fordham, 2014). The low population tail in the MIP dataset, for the smallest pore throat diameters ($d_{\text{pore}} < 10^1$ μm), is attributed to surface grooves in individual grains, as well as to the existence of micropores in the cementing materials, such as clay and silt, that require very high pressures to penetrate.

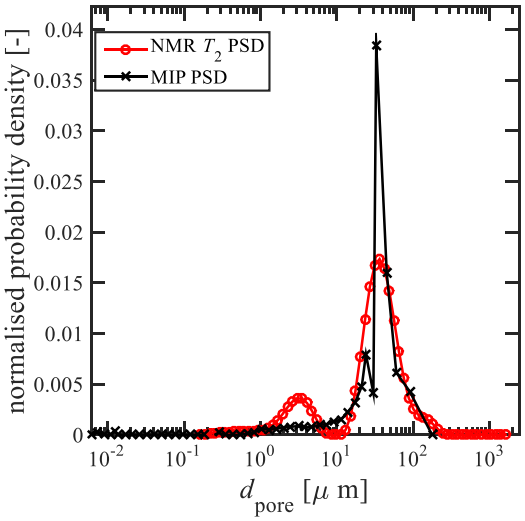

Figure 5.6. Pore throat size distributions (PSDs) of the Bentheimer core sample, acquired with MIP and NMR T_2 distributions on the brine-saturated sample. The NMR T_2 distributions were converted from a time-domain to pore size domain by determining the effective T_2 surface relaxivity through benchmarking against the MIP-PSD, as per the method described by Coates et al. (2001) – the difference between the integral areas of the T_2 distribution, relative to the MIP-PSD, was minimised to extract the effective T_2 surface relaxivity parameter, ρ_2, of the Bentheimer core.

Applying the effective surface relaxivity, ρ_2 = 27.2 μm s^{-1} across the reference L-T_2 map at S_w = 1, produced a spatially-resolved pore size distribution map along the length of the core, shown in Fig. 5.7.

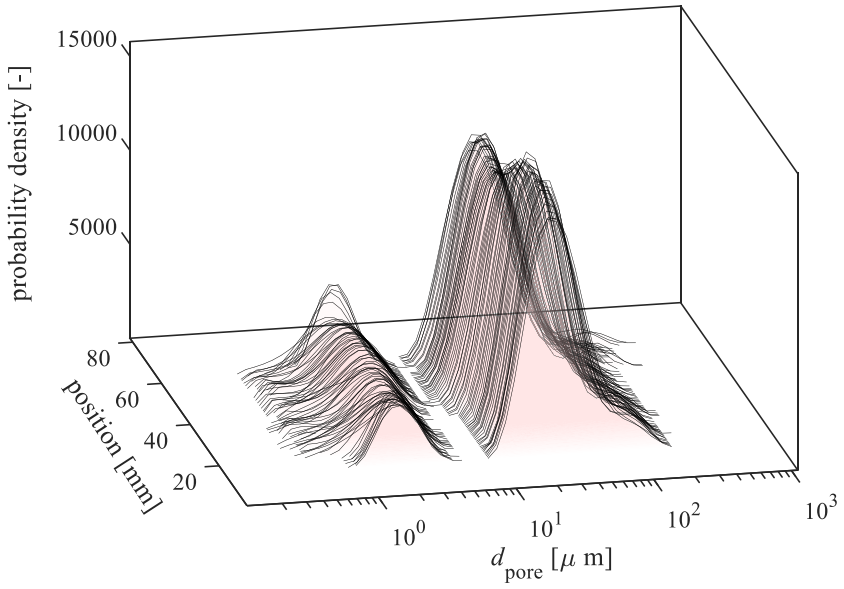

Figure 5.7. Spatially-resolved NMR PSD of the brine-saturated Bentheimer core, measured using the L-T_2 sequence. Conversion from the time-domain to the pore size domain was achieved using the effective T_2 surface relaxivity determined from Fig. 5.6.

Figure 5.7 highlights the spatially-homogeneous microstructure of the core, typical of Bentheimer sandstones, and agrees with the homogeneous distribution of signal intensity in Fig. 5.5.

Although in this particular core sample, the L-T_2 measurement confirmed a spatially-homogeneous structure, it is important to note the merit of the technique, particularly in its application to more structurally-heterogeneous cores. Further, not only does an L-T_2 map reveal localised variations in core microstructure, but it has broader applications within the wider context of SCA. Its capability to probe samples across both pore-micro- and core-macro-scales can be applied both to routine core characterisation protocols and for identifying length scales of heterogeneity (Pomerantz *et al.*, 2007; 2008). The latter is useful for determining core-representative elementary volumes.

5.3 Results

Figure 5.8 presents the changes in capillary pressure as dodecane is injected into the core. Figures 5.9 and 5.10 display a selection of spatially-resolved T_1-T_2 correlation plots at six independent time points in the primary drainage flood, acquired at values of S_w as identified by the shaded regions marked A-E in Fig. 5.8. Point F was acquired at no-flow conditions, once the core had reached its final saturation, S_{wir}.

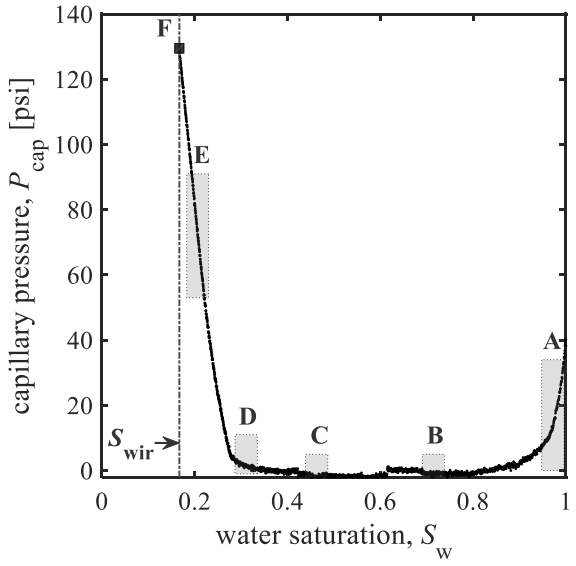

Figure 5.8. Capillary pressure response with decreasing water saturation, during primary drainage of dodecane into an initially brine-saturated Bentheimer sandstone core. Primary drainage was conducted using the porous plate method, with continuous injection at an interstitial flow rate of 0.3 ft day^{-1} (~1 µm s^{-1}). S_{wir} denotes when irreducible water saturation is reached. Shaded labels A-F denote the experimental time frames and corresponding points on the P_{cap}-S_w curve during which the selection of L-T_1-T_2 measurements, referred to in Figs. 5.9 and 5.10, were recorded. This dataset has been presented with pressure in psi units – a standard unit for reservoir pressure in the oil industry. For clarity, the pressure plot ranges 0-140 psi (~0-0.9 MPa), in increments of 20 psi (~0.14 MPa).

Considering first the capillary pressure curve shown in Fig. 5.8, the initial reduction in capillary pressure from 40 psi (~280 kPa) to 0 psi (0 kPa) (during the injection of the first 0.15 P.V. of dodecane), is attributed to pressure equilibration of the system following the preceding 2 P.V. brineflush. This brineflush was immediately followed by the dodecane injection and had been conducted at a comparatively greater flowrate – hence the pressure equilibration. It is recommended that should this experiment be repeated, the preceding brineflush should be conducted at the same flowrate conditions as the dodecane injection to avoid the initial pressure equilibration observed in Fig. 5.8. Alternatively, a core flooding system purge valve (V-10 or V-11, Fig. 4.3) should briefly be opened up to atmosphere to fully de-pressurise the system, inbetween the brineflush and dodecane injection stages. It is however important to ensure that no air is introduced to the core flooding system at this point – hence, the former protocol (slow brine injection) is the preferred recommendation.

Between $0.35 < S_w < 0.85$ the capillary pressure is stable, and below a water saturation $S_w = 0.3$, the capillary pressure begins to rise as the core approaches S_{wir}. This is explained by considering the increasing saturation of the non-wetting phase (dodecane); greater injection pressures are required to fill the smaller pores to overcome the capillary forces from the preferential wetting phase (in this system, brine) (Anderson 1986a;1987a; McPhee *et al.*, 2015).

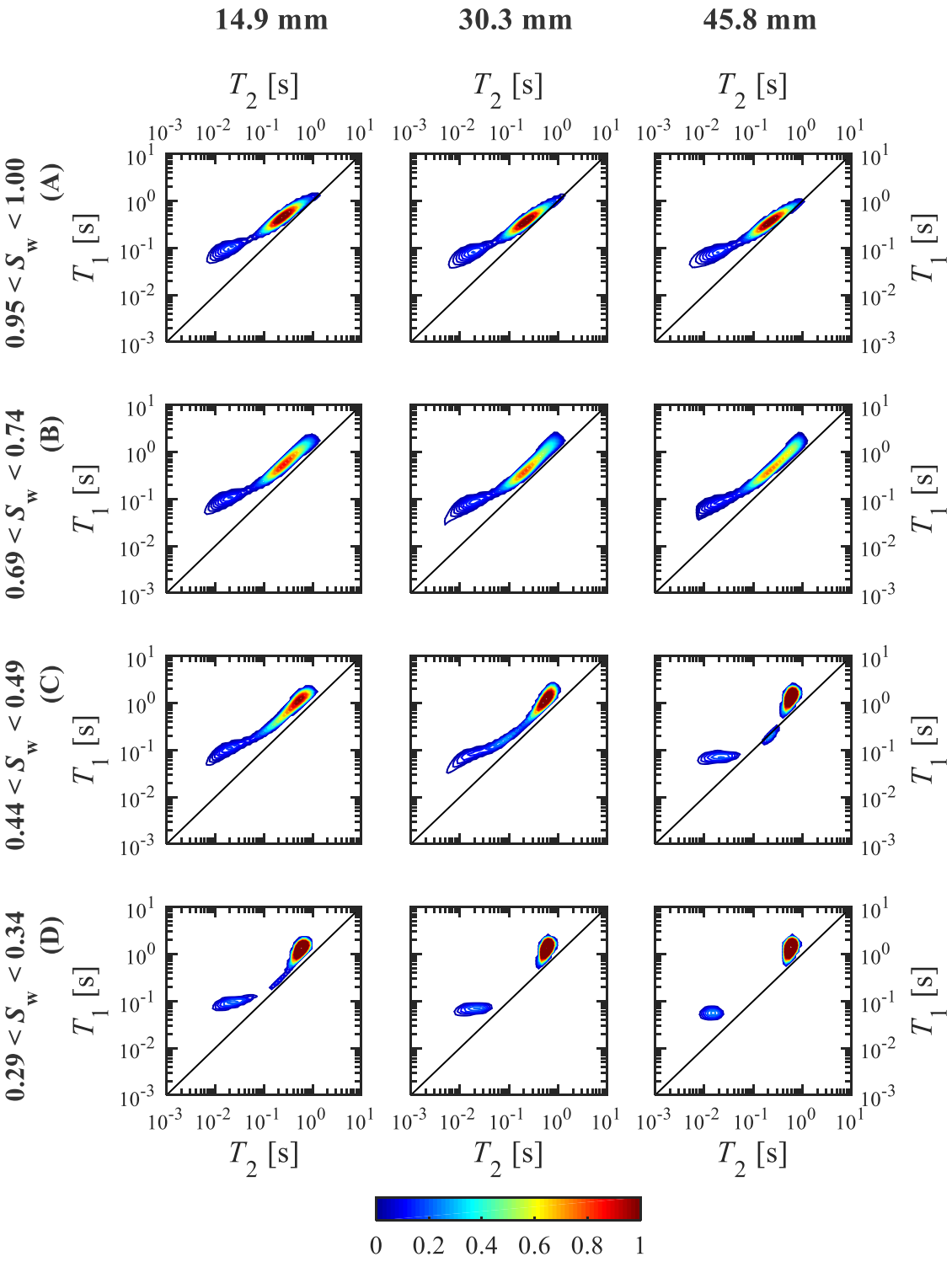

Figure 5.9. Four L-T_1-T_2 datasets acquired within the plateaued pressure region of the primary drainage process. Each dataset is shown along a row. For each dataset, three 2D T_1-T_2 correlation maps at different axial positions in the core are presented along the columns. Positions shown include 14.9 mm, 30.3 mm and 45.8 mm from the inlet face of the 60 mm core (fluid is injected from left-to-right). The saturation range over which each measurement is acquired, is labelled for each row, together with a letter. The letters correspond directly to the saturation regions A-D shown in Fig. 5.8. All datasets are shown presented on the same intensity colour scale, normalised with respect to the first datapoint acquired (A). A colourbar denoting the intensity scale is shown below the figures.

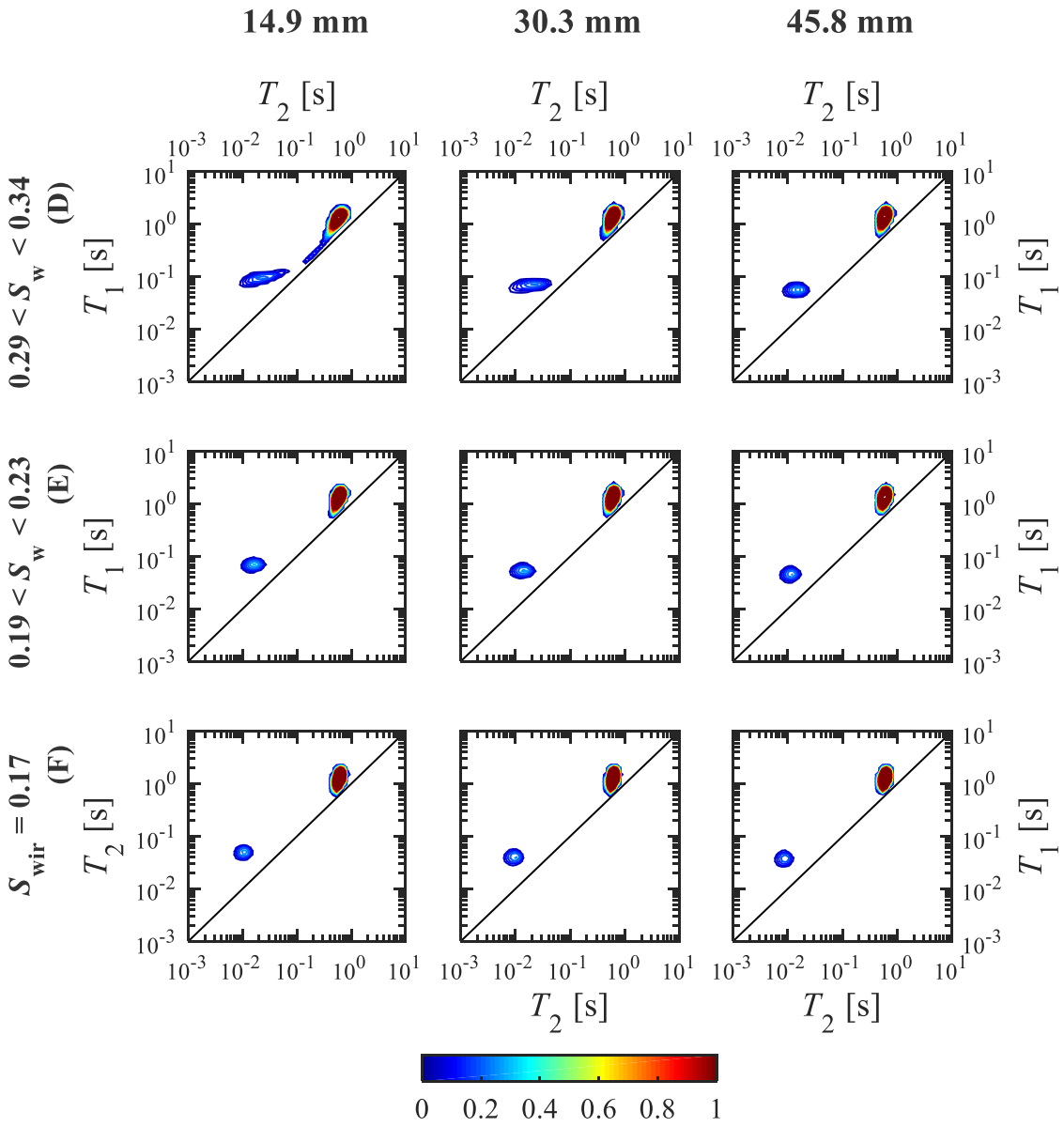

Figure 5.10. Three L-T_1-T_2 datasets acquired between the onset of capillary pressure rise and S_{wir}. Three datasets are shown, corresponding to saturation ranges D-F in Fig. 5.8. For each dataset, three 2D T_1-T_2 correlation maps at different axial positions in the core are shown along the columns – at 14.9 mm, 30.3 mm and 45.8 mm from the inlet face of the 60 mm core. All datasets are shown using the same intensity colourscale as in Fig. 5.9. A colourbar denoting the intensity scale is shown below all figures.

In Figs. 5.9 and 5.10 the six L-T_1-T_2 datasets, saturation ranges as identified in Fig. 5.8, are presented along the rows. For each dataset, three axially-resolved T_1-T_2 correlation plots are shown along the columns, extracted from image slices centred at 14.9 mm, 30.3 mm and 45.8 mm from the entrance to the 60 mm core, within the 82 mm imaging FOV. To illustrate the axial locations of these T_1-T_2 slices within the core, dashed lines indicating their position are presented in the reference MRI image of the core, Fig. 5.5b. Figure 5.9 displays the L-T_1-T_2 measurements acquired during the initial plateaued pressure region of the capillary pressure curve and the onset of the pressure rise; Figure 5.10 displays

measurements acquired at and beyond the onset of pressure rise, as the core approaches S_{wir}. For clarity, the fourth row in Fig. 5.9 ($0.29 < S_w < 0.34$) is repeated as the first row in Fig. 5.10.

In the subsequent discussion, signal regions within the T_1-T_2 correlation maps (Figs. 5.9, 5.10) will be described in terms of 'short' and 'long' relaxation time components. Respectively, these refer to comparatively smaller T_1, T_2 relaxation time values (that is, more fast-relaxing components) and longer T_1, T_2 relaxation time values (slow-relaxing components). Short relaxation times lie on the order of 1-100 ms, long relaxation time regions lie on the order of 1 s.

Figure 5.9 shows that at the start of the primary drainage flood ($0.95 < S_w < 1.00$) all axial positions along the core exhibit near-identical T_1-T_2 correlation maps, consisting of broad T_1 and T_2 distributions. For water saturations in the range $0.69 < S_w < 0.74$, the T_1-T_2 correlation at the entry point of the core (14.9 mm) remains largely unchanged with respect to that at the start of the flood, however changes begin to emerge most noticeably at the core outlet (45.8 mm). Here we observe a shift in the high-intensity, long T_1, T_2 component regions of the correlation map to even longer relaxation times. Next, at $0.44 < S_w < 0.49$ this behaviour is also observed at the core inlet regions (14.9 mm and 30.3 mm), although the greatest increase in the long T_1, T_2 component is still observed at the core outlet. In addition, a distinct separation between the high-intensity, long T_1, T_2 signal, and the low-intensity short T_1, T_2 signal is observed. The final dataset in Fig. 5.9, and all datasets in Fig. 5.10, are characterised by having two discrete regions of T_1-T_2 signal, as is first seen to develop in the 45.8 mm correlation map acquired at $0.44 < S_w < 0.49$. In particular, for the datasets acquired at near-S_{wir} conditions ($0.19 < S_w < 0.23$ and $0.29 < S_w < 0.34$), it is interesting to note the return to axially-homogeneous T_1-T_2 distributions along the length of the core.

Table 5.1 details the log-mean values of the T_1, T_2 and (T_1/T_2) distributions for both the short and long T_1, T_2 component regions of the correlation maps presented in Figs. 5.9 and 5.10 – denoted $T_{1,LM}$, $T_{2,LM}$ and $(T_1/T_2)_{LM}$, respectively. For the T_1-T_2 correlation maps in which these two components do not exist as discrete, unconnected regions, such as for $0.44 < S_w < 1.00$, the short-component and long-component regions were identified by applying cut-offs at the population minima of the projected T_1 and T_2 distributions. Table 5.1 highlights the shifting behaviour in the long-component T_1 and T_2 values to longer relaxation times, whilst the short-component T_1, T_2 region undergoes very little change. Despite the dominant trend of largely unchanging T_1, T_2 values in the short-component region, a small reduction is observed during the capillary pressure rise. Table 5.1 also presents the log-mean of the (T_1/T_2) distribution for both the short- and long-component signal regions. Whilst these values demonstrate slight variations in the T_1/T_2 ratio with the progress of the primary drainage flood, most crucially, at all stages of the flood $(T_1/T_2)_{LM}$ is always greater for the short-component signal region, than for the long-component region.

Table 5.1. Log-mean values of the T_1, T_2 and (T_1/T_2) distributions for both the short and long T_1, T_2 component regions of the correlation maps presented in Figs. 5.9 and 5.10. These are denoted $T_{1,LM}$, $T_{2,LM}$ and $(T_1/T_2)_{LM}$, respectively.

		$T_{1,\,LM}$ [s]		$T_{2,\,LM}$ [s]		$(T_1 / T_2)_{LM}$ [-]	
saturation	**position in core [mm]**	$(T_{1,\,LM})^{short}$	$(T_{1,\,LM})^{long}$	$(T_{2,\,LM})^{short}$	$(T_{2,\,LM})^{long}$	$\frac{(T_{1,\,LM})^{short}}{(T_{2,\,LM})^{short}}$	$\frac{(T_{1,\,LM})^{long}}{(T_{2,\,LM})^{long}}$
0.95 < S_w < 1.00 (A)	14.9	0.09	0.47	0.02	0.25	5.15	1.84
	30.3	0.08	0.38	0.02	0.23	4.60	1.66
	45.8	0.07	0.36	0.02	0.22	4.86	1.64
0.69 < S_w < 0.74 (B)	14.9	0.10	0.62	0.02	0.29	5.56	2.09
	30.3	0.08	0.52	0.02	0.27	4.68	1.89
	45.8	0.08	0.54	0.02	0.28	4.54	1.91
0.44 < S_w < 0.49 (C)	14.9	0.10	0.80	0.02	0.37	5.27	2.13
	30.3	0.10	1.09	0.03	0.53	4.06	2.02
	45.8	0.07	1.14	0.02	0.55	3.60	2.14
0.29 < S_w < 0.34 (D)	14.9	0.09	1.16	0.02	0.54	4.17	2.10
	30.3	0.07	1.20	0.02	0.56	3.52	2.15
	45.8	0.05	1.30	0.01	0.57	3.76	2.22
0.19 < S_w < 0.22 (E)	14.9	0.07	1.27	0.02	0.58	4.30	2.14
	30.3	0.05	1.29	0.01	0.59	3.86	2.15
	45.8	0.05	1.29	0.01	0.58	3.99	2.20
S_{wir} = 0.174 (F)	14.9	0.05	1.24	0.01	0.59	4.66	2.06
	30.3	0.04	1.25	0.01	0.60	4.19	2.06
	45.8	0.04	1.25	0.01	0.59	4.28	2.09

5.4 Discussion

In the following discussion, the L-T_1-T_2 datasets presented in Figs. 5.9 and 5.10 are interpreted, in parallel with the macroscopic capillary pressure response in Fig. 5.8. The goal is to achieve a pore-scale understanding of the fluid displacement processes that occurred during this laboratory primary drainage experiment. Interpretation of the T_1-T_2 correlation maps is based upon the pore size and surface wetting information which can be obtained from NMR relaxation time analysis. The following key statements summarise the essential principles by which Figs. 5.9, 5.10 have been interpreted:

- T_1 and T_2 distributions provide information on pore size distributions – signal at shorter T_1, T_2 values is characteristic of signal resulting from fluid in smaller pores; signal at longer T_1, T_2 values is characteristic of a more bulk liquid-type relaxation response, resulting from fluid in larger pores.
- Under a single-phase fluid saturation, there is no preferential wetting behaviour between different fluid molecules, as there is only one molecule type. Thus, all fluid can saturate the available pore space, at a particular pore pressure, and single phase fluid saturations can be used to infer pore size distributions from T_1 and T_2 distributions, which are unaffected by preferential wetting characteristics observed in multicomponent systems.
- Broad T_1, T_2 distributions are characteristic of a system displaying a range of pore sizes; narrow T_1, T_2 distributions are characteristic of a system with a narrow range of pore sizes.
- Greater T_1/T_2 ratios (observed as signal further from the $T_1 = T_2$ diagonal on the T_1-T_2 correlation maps) identify fluid signals with greater surface interaction strengths (more surface-wetting). Shorter T_1/T_2 ratios (signal closer to the $T_1 = T_2$ diagonal) belongs to signal with reduced surface interaction strengths.

The T_1-T_2 distributions at $0.95 < S_w < 1.00$ display broad T_1-T_2 distributions, with T_1-T_2 correlation maps that are identical with position along the core axis (to within experimental error). This spatial uniformity demonstrates that the Bentheimer core displays pore characteristics and brine interactions with the pore surface that are uniform with position along the core. At this starting point in the drainage flood, the brine phase is expected to fill all accessible pores. For clarity, a global, spatially-unresolved T_1-T_2 and its projected T_1, T_2 distributions (acquired at $S_w = 1$, prior to the start of the drainage process) is presented in Fig. 5.11. This global T_1-T_2 correlation map in Fig. 5.11 was produced by considering the signal resulting only from the core-occupied regions of the FOV of the L-T_1-T_2 measurement. Figure 5.11, in agreement with Figs. 5.6 and 5.7, illustrates that the core displays largely unimodal T_1, T_2 (and thus pore size) distributions that are broad, with respect to similar T_1-T_2 measurements on other Bentheimer and sandstone cores (Mitchell and Fordham, 2014).

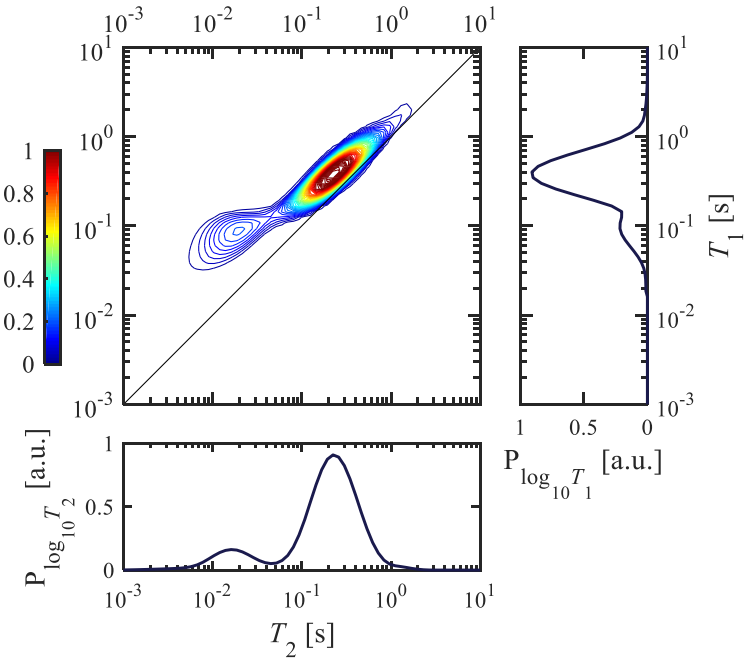

Figure 5.11. Reference global measurement of the T_1-T_2 correlation map of the brine-saturated Bentheimer core at $S_w = 1$, prior to commencing the primary drainage protocol and acquired using frequency-encoded spatially-resolved L-T_1-T_2 methods. The 3D dataset, consisting of 128 2D T_1-T_2 correlation maps at each axial position, has been projected onto one 2D map shown here. Projected T_2 and T_1 distributions derived from the 2D T_1-T_2 maps are shown positioned alongside the 2D correlation map, respectively. For both the T_1-T_2 2D correlation and projected distributions, only the signal regions pertaining to the rock core were considered in the global summation.

In light of the dodecane injection being the only variable introduced to the core system throughout the drainage process, it is expected that any changes observed in the T_1-T_2 distributions, relative to the T_1-T_2 distributions at the start of the flood, result from this dodecane intrusion. As most notably observed at $0.69 < S_w < 0.74$ and at $0.44 < S_w < 0.49$, the most significant changes in the T_1-T_2 distributions occur principally at the core outlet, rather than the inlet. This behaviour is interpreted as resulting from the method employed for achieving S_{wir} – the use of a ceramic disc held at the core outlet results in accumulation of dodecane at this outlet end to the core. This suggests that for primary drainage experiments following the ceramic disc protocol, injected oil will first flow along the preferential pathways through the core (an inefficient, macroscopic displacement). Upon reaching the core outlet, the oil is impeded by the low permeability ceramic disc and results in pore-filling processes occurring from the outlet-end to the inlet-end. As far as is known, this reverse filling process in ceramic disc primary drainage experiments has not been demonstrated before.

This accumulation of dodecane leads to a separation of the T_1-T_2 distributions into two, discrete and narrow distributions (first shown at the 45.8 mm dataset at $0.44 < S_w < 0.49$). Considering this particular saturation range, the long T_1, T_2 component at 45.8 mm exhibits an increase in relaxation times, relative to the start of the primary drainage process; in contrast, the short T_1, T_2 component remains unchanged (as presented in Fig. 5.9, Table 5.1, and previously acknowledged). In Fig. 5.10, both the trends in relaxation times and the separation of signal are further manifested in all spatial positions as the flood

develops (at $0.29 < S_w < 0.34$, $0.19 < S_w < 0.23$ and S_{wir}). This marked shift of the long-component signal and the fixed location of the short-component signal with the progression of the drainage process, coupled with their respective increasing and decreasing signal intensities (and therefore saturations), suggests that the discrete signal peak at long T_1, T_2 values can be attributed to intruding dodecane, and the signal at short T_1, T_2 to remaining brine. This assignment can be considered akin to the T_2 cutoff applied in NMR well-logging tools, used to identify the bound-fluid porosity which comprises of clay bound and irreducible water (also known as bulk volume irreducible, BVI) (Coates *et al.*, 2001). A T_2 cutoff of ~30 ms is typical for sandstone reservoirs (Coates *et al.*, 2001), comparable with the short-component T_2 values observed for this Bentheimer sample, as reported in Table 5.1.

Considering the physical processes occurring, the dodecane signal results from dodecane invading initially brine-filled pores. With reference to the long-component T_1, T_2 signal peak assigned to dodecane, at $0.44 < S_w < 0.49$ (45.8 mm) and for all three spatial positions at $0.29 < S_w < 0.34$, $0.19 < S_w < 0.23$ and S_{wir}, the long relaxation times and the lack of breadth in the T_1-T_2 distributions suggest that injected dodecane does not occupy a broad pore size distribution and only fills larger pores. This contrasts with the behaviour of the brine signal at $0.95 < S_w < 1.00$. The long dodecane relaxation times observed in Fig. 5.10 are characteristic of bulk-like fluid behaviours – evident when compared with the values extracted for bulk liquid dodecane: $T_1 = 1.18 \pm 0.01$ s, $T_2 = 0.90 \pm 0.02$ s. In addition, the log-mean spatially-averaged T_1/T_2 ratios of the discrete signal peaks at S_{wir} yield $(T_1/T_2)_{LM} = 2.07 \pm 0.02$ for dodecane, and $(T_1/T_2)_{LM} = 4.37 \pm 0.25$ for brine. This demonstrates that the brine phase has a greater T_1/T_2 ratio and thus a greater strength of surface adsorption, indicating that brine is the surface-wetting phase. This is expected as Bentheimer cores (clean, non-reservoir sourced outcrop quartz sandstone) are typically water-wetting (Worden and Morad, 2000). Further, the Soxhlet treatment applied prior to brine imbibition should have restored the core to initial strongly water-wetting conditions (McPhee *et al.*, 2015). Hence considering the brine signal existing at short T_1, T_2 with high T_1/T_2 ratios, this signal likely results from a convolution of the restricted, surface-wetting brine in a largely dodecane-filled pore, together with the signal resulting from any brine-filled small pores. These observations are consistent with the expected theoretical behaviour for a primary drainage process in a water-wet system, in which: the invading non-wetting phase fill the largest pore bodies first, in the order of capillary pressure; and the remaining wetting phase is left in the form of thin films along the pore-walls, as well as filling the smallest pore bodies (McPhee *et al.*, 2015). This is also consistent with observations made in prior studies (Dullien *et al.*, 1986; Datta *et al.*, 2014).

It is particularly interesting to note in Fig. 5.10 that the development of axially-uniform T_1-T_2 distributions (and therefore uniform pore-filling and surface-wetting characteristics) coincides with the onset of the pressure rise in Fig. 5.8 ($0.29 < S_w < 0.34$, location D). Further, this event is synchronous with the achievement of discrete signals in the T_1-T_2 distributions that are individually assigned to dodecane-filled pores and surface-wetting brine. Paired, these observations suggest that the onset of

capillary pressure rise marks the reduction of the wetting phase to a uniform wetting layer continuously throughout the core, as S_{wir} is approached. This characteristic in which transitionary behaviour in the wetting film is observed at the onset of pressure rise, as far as is known, has not previously been demonstrated in a rock core system; it has, however, been alluded to in a related system – a packed column of spheres with a wetting-oil/non-wetting-air fluid pairing (Haines, 1930). In this system, the pressure head at different heights of the column is analogous to the capillary pressure measurement herein; the oil saturation equivalent to the water saturation herein. Haines (1930) demonstrated that with increasing pressure, the wetting oil structures changed from fully saturating the pore space, to a funicular region, and ultimately to isolated pendular saturations – both regimes illustrated in Fig. 5.12. Although not explicitly remarked by the author, the onset of the strict pendular case is seen to coincide with the region of pressure rise, as shown in Fig. 6 within Haines (1930). This is similarly the case in an analogous, unconsolidated, soil-water-air system (King, 1897–1898, cited in Smith, 1933, p.437).

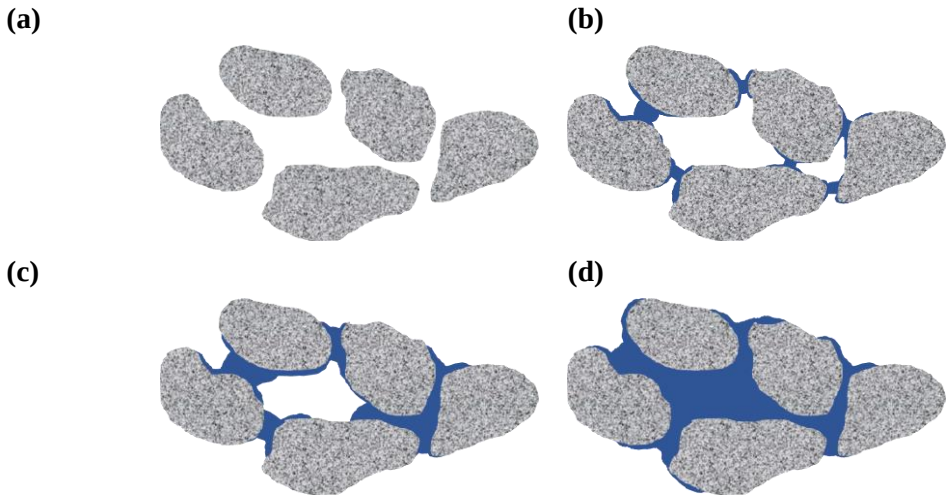

Figure 5.12. Schematic of saturation states: **(a)** dry; **(b)** pendular – lowest moisture state in a porous medium, giving rise to isolated discs of wetting-phase liquid between particle contact points; **(c)** funicular – liquid discs in the pendular state join to form a network, in which the non-wetting phase still occupies the largest pore spaces; **(d)** capillary – wetting liquid encloses a saturated region of the porous medium. Definitions as in Haines (1930).

Returning to Fig. 5.10 in this study, once the water saturation has reduced to this continuous wetting film ($0.29 < S_w < 0.34$ and $0.19 < S_w < 0.23$), further dodecane injection results in additional rise in the capillary pressure. In conjunction, the brine signal undergoes shortening of its T_1 and T_2 relaxation times whereas the dodecane relaxation times remain, comparatively, unchanged (at S_{wir}). This shortening in the surface-wetting film T_1 and T_2 relaxation times is characteristic of the film thinning — this provides direct experimental evidence that the continued reduction in S_{wir} with increasing capillary pressure observed in sandstone cores occurs *via* the thinning of wetting film layers. This agrees with the hypothesis provided by Dullien *et al.* (1986) and their demonstration in a glass micromodel.

As discussed in sections 5.2.2.4 and 5.2.2.5, the signal per unit volume of dodecane and brine has been calibrated, demonstrating the volumetrically quantitative nature of the L-T_1-T_2 technique. Given the

distinct separation in oil- and brine-phase signals at S_{wir}, it is possible to quantify their saturations, S_o and S_w, respectively. At the final measurement point acquired, the individual summations of all dodecane and brine in the core, corrected with their respective Hydrogen Indices, produce saturations of $S_o = 0.826 \pm 0.011$ and $S_w = 0.174 \pm 0.003$. This is in agreement with the volumetric data from the effluent collected in the measuring cylinder (volume of brine expelled = 12.7 ± 0.35 ml). For a gravimetrically measured P.V. of 15.23 ± 0.02 ml, this would produce an oil saturation of $S_o = 0.83 \pm 0.02$. This excellent agreement provides further validation for the assumptions made in assigning the different regions of the T_1-T_2 correlation maps to dodecane and brine phases.

Extending this methodology to all axial locations within the core facilitates the spatial assignment of brine and dodecane saturation along the core length. Figure 5.13 presents the axial oil-phase and brine-phase saturation profiles, with development of irreducible water saturation conditions at three points in the primary drainage process ($S_w = 0.199 \pm 0.003$, $S_w = 0.184 \pm 0.003$ and $S_{wir} = 0.174 \pm 0.003$); the inlet face of the core is shown on the left side of the plot. The axial saturation maps in Fig. 5.13 highlight several features of the saturation conditions in the core. For all three saturation points, S_o and S_w are approximately axially-uniform within the frontal 40 mm of the core, however elevated dodecane saturations exist in the outlet 20 mm of the core. Within the context of the axially-uniform core PSD (Fig. 5.7) and thus its expected axially-uniform pore saturation characteristics, Fig. 5.13 suggests that axial equilibration of capillary pressure, pore filling and saturation are not achieved throughout the entire core length. Likewise, the extent of reduction in S_w, which accompanies the rise in capillary pressure, also does not occur uniformly along the core length. This demonstrates the local variation in the extent of thinning in the wetting film. Both these observations are attributed to insufficient equilibration times, characteristic of the continuous injection primary drainage protocol. Due to the low hydraulic conductance (and low relative permeability, defined in Eq. 6.4) of the wetting phase at near-S_{wir} conditions, the wetting phase may not reach its equilibrium saturation within the timescale of an experiment (Jerauld and Salter, 1990) – a trade-off, compared with the impractically long experimental times of months, associated with alternative equilibrium capillary pressure methods.

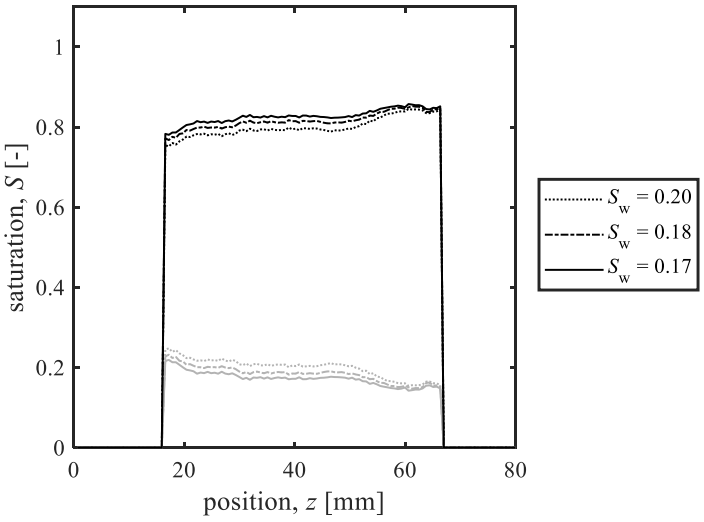

Figure 5.13. Saturation profile of the Bentheimer core obtained from spatially-resolved L-T_1-T_2 dataset at S_{wir}. Signal assignment to both oil/brine phases is achieved through distinct contrast observed in T_1-T_2 distributions. Dodecane and brine signals are displayed in black and grey, respectively. Saturations are normalised against the local pixel total saturation and scaled using species-specific Hydrogen Indices. The core is oriented with flow from the left-to-right and the ceramic disc on the right. Saturation profiles are presented at three points in the drainage process, corresponding to $S_w = 0.199$, $S_w = 0.184$, and $S_{wir} = 0.174 \pm 0.003$, marked by lines (·· . · – and – , respectively).

5.5 Conclusions

In this work the application of spatially-resolved NMR relaxometry measurements to monitoring a drainage process has been demonstrated. Irreducible water saturation in a Bentheimer core (with dodecane and 30,000 ppm NaCl synthetic brine) was achieved using a primary drainage protocol, *via* continuous injection using the semi-permeable ceramic disc method. The primary drainage flood was monitored dynamically and *in situ* using spatially-resolved T_1-T_2 (L-T_1-T_2) measurements.

These results have demonstrated that the spatially-resolved NMR T_1-T_2 measurement can provide a wealth of information, providing dynamic measurements within changing systems on: localised pore size distributions, local wetting characteristics, together with *in situ* and non-invasive detection of local fluid saturations, within reservoir-representative systems. Further, the spatial resolution provided in the technique allows for selection of only the physically-representative regions of the core to contribute to the region of interest, unlike in conventional, global, NMR relaxometry measurements.

Starting at an initially homogeneous brine saturation, the spatially-resolved NMR techniques revealed heterogeneities in the pore filling processes during primary drainage, in which oil-phase saturations increased preferentially at the core end closest to the porous disc barrier. T_1-T_2 correlations revealed that at $S_w = 1$, broad T_1 and T_2 distributions were observed, attributed to brine occupying a range of pore sizes. The injected oil-phase shifted the T_1-T_2 correlations to longer relaxation times and formed a discrete signal, separate from the low-intensity, short T_1, T_2, associated with undisplaced brine. These observations were attributed to dodecane invading and occupying the larger pores, while brine was the

surface wetting phase and remained undisplaced from the smallest pores. The expected water-wetting nature of Bentheimer sandstones was confirmed from the T_1/T_2 ratios of the signals, for which the ratio was greater for brine than dodecane. The onset of rising pressure in the capillary pressure curve, associated with achieving irreducible water saturation, was met with the return of the core to a spatially homogeneous T_1-T_2 correlation map of discrete dodecane and brine T_1-T_2 signals, throughout the core. It was thus concluded that at this onset of capillary pressure rise, and as S_{wir} conditions are approached, a continuous brine-wetting film formed throughout the core. In addition, as the pressure continued to rise and S_w further reduced, a thinning of the brine-wetting film occurred at all axial positions in the core, evidenced by reduction in the T_1 and T_2 values of only the brine signal. Quantification of the final volumetric saturation was achieved from the NMR L-T_1-T_2, which corroborated with external volumetric measurements. Finally, the axial variation in the extent of wetting-film thinning during the capillary pressure rise was obtained. This highlighted the mechanism of incomplete equilibration of localised saturations associated with the continuous injection method.

While prior work in the literature has experimentally demonstrated the presence of a continuous wetting film, this has either been in an optically-transparent model system, or when in a rock, has involved destructive, non-continuous methods using non-reservoir-representative fluids. In this work direct experimental evidence of the thinning of the wetting film throughout the capillary pressure rise is provided – previously only demonstrated in a glass micromodel and hypothesised to be the case in rock systems. These observations form important boundary conditions and validate assumptions, crucial to pore-scale modelling of primary drainage mechanisms.

Here the L-T_1-T_2 sequence has been applied to dynamically monitor the pore-filling mechanisms in a primary drainage process commonly employed within special core analysis laboratories. This has allowed certain characteristic features observed in capillary pressure curves to be related to internal core fluid distributions. Whilst in this case, only a simple outcrop core was tested, application of the technique to cores with locally-heterogeneous pore structures or wetting conditions is possible. This could provide insight into understanding capillary pressure curves and measurement protocols in outcrop cores used as routine SCAL model systems, as well as to reservoir-drilled cores – both of value to asset characterisation.

Chapter 6

Probing Xanthan Gum Polymer EOR Waterflooding in a Bentheimer Sandstone with Spatially-Resolved NMR Relaxometry

6.1 Introduction

Chemical EOR strategies consist of injecting polymers and surfactant solutions into reservoirs, as oil displacing fluids. Polymer strategies are the most widely deployed chemical EOR techniques worldwide. In the last twenty years, many studies probing the mechanisms underpinning polymer EOR have been conducted. Whilst significant developments have been made, the mechanisms at play are still much debated. Prior studies have mostly taken place in optically-transparent model systems, with little work in reservoir-representative core samples. Transparent model systems were required due to the lack of experimental techniques capable of non-invasively probing the mobility, saturation and pore residency of multiphase fluid systems, within opaque porous media.

This chapter builds upon the L-T_1-T_2 sequence development in Chapter 3, and its application to a primary drainage flood in Chapter 5. Here, the sequence is applied to continuously monitor a xanthan gum polymer EOR waterflood in a water-wet Bentheimer sandstone. The aim is to use L-T_1-T_2 to quantitatively track changes in saturation on a macroscopic scale, and to elicit a deeper understanding of the mechanism taking place at the pore level. With approximately 50% of oil reservoirs being sandstones (Bjørlykke and Jahren, 2015), a Bentheimer sandstone outcrop core was selected for its commercial relevance. Furthermore, as a strongly water-wetting sample with a homogeneous pore structure, its compositional and structural simplicity was desirable as a base case scenario. Xanthan gum, one of the two key commercially-used EOR polymers, was selected for this study. This area of research is further developed in Chapter 7, in which diffusion- and spectroscopy-based NMR techniques are used to study a partially hydrolysed polyacrylamide (HPAM) polymer EOR flood in a Bentheimer sandstone.

6.1.1 Putting Chemical EOR Strategies into Context

The overall displacement efficiency of a reservoir is described as a product of macroscopic and microscopic sweep efficiencies. The macroscopic sweep efficiency is described by mobility ratio, M_R, the effectiveness in the displacing fluid to volumetrically contact the oil (displaced) phase – a product of the areal sweep and vertical sweep efficiencies. The microscopic sweep efficiency is described by the capillary number, Ca, the effectiveness of the displacing fluid in mobilising trapped oil at the pore scale by capillary forces (Terry, 2001). A schematic illustrating macroscopic (areal and vertical) and microscopic sweep efficiencies is presented in Fig. 6.1.

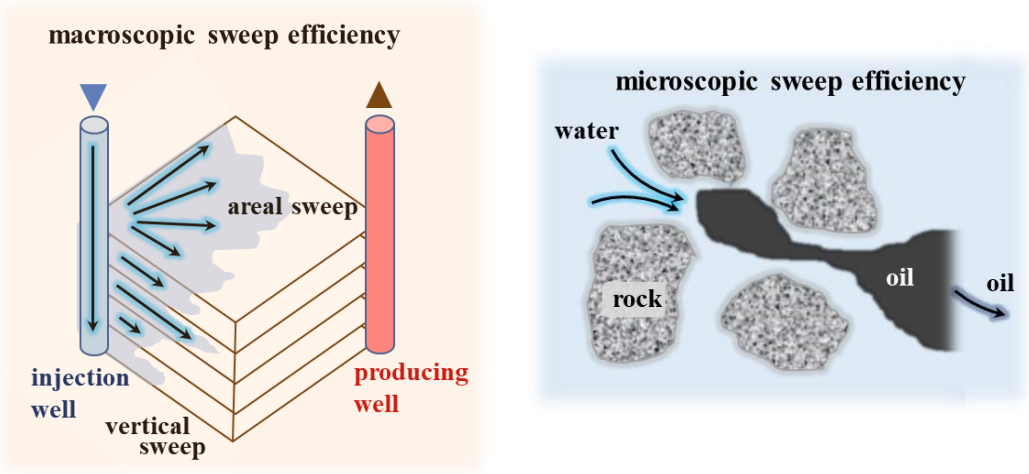

Figure 6.1. Schematic illustrating reservoir macroscopic and microscopic sweep efficiencies. Adapted from Lake (1989).

Oil displacement efficiency can be increased by improving macroscopic or microscopic sweep efficiencies. Definitions for M_R and Ca are given in Eqs. 6.1 and 6.2,

$$M_R = \left(\frac{k_{rD}}{\mu_D}\right)\Big/\left(\frac{k_{rd}}{\mu_d}\right) = \frac{k_{rw}\mu_o}{k_{ro}\mu_w} \tag{6.1}$$

$$Ca = \frac{\mu_D U_D}{\gamma_{o/w}} \tag{6.2}$$

where k_r indicates relative permeability, μ viscosity, U reservoir interstitial velocity and γ interfacial tension. Subscript D denotes the displacing phase, d the displaced phase, o oil phase, and w water phase.

For multiphase flow in porous media, the relative permeability of a phase is the ratio of the effective permeability of that phase to the absolute permeability, defined by the adapted Darcy's law for multiphase flow:

$$q_i = -\frac{k_i}{\mu_i}\nabla P_i \quad \text{for i = phase 1, 2} \tag{6.3}$$

where q_i is flux, ∇P_i is pressure drop, μ_i is viscosity and k_i is effective permeability of phase i. The relative permeability, k_{ri} is then described by:

$$k_{ri} = {k_i}/{k} \tag{6.4}$$

where k is the absolute permeability of the porous material, $0 < k_{ri} < 1$, and k_{ri} is a function of saturation.

The mobility ratio is thus the comparative ease in mobility of displacing and displaced phases, and Ca is the ratio of viscous to interfacial tension (capillary) forces.

Macroscopic sweep efficiency improves as M_R decreases. For example, for $M_R < 1$, oil displacement is efficient with 'piston-like' flow; for $M_R > 1$, oil displacement is inefficient resulting in poor oil recovery with non-uniform displacement fronts or viscous fingering (Dyes *et al.*, 1954; Habermann, 1960; Wei

et al., 2014). Microscopic sweep efficiency improves by increasing *Ca*: considering water-wet systems, mobilisation of residual oil requires the oil phase to be connected as a continuous flow channel. In the absence of oil continuity, oil saturation exists as isolated oil globules in pore centres. To mobilise trapped and unconnected oil drops, viscous forces should be increased relative to capillary forces. Capillary number correlations for reservoir flooding suggest $Ca > 10^{-5}$ is required for mobilisation of such trapped oil droplets (Chatzis and Morrow, 1984; Al-Fossail and Handy, 1989; Terry, 2001; Cense and Berg, 2009).

Chemical EOR strategies offer a means to alter M_R and *Ca*. In polymer EOR, injected water is viscosified with soluble long-chain macromolecules, increasing μ_w, reducing M_R and improving macroscopic sweep efficiency. For heterogeneous reservoirs with significant permeability variations, injection of cross-linking EOR polymer gels can additionally block off high permeability reservoir regions, diverting flow to low permeability zones and enhancing reservoir sweep efficiency therein. In surfactant EOR, oil-water interfacial tension is reduced, thereby increasing *Ca*.

Numerous field pilot studies have demonstrated polymer EOR is a successful and commercially feasible technology – notably, the commercial-scale Daqing field in China, where incremental recoveries of 300,000 barrels/day, for a total production rate of 1 million barrels/day, have been achieved (Wang *et al.* 2002, Wei *et al.*, 2014). Recoveries achieved depend on the reservoir and polymer strategy selected. Incremental recoveries of ~8% (Muggeridge *et al.*, 2014) and ~12-15% (Wei *et al.*, 2014) have been reported for HPAM EOR pilot tests; incremental recoveries of 5% have been reported for xanthan EOR pilots (Guo, 1999).

6.1.2 Polymer EOR: Materials Selection, Reservoir Suitability and Reservoir Flooding Protocols

This section provides a review of commercially used polymer EOR injectants, including polymer types, typical polymer concentrations, injection flooding protocols and suitable reservoir conditions.

EOR polymers must withstand the harsh conditions in an oil reservoir – high salt concentrations, calcium ions, high temperatures (> 70 °C) and long injection times (> 12 months). Salt negatively impacts viscosifying properties, calcium leads to flocculation, whilst high temperatures and long injection times lead to polymer chain degradation (Wever *et al.*, 2011; Zhong and Oostrom, 2013). Commercially viable EOR polymers include synthetically produced polyacrylamides and biological polysaccharides (xanthan gums). Today, HPAMs are among the most widely used commercial EOR polymers – offering a comparatively low-cost solution, resistant to bacterial degradation. The rheological properties of HPAM are influenced by salt concentrations, shear conditions, polymer concentrations and the molecular weight of its polymer chains, typically in the range 2-35 MDa (Wever *et al.*, 2011). For HPAM, A critical shear rate ($\dot{\gamma}_{\mathrm{onset}}$) has been observed, below which shear-thinning properties occur, and beyond which apparent shear-thickening behaviours occur (Ait-Kadi and Carreau, 1987; Dupuis *et al.*, 1994; Wever *et al.*, 2011; Howe *et al.*, 2015; Mitchell, 2016). HPAMs are particularly sensitive to mechanical

shear and salt concentrations (greater than 1-2 wt%), with significant reductions in viscosities occurring above their limiting salt concentrations (Terry, 2001).

In contrast, xanthan gum delivers excellent viscosifying effects with reduced susceptibilities to saline conditions and shear forces (Guo, 1999). However, it is more expensive than HPAM and can mould over prolonged periods of time. Biocides are often added to prevent biological degradation – typically, using formaldehyde concentrations of ~4 g l^{-1} (Terry, 2001; Ghannam *et al.*, 2014). Xanthan gums display shear-thinning properties and are used with molecular weights in the range 2-50 MDa. With increasing polymer concentration, greater viscosities and improved oil recoveries are achieved (Rangel *et al.*, 2012), however viscosity reduction effects from saline conditions are more pronounced (Martel *et al.*, 1998; Rangel *et al.*, 2012; Ghannam *et al.*, 2014).

Neither xanthan nor HPAM can withstand high salinity brines or high temperatures (with loss of solution viscosity occurring between 70-90 °C). Both are prepared with polymer concentrations in the range 250-2000 mg l^{-1} in brine, with successful applications observed in moderately heterogeneous reservoirs, with reservoir permeabilities between 20-2000 mD and with μ_o < 100 cP (0.1 Pa s) (Terry *et al.*, 2001). In practice, a polymer slug of *circa* a third to a half of the reservoir pore volume is injected after the secondary waterflood. This is followed by conventional waterflooding procedures, which drive reservoir fluids towards the production wells (Abidin *et al.*, 2012).

6.1.3 Emerging Research Trends in Polymer EOR

Research trends in polymer EOR have shifted towards synergising polymer flooding with other EOR strategies, such as surfactant flooding (Mitchell *et al.*, 2012b; Wang *et al.*, 2013b, Liu *et al.* 2016), and low salinity flooding (LSF) strategies (Johannessen and Spildo, 2012; Shiran and Skauge, 2013; Wang *et al.*, 2013a; Almansour, 2017; Li *et al.*, 2017). Developments into EOR polymer injectants have also been made, such as branched 'comb-like' polyacrylamides (PAMs) (Wever *et al.*, 2013) or PAMs with hydrophobic groups in their backbone, enabling improved polymer thickening capabilities (Wever *et al.*, 2011).

Whilst standard techniques for studying polymer floods have included high-resolution and high-speed photography in optically-transparent model systems (Al-Sharji *et al.*, 2001; Meybodi *et al.*, 2011; Sedaghat *et al.*, 2013; Clarke *et al.*, 2015), other techniques such as X-ray CT (Hou *et al.*, 2009; Johanessen and Spildo, 2012; Shiran and Skauge, 2013), AFM (Grattoni *et al.*, 2004) and in-flow adsorption tests (Ogunberu and Ashgari, 2005) have been used. MR techniques have also been used, revealing core saturations (Mitchell *et al.*, 2012b,d; Liu *et al.*, 2015), internal fluid distributions (Zhang *et al.*, 2008), information on pore filling environments (Liu *et al.*, 2016; Li *et al.*, 2017) and fluid flow characteristics (Johns *et al.*, 2003).

6.1.4 Current Understanding of Polymer EOR Displacement Mechanisms

Until recently polymer injections were thought to only influence macroscopic displacement efficiencies. Considering the definition of *Ca* (Eq. 6.2), augmentations of *Ca* by orders of 10^3 are typically required for improvements in pore-level oil recovery to be achieved (Chatzis and Morrow, 1984). Whilst achievable through surfactant-induced changes in $\gamma_{o/w}$, such increases in *Ca* through polymer viscosification alone is not normally possible. However, recent findings suggest that polymer EOR can improve microscopic displacement efficiencies, although the mechanisms at play are much debated (Wei *et al.*, 2014).

The mechanisms discussed in the literature are here reviewed to lay the foundations for the experimental protocols and results obtained in Chapters 6 and 7. The following subsections are structured as follows – first, established waterflooding mechanisms are introduced, then the proposed macroscopic and microscopic displacement mechanisms of polymer EOR are discussed in turn. Oil displacement mechanisms within water-wet systems are primarily discussed, as this is the focus of the research work conducted throughout this thesis. Mechanisms within oil-wet media are only briefly referred to.

6.1.4.1 Pore-scale Mechanisms of Secondary Waterflooding

Polymer EOR is typically conducted following an initial secondary waterflood. In water-wet systems, the start of the waterflood is marked by the presence of a wetting-brine film layering the pore surface at S_{wir}; non-wetting oil saturation exists in pore centres.

The waterflood mechanism is believed to occur by growth of wetting brine layers. As brine is injected, it advances along the grooves and edges of the solid surface, thickening the wetting layers. At points of pore constriction, such as crevices or pore throats, the oil phase increasingly develops elongated shapes, such that 'snap-off' events occur, wherein threads of oil-phase split and separate from the pore inlets. Once a volume of non-wetting phase has undergone several 'snap-off' events, it disconnects from the continuous oil phase providing hydraulic connectivity throughout the pore space and remains trapped in the pore (Dullien, 1992). Such snap-off events are accompanied by a local increase in capillary pressure (Al-Gharbi and Blunt, 2005). As the wetting-brine continues to invade pores *via* intermittent bursts, a series of trapped, discrete oil ganglia are left throughout the pore space (Datta *et al.*, 2014). A schematic illustrating oil-trapping during waterflooding is shown in Fig. 6.2.

Much work in studying these mechanisms has been conducted in optically-transparent model systems, although recent developments have been made in opaque rock systems using X-ray μCT (Berg *et al.*, 2013; Bartels *et al.*, 2017).

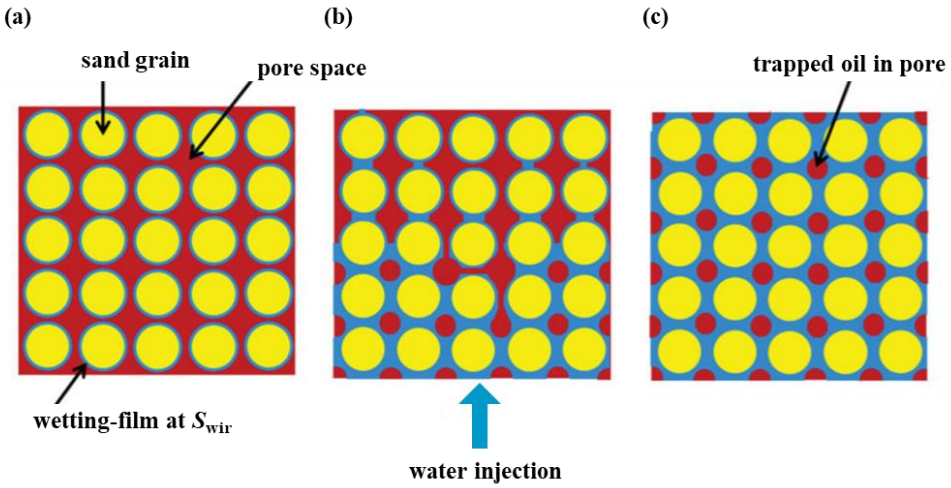

Figure 6.2. Schematic illustrating oil trapping following secondary waterflooding in a water-wet rock. Sand grains are in yellow, water-phase in blue, oil-phase in red. **(a)** At S_{wir}, water-wet sand grains are coated in a layer of water, oil resides in the pore space, **(b)** as water is injected during secondary flooding, the wetting film thickens and snap-off events occur, **(c)** residual oil phase exists trapped within pore centres and continuity of oil-phase is lost. Reproduced from Muggeridge *et al.* (2014).

6.1.4.2 Polymer EOR Mechanisms for Improved Macroscopic Displacement Efficiencies

Considering Eq. 6.1, polymer EOR is thought to improve M_R by reducing μ_o/μ_w and k_{rw}/k_{ro} – the latter, termed disproportionate permeability reduction (DPR). In DPR, relative permeability of the displacing phase is reduced while that of the oil-phase remains unchanged. DPR has been explained through several mechanisms: polymer retention and swelling, flow path segregation, and layer adsorption (Wei *et al.*, 2014). It has also been suggested that polymers alter the wettability of oil-wet rocks (Sharma and Wunderlich, 1987; Olatunde, 2013), to deliver improved oil recoveries (Zhang *et al.*, 2008).

The polymer retention and swelling mechanism suggests injected polymers adsorb onto grain surfaces, coating the rock surface in a hydrophilic film, and are entrapped, mostly in low permeability zones. In subsequent waterflushes, injected water passes over the polymer film, resulting in polymer swelling and reducing effective permeability. As oil passes over the film, no swelling occurs. This reduces permeability in reservoir zones of low oil saturation, diverting flow to regions of higher oil saturation (Sparlin, 1976; Meybodi *et al.*, 2011).

Flow path segregation (Nilsson *et al.*, 1998) suggest oil and water flow as distinct phases. An injected water-based polymer would follow the same flow path as water already existing in the pore space – coating water-wetting pore surfaces and filling the smallest pores, whilst oil exists in the centre of pore bodies. Some authors propose polymer aggregates are mechanically filtered-out by the rock structure, blocking the smallest pores. Concentrated in the smallest pore throats and along surface crevices, this retention facilitates adsorption entanglement in which additional polymer molecules adhere to retained polymer aggregates, forming a network (Nilsson *et al.*, 1998; Stavland and Nilsson, 2001). These flow

path segregation hypotheses were supported by photographic observations in oil-wet and water-wet optically-transparent micromodels (Meybodi *et al.*, 2011).

Layer adsorption is the most extensively discussed mechanism for explaining DPR processes, occurring by polymer adsorption, followed by layer growth. A schematic representation of the process is presented in Fig. 6.3.

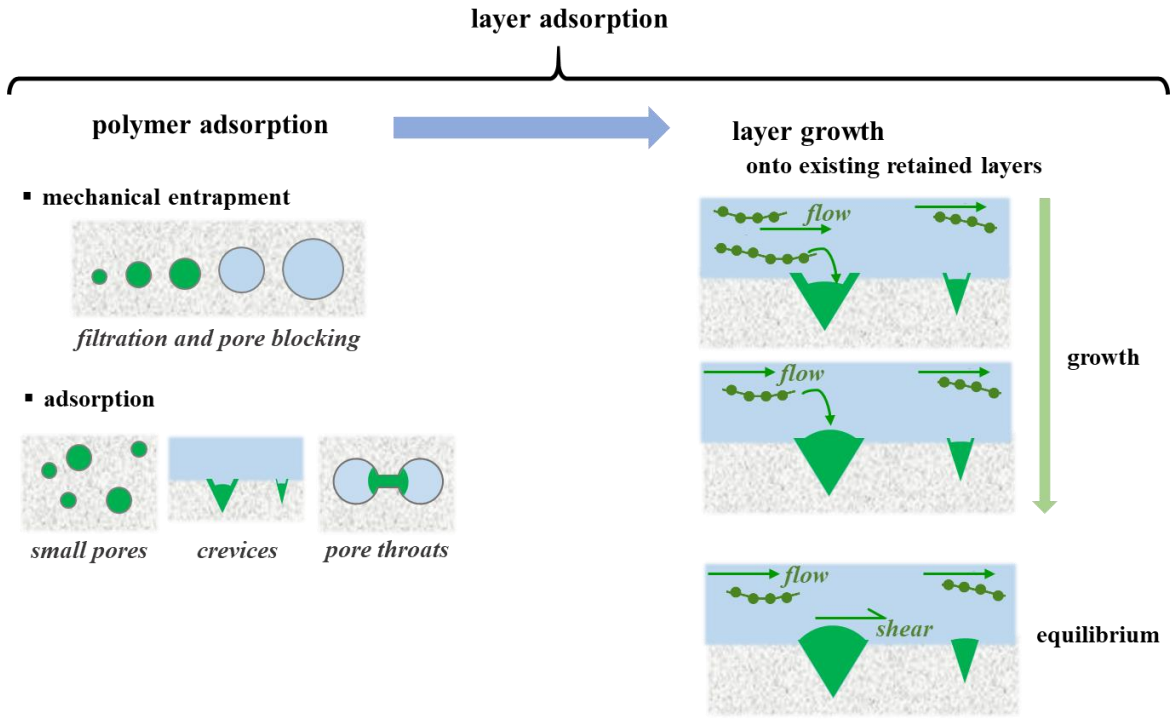

Figure 6.3. Schematic representation of the layer adsorption mechanism for DPR.

The first step of layer adsorption involves polymer adhering to the grain surface, facilitated by the grain surface roughness (Meybodi *et al.*, 2011). This occurs either by mechanical entrapment (filtration and pore blocking effects (Nilsson *et al.* (1998)), or by adsorption in small pores, crevices and pore throats (Al-Sharji *et al.*, 2001; Grattoni *et al.*, 2004; Ogunberu and Ashgari, 2005). Adsorption occurs under two regimes – static and flow-induced (Ogunberu and Ashgari, 2005). If there is no initial surface adsorption, no layer growth can occur (Grattoni *et al.*, 2004). The polymer layer grows by adsorption entanglement, whereby polymer tails and loops are adsorbed onto existing retained layers (Al-Sharji *et al.*, 2001). The adsorbed polymer layer continues to thicken until an equilibrium is reached – a balance between shear forces from flow, and molecular interaction strengths from entanglement. At greater injection flowrates, more polymer material is delivered enabling layer thickening. At too high flowrates, shear forces dominate and can prevent further layer growth (Ogunberu and Ashgari, 2005). Blocked pores and the thickest polymer layers are found in low velocity zones (Al-Sharji, 2001), in which smallest pores are first to block (Johns *et al.*, 2003). Pore bridging by layer adsorption has also been observed in pore throats, occurring more frequently in low permeability rocks (Denys *et al.*, 2001;

Ogunberu and Ashgari, 2005). The degree of polymer adsorption is influenced by polymer chemistry, reservoir rock composition, temperature, salinity, and polymer composition (Kamal *et al.*, 2015).

Surface roughness can also impact polymer adsorption. The majority of existing studies in the literature have involved modelling studies (Hone *et al.*, 1987; Ball *et al.*, 1989; Douglas, 1989; Baumgaertner and Muthukumar, 1991), with limited experimental work having been conducted (Huang and Gupta, 2001; Shu *et al.*, 2007; Venkatakrishnan and Kuppa, 2018). Numerical studies have employed varying modelling approaches and demonstrated that surface irregularities always enhance polymer-surface interactions relative to an idealised planar surface (Vilgis and Heinrich, 1994). This has been attributed to the greater probability of polymer-surface intersection with increasing surface roughness. Accordingly, this enables a rough surface to adsorb a polymer, whilst a correspondingly smooth surface of the same material will not adsorb a polymer (Douglas, 1989). Numerical studies have shown that a polymer will preferentially adhere to the deep holes or valleys on a rough surface (Hone *et al.*, 1987; Ball *et al*., 1989), although that entropic interactions can encourage polymer adsorption at surface roughness peaks (Ball *et al*., 1989; Douglas, 1989). These numerical studies have been supported by experimental work which have demonstrated increased polymer interfacial adhesion (Shu *et al.*, 2007) and greater rates of polymer adsorption (Huang and Gupta, 2001) with increased surface roughness.

The influence of surface rock and polymer chemistry on adsorption mechanisms is briefly discussed in section 6.1.4.3.

6.1.4.3 Influence of Molecular and Surface Chemistries in Polymer EOR Adsorption

The capacity for polymer adsorption is ultimately controlled by molecular surface interactions between polymer molecules and rock surfaces. HPAM tends to achieve greater extents of surface adsorption than xanthan gum; for both polymers, greater surface adsorption is achieved in carbonate over sandstone cores (Kamal *et al.*, 2015). The surface chemistries in carbonates and sandstones and molecular structures of HPAM and xanthan are here briefly discussed.

HPAM polymers are copolymers of PAM and acrylic acid, or its salt. The degree of hydrolysis of HPAM molecules is defined by the percentage of acrylate groups. With a greater degree of hydroxylation, HPAM molecules become increasingly negatively charged. The molecular structure of HPAM is shown in Fig. 6.4a. Likewise, xanthan gum polymer chains are also negatively charged; the charge is determined by the presence of negatively charged acetate and pyruvate groups. The molecular structure of xanthan gum is shown in Fig. 6.4b.

(a)

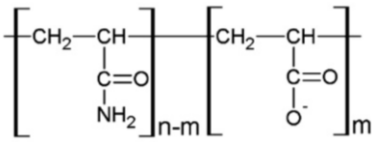

(b)

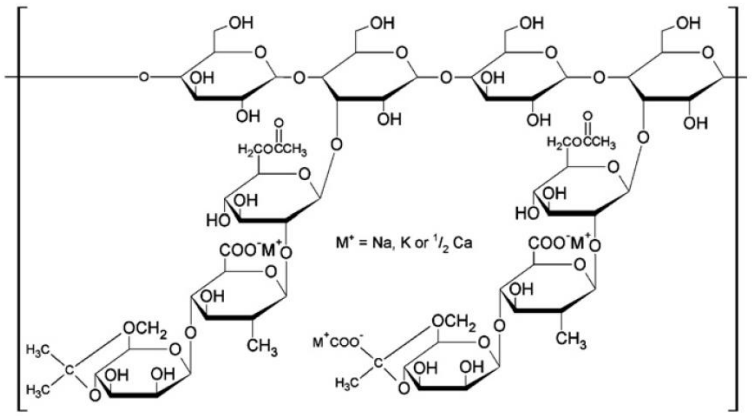

Figure 6.4. Chemical structures of **(a)** HPAM, **(b)** xanthan gum. Reproduced from Wever *et al.* (2011).

Carbonate surfaces exhibit both positive (Ca^{2+}, Mg^{2+}) and negative (CO^{3-}) surface charges; the population of each being dependent upon salinity, pH and temperature conditions, among others (Hiorth *et al.*, 2010). For the pH conditions present in most reservoirs, the surface state of a carbonate rock has a positive zeta potential (Hiorth *et al.*, 2010; Ahmadi *et al.*, 2017). Zeta potential is a term describing surface charge. Any surface immersed in an electrolyte solution disrupts the distribution of ions in solution, due to the interactions between the solid surface and electrolyte. This gives rise to a region of fluid termed the electrical double layer. The electrical double layer consists of two parallel layers of charged ions between the surface and the bulk fluid (the dispersion medium). The first layer (the surface charge) consists of ions adsorbed to the surface; the second layer consists of free ions attracted to the surface charge by electrostatic attractions (the diffuse layer). Part of this diffuse layer can be moved upon application of a tangential stress (the slipping plane). The zeta potential is the potential difference between the stationary layer of fluid (at the onset of the slipping plane) and the dispersion medium. These concepts are summarised in Fig. 6.5a, a schematic diagram of the double electrical layer. Figure 6.5b presents the zeta potential of different carbonate surfaces with varying pH, produced using data from Mahani *et al.* (2015).

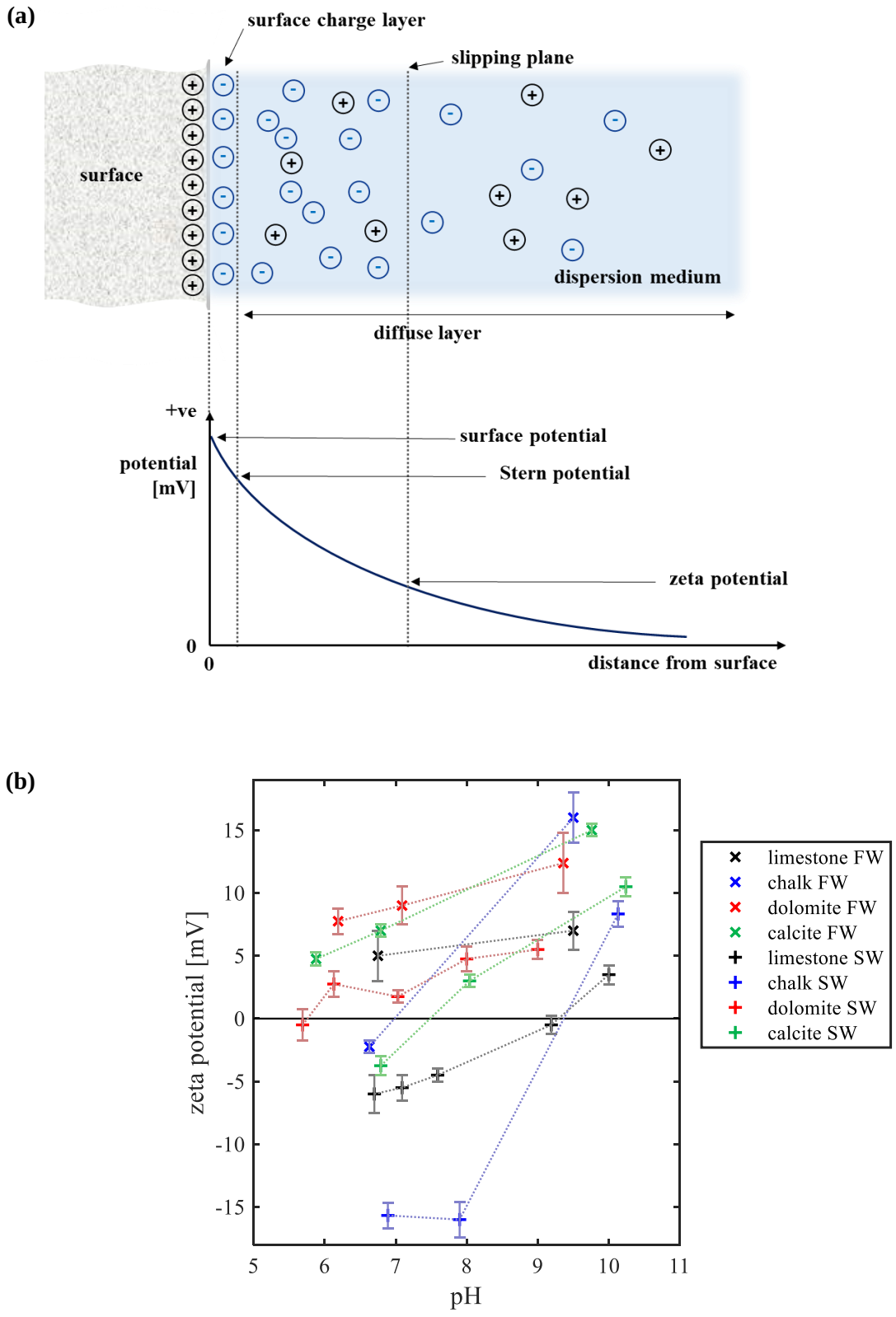

Figure 6.5. (a) Schematic representation of the electrical double layer on a surface immersed in an electrolyte solution, illustrating the zeta potential at the slipping plane. Modified from Freire *et al.* (2011). **(b)** Zeta potential of different reservoir carbonate surfaces with varying solution pH, in reservoir formation water from a Middle Eastern carbonate field (FW) and seawater (SW). Produced from data reported in Mahani *et al.* (2015).

Sandstone, mineralogically primarily composed of quartz (~93%), consists of a tetrahedral SiO_4 crystal network structure, with terminal silanol groups (SiOH). Sandstone has a small zero-point charge, ~1. The pzc describes the conditions in which electrical charge density on a surface is zero, related to an electrolyte pH value (for systems in which the concentration of H^+ and OH^- ions determine the surface potential). In this case, at a pH of 1 sandstone exhibits no net surface charge. For pH < 1, the electrolyte donates more protons to the surface, creating a positively-charged surface. In contrast, for pH > 1, a negatively-charged sandstone surface occurs. The sandstone pzc is significantly less than the value of pH in most reservoirs – that is, for most reservoir conditions, sandstone has a negatively-charged surface (Hilner *et al.*, 2015; Vinogradov and Jackson, 2015). Quartz surface silanols are capable of both strong, short hydrogen bonds, and weak hydrogen bonding (Sulpizi *et al.*, 2012).

In carbonates, adsorption is governed by the electrostatic attraction between carbonate surface cations and the negative acrylate groups in HPAM, or the negative pyruvate and acetate groups in xanthan. In sandstones, negative surface charges introduce a repulsion between the rock surface and polymer molecules, explaining the greater polymer adsorption achieved in carbonates over sandstone reservoirs. The degree of HPAM adsorption in sandstones can be improved with higher salinities and lower degrees of hydroxylation. Salinity is defined as the amount of salt dissolved in a volume of water, usually reported as grams of salt per kilogram of water. In high salinity systems, cations introduced in solution interact with the HPAM chain, reducing the size of the flexible chain and thus increasing surface adsorption.

For xanthan, adsorption in sandstones is a balancing of the electrostatic repulsion between the negative polyelectrolytes and the mineral surface, together with the hydrogen bonding between surface silanol and xanthan polar pyruvate groups. The degree of surface adsorption in sandstones decreases with increasing salt concentration, temperature and with presence of surfactants (Wever *et al.*, 2011; Kamal *et al.*, 2015).

6.1.4.4 Polymer EOR Mechanisms for Improved Microscopic Displacement Efficiencies

Improvements in microscopic displacement efficiencies, believed to result from the viscoelastic properties of injected polymer, are limited to HPAM rather than xanthan polymers, which are not viscoelastic. Microscopic displacement efficiencies can be improved by increasing contributions from viscous forces, or by reducing those from capillary forces (Eq. 6.2). The proposed pore level mechanisms responsible for this increase in oil recovery are grouped under: 'pulling effects' (Wang *et al.*, 2007; Hou *et al.*, 2009; Sedaghat *et al.*, 2013), elastic turbulences (Clarke *et al.*, 2015; Howe *et al.*, 2015; Mitchell *et al.*, 2016), oil thread/column stabilisation and flow (Huh and Pope, 2008; Meybodi *et al.*, 2011; Sedaghat *et al.*, 2013) and in oil-wet systems, surface oil film stripping (Sedaghat *et al.*, 2013). Considering *Ca*, the 'pulling effects', film stripping and elastic turbulence mechanisms result from increased local viscous forces; indirectly, the oil thread stabilisation mechanism response is akin to a local reduction in capillary forces. Each of these four mechanisms are now briefly discussed. Examples

of pulling effect, film stripping, elastic turbulences and oil thread stabilisation in micromodels are shown in Fig. 6.6, reproduced from the literature.

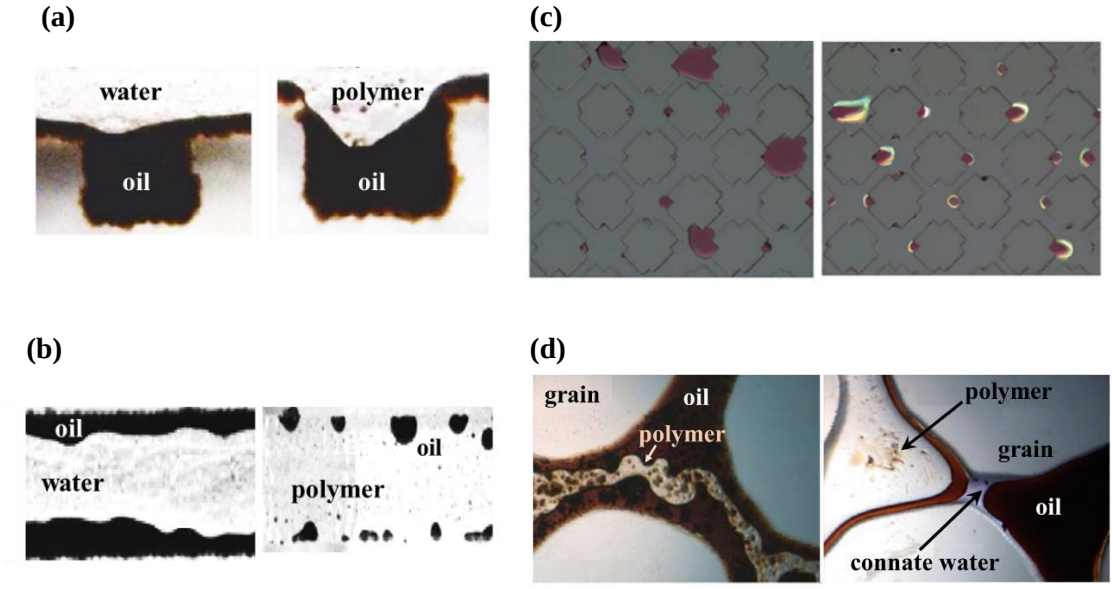

Figure 6.6. (a) Distribution of residual oil after waterflooding (left), and after polymer flooding (right); pulling effect from dead end pores (Figs. 10a, 10c. Sedaghat *et al.*, 2013). **(b)** Distribution of oil-wetting layer in oil-wet micromodel after waterflooding (left), and after polymer flooding (right); oil film stripping effect (Figs. 13a, 13c. Sedaghat *et al.*, 2013). **(c)** multiphase aqueous flow in water-wet glass micromodels, with xanthan gum (left) and HPAM (right), polymer phase shown in magenta; elastic turbulence effects in HPAM (Figs. 8a, 8c. Clarke *et al.*, 2015). **(d)** Continuous polymer solution string in oil-wet micromodel (left) and oil string in water-wet micromodel (right); thread/column stabilisation (Figs. 4h, 5d. Meybodi *et al.*, 2011).

The pulling effect mechanism, in which residual oil in dead end small pores and long thin throats is 'pulled out', is attributed to the viscoelasticity of HPAM and has been observed in micro-CT images of a water-wet quartz sandpack (Hou *et al.*, 2009), in oil-wet glass micromodels (Wang *et al.*, 2007; Sedaghat *et al.*, 2013) and modelled using micro flow line and force analyses (Wang *et al.*, 2007). Greater extents of 'pulling' occur with elevated polymer concentrations and reduced flowrates. At elevated concentrations, increased chain entanglement and Van der Waals forces are present between HPAM molecules. This makes polymer deformation more challenging, and the viscoelastic properties of the polymer increase – promoting the pulling mechanism. At elevated flowrates, higher shear rates reduce the effect of the pulling mechanism (Sedaghat *et al.*, 2013).

Oil film stripping from oil-wet surfaces has also been demonstrated in glass micromodels (Sedaghat *et al.*, 2013). At elevated polymer concentrations, this is more severe and is attributed to the increased viscoelasticity at greater HPAM concentrations. This results in broadened, flattened velocity profiles of the injected polymer through the pore space, giving more dramatic velocity gradients at pore walls and thus greater stripping forces.

Recently studies have shown that viscoelastic HPAM solutions deliver increased microscopic oil displacement efficiencies when aqueous phase shear rate exceeds a critical value. Beyond this critical shear rate, viscoelastic fluctuations in the continuous, aqueous phase are believed to occur, resulting in a flowfield that varies randomly in space and time – termed an 'elastic turbulence' (Clarke *et al.*, 2015; Mitchell *et al.*, 2016).

The onset of elastic turbulences is thought to give locally-fluctuating pressure fields, which promote breakup, destabilisation and mobilisation of otherwise trapped oil ganglia. This occurs at capillary numbers lower than the capillary numbers required for desaturations with a Newtonian liquid. This critical shear rate is coincident with an increase in apparent viscosity, μ_{app}, of the HPAM in porous media, termed apparent flow thickening. Measurements of apparent viscosity have been derived from the pressure gradient across the rock sample ∇p, during single-phase flow and using Darcy's law, where $\mu_{app} = kA\nabla p/q$, and the apparent shear rate is $\dot{\gamma} = Q/A\sqrt{k\varphi_p}$, where Q is volumetric flowrate, A is sample cross-sectional area, k is absolute permeability and φ_p is porosity. This apparent flow thickening is not observed with xanthan gum EOR polymers. Furthermore, conventional shear rheometry measurements of pure HPAM do not demonstrate these apparent flow thickening behaviours, in contrast to apparent viscosity-shear rate measurements in porous media.

Lastly, oil thread/column stabilisation and flow has been observed in optically-transparent water-wet glass micromodels (Meybodi *et al.*, 2011; Sedaghat *et al.*, 2013) and has been modelled based on force balances at the polymer-oil interface (Huh and Pope, 2008). It was proposed that polymer pushes oil into columns, to obtain thin, long oil threads. Without the polymer, such threads would destabilise and change shape, or break into droplets due to oil-water interfacial tension. In contrast, polymer viscoelasticity provides normal stresses that resist this deformation at the interface. Such conditions of stabilised oil threads promote greater continuity in the oil phase, relative to discrete oil droplets. This newly-found oil continuity may help produce more oil, by providing a continuous flow pathway.

A summary of mechanisms by which polymer EOR has been proposed to improve macroscopic and microscopic oil displacement efficiencies is given in Fig. 6.7.

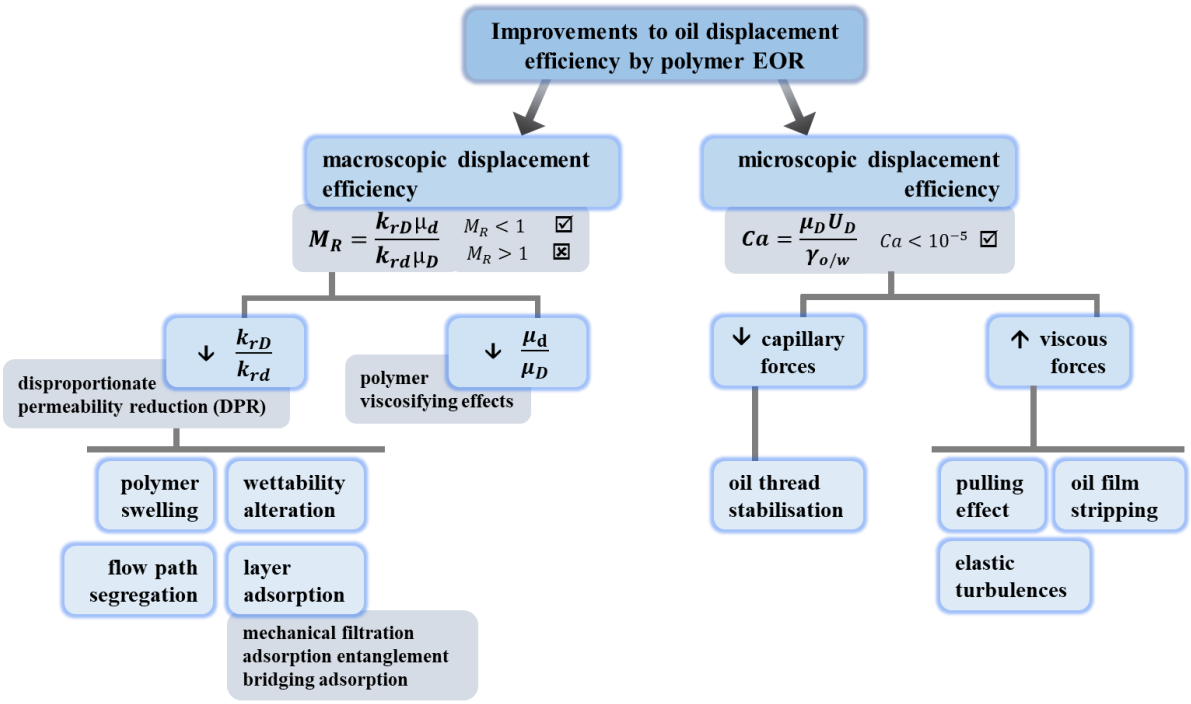

Figure 6.7. Summary of proposed mechanisms by which polymer EOR strategies improve macroscopic and microscopic oil displacement efficiencies.

6.2 Materials and Methods

6.2.1 Materials

This section outlines sample materials, including initial screenings for optimising EOR polymer concentration, and the core flooding equipment.

6.2.1.1 Chemicals

The same core sample in Chapter 5 was used in this EOR study, immediately following the primary drainage flood reported in Chapter 5. Herein, brine and dodecane were also used as representative aqueous- and hydrocarbon-phases, prepared as described in section 5.2.1.1. A xanthan gum polymer (Sigma LifeScience, from Xanthomonas campestris) prepared to a concentration of 600 mg l^{-1} in low-salinity 3.0 ± 0.1 g NaCl l^{-1} brine was used as the EOR injected phase.

Bulk liquid relaxation times of brine, dodecane and EOR polymer were measured as: $T_{1,brine}$ = 2.67 ± 0.02 s; $T_{2,brine}$ = 2.10 ± 0.04 s; $T_{1,dodecane}$ = 1.18 ± 0.01 s; $T_{2,dodecane}$ = 0.90 ± 0.02 s; $T_{1,polymer}$ = 2.54 ± 0.02 s; $T_{2,polymer}$ = 1.85 ± 0.04 s, using standard T_1-IR and CPMG methods. Hydrogen indices were measured as: HI_{brine} = 0.94 ± 0.01; $HI_{dodecane}$ = 1.02 ± 0.01; $HI_{polymer}$ = 0.97 ± 0.01.

6.2.1.2 EOR Polymer Concentration Screening

It was necessary to determine the optimal xanthan gum concentration and salinity of solvent brine, that enabled the desired EOR polymer injectant properties to be achieved. A polymer viscosity greater than

oil-phase viscosity was sought, enabling favourable macroscopic hydrocarbon mobility effects ($M_R < 1$) to be exploited for improved oil recovery (see section 6.1.1).

Given $\mu_{dodecane}$ = 1.49 ± 0.01 cP (1.49 ± 0.01 mPa s) at 20 °C, 1 atm (Knapstad *et al.*, 1989), an injectant polymer with viscosity ~10 cP at the expected shear rates under flow conditions was desired – a typical oil-polymer viscosity ratio used in EOR applications (Johannessen and Spildo, 2014). Back-of-the-envelope approximations were calculated to determine expected shear rate ranges: first, average pore space linear interstitial velocity, u_{int}, was determined for a given injectant flowrate, Q_{inj}, rock core cross-sectional area, A and porosity, φ_p, as per Eq. 6.5; secondly, by assuming a laminar flow profile within the pore space for a Newtonian fluid, the maximum shear rate, $\dot{\gamma}_{max}$, at the pore wall was determined using Eq. 6.6 (Darby, 2001), where d is average pore diameter.

$$u_{\text{int}} = \frac{Q_{\text{inj}}}{A\varphi_p} \tag{6.5}$$

$$\dot{\gamma}_{\text{max}} = \frac{8u_{int}}{d} \ . \tag{6.6}$$

For u_{int} in the range 1 to 35 ft day^{-1}, a maximum shear rate range of 0.4 to 14.2 s^{-1} was expected. This facilitated selection of a xanthan concentration capable of maintaining the desired viscosity (10 cP) under such shear conditions. Literature values suggested $\mu_{polymer}$ ~ 10 cP conditions could be achieved for these shear conditions, at xanthan concentrations in the range 600–1000 mg l^{-1} (Martel *et al.*, 1998; Rangel *et al.*, 2012; Ghannam *et al.*, 2014), with brine salinities up to 3 g l^{-1} (Martel *et al.*, 1998).

Based on these suggested compositions, screening experiments were conducted, whereby a range of polymer solutions were characterised to determine their flow behaviours, using a Rheometric Scientific ARES 320 rheometer. A smooth-walled concentric cylinder Couette cell, with an inner cylinder of O.D. 32 mm and length 34 mm, was used for all samples. The wall gap was 1 mm and the temperature was maintained at 20.0 ± 0.5 °C. The rheometer was operated under controlled strain mode, to determine the variation in apparent viscosity of the samples, using a shear rate sweep in the range 500 to 0.5 s^{-1}.

Eight polymer solutions were tested at this preliminary screening stage. These consisted of: 400 ± 10 mg l^{-1}, 600 ± 10 mg l^{-1}, 800 ± 10 mg l^{-1} and 1000 ± 10 mg l^{-1} polymer concentrations, prepared in both low salinity brine (LSB) (3.0 ± 0.1 g NaCl l^{-1} in deionised water), and pure deionised water. Four saline, and four non-saline polymer solutions, were prepared by diluting concentrated 4.00 ± 0.01 g l^{-1} polymer stock solution to the desired concentrations. Accordingly, two polymer stock solutions were prepared – one in 3.0 ± 0.1 g l^{-1} brine, and the second in deionised water. These were prepared using an electric mixer (IKA RW 20 Overhead Stirrer, Janke and Kunkel Ika-Werke), and were mixed for 24 h with rotational speed 240 ± 30 rpm. During mixing, the agitator was submerged well below the solution surface to prevent entrainment of air, and the containers were covered with plastic film to prevent

intrusion of contaminants. Subsequent dilution of stock solutions was conducted at 240 ± 30 rpm for 1 h. Figure 6.8 presents the measured flow behaviours for the polymer solutions.

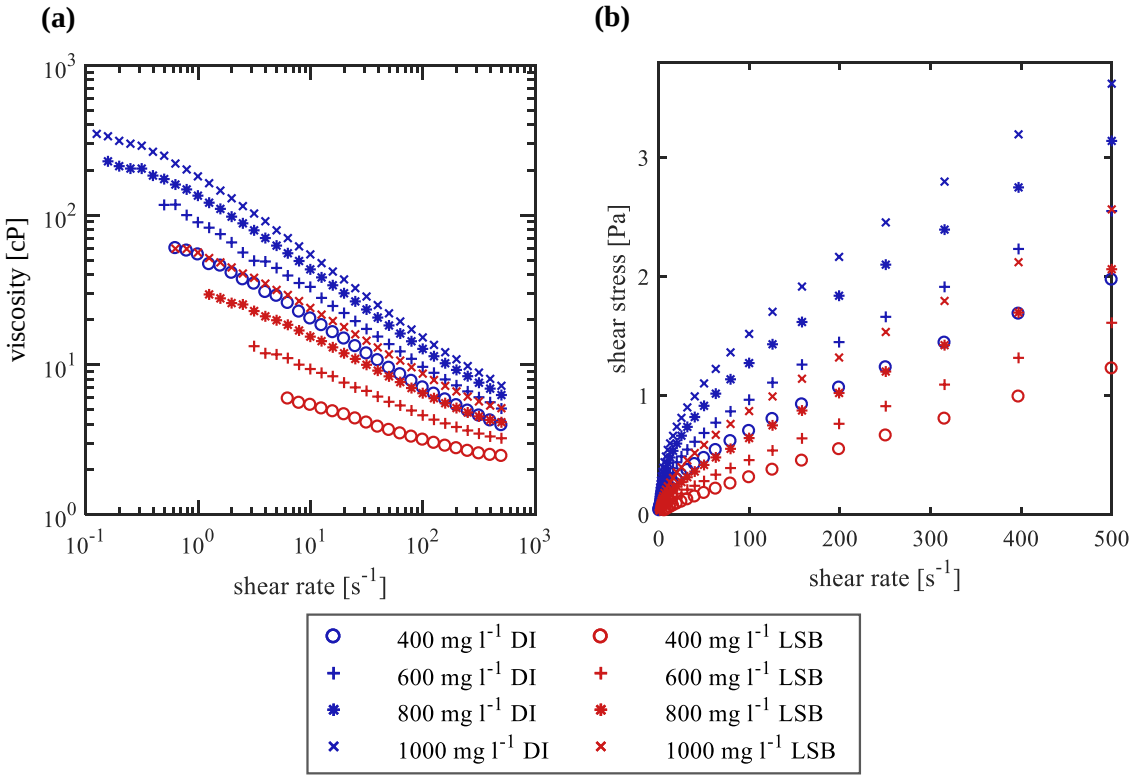

Figure 6.8. Flow behaviour of xanthan gum polymers prepared to different concentrations, in deionised water and in low-salinity brine (LSB) at 3 g l^{-1} NaCl in DI. **(a)** effect of shear rate on apparent viscosity. Viscosity is presented in unit of cP, where 1 cP = 1 mPa s. **(b)** effect of shear stress on shear rate.

Figure 6.8 demonstrates that the xanthan solutions were shear thinning. With increasing concentration, viscosity and shear stress also increased for a given shear rate. Saline conditions resulted in reduced xanthan viscosities and shear stresses, as expected from the literature (Martel *et al.*, 1998; Terry, 2001; Zhong and Oostrom, 2013). The viscosity and shear stress responses to increasing salt concentration can be explained from the xanthan molecular conformation state. It is reported that xanthan gum chains exhibit two molecular conformations – a disordered structure in which the molecule occupies a large hydrodynamic volume, thus increased viscosity; and an ordered structure in which side chains (see Fig. 6.4b) fold inwards towards the polymer backbone, resulting in a helical structure that occupies a smaller hydrodynamic volume and thus reducing solution viscosity. The disordered conformation occurs in salt-free solutions, in which strong electrostatic repulsions between the negative xanthan polyelectrolyte stretch and elongate the individual xanthan chains. The ordered conformation occurs for low xanthan concentrations (< 2000 mg/L) under saline conditions, in which the addition of salt neutralises the ionic charge of the xanthan polyectrolyte molecules (Zhong and Oostrom, 2013).

For shear rate ranges up to 15 s^{-1}, the desired polymer viscosity of 10 cP (10 mPa s) is best achieved by either the 600 mg l^{-1} LSB, or 400 mg l^{-1} DI xanthan solutions. Within an EOR flooding protocol, the injected polymer slug is expected to mix with the brine from both preceding secondary and succeeding EOR waterfloods. Accordingly, an increase in polymer salinity would occur, for which the degree of mixing is likely to be more significant for the non-saline polymer, due to greater concentration gradients. To minimise this dilution and subsequent reduction in injected EOR polymer viscosity, the 600 mg l^{-1} LSB xanthan gum polymer was selected.

6.2.1.3 Core Flooding Equipment

The core flood was conducted using the MRRC CFS, with the arrangement as shown in in Fig. 4.2 and as discussed in section 4.3.5.1.

As stated in section 6.2.1.1, the polymer EOR floods reported herein were conducted immediately after the primary drainage flood reported in Chapter 5. The RCH loading method and assembly in this Chapter was thus equivalent to that in section 5.2.1.2.

6.2.2 Methods

This section outlines the various methods used in the experiment, including core flooding protocols and NMR measurement techniques.

6.2.2.1 Core Flooding Protocol Design

All core flooding stages were conducted in the equipment described in section 6.2.1.3. The protocol of the EOR polymer core flood were conducted as follows:

1. *Primary drainage* – to achieve S_{wir} conditions, dodecane was injected into the initially brine-saturated core at 0.016 ml min^{-1} (0.30 ft day^{-1} linear), using the ceramic disc method. The ceramic disc (ELE International) was rated to 15 bar (218 psi, 1.5 MPa) – details provided in section 5.2.1.2. This process was continuously monitored with NMR – results discussed in Chapter 5.
2. *Secondary waterflood* – 1.5 P.V. of 30.0 g NaCl l^{-1} brine was injected at 0.016 ml min^{-1}. Following this stage, the partially-permeable ceramic disc was removed from the outlet-end of the RCH assembly.
3. *EOR polymer slug injection* – 0.55 P.V. of 600 mg l^{-1} xanthan gum in 3.0 g l^{-1} NaCl brine was injected at 0.016 ml min^{-1}.
4. *Tertiary waterflood* – 2.0 P.V. of 30.0 g NaCl l^{-1} brine was injected at 0.016 ml min^{-1}.

A summary of the core flooding protocol is illustrated in Fig. 6.9. The sharp fluid fronts at each transition stage are purely schematic, used for illustrating the change in the flooding procedure. No assumptions on the form of the invading fluid fronts are here made.

NMR measurements were used to dynamically track the continuous flooding processes at each stage in the core flood. Produced effluent fluid volumes were collected in measuring cylinders and the pump injection pressures were continuously recorded.

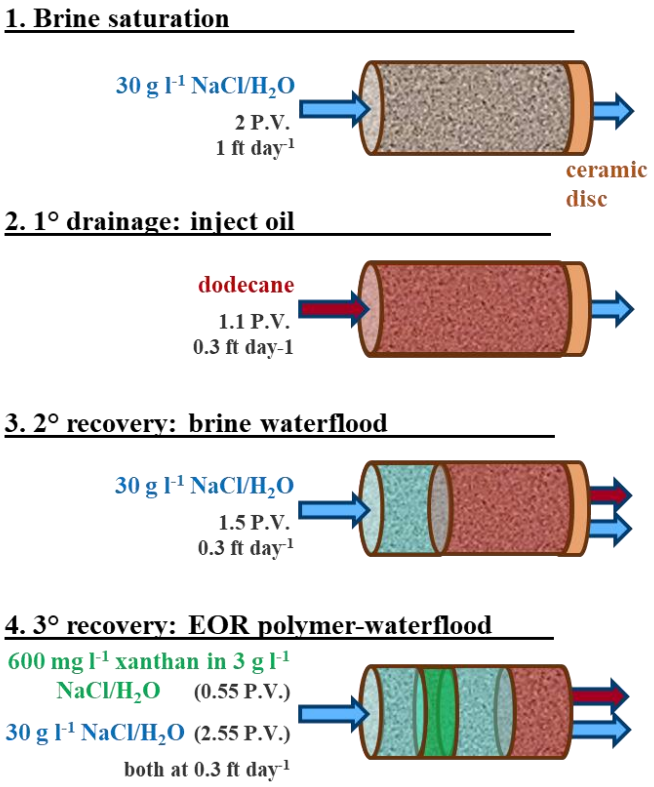

Figure 6.9. Schematic illustrating the EOR core flooding flow protocol used.

6.2.2.2 Operational Errors in Core Flooding Protocol

As illustrated in Fig. 6.9, the ceramic disc was only removed from the RCH once the secondary waterflood was complete. This choice in protocol was intentional – a decision made to both minimise operational hazards and preserve core conditions between primary drainage and secondary waterflooding stages. The rationale being: to remove the ceramic disc from the heat-shrunk core assembly, it is necessary to open the RCH to atmosphere, remove the core, cut the region of heat shrink encasing the disc to the core, and subsequently re-insert the core into the RCH. This process risks introducing air pockets into the RCH. Procedurally, this can be avoided by conducting such changeovers with the RCH submersed under liquid – the submersion fluid used being that with which the prior forced injection stage was conducted. In this way, no further saturation changes would occur to the core, provided a stable equilibrium saturation is reached in the preceding forced injection stage. For safety reasons it was decided to conduct this submersion stage post-secondary waterflooding – so that the experimentalist would immerse the core in large volumes of brine, rather than dodecane.

To maintain reservoir-representative conditions, operating the secondary waterflood with the ceramic disc is acceptable, provided the flow direction is reversed such that the ceramic disc is at the inlet. This works as the ceramic disc (pressure rated to 15 bar (218 psi, 1.5 MPa)) is permeable to aqueous-phase fluids, and impermeable to oil phases, up to these limiting pressure conditions. Unfortunately, two operational errors were made: (i) following primary drainage, dodecane was injected until it broke through the ceramic disc; (ii) the flow direction was not reversed during secondary waterflooding. The implications of these operational errors are as follows:

1. The saturation of the ceramic disc changed from $S_w = 1.0$ to $S_w = 0.72 \pm 0.09$, (volumetrically determined from the change in produced dodecane volumes, about the point of breakthrough and pressure plateau at the end of the primary drainage).
2. As a result of (1.), the relative permeability of the ceramic disc to both water and oil would have changed.
3. With the ceramic disc at the outlet during secondary waterflooding, axial variations in core pressure, pore conditions and saturation would be expected.
4. As a result of (1.), an additional uncertainty in the produced volumes from the waterflooding stage is incurred.

These implications do not impact the ability to: produce oil and achieve equilibrium saturation in the secondary waterflood, quantify core saturations during the waterflood, quantify core saturations and obtain axially-resolved pore filling information in the polymer EOR waterflood. However, this negates interpreting any spatially-resolved pore filling mechanistic information in the secondary waterflood as having any reservoir-representative significance.

6.2.2.3 NMR Methods

All NMR experiments were conducted at room temperature (20 ± 1 °C) in a 2 T (85 MHz for ^{1}H nuclei) horizontal bore superconducting magnet, controlled by a Bruker AV spectrometer. A 63 mm inner diameter r.f. birdcage coil, tuned to 85.2 MHz was used for excitation and signal detection. Spatial resolution along the direction of superficial flow (z) was achieved by applying a magnetic field gradient of maximum gradient strength 10.7 G cm^{-1}, along the z-direction.

Spatially-resolved L-T_1-T_2 measurements, acquired in immediate succession, were used to dynamically monitor both recovery floods. These were interleaved with NMR spectral measurements, although insufficient contrast between oil- and water-phases was achieved. Such limited spectral resolution is typical in sandstone rocks, for which the presence of magnetic field inhomogeneities can result in line broadening. This is typically attributed to paramagnetic clay impurities often present in sandstone samples (Mitchell *et al.*, 2013c). In addition, a series of reference measurements were acquired at each flooding endpoint, at no-flow conditions, and under the same confining pressures as during the core floods. The reference measures consisted of:

(i) Spatially-resolved L-T_1-T_2 map;

(ii) Spatially-unresolved measurement of the contribution of internal magnetic field gradients to T_2 relaxation, T_2-g;

(iii) 1D axially-resolved profile;

(iv) Spatially-unresolved relaxation time measurements T_1, T_2 and T_1-T_2.

Experiment (i) was acquired to determine the core end-point reference state, without any axial blurring effects incurred during injection. Experiment (ii) was acquired to facilitate an internal gradient correction in the T_2 dimension of L-T_1-T_2 measurements. Experiment (iii) was a 'sanity-check' to verify that no air bubbles were injected into the system and that the core remained uniformly-saturated throughout the flooding process. Likewise, experiments (iv) were 'sanity-checks' to benchmark the L-T_1-T_2 measurement.

Hard r.f. pulses were used for all NMR experiments. Pulse durations, t_{90} and t_{180}, were calibrated prior to the start of each flooding stage. All experiments within the secondary waterflood were acquired using t_{90} = 19.6 µs and t_{180} = 39.2 µs; all experiments within the polymer EOR waterflood were acquired with, t_{90} = 20.28 µs and t_{180} = 40.56 µs. This difference in optimal pulse lengths is likely to have resulted from the differing saturations, S_w, at the start of each respective flooding stage. As discussed in section 5.2.2.5, elevated salt concentrations reduce coil receiver efficiency, requiring elongated pulse lengths to achieve a given tip angle.

Across both flooding stages, L-T_1-T_2 measurements were acquired using 128 pixels with FOV = 82 mm, giving a slice resolution of 0.64 mm pixel^{-1}. Sixteen different t_{vd} values in the range t_{vd} = 1 ms to t_{vd} = 6 s were used in recording the T_1 dimension, and 1024 echoes with an inter-echo time t_E = 3.6 ms, were recorded along the T_2 echo train. Using RD = 6 s, together with NS = 16, resulted in t_{ACQ} = 47 min per L-T_1-T_2 experiment. Given the core flooding interstitial velocity of 0.3 ft day^{-1} and considering only displacement in one axial (z) direction, it is expected that pore fluids would have displaced by 3 mm during each acquisition time, resulting in some pixel blurring of the T_1-T_2 correlations extracted per 0.64 mm slice.

Reference spatially-unresolved relaxation time measurements (T_1-IR, one-shot CPMG) were acquired using the same parameters as their respective T_1 and T_2 dimensions in the L-T_1-T_2 experiments. Spatially-unresolved contributions of internal magnetic field gradients to T_2 relaxation were measured using a variable inter-echo time one shot CPMG experiment (Mitchell *et al.*, 2010a); these were acquired with variable t_E in the range t_E = 750 µs to t_E = 8 ms, RD = 6 s and NS = 16, resulting in t_{ACQ} = 30 min. The one-dimensional axial profile was measured using 256 pixels, with FOV = 82 mm, giving a slice resolution of 0.32 mm pixel^{-1}. Eight scans for signal averaging were used, together with RD = 6 s, resulting in t_{ACQ} = 1 min.

Processing of L-T_1-T_2 measurements was conducted using the same approach as in section 3.2.2.2. Selection of an appropriate universal alpha smoothing parameter followed the same methodology as in section 5.2.2.4.

The secondary brineflood was continuously tracked using L-T_1-T_2 over a period of ~30 h. The polymer EOR injection and subsequent brineflush were continuously tracked using L-T_1-T_2 over a period of ~37 h. The total experimental time (including magnet set-up, various pulse and sequence optimisations, core flooding system set up and end-point reference experiments) was ~2 weeks.

6.3 Results

This section presents the experimental results recorded across the secondary waterflood and EOR polymer stages. The data is presented as follows:

(i) End-point volumetrically determined saturations;
(ii) Global T_1-T_2 and projected T_1 datasets at core flood end points;
(iii) Spatially-resolved T_1-T_2 datasets and L-T_1 maps, dynamically tracked throughout each core flooding process.

First, the physical conditions are presented to understand the core conditions. Next, end-point reference NMR measurements are considered to understand the boundary conditions to each flood. Building upon this, the axial variations and time-dependencies in the core relaxation properties within the dynamically-tracked stages of the flood are shown. In the discussion (section 6.4), following interpretation and fluid signal assignment, continuous monitoring of core saturations is also presented.

6.3.1 End-point saturations

Following completion of the initial primary drainage, the core reached an irreducible water saturation S_{wir} = 0.17 ± 0.02 (volumetrically) and S_{wir} = 0.174 ± 0.003 (NMR) – see Chapter 5. Prior to starting the secondary waterflood, primary drainage was continued until dodecane broke through the ceramic disc. This resulted in a final core saturation of S_{wir} = 0.14 ± 0.03 (volumetrically) and S_{wir} = 0.157 ± 0.002 (NMR) – this NMR saturation was determined using the same methodology as in Chapter 5. After the secondary waterflood, the core reached S_w = 0.63 ± 0.07; after the polymer EOR flood, this changed to S_w = 0.66 ± 0.08 – these saturations were determined from the volumetric measurements of the core flood effluents. As can be noted, the uncertainty in volumetrically-determined saturations consistently increased from the second to fourth core flooding stages (stage labels as in Fig. 6.9). This is due to the error propagated in building upon saturation calculations from preceding core flooding stages. For the secondary waterflood, an additional error is incurred due to the altered saturation of the ceramic disc following oil-breakthrough (see section 6.2.2.2).

6.3.2 Global, spatially-averaged relaxation time measurements – a comparison at core flood endpoints

Figure 6.10 presents the global, spatially-averaged T_1-T_2 correlations obtained from endpoint reference L-T_1-T_2 measurements. Only the signal pertaining to the core is considered. Each endpoint T_1-T_2 can crudely be separated into two regions, consisting of (i) a shorter and (ii) a longer T_1, T_2 signal.

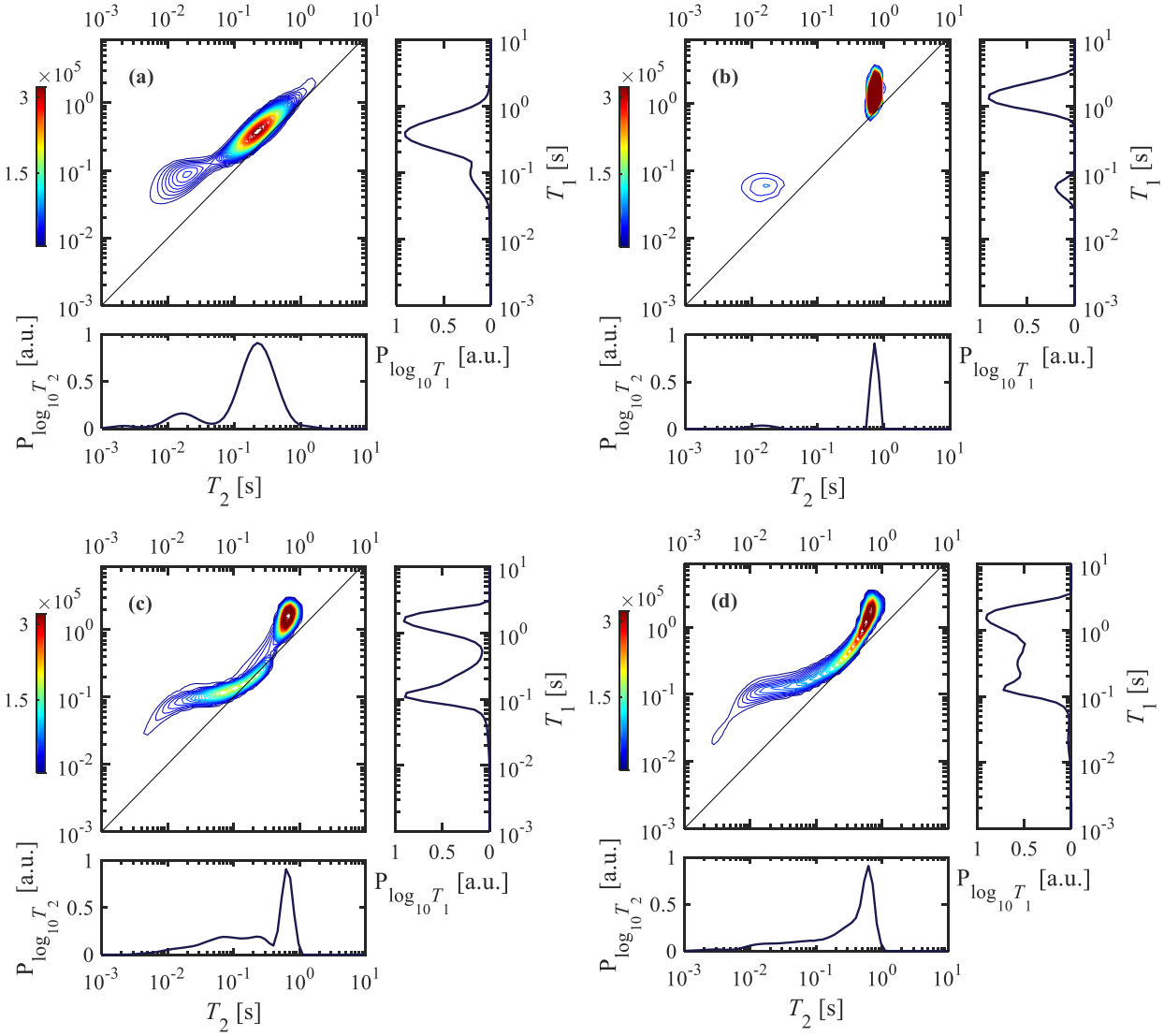

Figure 6.10. Spatially-averaged T_1-T_2 plots, and projected T_1 and T_2 distributions at the end of each core flooding stage, obtained from reference, no-flow L-T_1-T_2 datasets. All 2D T_1-T_2 maps are plotted on the same colourscale relative to the post-EOR state. **(a)** Core at initial S_w = 1, **(b)** post-primary drainage, S_{wir}, **(c)** post-secondary waterflood, **(d)**, post-polymer EOR waterflood.

Table 6.1 presents the log-mean T_1 and T_2 values for these two regions at each endpoint signal shown in Fig. 6.12.

Table 6.1 Log-mean T_1 and T_2 for the short and long T_1, T_2 peaks at each core flooding endpoint.

	$T_{1,\,LM}$ [s]		$T_{2,\,LM}$ [s]	
saturation	$(T_{1,\,LM})^{short}$	$(T_{1,\,LM})^{long}$	$(T_{2,\,LM})^{short}$	$(T_{2,\,LM})^{long}$
$S_w = 1$	0.06	0.39	0.01	0.23
S_{wir}	0.06	1.41	0.01	0.72
post-waterflood	0.13	1.41	0.07	0.64
post-EOR flood	0.19	1.34	0.07	0.59

At $S_w = 1$ (Fig. 6.10a), broad T_1, T_2 distributions are observed, consistent with the pore size distributions, obtained using MIP (see section 5.2.2.6). Following completion of the primary drainage (Fig. 6.10b), the T_1-T_2 distribution distinctly splits into two signal regions – a high intensity peak at long T_1, T_2 and a low intensity peak at short T_1, T_2. As introduced in section 5.3, signal regions within the T_1-T_2 correlation maps are herein similarly described in terms of 'short' and 'long' relaxation time components, referring to fast- and slow-relaxing components respectively (on the order of 1-100 ms and 1 s).

Comparing S_w = 1 and S_{wir}, Table 6.1 highlights that the location of the short $T_{1,2}$ signal remains unchanged, whereas that of the long $T_{1,2}$ signal shifts towards longer relaxation times. As discussed in Chapter 5, the region of long T_1, T_2 is assigned to the injected dodecane, residing in the centre of the pores. The short, low intensity T_1, T_2 peak is assigned to remaining surface-wetting brine and brine trapped in the smallest pores.

Post-waterflood (Fig. 6.10c), the range in values of the long T_1, T_2 component remain almost unchanged, relative to S_{wir} (Fig. 6.10b). In contrast, the short T_1, T_2 component occupies a broader range of relaxation times, and $(T_{1,LM})^{short}$ and $(T_{2,LM})^{short}$ increase. Additionally, the proportion of signal intensity in each T_1, T_2 region changes – post-waterflood, significantly more signal resides in the short T_1, T_2 region.

Finally post-EOR (Fig. 6.10d), the T_1-T_2 correlation continues to show a large proportion of its signal concentrated in the long T_1, T_2 region, for which only small changes in $T_{1,LM}$ and $T_{2,LM}$ occur relative to the post-waterflood case (see Table 6.1). Similarly, the short T_1, T_2 'tail', first seen in Fig. 6.10c, is still present. However, this has now broadened to longer relaxation time values, appearing 'bridged' with the long T_1, T_2 region. Whilst the 2D correlation does not show discrete regions of signal, it is interesting to note that clearer separation is seen in the projected 1D relaxation distributions, with the greatest contrast observed in T_1. The 1D T_1 distribution also shows the greatest contrast in the post-waterflood state (Fig. 6.10b). Figure 6.11 presents the projected global T_1 distributions, for all coreflood endpoints.

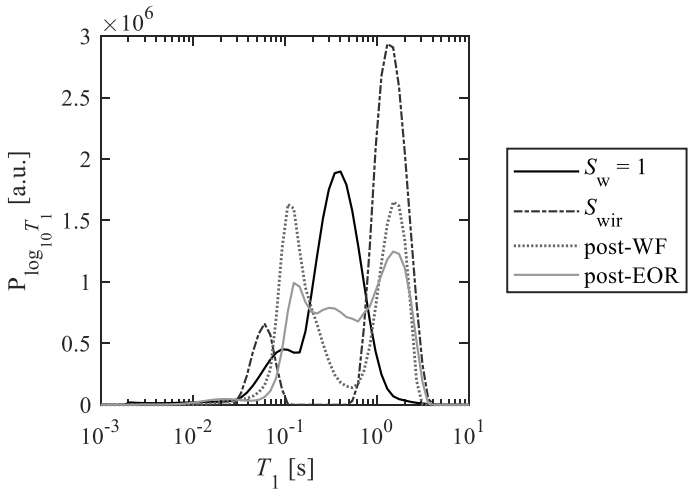

Figure 6.11. Projected T_1 distributions from L-T_1-T_2 datasets at each core flooding stage endpoint; 'post-WF' denotes the measurement post-secondary waterflood, 'post-EOR' denotes the measurement following the polymer EOR-waterflood stage.

Intuitively, the changes in T_1 distributions shown in Fig. 6.11 follow the same trends as those observed in the 2D T_1-T_2 datasets (Fig. 6.10). It is interesting to compare the T_1 peak positions post-waterflood and post-EOR to the two saturation extremes – $S_w = 1$ and S_{wir}. At $S_w = 1$, the core is fully-brine saturated and thus it is known that all the T_1 signal originates from brine. At S_{wir}, the core has the highest oil saturation achievable for the capillary pressure conditions delivered by the ceramic disc. Considering the post-waterflood T_1 distribution, two distinct T_1 peaks are seen: the first coincides with the shorter T_1 region in $S_w = 1$ state; the second directly overlaps with the oil-assigned peak in the S_{wir} state. Post-EOR, three distinct T_1 peaks are now seen. The first and third peaks (viewed from left to right) occupy the same regions as the two peaks observed post-waterflood. However, the central peak now coincides with the longest T_1 regions present in the $S_w = 1$ condition.

6.3.3 Dynamically-tracked L-T_1-T_2 correlations and L-T_1 maps during the secondary and polymer EOR waterfloods

This section presents spatially-resolved relaxation time datasets acquired dynamically during the secondary waterflood and polymer EOR waterflood processes. For each flooding stage, two figures are shown, consisting of a series of L-T_1-T_2 datasets and L-T_1 maps at different timepoints in the flood. Each L-T_1 map is obtained by projecting T_1 distributions from each localised 2D T_1-T_2 correlation within an L-T_1-T_2 dataset.

Figures 6.12 and 6.13 respectively present five L-T_1-T_2 datasets and 12 L-T_1 maps, acquired during the secondary waterflood. As noted in section 6.2.2.2, the axial information in the secondary waterflood should not be interpreted as being mechanistically reservoir-representative. The development of saturation is nonetheless presented, as the signal assignment is important for the subsequent interpretation of the polymer EOR datasets. In Fig. 6.13 each separate dataset is presented along the rows, and its three axially-resolved T_1-T_2 maps are presented along the columns. The 2D correlations

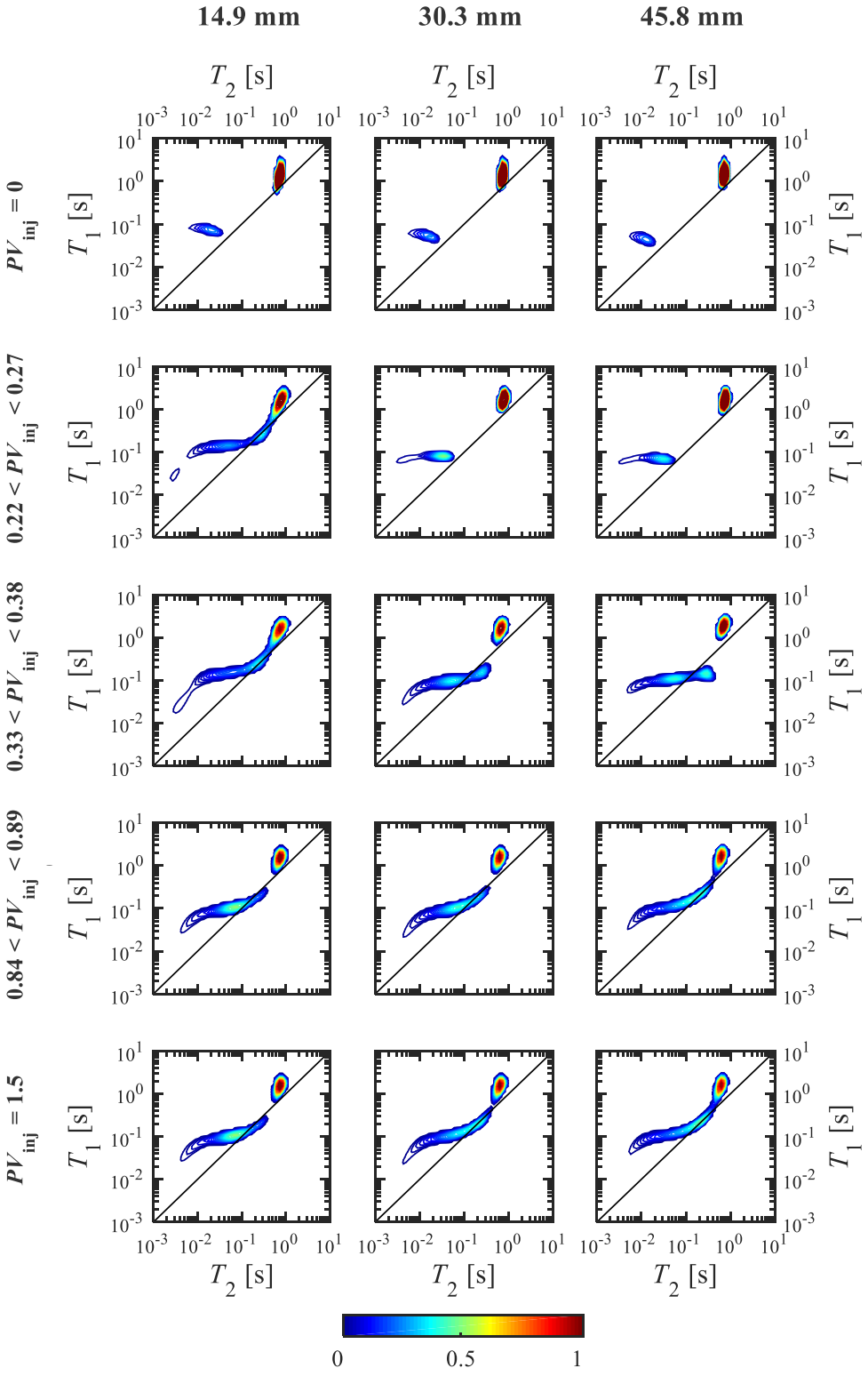

Figure 6.12. Five L-T_1-T_2 datasets acquired during the secondary waterflood. Each dataset is shown along a row. For each dataset, three 2D T_1-T_2 correlation maps at different axial positions in the core are presented along the columns. Positions shown include 14.9 mm, 30.3 mm and 45.8 mm from the inlet face of the 60 mm core (*i.e.*, here, fluid is injected from left-to-right). The range in the cumulative pore volumes of injected brine (PV_{inj}), over which each measurement was acquired, is labelled for each row. All datasets are presented on the same intensity colour scale and normalised with respect to the final dataset acquired.

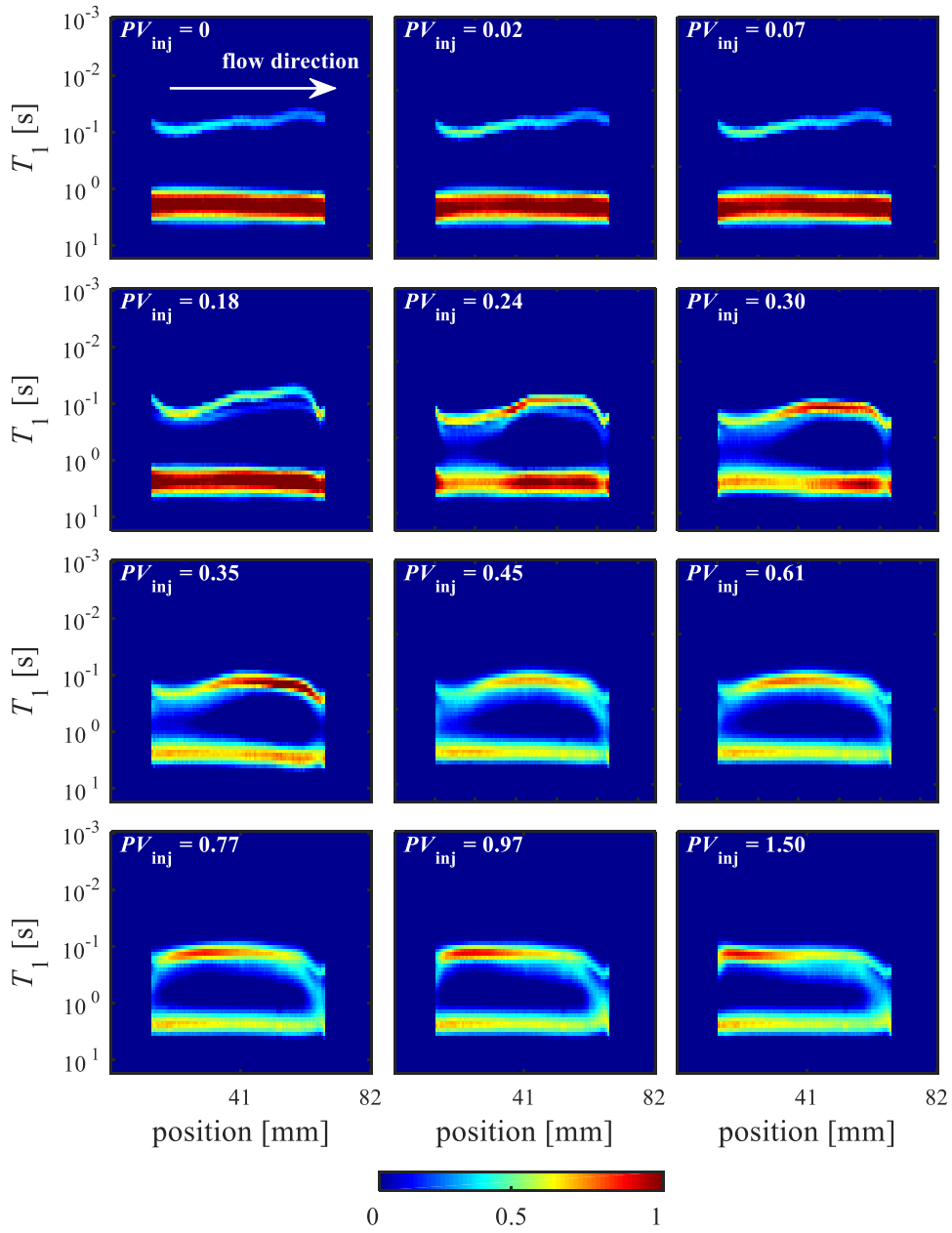

Figure 6.13. Twelve L-T_1 maps acquired throughout the secondary waterflood. The cumulative pore volumes of brine injected, PV_{inj}, over which each measurement was acquired, is labelled for each L-T_1 map. For all maps, the direction of brine injection is left-to-right. All datasets are presented on the same colour scale, normalised with respect to the first dataset acquired ($PV_{inj} = 0$).

shown are extracted from imaging slices centred at 14.9 mm, 30.3 mm and 45.8 mm from the entrance to the 60 mm plug, within the 82 mm imaging FOV. The cumulative injected brine volume, over which each L-T_1-T_2 measurement was acquired, is labelled for each row. To illustrate the axial locations of the three T_1-T_2 slices within the core plug, dashed lines indicating their position are presented in the reference MRI image of the initial brine-saturated core in Fig. 5.5, section 5.2.2.6.

Figure 6.12 shows that at the start of the secondary waterflood ($PV_{inj} = 0$), all axial positions along the core exhibit near-identical T_1-T_2 correlations, akin to those observed at S_{wir}. As brine is injected into the

core, changes in T_1-T_2 distributions are most noticeably observed at the core inlet ($0.22 < PV_{inj} < 0.27$). A broadening in the short T_1, T_2 to longer relaxation times, together with an increase in its signal intensity, are observed. The long T_1, T_2 region also decreases in intensity and the two signal regions appear to meet. With additional brine injection ($0.33 < PV_{inj} < 0.38$), this trend is continued at the centre (30.3 mm) and outlet (45. 8 mm) of the core. In the second half of the waterflood ($0.84 < PV_{inj} < 0.89$), all core regions display this increased signal intensity and relaxation time broadening in the short T_1, T_2 region. The outlet-side of the core shows bridged regions of T_1-T_2 intensity, the inlet-side shows discrete signal regions. The endpoint dataset ($PV_{inj} = 1.5$) shows almost no noticeable difference with that acquired $\sim PV_{inj} = 0.87$ – the greatest changes in the L-T_1-T_2 response occur in the early stages of the waterflood.

Figure 6.13 presents 12 L-T_1 maps acquired during the secondary waterflood. The average cumulative injected brine volume over which each measurement was acquired is labelled on each L-T_1 map. At $PV_{inj} = 0$, two discrete regions of T_1 intensity are observed along the core axis. For $0.18 \leq PV_{inj} \leq 0.35$, an increased intensity in the short T_1 region and a reduced signal intensity in the long T_1 region is observed. These changes first occur at the core inlet ($PV_{inj} = 0.18$), then at the core centre ($PV_{inj} = 0.24$), and finally at the core outlet ($PV_{inj} = 0.30$ and 0.35). In these four datasets a sharp shift to longer T_1 values is seen in the short T_1 signal region at the core outlet. For $0.45 \leq PV_{inj} \leq 0.61$, the high intensity signal regions are less axially-polarised and are more evenly distributed at the core centre. In addition, bridging in the two T_1 signal regions occurs at the core outlet – this bridging is further pronounced for $0.77 \leq PV_{inj} \leq 1.50$. Very little change is observed between datasets $PV_{inj} = 0.97$ and $PV_{inj} = 1.50$.

Next considering the polymer EOR flood, Figs. 6.14 and 6.15 present twelve L-T_1 and five L-T_1-T_2 maps acquired during this final core flooding stage. Datasets marked $0 < PV_{inj} < 0.55$ were acquired during the polymer slug injection, datasets marked $0.55 < PV_{inj} < 2.55$ were acquired during the subsequent EOR waterflood. Considering first Fig. 6.14, at $PV_{inj} = 0$, two clear T_1 signal peaks are observed along the core axis. Based on these distinct signal regions, three ranges of T_1 are hereby defined: short T_1, mid-range T_1 and long T_1. These are labelled in Fig. 6.14, dataset $PV_{inj} = 0$. For $0.08 < PV_{inj} < 0.49$, T_1 signal emerges in the mid-T_1 region; simultaneously a reduction in intensity occurs in the short- and long-T_1 regions. These changes first occur at the core inlet (at $PV_{inj} = 0.08$), before moving towards the core outlet. Throughout the entire polymer EOR process, the most significant changes to signal intensity in the long-T_1 region occur in the initial stages of polymer injection. By $PV_{inj} = 0.38$, an equilibrium in the axial-intensity profile of the long-T_1 region is reached – no further major changes are observed with additional fluid injection. This early-equilibration is not observed in the short- and mid-T_1 regions. For $0.54 < PV_{inj} < 1.51$, the EOR waterflood is followed by a change in T_1 characteristics in the mid- and short-T_1 regions: a reduction, and subsequent increase, in the mid-T_1 region signal intensity is seen to propagate along the core. The signal intensity reduction is accompanied with a signal intensity increase to the short-T_1 region, and vice versa. For $1.79 < PV_{inj} < 2.55$, an equilibrium state is reached in which

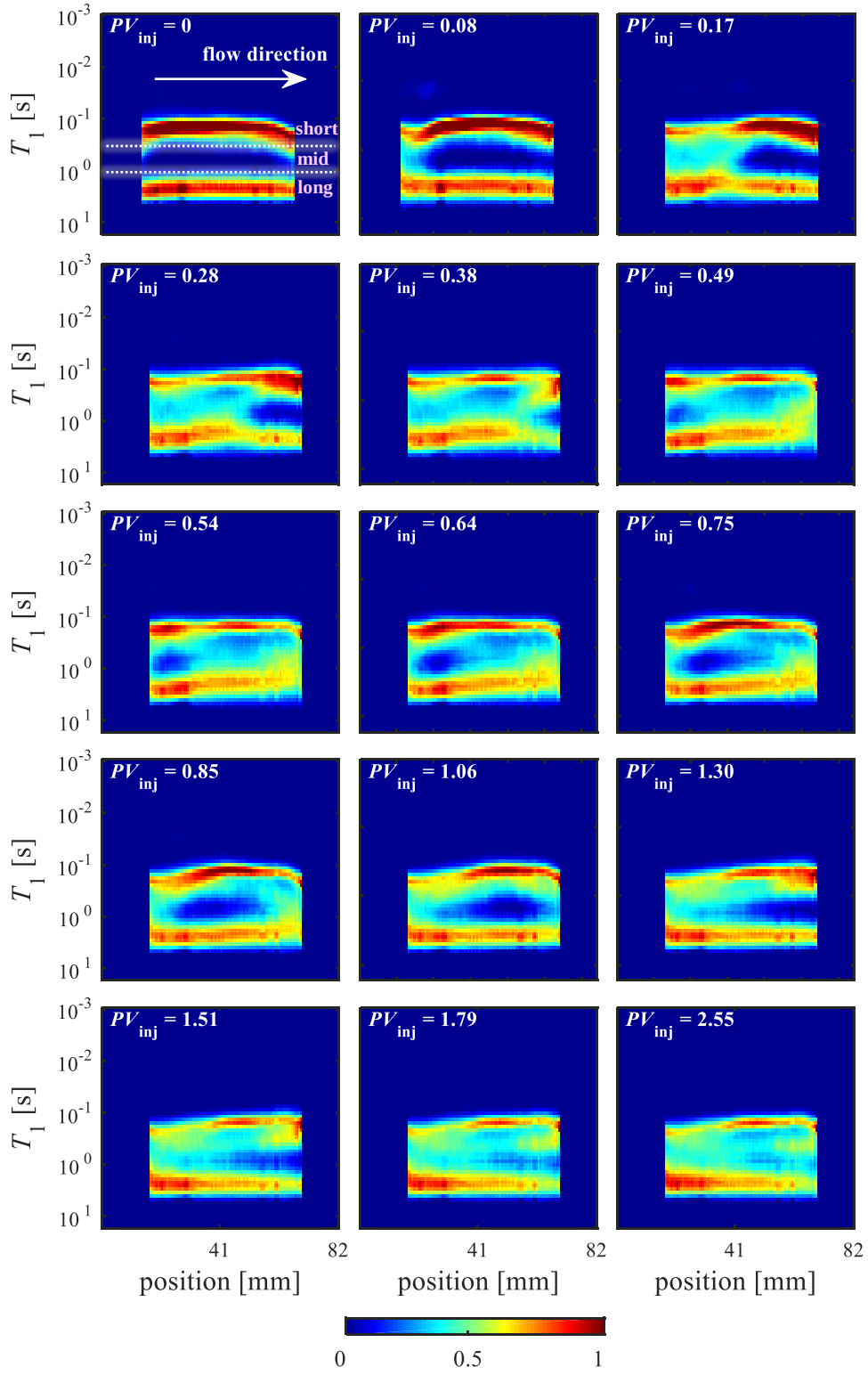

Figure 6.14. *L*-T_1 maps, obtained from *L*-T_1-T_2 datasets acquired during polymer injection and EOR waterflooding. Average cumulative pore volumes of injected fluid PV_{inj}, over which each measurement were acquired, are labelled for each *L*-T_1 map. For all maps, the direction of brine injection is left-to-right. All datasets are presented on the same colour scale, normalised with respect to the final dataset acquired (PV_{inj} = 0). Maps labelled 0-0.54 P.V. were acquired during polymer injection, maps labelled 0.64-2.55 P.V. were acquired during the subsequent EOR waterflood.

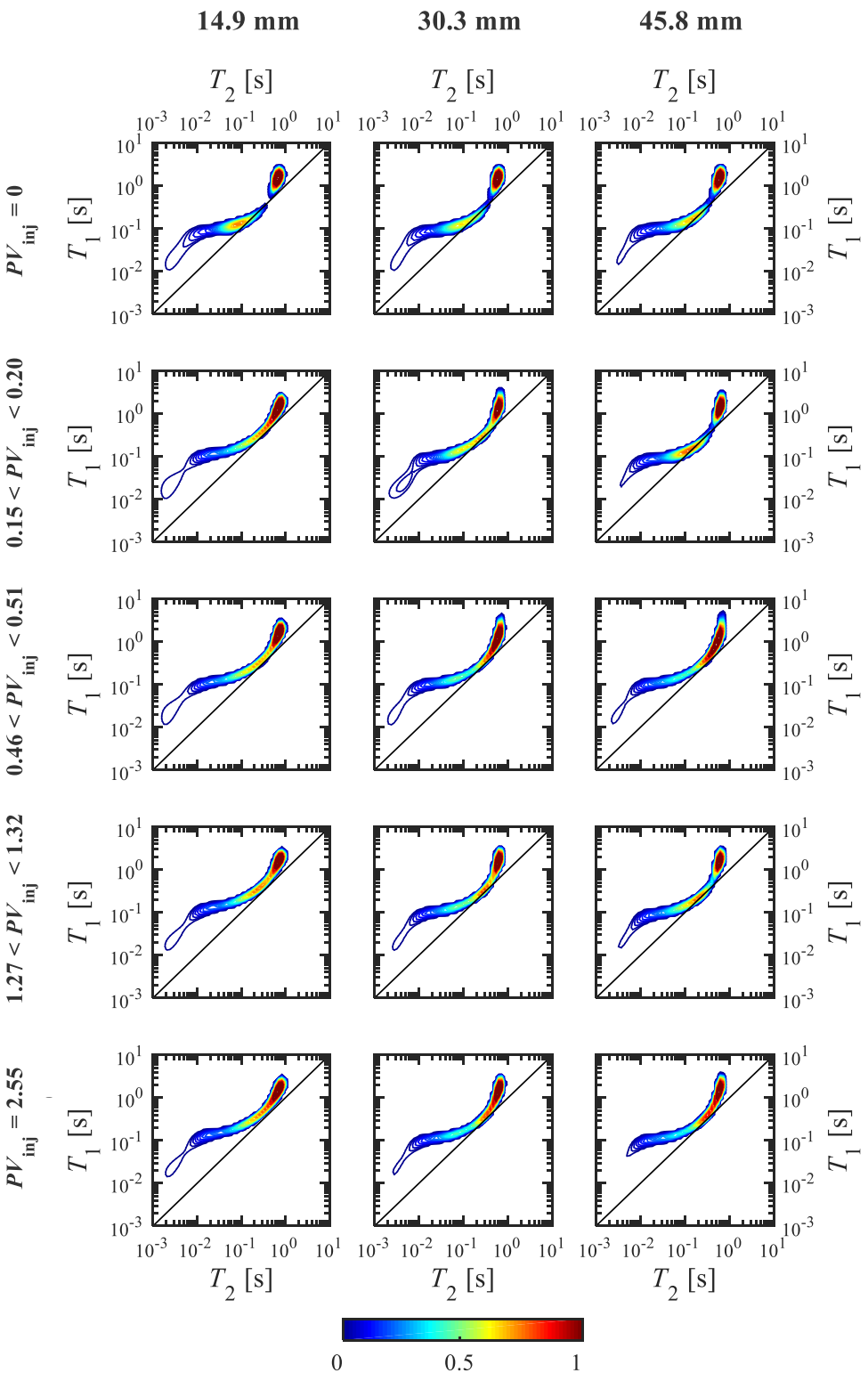

Figure 6.15. Five *L*-T_1-T_2 datasets acquired during polymer EOR waterflooding. Each dataset is shown along a row. For each dataset, three 2D T_1-T_2 correlation maps at different axial positions in the core are presented along the columns. Positions shown include 14.9 mm, 30.3 mm and 45.8 mm from the inlet face of the 60 mm core (*i.e.*, here, fluid is injected from left-to-right). The range in the cumulatively injected pore volumes (PV_{inj}) over which each measurement was acquired, is labelled for each row. All datasets are presented on the same intensity colour scale, normalised with respect to the first dataset acquired. Datasets labelled 0-0.51 P.V. were acquired during polymer injection, those labelled 1.27-2.55 P.V. were acquired during the subsequent EOR waterflood.

all three T_1 regions are saturated along the core axis. Distinction in these three T_1 regions was similarly observed in Fig. 6.10.

In Fig. 6.15, five L-T_1-T_2 maps are shown, each with three-axially resolved 2D T_1-T_2 correlation maps. Similar trends as previously observed in the L-T_1 maps are noted. At $PV_{inj} = 0$, axially-uniform T_1-T_2 distributions with two intensity regions are seen. For $0.15 < PV_{inj} < 0.51$, a blurring in the short and long relaxation times occur – first at the core inlet, this then propagates along the core axis. For $1.27 < PV_{inj} < 1.32$, fluid redistribution in the mid-range T_1, T_2 occurs, and at the end point ($PV_{inj} = 2.5$), axially-uniform conditions are observed.

In section 6.4, the results presented herewith are discussed and interpreted, within the context of pore-filling mechanisms and the existing research literature. Through signal assignment in the L-T_1-T_2 datasets to both dodecane and brine, continuous, *in situ* quantification of the NMR global saturation conditions, S_o and S_w, are attained. This NMR saturation is compared with the volumetrically-measured produced volumes throughout the core flooding process. Building upon this, the use of L-T_1-T_2 as a tool for dynamically measuring axially-resolved saturations during laboratory core floods is demonstrated.

6.4 Discussion

The results presented in section 6.3 are here interpreted. The goal is to achieve an understanding of the distribution of fluid saturation within the pore space throughout the oil recovery floods studied, and to obtain a continuous measurement of core saturation using NMR. This will then be placed into the context of the existing literature discussions on the proposed mechanisms for polymer EOR flooding (section 6.1). The interpretation of the T_1-T_2 datasets is based upon the pore size and surface wetting information that can be obtained from NMR relaxation time analysis. The key statements summarising the essential principles by which these datasets can be interpreted were previously outlined in section 5.4. The signal assignments and interpretation made of the 2D T_1-T_2 correlation maps following primary drainage (section 5.4), are built upon and form the starting point of this discussion.

At the start of the waterflood, the core is at irreducible water saturation. Its global T_1-T_2 measurement (Fig. 6.10b) consists of two discrete signal regions – a low intensity, short T_1, T_2 region corresponding to surface-wetting brine and brine residing in the smallest pores; and a high intensity, long T_1, T_2 region corresponding to oil held in pore centres. Based on these assignments and the observations of changed T_1-T_2 and T_1 distributions in Fig. 6.10b and Fig. 6.11, the broadened short T_1, T_2 peak post waterflood is interpreted as injected brine flowing through the continuous wetting layer, resulting in its thickening and filling progressively larger pores. This brine displaces some of the oil saturation held in the large pore centres, reducing the oil signal intensity. The unchanged oil T_1, T_2 values suggest the pore residency of the dodecane remains unchanged – trapped in the largest pores and not in contact with the water-wetting surface. This interpretation is consistent with the existing knowledge of waterflooding mechanisms discussed in the literature (section 6.1.4.1). Considering the dynamically tracked datasets

(Figs. 6.12 and 6.13), these same trends are observed. As brine is injected to the core from left to right, brine signal intensity increases and occupies progressively larger pores (longer T_1, T_2 values), whilst the oil saturation (intensity) decreases.

The greatest contrast in the oil and brine-phase signals are achieved in the T_1 dimension. By applying a cut-off in the signal intensity at the minimum of the projected global T_1 distributions (as seen in Fig. 6.10), the NMR core saturation post-secondary waterflood can be determined. A deconvolution of the two peaks was conducted to improve the accuracy of this cut-off. This resulted in an NMR saturation of $S_w = 0.59 \pm 0.03$, $S_o = 0.41 \pm 0.02$, in agreement with the volumetrically-determined saturations (section 6.3.1), providing further confirmation that the above interpretation of the signal assignment is correct. The uncertainty in the NMR saturations was calculated based on the fit error in the 2D T_1-T_2 correlations, the random error of the L-T_1-T_2 measurement, the uncertainty in the hydrogen indices and in the peak deconvolution. The sharp shift to longer T_1 values at the core outlet (for datasets $0.18 \leq PV_{inj} \leq 0.35$ in Fig. 6.13) is believed to result from oil banking at the core outlet, due to the operational error associated with using the ceramic disc during secondary waterflooding (see section 6.2.2.2).

In the polymer EOR flood, three liquids are present – dodecane, brine and xanthan gum solution. It is expected that the polymer, as an aqueous phase, would follow the existing aqueous phase flow pathways. In addition, as the bulk liquid T_1 and T_2 responses for the brine and xanthan polymer exhibit very similar results (section 6.2.1.1), it is expected that within the pore space the two fluids would also exhibit very similar relaxation times. As highlighted in section 6.3.2, with polymer EOR injection the short T_1, T_2 brine signal is broadened until it bridges with the long T_1, T_2 oil signal. In Fig. 6.10d, the projected global T_1 distributions post-polymer EOR display three signal peaks: from left, the first two peaks occupy the same regions as in the $S_w = 1$ state and are assigned to the brine-phase. The third peak is assigned to dodecane – it occupies the same region as the dodecane signal in the prior endpoint states. By applying a cut-off and deconvolution of assigned T_1 peaks, an NMR saturation was obtained at the end of the polymer EOR stage. This resulted in an NMR saturation of $S_w = 0.63 \pm 0.06$ and $S_o = 0.37 \pm 0.06$, in agreement with the volumetric saturation (section 6.3.1). The increased error margin was due to the greater uncertainty in the T_1 peak deconvolution, compared to that post-waterflood.

The broadening of brine signal towards longer relaxation times suggests that the xanthan enables the brine phase to fill larger pores. During the polymer slug injection (0-0.55 P.V., Fig. 6.14), the highest xanthan concentration is present in the core, before any possible dilutions from the subsequent EOR waterflood. When the core is first exposed to the polymer, a sharp reduction in the short-T_1 intensity and sharp increase in the mid-T_1 intensity occurs. This is interpreted as the injected polymer following the continuous wetting path, filling the smallest pores, diverting the brine and allowing it to access larger pores. During the subsequent EOR-waterflood, a slight reversal in this trend is observed with a reduction in the mid-range T_1 intensity and an increase in the short T_1 signal intensity. This is interpreted as a dilution effect – with the injected brine reducing the polymer concentration, such that fewer small pores

are occupied by the polymer. This dilution effect reaches an equilibrium in the final stages of the EOR-brine injection (1.7-2.55 P.V.) which appears to reach an equilibrium in the L-T_1 dataset.

This signal assignment and interpretation suggests that for xanthan polymer EOR, injected polymer supports the DPR mechanism, providing a reduced permeability of the brine phase through the polymer filling the smallest pores. The initial pore filling could either be simply due to the blocking from xanthan debris, or alternatively due to polymer adsorption on the core surface. As there are no detectable changes to the T_1/T_2 ratios in the short T_1, T_2 (small pores) signal region, it is concluded that the xanthan does not have stronger surface interactions to preferentially adsorb to the core surface in place of brine – therefore in this system, the DPR behaviour is attributed to xanthan debris blocking the smallest of pores. This interpretation is consistent with other observations reported in the literature, in which xanthan gum has been noted as being susceptible to pore plugging from cellular debris (Sun *et al.*, 2012; Kamal *et al.*, 2015). Furthermore, Huh *et al.* (1990) demonstrated that with greater polymer concentrations, greater retention of xanthan gum is seen in sandstones. This would be consistent with the interpretation presented here, in which dilution from the injected brine flushes out some of the polymer debris, reducing the polymer retention in small pores.

Figure 6.16 presents the continuous global NMR saturations of the core during the secondary waterflood and EOR-polymer stages of the core flood. These were obtained by applying the T_1 cut-off to the projected T_1 distributions from the L-T_1-T_2 datasets.

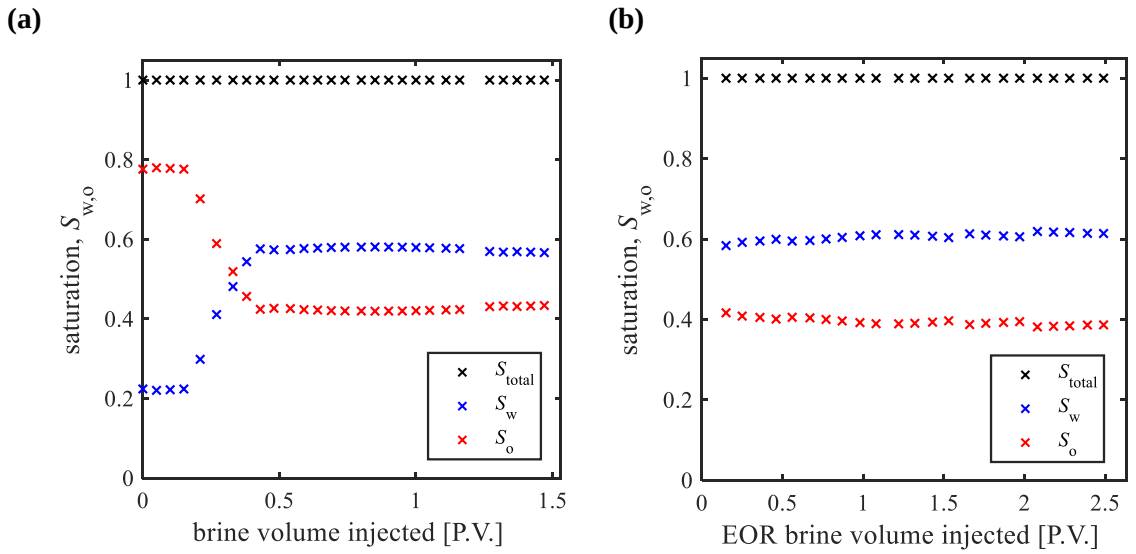

Figure 6.16. Saturation data obtained from the NMR measurement during **(a)** secondary waterflooding, and **(b)** polymer EOR flooding stage. NMR saturation data were obtained by applying oil-phase and aqueous-phase specific cut-offs in the projected T_1 distributions from the L-T_1-T_2 datasets.

Figure 6.16 demonstrates that during secondary waterflooding, the majority of changes to the core saturation occur in the first 0.5 P.V. of injected brine. Thereafter, as water breakthrough occurs, little

further increase in oil recovery is achieved. This is attributed to the formation of a preferential pathway of least resistance for water flow, once breakthrough has occurred. This results in no further significant oil recovery as no new regions of the core are swept. A similar trend is observed in the polymer EOR stage, in which the major saturation changes occur in the early stages of the flood. The small offsets in saturation at 1.5 P.V. and 2 P.V. in Fig. 6.16b are processing artefacts due to the progressive shift in the optimal T_1 cut-off, with increasing water saturation. A total recovery of 56.1% of the original oil in place is achieved, of which 4.9% is from the polymer EOR stage – the polymer delivers an incremental recovery of 9.8%, after the secondary waterflood. These results are in line with typical recoveries achieved for xanthan gum polymer EOR strategies reported in the literature (section 6.1.1).

In addition, it is interesting to note the capability of the L-T_1-T_2 technique for dynamically tracking local variations in core saturation, in systems with sufficient contrast in relaxation times. This is demonstrated in Fig. 6.17 for which the axial variation in oil and brine saturation with progression of the secondary waterflooding stage is shown.

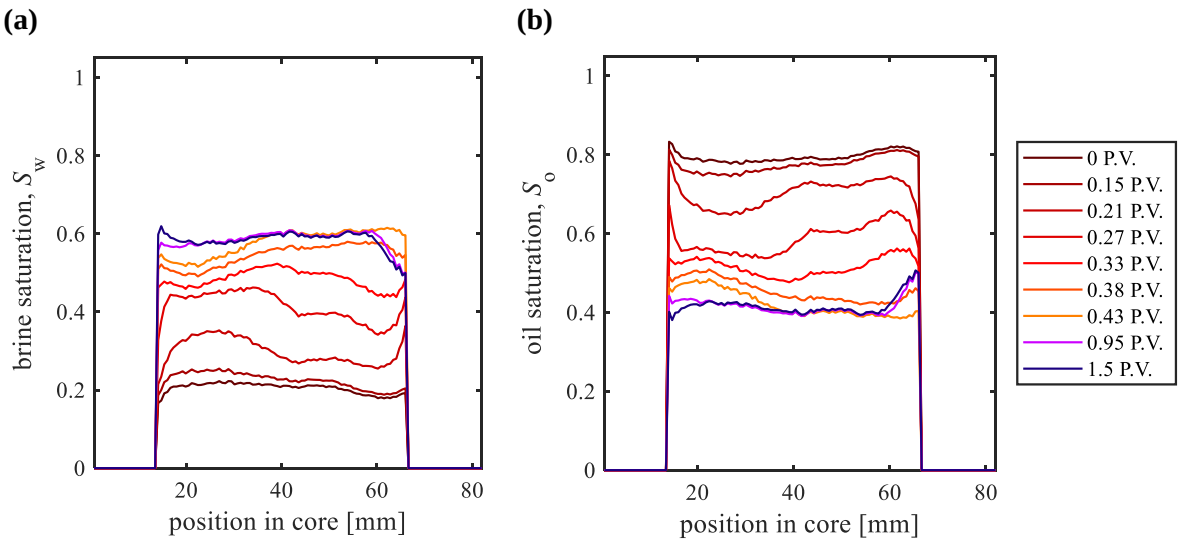

Figure 6.17. Continuous monitoring of changes in axial saturation during the secondary waterflooding process, **(a)** axial brine saturation, **(b)** axial oil saturation. Saturations determined using oil- and brine-phase contrast in projected T_1 distributions in the L-T_1-T_2 datasets.

Figure 6.17 demonstrates oil banking at the core outlet, likely resulting from the ceramic disc present in the secondary brineflood. Whilst this is an artefact of the error in flooding protocol, the potential application of the technique for determining axial changes in saturation of mechanistic relevance in heterogeneous core samples is clear.

6.5 Conclusions

In this chapter a xanthan gum polymer EOR flood within a Bentheimer sandstone was continuously monitored using a spatially resolved NMR relaxometry technique – L-T_1-T_2. The aim of the study was

to use this technique to probe the oil displacement mechanisms taking place at the pore level and to continuously track the core saturation throughout the flooding process.

By using chemical contrast provided through relaxation time measurements, the core saturation throughout the flooding process was continuously tracked. This provided an *in situ*, non-invasive, axially-sensitive and volumetrically quantitative measurement of the core saturation conditions. The endpoint NMR measurements of core saturation agree with external measurements of volumetrically produced effluent. Across the overall flooding protocol, a total recovery of 56.1% of the OOIP was achieved, of which 4.9% was from the polymer EOR flooding stage, in agreement with typical values reported for xanthan gum pilot field tests.

Interpretation of the T_1-T_2 relaxation time values showed that at the end of the secondary waterflood residual oil remained trapped in the centre of large pores, whilst brine was held in small pores and throughout the wetting surface layer. This agrees with established theories on waterflooding within water-wet cores. During xanthan polymer EOR flooding, it was interpreted that the injected polymer blocked the smallest pores through mechanical filtration of xanthan cellular debris. This diverted the existing brine to larger pores, enabling greater oil displacement in these regions. This pore blocking effect was reduced upon further injection of brine, attributed to both a dilution of the polymer and the flushing out of some xanthan debris. No detectable increases in surface interaction strength from NMR T_1/T_2 ratios were detected, suggesting that xanthan is not able to competitively adsorb to the rock, in place of brine. In the context of existing literature discussions on the proposed displacement mechanisms for polymer EOR, these results are consistent with xanthan gum achieving macroscopic improvements to sweep efficiency *via* deposition of polymer debris in small pores. This results in the disproportionate permeability reduction of the brine-phase. Whilst much prior work on the mechanisms of polymer EOR recovery have been conducted in optically-transparent model systems, very little work has been conducted in reservoir-representative core samples. Here, this mechanism has been demonstrated and continuously monitored with spatial resolution at reservoir-representative conditions.

Other mechanisms influencing the microscopic displacement efficiencies have been proposed in the literature for explaining polymer EOR processes in water-wet cores, such as viscoelastic turbulences, oil thread stabilisation and pulling effects from dead end pores. These have previously only been demonstrated with HPAM polymers, and not with xanthan gums. No comment can be made on whether these mechanisms took place in this particular study as the L-T_1-T_2 technique is not sensitive to these processes. In Chapter 7, these ideas are further explored for an EOR study using HPAM polymer and NMR spectral- and diffusion-based techniques – the use of which enables the probing of transport mechanisms at the pore and core scale.

Chapter 7

Probing an HPAM Polymer-EOR Flood in Bentheimer Sandstone using a Multifaceted MR Approach

7.1 Introduction

This chapter studies a hydrolysed polyacrylamide (HPAM) EOR waterflood in a water-wet sandstone, using a multifaceted MR approach. As introduced in section 6.1.4, HPAM-EOR is thought to drive increased oil recoveries through improvements in both macroscopic and microscopic displacement efficiencies. The former, common to xanthan and HPAM EOR polymers, includes disproportionate permeability reduction and altered viscosity ratios. The latter, unique to HPAM, is thought to include oil thread/column stabilisation, elastic turbulences, oil film stripping and pulling effects. Prior work in studying microscopic displacements has primarily been conducted in optically-transparent model systems, little work has taken place in reservoir-representative core systems. Such *in situ*, non-invasive tracking within reservoir-representative samples is invaluable – enabling validation of prior interpretations and assumptions obtained from measurements in artificial models, or *via* computational reservoir modelling simulations.

This chapter focuses on studying an HPAM EOR flood, in a reservoir-representative system. The aims are to develop understandings of HPAM-EOR pore-level mechanisms. Combined spectroscopy and spectrally-resolved relaxometry techniques are used to quantify core saturations and determine the pore residency of hydrocarbon and aqueous phases. Spatially-resolved T_2 propagator and pulsed field gradient (PFG) diffusion measurements are respectively used to detect changes in fluid mobilities and oil ganglia size post-EOR.

7.2 Materials and Methods

7.2.1 Materials

This section outlines the materials used, including the core properties, fluid compositions, polymer rheology and bulk fluid NMR properties. The core flooding system is also discussed.

7.2.1.1 Materials and Chemicals

A Soxhlet-cleaned Bentheimer sandstone outcrop core plug (Kocurek Industries, Houston), 38.35 ± 0.02 mm in diameter and 60.14 ± 0.02 mm in length, was used as a representative reservoir system. The pore size distribution was unimodal, with logarithmic-mean pore size and variance 32 μm and 18 μm respectively, as determined by MIP – see Fig. 7.1.

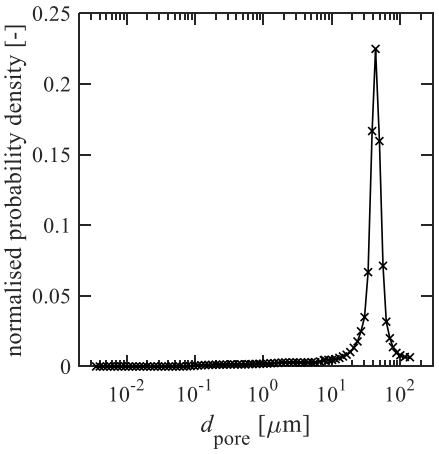

Figure 7.1. MIP core pore size distribution.

The core pore volume (P.V.) and porosity were 17.18 ± 0.03 ml and φ_p = 24.72 ± 0.05% by gravimetric analyses. The core was cleaned by Soxhlet methods (protocol outlined in section 4.2.1), dried at 95 °C for 48 h, vacuum dried for 6 h and vacuum saturated in synthetic brine for over 12 h. Low salinity, benign synthetic brine (30.0 ± 0.1 g l^{-1} NaCl) was prepared using sodium chloride (99%, Sigma Aldrich) and deionised water. MRI characterisation of the initial brine-saturated core (S_w = 1) was conducted using 3D high-resolution RARE imaging – Fig. 7.2 presents 2D slice sections therein, confirming a homogeneous texture.

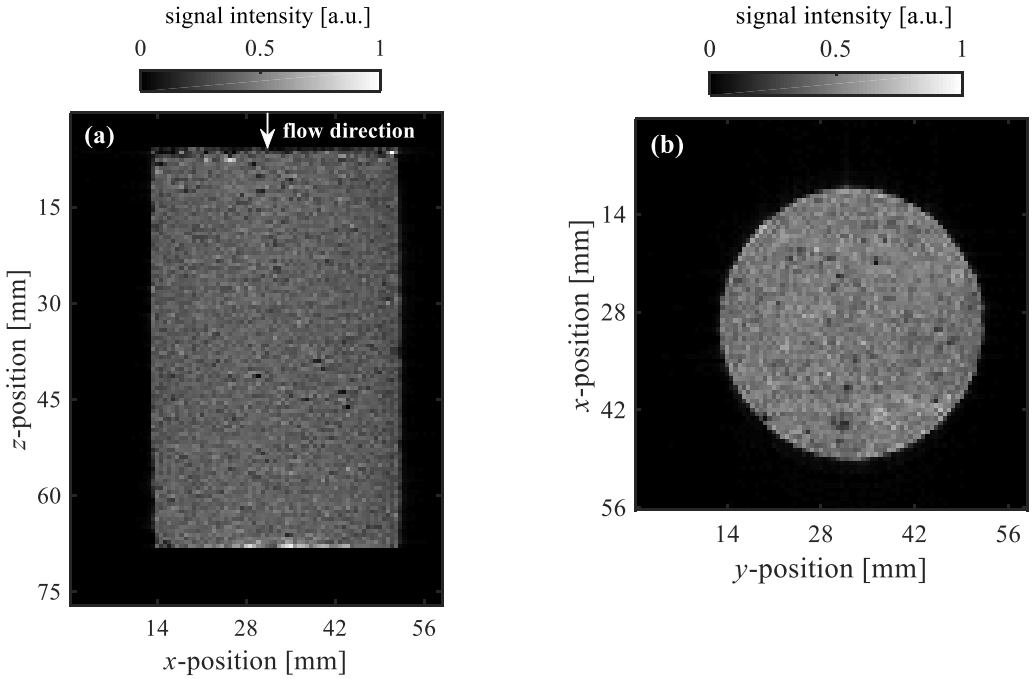

Figure 7.2. Reference image at S_w = 1, from a 3D RARE experiment. **(a)** central slice in *z*-*x* plane – arrow indicates flow direction during flooding. **(b)** central slice in *x*-*y* plane. Datasets acquired using Gaussian-shaped 90° excitation and 180° refocusing r.f. pulses, duration 512 μs, and power 27 dB, 21 dB (respectively). An imaging field-of-view (FOV) of 75 mm × 58 mm × 58 mm (*z*,*x*,*y*) with respective resolution 0.58 mm $pixel^{-1}$ × 0.64 mm $pixel^{-1}$ × 0.64 mm $pixel^{-1}$ was used. A 3.23 ms echo time and RARE factor 8, gave an 8 h acquisition time.

Dodecane (99%, Acros Organics) was used as the representative hydrocarbon. Commercially-available FP 3230S HPAM (provided by STCH), with average molecular weight ~6 MDa, was used as the EOR polymer and prepared to 4000 mg l^{-1} HPAM in 30.0 ± 0.1 g l^{-1} NaCl/DI. 500 ml of EOR polymer was prepared as follows:

- 495.3 ± 0.1 g of 30.0 ± 0.1 g l^{-1} NaCl/DI brine was filtered over a 0.45 µm Millipore filter, then continuously stirred in a round-bottomed flask using a magnetic stirrer at 350 rpm, forming a water vortex, and O_2-purged with N_2 gas for 30 min;
- 2.670 ± 0.001 g of a protective package (composed of 15 wt% isopropanol (99.5%, Sigma Aldrich), 7.5 wt% thiourea (99%, Sigma Aldrich) and 77.5 wt% DI) was added;
    - [O_2 purging and addition of a protective package prevent chemical degradation of the HPAM polyacrylamide vinyl backbone *via* radical mechanisms, or reactions between oxygen and any impurities. The protective package contains radical scavengers (isopropanol and thiourea).]
- 2.000 ± 0.001 g of HPAM powder was added (ensuring no agglomerate formation) and stirred at full-vortex for 5 min under N_2 atmosphere;
- mixture was continuously stirred at 250 rpm, at room temperature and under N_2 for 48 h, then vacuum-filtered over a 3 µm Millipore filter (Merck).

7.2.1.2 Bulk HPAM Rheology

The flow behaviour of bulk HPAM solution was characterised using a Rheometric Scientific ARES 320 rheometer. A smooth-walled concentric cylinder Couette cell, with inner cylinder of outer diameter 32 mm, length 34 mm, and wall gap 1 mm was used. The rheometer was operated at 20.0 ± 0.5 °C, under controlled strain mode, to determine variation in apparent viscosity, using a shear rate sweep (500 to 0.5 s^{-1}). Accordingly, the HPAM sample was shear-thinning, with a low-shear viscosity of ≈37 cP (37 mPa s). With respect to the similarly-measured synthetic brine viscosity (1.1 cP) and a reported dodecane viscosity of 1.49 ± 0.01 cP (1.49 ± 0.01 mPa s) at 20.0 ± 0.5 °C (Lemmon *et al.*, 2018), the improvement in viscosity ratio delivered by HPAM is apparent (see Eq. 6.1).

Although not measured herein, for HPAM flow measurements within porous media (in which apparent viscosities and shear rates are inferred from pressure gradients and flowrates in the core), a critical shear rate ($\dot{\gamma}_{\mathrm{onset}}$) exists beyond which HPAM displays apparent shear thickening – coinciding with the believed onset of elastic turbulences (see section 6.1.4.4). This onset is independent of polymer concentration, c (for $10c^* < c < 100c^*$), where c^* is the overlap concentration – at which polymer coils touch in supporting solution, where for HPAM 3230S c^* ~ 0.025 wt% and $\dot{\gamma}_{\mathrm{onset}}$ ~ 50 s^{-1}. (Howe *et al*, 2015; Mitchell *et al.*, 2016). The HPAM solution used in this study falls within $10c^* < c < 100c^*$ and thus its literature-reported $\dot{\gamma}_{\mathrm{onset}}$ is assumed.

7.2.1.3 Bulk Material NMR Properties

Bulk liquid relaxation times and self-diffusivities were measured as: $T_{1,\mathrm{brine}}$ = 2.59 ± 0.05 s, $T_{2,\mathrm{brine}}$ = 2.02 ± 0.04 s, D_{brine} = 2.02 ± 0.01 × 10^{-9} m^2s^{-1}; $T_{1,\mathrm{dodecane}}$ = 1.16 ± 0.02 s, $T_{2,\mathrm{dodecane}}$ = 0.72 ± 0.01 s, D_{dodecane} = 0.84 ± 0.04 × 10^{-9} m^2s^{-1}; $T_{1,\mathrm{HPAM}}$ = 2.32 ± 0.05 s, $T_{2,\mathrm{HPAM}}$ = 1.60 ± 0.03 s, D_{HPAM} = 1.98 ± 0.01 × 10^{-9} m^2s^{-}

[1] (*via* T_1-IR, T_2-CPMG and APGSTE diffusion methods, the latter using observation time, Δ = 300 ms). The self-diffusivity of brine in the brine-saturated core was $D_{\text{core-brine}} = 1.65 \pm 0.10 \times 10^{-9}\ \text{m}^2\text{s}^{-1}$, at Δ = 300 ms. Hydrogen indices were measured as: $HI_{\text{brine}} = 0.96 \pm 0.02$; $HI_{\text{dodecane}} = 1.06 \pm 0.02$; $HI_{\text{polymer}} = 0.96 \pm 0.02$. All measurements were acquired in an 85 MHz spectrometer (details in section 7.2.2.4), at 20.0 ± 0.5 °C and atmospheric pressures.

7.2.1.4 Core Flooding System

All core floods were conducted using the MRRC CFS – see Fig. 4.2 and discussion in section 4.3.5.1. Following brine saturation, the core was enclosed in PTFE heat-shrink (Adtech Polymer Engineering, UK), loaded into an Aflas sleeve, and into a PEEK RCH flow cell (ErgoTech, Conwy, UK), see section 4.3.5.1. A 15-bar rated semi-permeable ceramic pressure disc (ELE International) was loaded at the core outlet – used for achieving irreducible water saturation, S_{wir}. A 290 ± 25 psig (~2 ± 0.2 MPaG) confining pressure was used, all RCH outlet lines were open to atmosphere.

The RCH confining loop was filled, purged of air, pressure and leak tested externally to the magnet. Subsequently, the CFS injection loop was connected to the RCH and leak tested externally to the magnet. Following RCH assembly, 2 P.V. brine was injected at 0.061 ml min^{-1} (equivalent to linear interstitial velocity within the core, u_{int} = 1 ft day^{-1} (~ 3.5 µm s^{-1})), to ensure uniform core saturation and removal of any air within the core and RCH assembly.

7.2.2 Methods

This section outlines core flood protocols, an introduction to the NMR propagator measurement, the NMR measurement protocol and experimental parameters used.

7.2.2.1 Core Flood Protocol

Floods were conducted in the assembly described in section 7.2.1.4, as follows:

1. *Primary drainage* – to achieve S_{wir}, dodecane was continuously injected into the brine-saturated core at 0.0305 ml min^{-1} (u_{int} = 0.5 ft day^{-1}), using the ceramic disc method. Subsequently, the ceramic disc was removed from the RCH.
2. *Secondary waterflood* – 5 P.V. brine was injected in three stages – 1 P.V. at 0.0305 ml min^{-1} (u_{int} = 0.5 ft day^{-1}), 1 P.V. at 0.061 ml min^{-1} (u_{int} = 1 ft day^{-1}), 3 P.V. at 0.1512 ml min^{-1} (u_{int} = 2.5 ft day^{-1}).
3. *EOR polymer slug injection* – 0.5 P.V. HPAM solution was injected at 0.0305 ml min^{-1} (u_{int} = 0.5 ft day^{-1}).
4. *EOR waterflood* – 4.5 P.V. brine was injected in three stages – 0.5 P.V. at 0.0305 ml min^{-1} (u_{int} = 0.5 ft day^{-1}), 1 P.V. at 0.061 ml min^{-1} (u_{int} = 1 ft day^{-1}), 3 P.V. at 0.1512 ml min^{-1} (u_{int} = 2.5 ft day^{-1}).

Prior to injection, all fluids were vacuum-degassed for 30 min, or until no further bubbles were released. Across all stages $u_{\text{int}} \leq$ 2.5 ft day^{-1} (~8.8 µm s^{-1}), to ensure reservoir-representative flooding conditions

(Webb *et al.*, 2008). Comparatively large brine volumes (5 P.V.) were injected during secondary and EOR waterflooding, following recommended practice (Langnes *et al.*, 1985; Feng and Yu, 2015), and 0.5 P.V. polymer was injected, as per typical reservoir polymer-EOR procedures (see section 6.1.2). Both waterflooding stages used incrementally-increased flowrates, to minimise capillary end effects (Shiran and Skauge, 2013). At all stages, produced effluent volumes were collected in measuring cylinders. Figure 7.3 presents a schematic of the flooding protocol.

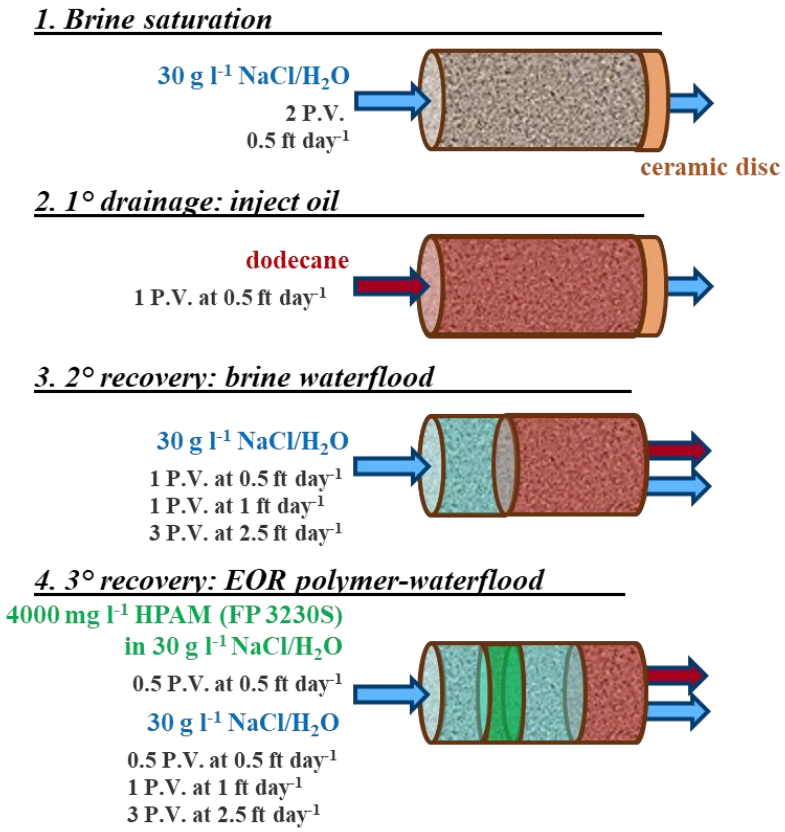

Figure 7.3. EOR core flooding protocol.

7.2.2.2 The NMR Ensemble-Average Propagator

As introduced in section 2.3, NMR PFG methods and spin echo (SE) techniques can measure average molecular displacements. An initial spin position is phase-labelled by a first gradient pulse and after time Δ, its final position is phase-labelled by a second gradient pulse of opposite polarity, equal duration. Incoherent motion (such as from Brownian motion) will result in NMR signal attenuation, coherent motion (such as from flow processes) will lead to spins accruing a phase shift by moving from location $\mathbf{r}$ to $\mathbf{r}'$:

$$phase\ shift = \gamma \delta_G \mathbf{g} \cdot (\mathbf{r}' - \mathbf{r}) \tag{7.1}$$

where δ_G is gradient pulse duration, and $|\mathbf{g}|$ is magnetic field gradient pulse strength.

Such molecular displacements can be described using conditional probability $P_s(\mathbf{r}|\mathbf{r}', \Delta)$, for a spin starting at position $\mathbf{r}$, and moving to $\mathbf{r}'$ during Δ. Building upon the NMR signal attenuation definitions in section 2.3, the ensemble echo signal amplitude, E, is given by Eq. 7.2 (in the case where the gradient

pulse duration, δ_G, is much shorter than the observation time Δ – the 'narrow gradient pulse approximation'):

$$E(\mathbf{g},\Delta) = \iint \rho(\mathbf{r})P_s(\mathbf{r}|\mathbf{r}',\Delta)\exp[i\gamma\delta_G\mathbf{g}\cdot(\mathbf{r}'-\mathbf{r})]\,d\mathbf{r}\,d\mathbf{r}' \tag{7.2}$$

where $\rho(\mathbf{r})$ is the spin density at position $\mathbf{r}$. The *ensemble-averaged* probability for a molecule to displace by $\mathbf{R} = \mathbf{r}' - \mathbf{r}$, irrespective of its starting position, during Δ (termed the ensemble-average propagator $\bar{P}_s(\boldsymbol{r},\Delta)$) is:

$$\bar{P}_s(\mathbf{R},\Delta) = \int \rho(\mathbf{r})P_s(\mathbf{r}|\mathbf{r}+\mathbf{R},\Delta)\;d\mathbf{r}\,. \tag{7.3}$$

Combining equations 7.2 and 7.3, the NMR signal amplitude is:

$$E(\mathbf{g},\Delta) = \int \bar{P}_s(\mathbf{R},\Delta)\exp[i\gamma\delta_G\mathbf{g}\cdot\mathbf{R}]d\mathbf{R}\,. \tag{7.4}$$

Conveniently, the gradient pulse power is defined by wavevector $\mathbf{q}$:

$$\mathbf{q} = \frac{\gamma\delta_G\mathbf{g}}{2\pi}, \tag{7.5}$$

such that the NMR signal amplitude is:

$$E(\mathbf{q},\Delta) = \int \bar{P}_s(\mathbf{R},\Delta)\exp[2\pi i\mathbf{q}\cdot\mathbf{R}]d\mathbf{R}\,. \tag{7.6}$$

By maintaining echo time constant as $\mathbf{q}$ is incremented, relaxation time effects on NMR signal are eliminated, enabling the ensemble-averaged propagator to be obtained from:

$$\bar{P}_s(\mathbf{R},\Delta) = \int E(\mathbf{q},\Delta)\exp[-2\pi i\mathbf{q}\cdot\mathbf{R}]d\mathbf{q}\,. \tag{7.7}$$

Accordingly, displacement propagators can be acquired using PFG-NMR, by measuring signal intensity, E, as a function of $\mathbf{q}$, where $\mathbf{q}$-space is usually sampled from $-\mathbf{q}_{max}$ to $+\mathbf{q}_{max,}$ with fixed increment $\Delta\mathbf{q}$. Sampling from negative to positive ensures that the direction of displacements can be determined. The maximum displacement that can be observed is dependent upon the density of points sampled, such that the propagator width ($-\mathbf{r}_{max}$ to $+\mathbf{r}_{max}$) is given by $1/\Delta\mathbf{q}$ and the displacement resolution is given by $\Delta\mathbf{r} = 1/(2|\mathbf{q}_{max}|)$ (Callaghan, 1991, 2011; Barrie, 2000).

To date, globally-averaged propagators have been used for characterising flow and transport heterogeneities in petrophysical applications (Waggoner and Fukushima, 1996; Johns *et al.*, 2003; Scheven *et al.*, 2005; Mitchell *et al.*, 2008; Hussain *et al.*, 2010). Spatially-resolved propagators additionally enable the detection of localised flow inhomogeneities. This is advantageous, considering the naturally-heterogeneous structures inherent to rock samples. Spatially-resolved propagators (Scheenen *et al.*, 2000; Windt *et al.*, 2007; de Kort *et al.*, 2018) can be attained by combining the displacement-encoded PFG experiments used to acquire $\mathbf{q}$-space, with an imaging experiment to acquire $\mathbf{k}$-space – subsequent Fourier transformation of the combined $\mathbf{q}$,$\mathbf{k}$-space yields a spatially-resolved propagator.

In this work, a 1D axially-resolved propagator was recorded – for which **k**-space was sampled using a read gradient. A 13-interval alternating pulsed-gradient stimulated echo (APGSTE) sequence was used for the displacement-encoding PFG experiment (see section 2.3.2). This particular PFG sequence was selected as it compensates for the phase errors introduced by internal magnetic field gradients often present in porous media (Cotts *et al.*, 1989; Leu *et al.*, 2005). In addition, the stimulated-echo-based experiment is advantageous considering the T_2 of fluids in porous media are often short, relative to their T_1 values. This APGSTE sequence was further followed by a RARE CPMG train, providing axially-resolved, T_2-sensitive propagator measurements. This T_2-senstivity offers the potential for an additional contrast mechanism within a multicomponent fluid system. A timing diagram of the sequence used in this work is illustrated in Fig. 7.4.

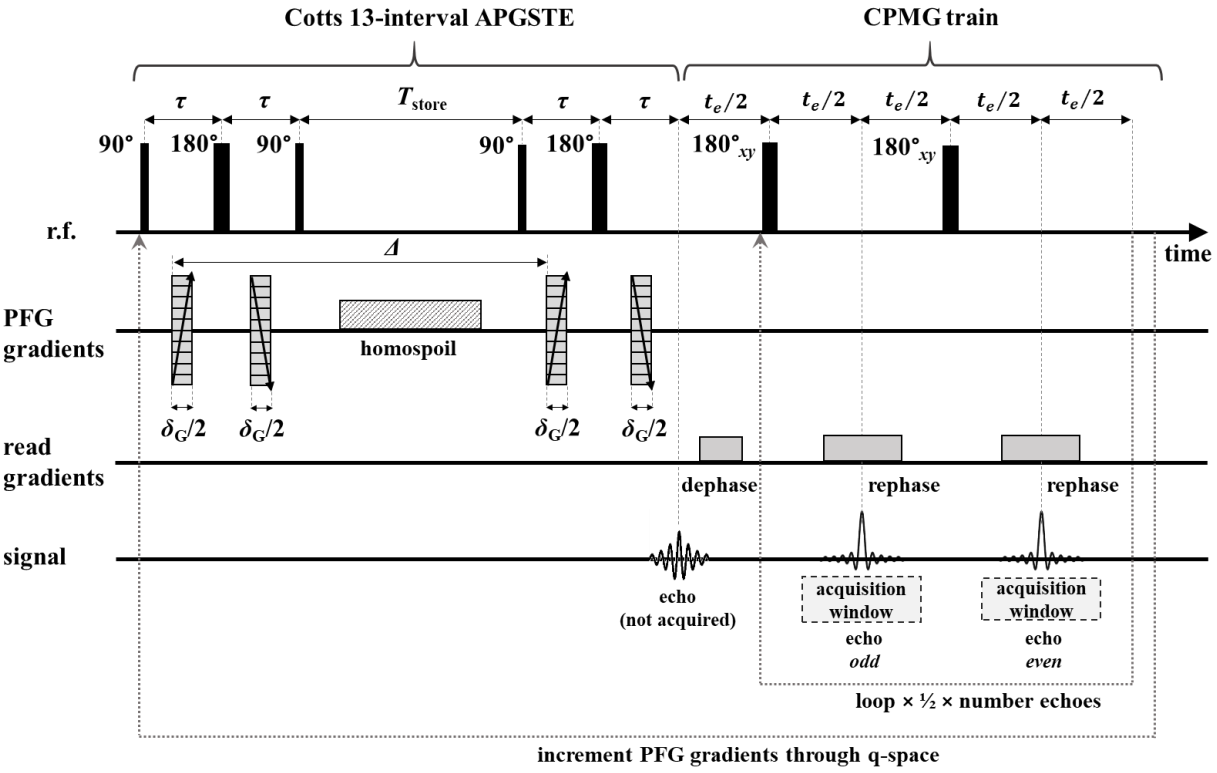

Figure 7.4. APGSTE-RARE sequence for axially-resolved, T_2-sensitive propagators – a 13-interval APGSTE followed by a CPMG train, with imaging read gradients. $\boldsymbol{\tau}$ is PFG half-interecho time; 180° and 90° are the r.f. pulse tip angles, T_{store} is stimulated echo storage time, Δ is observation time, $\delta_G/2$ is duration of each pulsed gradient, t_e is CPMG interecho time. Adapted from de Kort *et al.* (2018).

Figure 7.4 highlights that the APGSTE-RARE sequence separately acquires odd and even echoes within the CPMG train. For each odd-even echo pair, a Hermitian symmetry exists in the phase development, resulting from the preceding APGSTE experiment (Ahola *et al.*, 2006). Prior to recombining the odd and even datasets, during data processing, it is thus necessary for the **q**-space of the odd and even echoes to be flipped about $\mathbf{q} = 0$ m^{-1}, and hence for propagators to be acquired symmetrically in **q**-space. This odd/even dataset flipping is conducted following a zeroth-order phase correction, applied by optimising the phase for the maximum intensity point in each dataset. A two-dimensional Fourier transformation in $\mathbf{k}_{read}$ and **q** is next applied, followed by a first order phase correction to the resulting spatially-resolved

propagator (de Kort *et al.*, 2018). Analysis of the rate of signal decay for the resultant axially-resolved propagators along the CPMG train can next be used for obtaining T_2-resolved propagators.

7.2.2.3 NMR Measurement Protocol

NMR measurements were acquired at each core flood endpoint, and continuously throughout each flood. NMR spectra and relaxation time measurements were acquired to monitor pore-filling conditions and quantify core saturations throughout the floods. PFG diffusion measurements, measured using a series of observation times, were acquired to probe for changes in restricted diffusion (and thus changes in oil ganglia size) post-EOR, relative to post-secondary waterflooding (see section 2.4.5). Finally, axially-resolved propagator measurements were acquired to compare the mobilities of hydrocarbon and aqueous phases post-secondary waterflooding and post-EOR. This suite of NMR experiments was acquired as follows:

- at each flooding stage endpoint (acquired under no-flow) – NMR spectra, L-T_1-T_2, spectrally-resolved T_2 and PFG diffusion measurements (with varied observation times);
- during each core flooding stage (acquired dynamically) – NMR spectra and L-T_1-T_2;
- at the fully-brine saturated (S_w = 1), post-secondary waterflood and post-EOR endpoints (acquired under flow) – T_2-sensitive axially-resolved propagators.

The experimental parameters and pulse sequences used for all NMR acquisitions are discussed in section 7.2.2.4.

The very low flowrates required for core floods to be reservoir-representative (~ 1ft day^{-1}) prevented propagators from being acquired dynamically during the floods. At such flowrates, propagators are dominated by self-diffusion effects and displacements from flow cannot be detected. This can easily be demonstrated through back-of-the-envelope calculations comparing the 1D axial root-mean-square displacement from unrestricted self-diffusion, s_{diff}, and the displacement from flow, s_{flow} (assuming displacement only occurs along the applied flow direction), for:

$$s_{\text{diff}} = \sqrt{2Dt} \tag{7.8}$$

$$s_{\text{flow}} = u_{\text{int}} t \tag{7.9}$$

where D is species self-diffusivity, t is diffusion time.

Considering a brine-saturated core ($D_{\text{core-brine}}$ ~ 1.65 × 10^{-9} m^{2}s^{-1} (section 7.2.1.3)), using typical propagator observation times applied in rock cores (100-2000 ms, (Gladden and Sederman, 2017)), u_{int} >> 1 ft day^{-1} is required for propagator measurements to display greater sensitivity to s_{flow} than s_{RMS}.

Screening experiments at S_w = 1 demonstrated that propagators were sensitive to s_{flow} at injection flowrates Q_{inj} = 3 and 6 ml min^{-1} (equivalent to u_{int} = 50 ft day^{-1}, 100 ft day^{-1}). These flowrates correspond to shear rates greater than the assumed $\dot{\gamma}_{\text{onset}}$ for the HPAM solution (calculation based upon the expected shear rate, determined using Eq. 6.6, section 6.2.1.2). To preserve reservoir-representative

flooding conditions, propagators were thus acquired at core flood endpoints, after the reference relaxometry and diffusion datasets at no-flow were acquired. This protocol assumes that elevated flowrates do not significantly alter core saturations. Whilst prior research suggests such flowrates impart minimal change to core saturations post-waterflooding, greater effects would be expected for a HPAM-saturated core (Mitchell *et al*. 2016). To verify that no further saturation changes occurred following the propagator measurements post-waterflood and post-EOR, additional relaxation time, spectral and diffusion reference measurements were acquired (at no-flow conditions) and all produced volumes were collected to quantify any produced oil.

7.2.2.4 NMR Methods and Parameters

All NMR experiments were conducted at room temperature (20 ± 1 °C) in a 2 T (85 MHz for ^{1}H nuclei) horizontal bore superconducting magnet, controlled by a Bruker AV spectrometer. A 60 mm inner diameter r.f. birdcage coil, tuned to 85.2 MHz was used for excitation and signal detection. Spatial resolution along the direction of superficial flow (z) was achieved by applying a magnetic field gradient, capable of a maximum gradient strength, G_{max} = 10.7 G cm^{-1}, along the z-direction.

Hard r.f. pulses were used for all NMR experiments. Pulse durations, t_{90} and t_{180}, were calibrated prior to the start of each flood. All experiments at S_w = 1 were acquired using t_{90} = 20.5 µs, t_{180} = 41.0 µs; during primary drainage using t_{90} = 17.7 µs, t_{180} = 35.4 µs; during secondary waterflooding using t_{90} = 19.1 µs, t_{180} = 38.2 µs; and during EOR flooding using t_{90} = 19.5 µs, t_{180} = 39.0 µs. Differences in optimal pulse lengths are likely to have resulted from differing brine saturations at each state (see section 5.2.2.5).

NMR spectra were acquired with RD = 8 s, and NS = 8, resulting in an acquisition time, t_{ACQ}, less than 2 min. T_2-CPMG datasets were acquired with 32 variable echo-loop counter times, in the range N_{vc} = 2 – 4096, with t_E = 3.6 ms, NS = 8 and RD = 8 s, giving t_{ACQ} = 51 min.

Spatially-resolved L-T_1-T_2 were acquired using 128 pixels with FOV = 82 mm, giving a slice resolution of 0.64 mm pixel^{-1}. Sixteen t_{vd} variable delay values in the range t_{vd} = 1 ms – 8 s were used, and 1024 echoes with inter-echo time t_E = 3.6 ms were recorded along the echo train. Using NS = 8 and RD = 8 s resulted in t_{ACQ} = 30 min. L-T_1-T_2 measurements were processed using the methodologies outlined in section 3.2.2.2 and 5.2.2.4. Herein, an internal gradient correction was not applied as the pore size distribution obtained from MIP suggested that the core pore dimensions were not in the appropriate preasymptotic LOC regime to facilitate valid application of the internal gradient correction technique (Mitchell *et al.*, 2010a) – see section 2.4.6.

Diffusion datasets were measured using the 13-interval alternating pulsed-gradient stimulated echo (APGSTE) sequence. Diffusion datasets were acquired with Δ in the range 20 – 1000 ms. Trapezoidal gradient pulses were used with duration $\delta_G/2$ = 4 ms, gradient ramp time, t_ε = 150 µs, gradient stabilisation time, t_{GST} = 250 µs and fixed half-interecho time, τ = 5 ms. Using RD = 8 s and NS = 8,

resulted in t_{ACQ} varying between 35 – 43 min (dependent upon Δ). For experiments with Δ > 50 ms, the gradient amplitude was ramped linearly from G_z = 0.056 G cm^{-1} to 10.165 G cm^{-1} in 32 increments. For $\Delta \leq 50$ ms, insufficient attenuation was achievable with gradients applied only along *z*. Accordingly, diffusion-encoding gradients were used along *x*, *y* and *z*, resulting in a spatially-averaged $G_R = \sqrt{G_x^2 + G_y^2 + G_z^2}$, for which the maximum deliverable gradient strength along each gradient coil is 10.7 G cm^{-1}. Therein, gradient amplitudes were ramped linearly from G_R = 0.098 G cm^{-1} to 17.606 G cm^{-1} in 32 increments. A homospoil gradient was applied during the stimulated echo storage with duration, t_{homo} = 3 ms, and gradient strength $G_{x,y,z}$ = 5.0 G cm^{-1} along the three axial directions.

Axially-resolved, APGSTE-CPMG propagators were acquired at Q_{inj} = 0, 3 and 6 ml min^{-1}. Both the slice and flow encoding directions were parallel to the superficial flow, along *z*. Four observation times (250 ms, 500 ms, 1000 ms and 1500 ms) were used to probe motion at different length scales: at short Δ, the propagator is governed by flow and diffusion within single pores; as Δ increases, the propagator reflects motion between pores. At the upper end, Δ was selected to maximise diffusion encoding time while maintaining a useful SNR.

The APGSTE block was acquired with 128 **q**-points, sampled from $-\mathbf{q}_{max}$ to $+\mathbf{q}_{max}$ in equidistant steps. A pair of flow-encoding gradients of duration $\delta_G/2$ and strength **g** were used, with values in the range 1.8 ms $\leq \delta_G/2 \leq$ 7.4 ms and $0.9\mathbf{G}_{max} \leq \mathbf{g} \leq 0.98\mathbf{G}_{max}$, depending upon the field of flow (FOF) and resolutions ($\Delta\mathbf{r}$) required to optimally capture the propagators at each observation time and flow conditions. Across all flow and observation times, the FOF and resolutions were in the range: 1.4 mm $\leq$ FOF $\leq$ 4 mm, and 11 µm $\leq \Delta\mathbf{r} \leq$ 32 µm. Additional constraints to $\delta_G/2$ and **g** included: minimising the echo time to limit relaxation time effects and ensuring the δ_G/Δ ratio satisfied the narrow gradient pulse approximation. A homospoil gradient during the stimulated echo storage was applied with duration, t_{homo} = 10 ms, and gradient strength $G_{x,y,z}$ = 5.4 G cm^{-1} along the three axial directions. In the $\mathbf{k}_{read}$ dimension, 128 points were acquired with FOV = 76 mm, giving a slice resolution of 0.6 mm pixel^{-1}. The CPMG train was acquired with 256 echoes and a half interecho time, t_e = 3 ms. Using *NS* = 4 and *RD* = 1.5 s resulted in t_{ACQ} varying from 28 – 37 min (dependent upon Δ).

For all pulse sequences used, three repeat experiments were conducted under fixed, no-flow conditions to determine the random error associated with each technique.

The total experimental time (including continuous flood tracking, end-point reference measurements, end-point propagator experiments and magnet set-up (pulse and sequence optimisations, CFS set up)) was ~4 weeks.

7.3 Results and Discussion

The results and discussion are presented as follows: first, the volumetrically-determined oil recoveries; next, the NMR spectral and relaxation time datasets; and finally, the PFG diffusion and propagator measurements.

7.3.1 Volumetrically-determined core saturations

The core saturations at core flood endpoints (see Table 7.1) were determined from the produced volumes at each stage, with respect to the gravimetrically-determined core P.V. (see section 7.2.1.1).

Table 7.1 Volumetrically-determined saturations at flooding endpoints.

State	Brine saturation, S_w [-]	Oil saturation, S_o [-]
$S_w = 1$	1	0
S_{wir}	0.07 ± 0.03	0.93 ± 0.03
post-waterflood	0.61 ± 0.06	0.39 ± 0.06
post-EOR flood	0.65 ± 0.06	0.35 ± 0.06

The uncertainties in the saturations presented in Table 7.1 consistently increase with core flooding progression. This is due to the error propagated in building calculations upon saturations determined at preceding flooding endpoints.

Table 7.1 demonstrates a total recovery of 62.4% of the original oil in place (OOIP) was achieved, of which 4.3% was from polymer-EOR – the polymer delivers an incremental recovery of 10.3%, after secondary waterflooding. These results agree with typical recovery factors (RFs) reported in the literature for HPAM EOR (see section 6.1.1).

7.3.2 NMR Relaxation Time and Spectral Measurements

This section presents and discusses the NMR spectral and relaxation time measurements acquired at each flooding endpoint, and continuously throughout the secondary and tertiary flooding procedures.

Interpretation of the relaxation time datasets follows the same approach as in Chapters 5 and 6. This is based upon the pore size and surface wetting information that can be obtained from NMR relaxation time analysis. The key statements summarising the essential principles by which these datasets can be interpreted were previously outlined in section 5.4. Throughout this section, ‘long’ and ‘short’ relaxation time descriptors are used to refer to the slow- and fast-relaxing components, respectively.

7.3.2.1 L-T_1-T_2 Measurements – a comparison of core flooding endpoints

Figure 7.5 presents the L-T_1-T_2 measurements acquired at each flooding endpoint, presented as: globally-averaged 2D T_1-T_2 correlations, L-T_1 and L-T_2 maps. In addition, 1D T_1 and T_2 distributions (obtained through projection of globally-averaged 2D T_1-T_2 datasets) are presented for each saturation state. Only signal regions pertaining to the core, within each L-T_1-T_2 measurement, are considered.

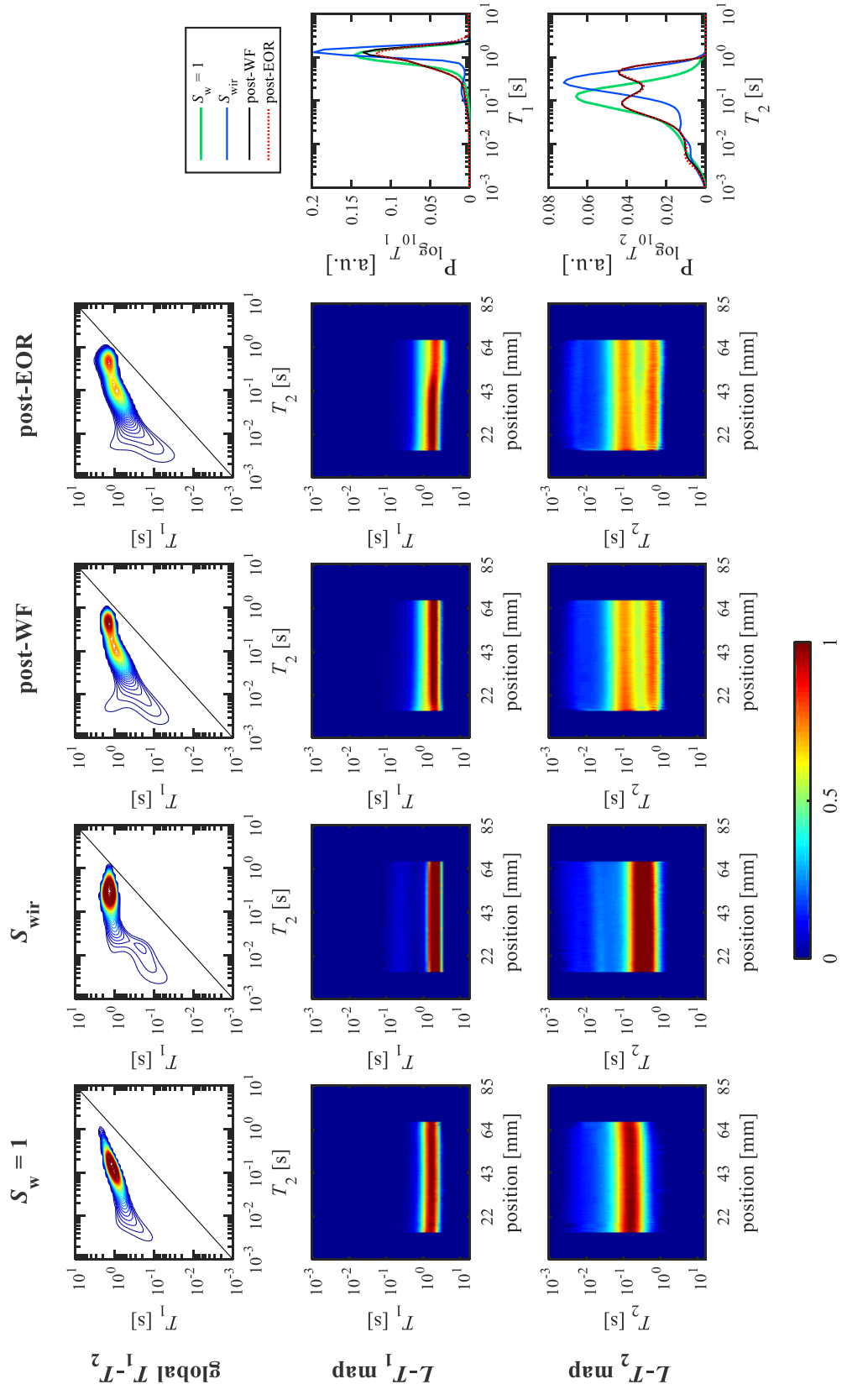

Figure 7.5. L-T_1-T_2 datasets at each flooding endpoint (S_w = 1, S_{wir}, post-secondary waterflooding (denoted post-WF), post-EOR). For each dataset, a globally-averaged T_1-T_2 correlation, an L-T_1 and L-T_2 axial map are presented. Flooding endpoints are presented along four columns, dataset types along three rows. Each dataset type is presented on the same colour scale, normalised to that at S_w = 1. Global T_1 and T_2 distributions (projected from the global T_1-T_2 correlations) are also presented.

At S_w = 1, the T_1-T_2 correlation displays broad distributions in both dimensions, with all signal regions located away from the $T_1 = T_2$ diagonal; the L-T_1 and L-T_2 maps display an axially-uniform response. At S_{wir}, the T_1-T_2 correlation is still broad, maintaining an axially-homogeneous response in the L-T_1 and L-T_2 maps. The T_1-T_2 correlation shows a shift in signal now predominantly occupying longer T_1 and T_2 times. This is clearly observed in the overlaid 1D relaxation time distributions and L-T_1 and L-T_2 maps. In addition, a low-intensity signal appears at short T_1 (on the order of 100 ms), and the signal at long T_1, T_2 values (on the order of 1 s) now contacts the $T_1 = T_2$ diagonal.

Post-secondary waterflooding, the core maintains an axially-homogeneous response. The T_1-T_2 correlation map further broadens and displays two peaks – the greatest contrast is observed in T_2. Signal at long T_1, T_2 values continues to contact the $T_1 = T_2$ diagonal, whilst signal at shorter T_1, T_2 values is furthest from the $T_1 = T_2$ diagonal. Post-EOR, no further change is observed. At all flooding endpoints, no clear discrete contrast in the T_1-T_2 nor projected T_1 dimension exists. The greatest contrast is achieved in the projected T_2 dimension.

The results presented in Fig. 7.5 are hereby discussed and interpreted. At S_w = 1 the core is saturated in a single phase and thus the 1D T_1, T_2 distributions reflect the core pore size distributions (see section 5.4). Herein, this indicates a broad, unimodal pore size distribution, in agreement with the MIP characteristics (Fig. 7.1). The axial-uniformity in L-T_1 and L-T_2 suggest the core displays axially-homogeneous pore structure and wetting characteristics.

For a water-wet core at S_{wir}, it is expected that: hydrocarbon resides as isolated globules in the large pore centres; and brine fills the smallest pores, maintaining a continuous wetting film throughout the core. In Chapters 5 and 8 (sections 5.4, 8.3.2.2), at S_{wir} two discrete signals within the T_1-T_2 maps were observed – a high-intensity signal, located on the $T_1 = T_2$ diagonal at long T_1, T_2 (assigned to hydrocarbon); and a low-intensity signal with elevated T_1/T_2, indicative of strong interaction strengths, at short T_1, T_2 (assigned to wetting-brine). The system materials tested herein are near-identical to those studied in Chapters 5 and 8 – water-wet sandstone, equivalent brine composition and a medium-chain alkane. It is thus expected that similar physical conditions, and hence T_1-T_2 responses, would have occurred. Although Fig. 7.5 demonstrates that some expected T_1-T_2 trends are observed (shift of high -intensity signal to longer T_1 and its contacting the $T_1 = T_2$ diagonal, the appearance of a low-intensity tail at short T_1, with elevated T_1/T_2 ratio); critically, the T_1-T_2 correlation does not display discrete signal regions. Herein it is therefore not possible to unambiguously assign signal to either aqueous- or hydrocarbon saturations from T_1-T_2 alone. This lack of T_1-T_2 contrast is attributed to greater pore sizes than those in Chapter 5 (evidenced in the MIP datasets: Fig. 7.1, Fig. 5.6). Larger pores would result in the wetting phase displaying a more bulk-liquid-type response, resulting in longer relaxation times and a reduced contrast in T_1 and T_2.

Post-secondary waterfloods and EOR, the lack of change in T_1-T_2 between these endpoints suggests little further change in pore saturation environments. The uniformity in L-T_1, L-T_2 maps suggest axially-

homogeneous pore saturation environments. Based upon results in Chapters 5-8, it is expected that the high-intensity signal at longer relaxation times (contacting $T_1 = T_2$) likely pertains to hydrocarbon and the low-intensity signal at shorter relaxation times (elevated T_1/T_2), to wetting brine. However, again, insufficient T_1-T_2 contrast means signal cannot be assigned unambiguously to aqueous- or hydrocarbon-phases – an additional contrast mechanism is required.

7.3.2.2 NMR spectra – a dynamic saturation measurement

Figure 7.6 presents the NMR spectra dynamically acquired during primary drainage, secondary waterflooding and EOR flooding. Chemical shift was recorded in Hz and then converted to ppm for plotting.

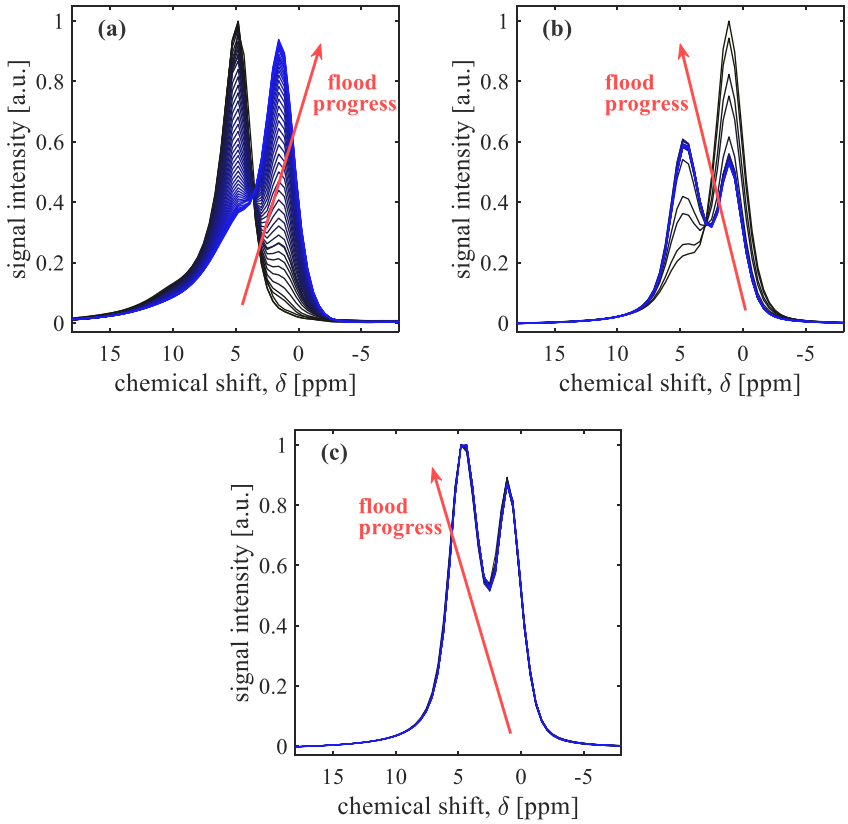

Figure 7.6. Spectra acquired during **(a)** primary drainage, **(b)** secondary waterflooding, **(c)** EOR. Spectra are normalised to the maximum point of the first spectrum in each flood, plotted in black pre-flooding, transitioning to blue post-flooding. Arrows denote the shifting maximum signal with flood progression.

Figure 7.6 demonstrates that the NMR spectra consist of two peaks, consistently at 4.8 ppm and 1.3 ppm – this chemical shift difference is in line with that expected for a water peak, alkyl -CH_2 and -CH_3 group peaks (Callaghan, 1991). During primary drainage (Fig. 7.6a), spectra transition from a single peak at 4.8 ppm, to two peaks – a high intensity peak at 1.3 ppm, with a low-intensity shoulder at 4.8 ppm. During secondary waterflooding (Fig. 7.6b), two-peaks are maintained throughout. With increasing water injection, the 4.8 ppm peak increases in intensity, that at 1.3 ppm decreases. During polymer EOR (Fig. 7.6c), a small growth and reduction in the 4.8 ppm and 1.3 ppm peaks are observed, respectively.

These results are hereby discussed and interpreted. Considering Fig. 7.6a, the core is known to start primary drainage fully-brine saturated. The peak set at 4.8 ppm is thus assigned to brine. Similarly, the peak at 3.5 ppm, increasing in intensity, is assigned to dodecane. This peak assignment is translated to Figs. 7.6b and 7.6c. Accordingly, Fig. 7.6b demonstrates the increasing brine saturation, and reducing dodecane saturation during secondary waterflooding; and Fig. 7.6c demonstrates only small changes to core saturation during polymer-EOR.

This spectral contrast was used to obtain global saturation measurements. This was achieved by producing model NMR spectra: the original spectral lineshape of the fully-brine saturated core (acquired at $S_w = 1$) was linearly summed with the same spectral lineshape, offset to lie in the chemical shift location assigned to dodecane. By varying the fractional contribution of each peak, NMR spectra were simulated for a range of saturations – including scaling for *HI* (see section 7.2.1.3). The simulated spectra were fitted to the experimentally acquired spectra, optimised using a least-squares fitting approach. The NMR-determined saturations at each flooding endpoint are presented in Table 7.2. The errors are based upon the uncertainties in the fits, *HI* and random errors in NMR spectral measurements.

Table 7.2 Saturations at flooding endpoints, from NMR spectra.

State	Brine saturation, S_w [-]	Oil saturation, S_o [-]
S_{wir}	0.10 ± 0.05	0.90 ± 0.05
post-waterflood	0.597 ± 0.009	0.403 ± 0.009
post-EOR flood	0.601 ± 0.009	0.399 ± 0.009

Table 7.2 demonstrates that within measurement uncertainties, spectrally-determined saturations agree with volumetrically-determined saturations (Table 7.1). Using the same approach, continuous saturation measurements during secondary waterflooding and EOR were obtained, as presented in Fig 7.7.

Figure 7.7a demonstrates that most oil is recovered during the first 0.5 PV of injected brine. As water breakthrough occurs, little further oil is recovered – attributed to the formation of a preferential pathway of least resistance for water flow, such that no new core regions are swept.

Figure 7.7b demonstrates that polymer EOR yields only an incremental recovery, most of which is achieved within the first P.V. of injected fluids – coincidental with the polymer slug. The subsequent brineflush does not further increase oil recovery. Across both floods, the progressively increased injection flowrates do not impact the core saturation.

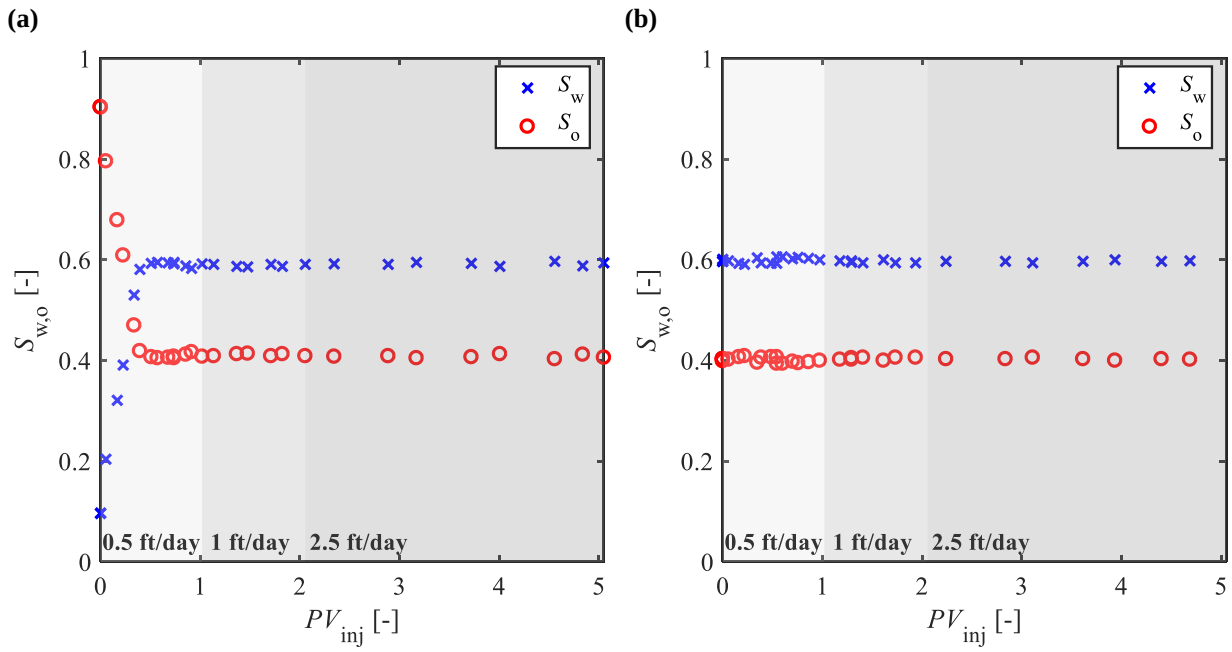

Figure 7.7. Core brine and oil saturations (S_w, S_o) during **(a)** secondary waterflooding, **(b)** EOR flooding. Obtained from NMR spectra.

7.3.2.3 Spectrally-resolved T_2 at flooding endpoints

Figure 7.5 demonstrated that the greatest contrast in the T_1-T_2 correlation maps was achieved in T_2. Figure 7.6 demonstrated that in this core system, sufficient chemical shift contrast exists to facilitate brine/dodecane signal assignment.

Spectrally-resolved, standard T_2 CPMG measurements have both T_2, and chemical shift contrast mechanisms. This section presents global spectrally-resolved T_2 datasets, acquired at flooding endpoints, with a view to enabling reliable brine and dodecane signal assignment in the T_2-dimension. Figure 7.8 presents the NMR spectra with T_2 decay at each flooding endpoint.

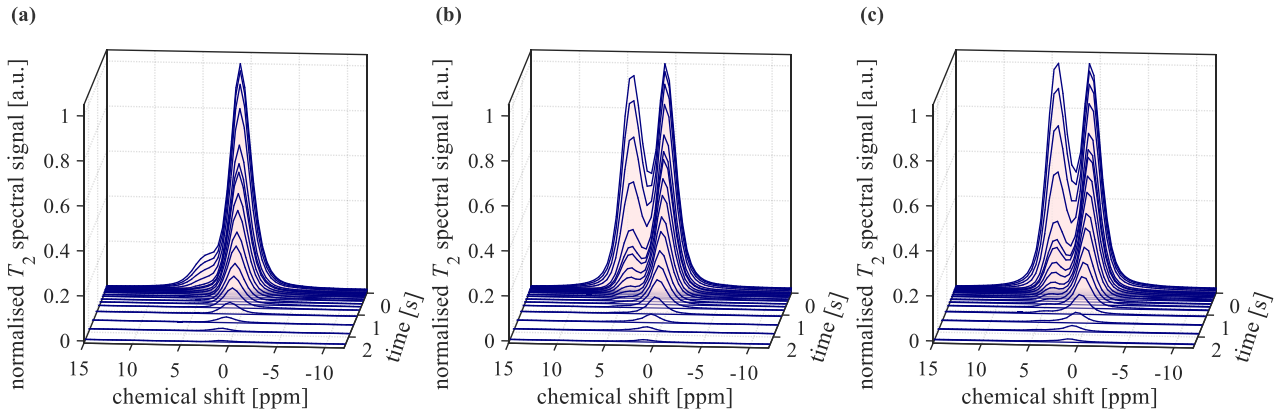

Figure 7.8. Spectra acquired at CPMG variable delays: **(a)** post-primary drainage; **(b)** post-secondary waterflooding; **(c)** post-EOR. Spectral intensities are scaled to the first spectrum in each echo train.

At all three saturations, spectra acquired at the shortest CPMG delay time show two peaks (at 4.8 ppm and 1.3 ppm) – consistent with Fig. 7.6. With increasing CPMG delay time, the two peaks display differing T_2 decays. Based upon the peak assignment in section 7.3.2.2, it can be inferred that brine has a faster T_2 decay than dodecane. By applying the same simulated peak-fitting strategy, as in section 7.3.2.2, the dodecane and brine peaks along the spectral-CPMG trains were isolated.

Signal segmentation along the spectral-CPMG train, together with 1D inversion protocols, allowed for species-specific T_2 distributions to be obtained – shown in Fig. 7.9. The total T_2 distributions, obtained by summation of the spectrally-segmented signals, are presented overlaid.

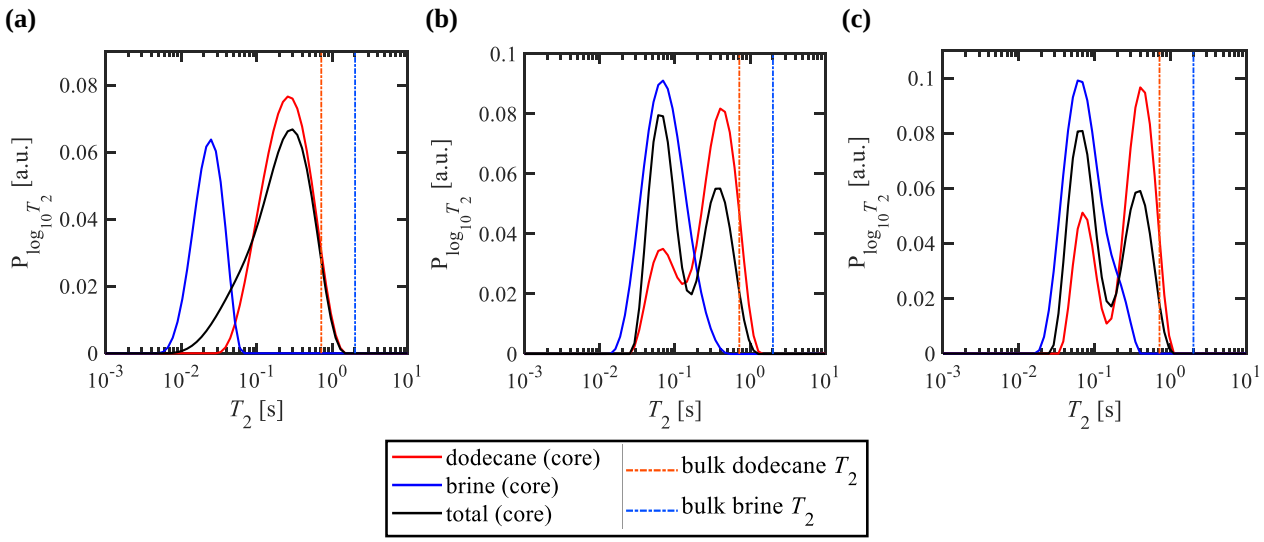

Figure 7.9. Dodecane and brine T_2 distributions obtained *via* spectral segmentation and inversion of CPMG datasets: **(a)** post-primary drainage; **(b)** post-secondary waterflood; **(c)** post-EOR. Total distributions are obtained from summed spectrally-segmented signal. Each probability distribution is independently normalised. Bulk liquid T_2 are shown for comparison.

The accuracy of the spectral segmentation and subsequent inversion can be assessed by comparing the total T_2 distribution (through summation, post-spectral segmentation) with the total T_2 distribution (obtained without spectral segmentation). This is presented in Fig. 7.10.

Figure 7.9 demonstrates that at all saturations, the shortest T_2 values pertain to brine, the longest T_2 values to dodecane. For all saturations, brine displays a monomodal peak with T_2 values several orders of magnitude smaller than that of bulk liquid brine. In contrast, dodecane shows a broad monomodal peak at S_{wir}, and a bimodal T_2 distribution post-secondary waterflooding and post-EOR (with the greatest population at long-T_2). The dodecane short T_2-component coincides with the brine T_2, the dodecane long-T_2 component coincides with bulk liquid dodecane T_2. Post-spectral segmentation, the species-specific T_2 distributions are broader than the total T_2 – attributed to the reduced signal-to-noise ratio in the signal-segmented echo trains, which can impact the inversion and result in broader distributions.

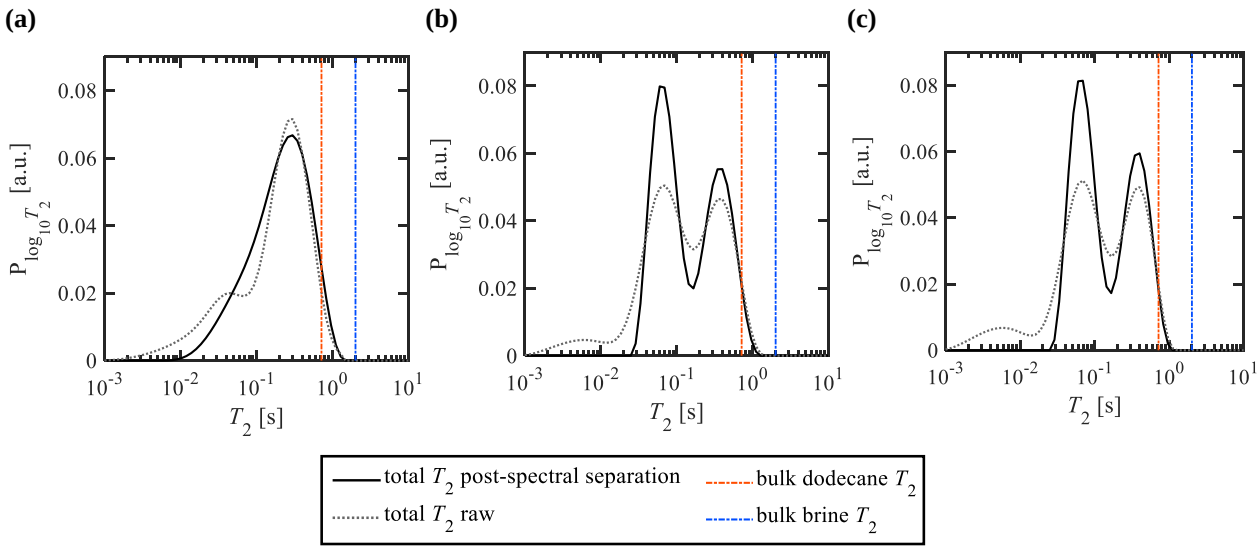

Figure 7.10. T_2 distributions obtained by total signal summation post-spectral separation, and from raw non-segmented signal: **(a)** post-primary drainage; **(b)** post-secondary waterflood; **(c)** post-EOR. Each probability distribution is independently normalised. Bulk liquid T_2 are shown for comparison.

Figure 7.10 demonstrates that for T_2 > 20 ms, T_2 distributions obtained by summation of spectrally segmented signal closely match those from the raw T_2 datasets. For T_2 < 20 ms (henceforth denoted short-range T_2 values), spectral segmentation results in information loss. Accordingly, this alters the relative peak populations at mid-range to long-range T_2 values (where mid-range refers to 20 ms < T_2 < 200 ms; long-range refers to T_2 > 200 ms). Table 7.3 presents a comparison of log-mean T_2 values extracted using both techniques, together with the segmented oil and brine T_2 values.

Table 7.3. Log-mean T_2 ($T_{2,LM}$) from CPMG datasets at flooding endpoints. $T_{2,LM}$ extracted from: non-spectrally segmented data (total T_2 (raw)); individual signal summation post-segmentation (total T_2 (segmented)); individual segmented signals (dodecane T_2, brine T_2). $T_{2,LM}$ are reported partitioned as: short-range (T_2 < 20 ms), mid-range (20 ms < T_2 < 200 ms), long-range (T_2 < 200 ms). Uncertainties calculated as in section 3.2.2.3.

		$T_{2,LM}$ [s] *(short-range)*	**$T_{2,LM}$ [s]** *(mid-range)*	**$T_{2,LM}$ [s]** *(long-range)*
post-primary drainage	total T_2 (raw)	-	0.025 ± 0.002	0.27 ± 0.07
	total T_2 (segmented)	-	-	0.19 ± 0.03
	dodecane T_2	-	-	0.24 ± 0.05
	brine T_2	-	0.022 ± 0.003	-
post-secondary waterflood	total T_2 (raw)	0.005 ± 0.001	0.07 ± 0.01	0.38 ± 0.07
	total T_2 (segmented)	-	0.07 ± 0.01	0.38 ± 0.06
	dodecane T_2	-	0.07 ± 0.01	0.39 ± 0.07
	brine T_2	-	0.07 ± 0.02	-
post-EOR	total T_2 (raw)	0.005 ± 0.001	0.07 ± 0.01	0.38 ± 0.07
	total T_2 (segmented)	-	0.07 ± 0.01	0.38 ± 0.06
	dodecane T_2	-	0.07 ± 0.01	0.40 ± 0.06
	brine T_2	-	0.07 ± 0.02	-

The results in Table 7.3 demonstrate excellent agreement in mid-range and long-range $T_{2,LM}$, extracted from spectrally-segmented and raw T_2 datasets. Post-primary drainage, a difference in $T_{2,LM}$ values occurs – resulting from insufficient contrast in the spectrally-segmented T_2 distribution (see Fig. 7.10a). However, the independent brine and dodecane signals therein display excellent $T_{2,LM}$ agreement with the raw-T_2 distribution. Despite the loss of information at short-range T_2, the $T_{2,LM}$ analysis confirms that this spectral segmentation method can be used for unambiguously assigning T_2 responses to either brine or dodecane, based upon chemical shift.

Combining this spectral-T_2 analysis with the L-T_1-T_2 results in Fig. 7.5, it can be concluded that the short-T_2 signal primarily belongs to brine, with relaxation times far from its bulk value and an elevated T_1/T_2 ratio – confirming that brine occupies the smallest pores, acting as a wetting film throughout the pore space. Likewise, all long-range T_2 belongs to dodecane exhibiting a near-bulk liquid response, with $T_1/T_2 \approx 1$ – confirming dodecane occupies the pore centres as non-wetting, isolated ganglia. In addition, spectral-T_2 analysis demonstrates that dodecane additionally yields a shortened T_2 response in the mid-T_2 region. From Fig. 7.5, this region is known to have an elevated T_1/T_2 ratio. This suggests that some dodecane could be in surface contact.

7.3.3 NMR PFG Propagator and Diffusion Measurements

This section presents and discusses the NMR propagator and diffusion measurements acquired at S_w = 1, post-secondary waterflooding and post-EOR flooding.

7.3.3.1 Propagator core structure-flow analysis at $S_w = 1$

Figure 7.11 presents reference propagators acquired at S_w = 1, at Q_{inj} = 3 and 6 ml min^{-1}, for observation times, Δ = 250, 500, 1000 and 1500 ms. Globally-averaged propagators are presented at all observation times, axially-resolved propagators are presented at either flow extremes probed.

As observation time in Fig. 7.11a is increased, the propagator changes from a near-Gaussian shape, centred close to zero-displacement, towards a propagator with two distinct regions: a sharp stagnant peak at zero-displacement and a flowing region showing progressively increasing displacement with greater Δ. This is similarly observed in Fig. 7.11b, with starker separation between stagnant and flowing regions – first apparent at Δ = 250 ms. The greater flow displacements observed in Fig. 7.11b are expected – due to the increased injectant flowrate. These single-phase flow observations are consistent with the literature (Johns *et al.*, 2003; Gladden and Sederman, 2017). Fig. 7.11c,d demonstrates that at both extremes of fluid mobility probed, axially-uniform propagators (and hence flow characteristics) are observed in the core – agreeing with the axially-homogeneous pore structure observed with L-T_1-T_2 (section 7.3.2.1).

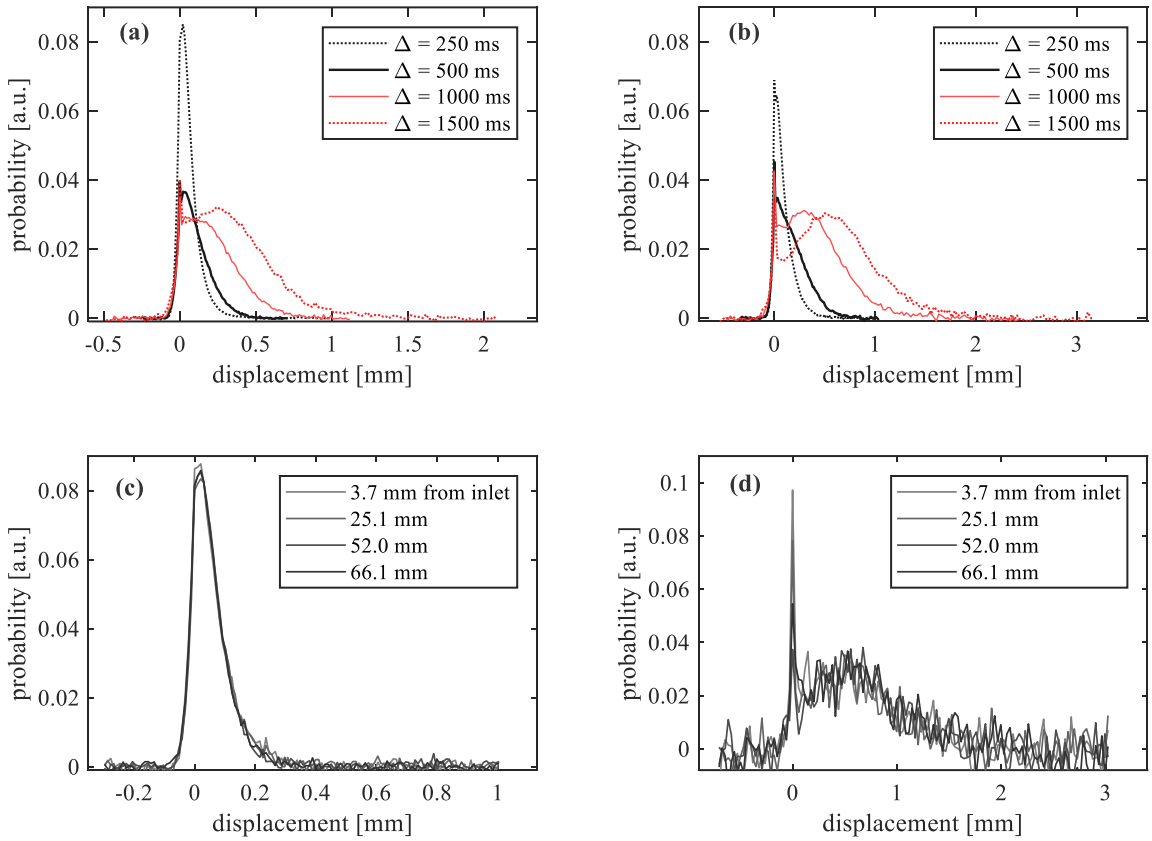

Figure 7.11. Globally-averaged propagators at S_w = 1. **(a)** Q_{inj} = 3 ml min^{-1}, **(b)** Q_{inj} = 6 ml min^{-1}, acquired using Δ = 250, 500, 1000 and 1500 ms. **(c)**, **(d)** present propagators at four axial positions (3.7 mm, 25.1 mm, 52.0 mm and 66.1 mm from the core inlet) – acquired at **(c)** Q_{inj} = 3 ml min^{-1}, Δ = 250 ms; **(d)** Q_{inj} = 6 ml min^{-1}, Δ = 1500 ms.

The accuracy of the propagators, as measures of displacement, was benchmarked against expected flow displacements. This was conducted for Q_{inj} and Δ conditions at which a clear separation in the diffusion and flow displacements existed within the propagators. The results are summarised in Table 7.4.

Table 7.4. Expected displacements from flow (s_{flow}) and diffusion (s_{diff}), compared with propagator-observed modal displacements ($s_{propagator\ (modal)}$). Percentage difference in s_{flow} and $s_{propagator\ (modal)}$ is reported. Expected displacements are calculated using Eqs. 7.8, 7.9.

Q_{inj} [ml min^{-1}]	Δ [ms]	s_{diff} [mm]	s_{flow} [mm]	$s_{propagator\ (modal)}$ [mm]	% difference s_{flow} - $s_{propagator}$
3	1500	0.070	0.263	0.266 ± 0.022	1.2
6	1000	0.057	0.350	0.327 ± 0.025	6.7
6	1500	0.070	0.525	0.546 ± 0.032	3.9

Table 7.4 demonstrates excellent agreement between the expected flow displacement and the modal propagator displacement from flow, within the resolution of the propagator measurements. This benchmarking exercise at S_w = 1 justified using the propagator as a displacement measurement in the subsequent multiphase systems.

7.3.3.2 The influence of HPAM-EOR on fluid mobilities – a propagator analysis

Figure 7.12 presents the globally-averaged propagators acquired at Q_{inj} = 3 and 6 ml min^{-1} for observation times in the range Δ = 250 ms – 1500 ms. At each flowrate and observation time, datasets are presented for: S_w = 1, post-secondary waterflooding and post-EOR. Figure 7.13 presents axially-resolved propagators from four slices along the core, post-secondary waterflooding and post-EOR – at either extremes of the mobilities probed (Q_{inj} = 3 ml min^{-1} at Δ = 250 ms, and Q_{inj} = 6 ml min^{-1} at Δ = 1500 ms). During acquisition of the propagator measurements, no further oil was produced in the effluent, and no change in spectral saturation was observed – for both post-secondary waterflooding and post-EOR states.

In Fig. 7.12, all propagators display both stagnant and moveable fluid regions. No change is observed between post-waterflooding and post-EOR flooding, suggesting that the mobility of pore fluids (wetting brine and isolated hydrocarbon ganglia) following EOR flooding protocols remain unchanged. The spatially-resolved propagators in Fig. 7.13 demonstrate axially-uniform displacements in the core under applied flow – both at post-secondary waterflooding and post-EOR.

The propagators post-waterflooding and post-EOR show stark differences with those at S_w = 1. Post-waterflood and post-EOR, a sharp, high-intensity peak in the stagnant region exists, and a low-intensity, broad peak exists in the moveable-fluid region. In contrast, at S_w = 1, the moveable-fluid displays a much greater intensity.

This behaviour can be explained from the propagator measurement, which was acquired as a propagator with a CPMG train (as highlighted in Fig. 7.4). Along the CPMG train, signal in the moveable-fluid region of the propagator decayed more rapidly than the signal in the stagnant-fluid region. This suggests that the moveable fluid region has a faster relaxation time (smaller T_2 constant) than the stagnant fluid region (larger T_2 constant). This was verified by comparing propagator measurements conducted at variable echo times, in which more rapid decay in the moveable-fluid region occurred with increased echo time (results not presented herein for brevity).

A change in relaxation time behaviours is expected when comparing a multicomponent environment to a single-phase environment (as shown in Fig. 7.5); that is, the T_1 and T_2 relaxation time characteristics, and thus relaxation time-weighting effects, differ post-waterflooding from those at S_w = 1.

In Fig. 7.12 the low intensities for the moveable-fluid in the propagators acquired post-waterflooding and post-EOR, result from greater relaxation time-weighting effects in the moveable-fluid compared to the stagnant fluid. These effects are further highlighted in Fig. 7.12 as the propagator measurements in all saturation states are each presented as a probability distribution, and thus each signal is normalised to unity.

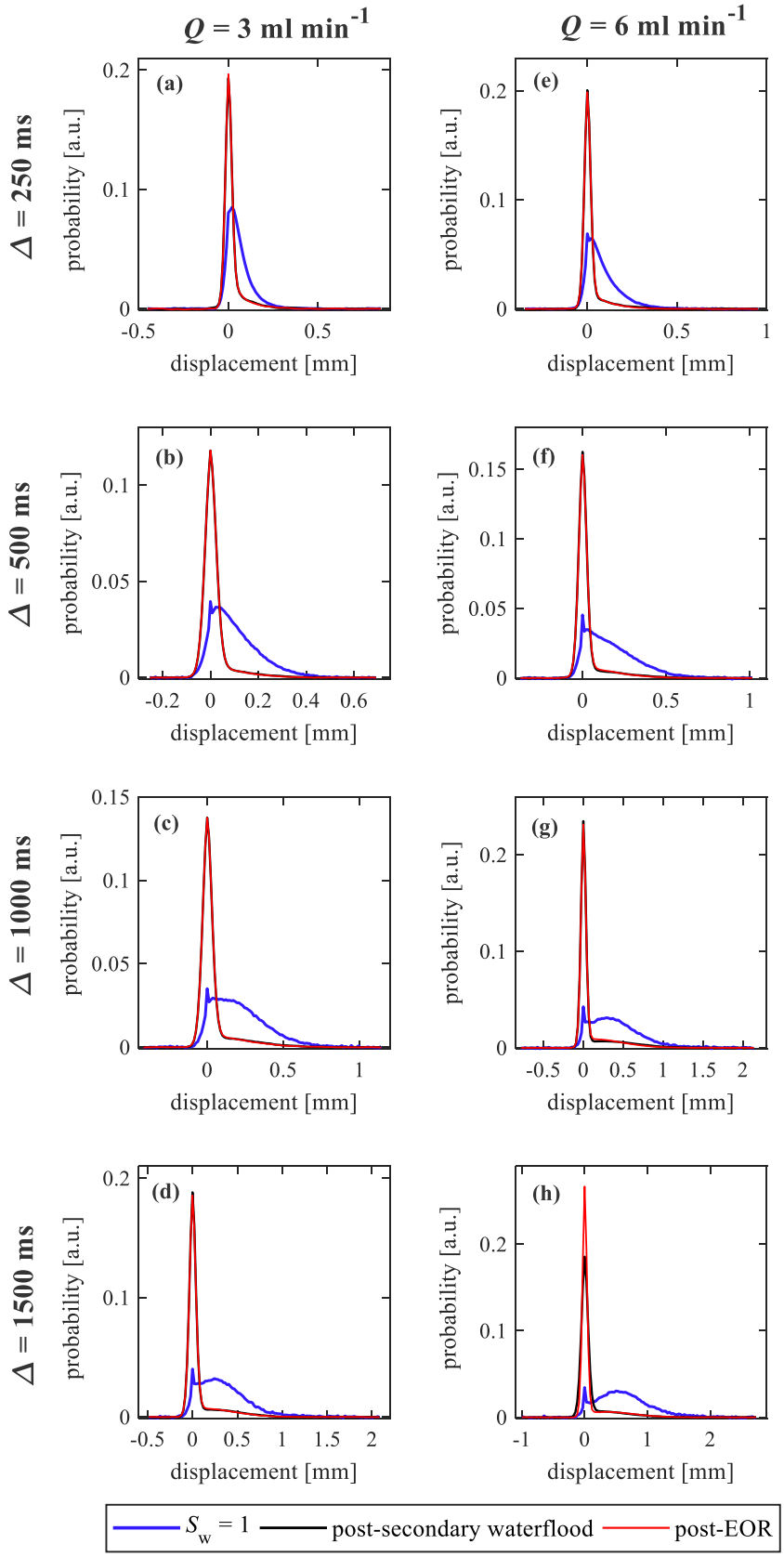

Figure 7.12. Globally-averaged propagators at **(a-d)** Q_{inj} = 3 ml min^{-1}, **(e-h)** Q_{inj} = 6 ml min^{-1}, for: **(a,e)** Δ = 250 ms, **(b,f)** Δ = 500 ms, **(c,g)** Δ = 1000 ms and **(d,h)** Δ = 1500 ms. Datasets include: S_w = 1, post-secondary waterflooding, post-EOR.

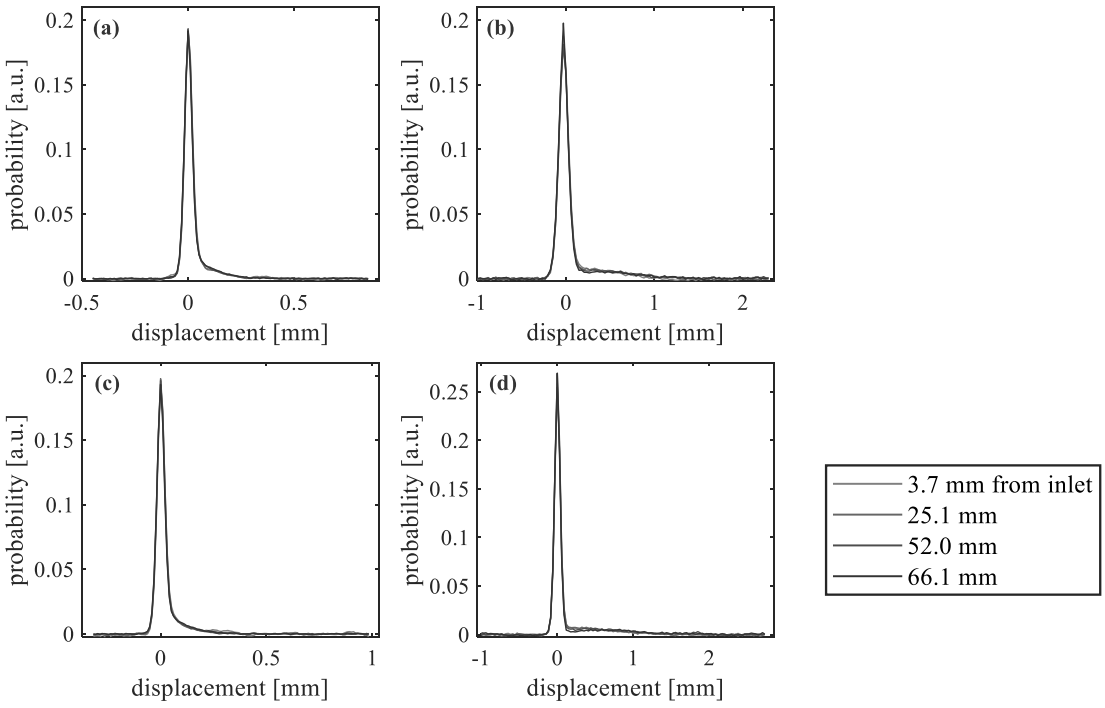

Figure 7.13. Spatially-resolved propagators at four axial positions (3.7 mm, 25.1 mm, 52.0 mm and 66.1 mm from the core inlet) – **(a,c)** at Q_{inj} = 3 ml min^{-1}, Δ = 250 ms; **(b,d)** at Q_{inj} = 6 ml min^{-1}, Δ = 1500 ms. Datasets acquired: **(a,b)** post-secondary waterflooding **(c,d)** post-EOR.

To enable unambiguous assignment of stagnant and moving fluids in the propagator, the T_2 contrast delivered through the propagator CPMG-train was exploited to attain T_2-resolved measurements of the stationary and moving fluid signals.

The following discussion outlines the methods by which a T_2-resolved analysis of the stagnant and moveable fluid regions within the globally-averaged propagators was achieved. Firstly, the propagator signal pertaining to moveable and stationary fluid was segmented. This segmentation was subsequently applied along the propagator T_2 decay. The segmented signals along the echo train were separately summed, giving decaying signal intensities with time. These were processed using 1D inversion protocols, producing T_2 distributions for both flow regimes.

To segment the raw propagators, stagnant flow was first identified – achieved by assuming stagnant flow possesses a symmetrical, Gaussian-shaped propagator about zero-displacement (Barrie, 2000). Firstly, propagator signal with negative displacement (opposing direction of applied flow) was assumed to pertain to stagnant fluid. A part-simulated stagnant-fluid propagator was then produced by reflecting this negative-displacement signal. To validate this assumption, reference no-flow propagators (acquired using the same parameters) were directly compared – to verify that the part-simulated propagator yielded equivalent displacements about zero, as the propagator recorded at true stagnant conditions. Finally, subtraction of the part-simulated stagnant propagators from the full propagators measured at flow produced a displacement map consisting only of moveable fluid signal. This signal segmentation is demonstrated in Fig. 7.14 for propagator measurements acquired at S_w = 1, post-secondary

waterflooding and post-EOR at Q_{inj} = 6 ml min^{-1}, Δ = 1000 ms. Therein, at each saturation condition an excerpt of the decaying propagators along the CPMG echo train are presented, demonstrating the differing rates of relaxation-time weighting within the propagators. In addition, segmentation of moveable and stagnant signal within the propagator is presented for the first echo within each propagator echo train.

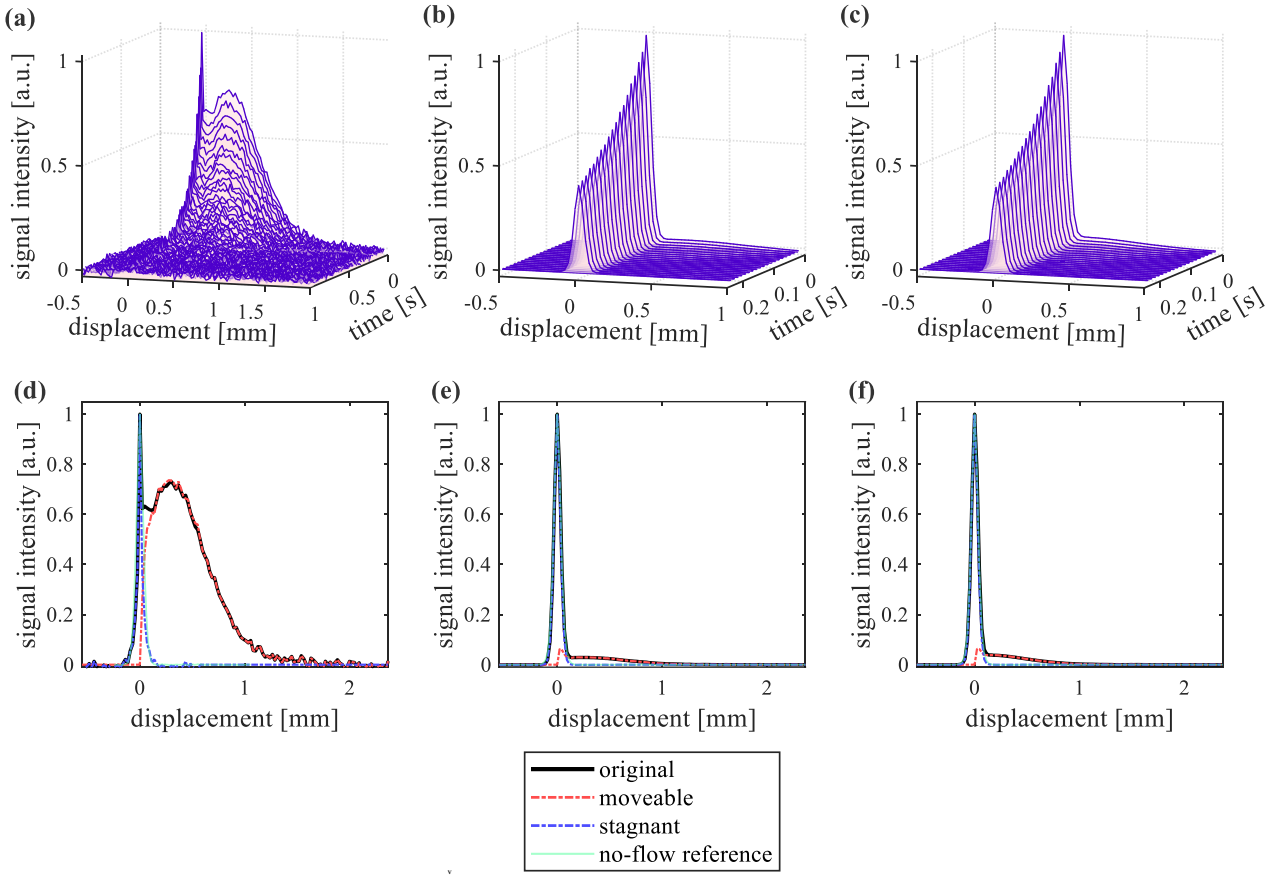

Figure 7.14. Globally-averaged propagators, acquired with Q_{inj} = 6 ml min^{-1}, Δ = 1000 ms at: **(a,d)** S_w = 1, **(b,e)** post-secondary waterflood, **(c,f)** post-EOR. (a-c) illustrate propagator delay along CPMG train. (d-f) illustrate propagator signal segmentation for the first echo. Signals shown: original non-segmented propagator, stagnant fluid, moveable fluid, reference no-flow propagator.

Following segmentation of the propagators into moveable and stagnant signals, T_2 distributions were obtained *via* 1D regularisation and inversion protocols – Fig. 7.15. Figure 7.15 clearly demonstrates bimodal T_2 responses post-secondary waterflooding, post-EOR, and a monomodal T_2 response at S_w = 1. The log-mean T_2 values of the resultant T_2 distributions are summarised in Table 7.5.

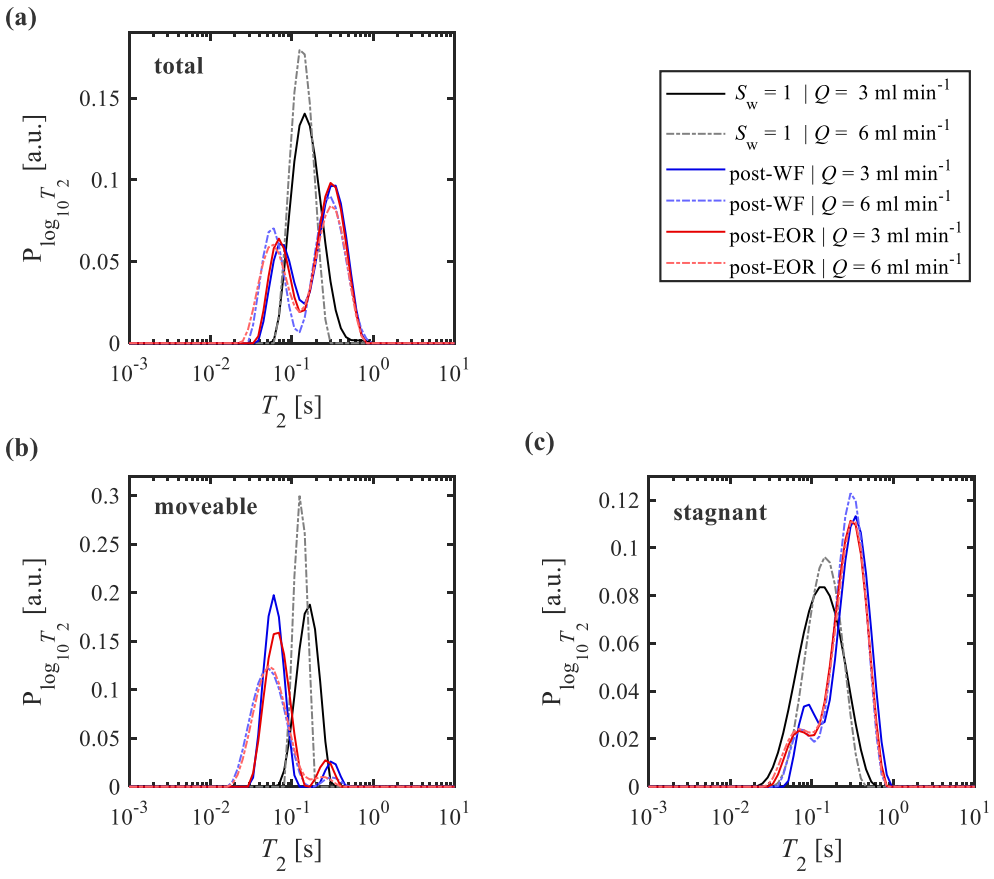

Figure 7.15. T_2 distributions from globally-averaged propagator-T_2 measurements with Δ = 1000 ms at S_w = 1, post-secondary waterflooding, post-EOR. Distributions from: **(a)** total, non-segmented propagators; **(b)** segmented, moveable-fluid signal; **(c)** segmented, stagnant-fluid signal. Datasets are presented for Q_{inj} = 3, 6 ml min^{-1}.

Table 7.5. $T_{2,LM}$ of short- and long-component T_2 peaks obtained from T_2 distributions from total (non-segmented), moveable (segmented) and stagnant (segmented) propagator-CPMG decays. Datasets presented: S_w = 1, post-secondary waterflooding (post-WF), post-EOR. Uncertainties calculated as in section 3.2.2.3.

		total signal $T_{2,LM}$ [s]		**moveable signal $T_{2,LM}$ [s]**		**stagnant signal $T_{2,LM}$ [s]**	
state	**Q_{inj} [ml min^{-1}]**	**short-T_2 component**	**long-T_2 component**	**short-T_2 component**	**long-T_2 component**	**short-T_2 component**	**long-T_2 component**
S_w = 1	3	0.16 ± 0.05	-	0.16 ± 0.02	-	0.13 ± 0.02	-
	6	0.13 ± 0.02	-	0.13 ± 0.02	-	0.14 ± 0.02	-
post-WF	3	0.08 ± 0.01	0.31 ± 0.05	0.06 ± 0.01	0.31 ± 0.04	0.09 ± 0.01	0.33 ± 0.06
	6	0.06 ± 0.01	0.30 ± 0.06	0.05 ± 0.01	0.30 ± 0.05	0.08 ± 0.01	0.30 ± 0.05
post-EOR	3	0.07 ± 0.01	0.31 ± 0.05	0.07 ± 0.01	0.26 ± 0.03	0.07 ± 0.01	0.30 ± 0.05
	6	0.06 ± 0.01	0.30 ± 0.05	0.05 ± 0.01	0.23 ± 0.03	0.07 ± 0.01	0.30 ± 0.05

For all saturation states and T_2-component regions, small reductions in T_2 are observed at increased flowrates. This is expected – with greater flowrates, greater signal attenuation would occur as a greater proportion of spins would (i) flow into the active r.f. region of the coil, after initial excitation; and (ii) initially-excited spins would flow out of the active r.f. region of the coil, prior to completion of the propagator acquisition.

At $S_w = 1$, a monomodal T_2 distribution centred about $T_2 \sim$ 130-160 ms is observed (occurring for both total and segmented propagators signals). This T_2 range is consistent with the L-T_1-T_2 measurements (Fig. 7.5). The broad T_2 distribution observed for stagnant fluid results from reduced SNR (relative to the moveable signal), leading to broader distributions, following regularisation and inversion.

Post-secondary waterflooding and post-EOR, no change in the T_2 response occurs. Considering first their total, non-segmented signals – T_2 peaks occur at ~70 ± 10 ms and ~310 ± 50 ms, in excellent agreement with the species-specific T_2 responses obtained through spectral-T_2 analysis post-waterflooding and post-EOR (section 7.3.2.3, Table 7.3). Therein, brine resulted in a T_2 response centred at ~ 70 ms, and dodecane resulted in a bimodal response at ~70 ± 10 ms and ~390 ± 70 ms. It is thus equivalently interpreted that post-waterflooding and post-EOR, the short-T_2 component results from both brine and dodecane fluids, whereas the long-T_2 component results from dodecane only.

Next, considering the segmented propagators post-waterflooding and post-EOR (Figs. 7.15b,c) it is interpreted that the stagnant fluid is comprised primarily of dodecane, evidenced by the high population of the long-T_2 component (attributed solely to dodecane). A small fraction of stagnant fluid can be attributed either to brine or dodecane – this ambiguity exists, as both fluids display T_2 signal at 70 ms (see Table 7.3). Similarly, the moveable fluid is comprised primarily of brine, with some contributions from dodecane (evidenced by the long-T_2 peak).

In the context of probing mechanisms of HPAM-EOR flooding in water-wet systems, this combined T_2-propagator and spectral-T_2 results have demonstrated that:

i. under applied brine flow at $S_w = 1$, post-waterflooding and post-EOR, the core is comprised of both stagnant and moveable fluids;
ii. post-waterflooding and post-EOR, the stagnant fluid is primarily comprised of oil-phase signal, with the possibility of small contributions from the aqueous-phase;
iii. post-waterflooding and post-EOR, the moveable fluid is primarily comprised of aqueous-phase signal, with small contributions from the oil-phase;
iv. comparing post-waterflooding and post-EOR states, no change is observed in the T_2 of both stagnant and moveable fluids – suggesting that HPAM does not influence which fluid is stagnant or moving.

These results largely agree with the expected behaviours that brine is the major component in the moveable fluid. Interestingly, dodecane also contributes to the moving fluid response – despite the

produced effluent volumetric measurements, indicating no further oil was produced during flow-propagator measurements. This suggests that the 'moveable' oil results from oil ganglia displaying fluctuating, oscillatory motions within the pore space, and are not necessarily flowing out of the core.

These oscillatory behaviours of oil ganglia within a water-wet pore space are similar to the observations of intermittent fluctuations of oil ganglia within a water-wet Bentheimer sandstone, under high Capillary number flows (for *Ca* on the order of 10^{-6}) (Gao *et al*., 2017). Therein, the authors used a differential X-ray imaging method to identify changes in pore fluid occupancy of the wetting (brine) and non-wetting phases (decane) within the pore space, relative to an initial brine-saturated condition.

Gao *et al*. demonstrated that at high capillary numbers a significant fraction of the pore space would occasionally be occupied by oil ganglia, and occasionally by brine. The authors interpreted this intermittent occupancy as regions of pore space having contained both fluid phases at different periods of time during the X-ray image acquisition. Further, the authors suggested that these intermittent occupancy regions are necessary to allow oil ganglia to flow, even if their connectivity is only periodically occurring. For comparison, the results herein presented in Fig. 7.15 were conducted using a near-identical oil, brine and rock system as Gao *et al*. (2017). In addition, the high flowrate steady-state brine injection conditions of 6 ml min^{-1} reported in Fig. 7.15 delivered a *Ca* number of 6.6×10^{-6} (calculated using the linear interstitial brine flow velocity (considering porosity effects), and a dodecane-brine interfacial tension of 0.0528 N m^{-1} at 20 °C (Zeppieri *et al*., 2001)). These *Ca* conditions are comparable to the flow conditions in which intermittent oil ganglia fluctuations were reported by Gao *et al*. (2017).

The oil-phase flow behaviour in Fig. 7.15 is also in agreement with the elastic turbulence model proposed by Mitchell *et al.* (2016) and Clarke *et al.* (2015). In addition, based upon this interpretation of the T_2-propagator results, the oil-oscillatory flow behaviour is herein also observed post-secondary waterflooding, and is not limited to the post-EOR saturation state. This contrasts with the observations in Mitchell *et al.* (2016), which indicate that such elastic turbulences are limited to HPAM flow. To form an unambiguous conclusion from the observations noted herein, further work would be required. In particular, it would be advisable to use aqueous- and hydrocarbon-phases displaying explicit T_2 contrasts.

7.3.3.3 The influence of HPAM-EOR on oil ganglia size – a PFG diffusion analysis

The influence of HPAM on oil ganglia size was assessed by acquiring diffusion measurements at multiple observation times, under stationary and no-flow conditions post-waterflooding, and post-EOR.

To unambiguously probe only dodecane within the pore space, a similar spectral segmentation approach as conducted for the spectrally-resolved T_2 measurements (section 7.3.2.3) was employed in analysing the APGSTE measurements. Interpretation of the diffusion datasets, with regards to oil ganglia size, is based upon the onset of restricted diffusion effects (see section 2.4.5). For spins undergoing non-

restricted free diffusion within a fixed Δ, their displacement during Δ indicates the sample self-diffusion coefficient. In contrast, spins undergoing restricted diffusion within an equivalent Δ, will display a reduced displacement (limited by the bounds in which they are restricted). In turn, this is manifested as a slower apparent diffusion coefficient. Accordingly, restricted diffusion behaviours can be inferred from the onset of shrinking effective self-diffusion coefficients, with increasing PFG observation times. Figure 7.16 presents the 1D effective diffusion distributions of the dodecane-signal post-secondary waterflooding and post-EOR. Their log-mean diffusion coefficients are presented in Table 7.6.

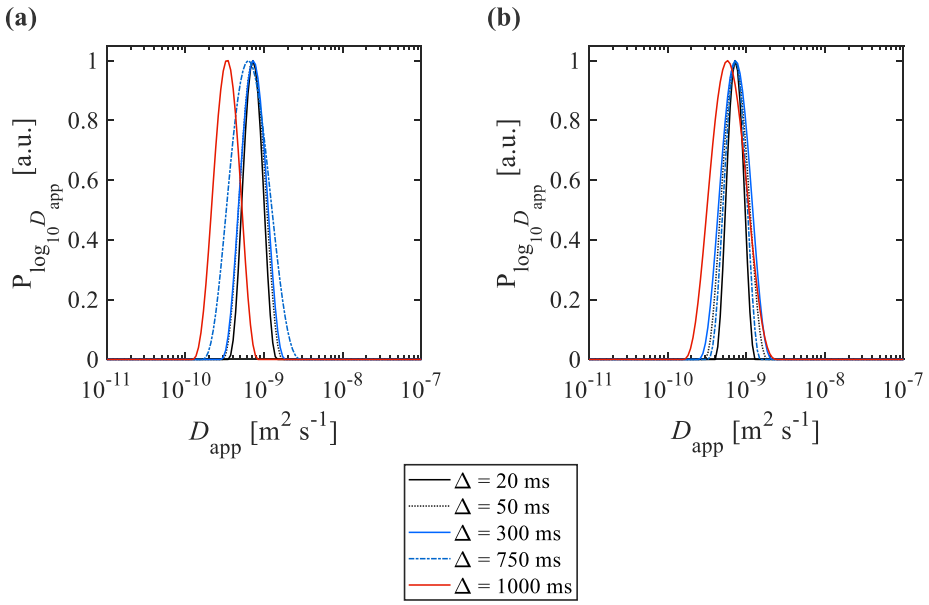

Figure 7.16. Apparent dodecane self-diffusivities **(a)** post-secondary waterflooding, **(b)** post-EOR, presented for Δ in the range 20-1000 ms. Obtained through 1D inversion of dodecane signal in spectrally-segmented APGSTE datasets. All distributions are normalised to unity, facilitating direct comparisons of peak locations.

Table 7.6. Log-mean apparent self-diffusivities (D_{LM}) of dodecane (spectrally-segmented), measured using variable Δ, post-secondary waterflooding and post-EOR. Uncertainties calculated as in section 3.2.2.3.

state	observation time, Δ [ms]	D_{LM} ($\times 10^{-9}$) [m^2 s^{-1}]
post-secondary waterflooding	20	0.72 ± 0.05
	50	0.72 ± 0.06
	300	0.73 ± 0.06
	750	0.66 ± 0.06
	1000	0.33 ± 0.03
post-EOR	20	0.72 ± 0.05
	50	0.73 ± 0.06
	300	0.73 ± 0.06
	750	0.72 ± 0.05
	1000	0.59 ± 0.06

The results in Fig. 7.16 and Table 7.6 demonstrate that post-secondary waterflooding and post-EOR, at short observation times (Δ < 300 ms) the apparent dodecane self-diffusion coefficients reside at the same values. As the observation time is increased, the apparent self-diffusion coefficients reduce. Post-secondary waterflooding, this reduction occurs for $\Delta \geq 750$ ms. Post-EOR, this onset occurs at $\Delta = 1000$ ms. These trends are similarly reflected in the log-mean apparent self-diffusion coefficients in Table 7.6. In addition, comparing equivalent observation times in post-secondary waterflooding and post-EOR states, at which restricted diffusion effects occur, Table 7.6 highlights that at $\Delta = 750$ ms and $\Delta = 1000$ ms, D_{LM} values post-secondary waterflooding are smaller than those post-EOR. These observations suggest that the onset of restricted diffusion behaviours occurs at shorter observation times in the post-secondary waterflooding state. This is interpreted as the oil ganglia having increased in size following HPAM-EOR, suggesting that HPAM encourages oil ganglion coalescence, thereby increasing ganglion size. This interpretation assumes the pore structure and tortuosity bear no influence on the dodecane-only diffusivity, in turn assumed to exist as isolated ganglia within the pore space.

This conclusion supports previously proposed mechanisms in the literature in which HPAM is purported to promote oil thread/column stabilisation (Huh and Pope, 2008; Meybodi *et al.*, 2011; Sedaghat *et al.*, 2013) – see section 6.1.4.4. These previous works proposed that without HPAM, oil threads destabilise, change shape, or break into droplets due to oil-water interfacial tension. The viscoelastic nature of HPAM was hypothesised to provide normal stresses that resist this deformation, promoting greater continuity in the oil phase. These prior works were conducted both using simulations and optically-transparent glass micromodels. As far as is known, this effect has not previously been demonstrated in opaque, reservoir-representative rock samples. The results presented in Fig. 7.16 and Table 7.6 suggest that NMR PFG protocols can be used to probe these proposed mechanisms within reservoir-representative systems. Further experimentation in this area could provide an interesting area of work. In particular, it would be interesting to do so at higher magnetic field gradient strengths. This would provide greater resolution to displacements, and thus in quantifying the oil ganglion size.

7.4 Conclusions

In this chapter, a reservoir-representative HPAM EOR flood was non-invasively studied in a water-wet Bentheimer sandstone core, using a multifaceted MR approach. Through combining L-T_1-T_2, spectral and spectral-T_2 analyses, the fluid residency within the pore space was assigned – demonstrating that wetting-brine fluid contacted the pore walls and filled small pore regions, while dodecane existed as globules held in pore centres. No further change in this pore fluid residency was observed post-EOR. The L-T_1-T_2 sequence identified an axially-uniform pore structure and pore saturation environment following each flooding stage. Spectral contrast facilitated dynamic tracking of core saturations throughout flooding – the final oil recoveries agreed with those measured through volumetric approaches, and with typical literature-reported recovery factors for HPAM-EOR. The flooding protocol

yielded a total recovery of 62.4% of OOIP, of which 4.3% was from polymer-EOR – the polymer delivered an incremental recovery of 10.3%.

The influence of HPAM-EOR on fluid mobilities was studied using PFG T_2-propagators. At $S_w = 1$, post-waterflooding and post-EOR, the core is comprised of both stagnant and moveable fluid regions. Post-waterflooding and post-EOR, the stagnant fluid is primarily dodecane whereas the moveable fluid is primarily brine. No further changes in the proportions, nor T_2 properties, of moveable and stagnant fluids were noticed post-EOR, suggesting HPAM did not directly influence the mobility of either phase. Post-waterflooding and post-EOR, a small fraction of moveable signal was attributed to dodecane, although no further dodecane was produced. This agrees with prior literature findings of oil ganglion elastic turbulences. Interestingly, it was herein observed that such elastic turbulence effects were similarly observed post-secondary waterflooding. This interpretation contrasts with prior work in the literature which has only observed elastic turbulences under HPAM, and not secondary waterflooding, flow conditions.

The influence of HPAM-EOR on oil ganglia size was studied using PFG diffusion measurements conducted at multiple observation times, under no-flow conditions. Post-secondary waterflooding, the onset of restricted diffusion behaviours was observed at shorter observation times than post-EOR – suggesting HPAM encourages oil ganglion coalescence and stabilisation, and thus larger oil ganglia. This agrees with literature-reported observations in optically-transparent micromodels – termed the 'oil thread/column stabilisation' mechanism. As far as is known, this effect has not previously been demonstrated in natural, opaque, reservoir-representative rock samples.

The key challenge in this work was the unambiguous assignment of relaxation times to aqueous- and hydrocarbon-phases, based on T_1-T_2 contrast alone – chemical shift contrast was required to enable signal identification. It was found that internal core pore structures play a significant role in achieving relaxation time contrast. It is recommended that future studies should conduct a comprehensive preliminary core screening programme to ensure that sufficient relaxation time contrast can be achieved – if so desired. Potential areas of future work include further studies on the influence of HPAM on oil ganglia size. In particular, conducting this work at higher magnetic field gradient strengths (herein limited by the magnet system used) would provide an improved resolution to quantifying oil ganglion size.

Chapter 8

Benchmarking Low-Field NMR Relaxation Time Wettability Measurements to Industry Standard Amott-Harvey Protocols

8.1 Introduction

Non-invasive, *in situ* wettability characterisation of rock core plugs is of significant interest within SCAL; not only for assessing the wetting state of a reservoir formation, but also for probing wettability alterations during laboratory-screening EOR core floods.

Industry-standard measurements of core wettability include contact angle methods for individual mineral surfaces, together with the US Bureau of Mines (USBM) and Amott-Harvey (AH) protocols for rock core plug samples. Whilst the latter two, as measurements across a core rather than an individual grain, deliver results that are more closely representative of the overall reservoir wettability, they have several limitations. Not least, they are: invasive, slow, insensitive to local wettability heterogeneities and critically, cannot be conducted downhole – at true reservoir conditions. Due to these limitations, there is considerable impetus for developing new approaches to measuring core wettabilities.

NMR T_1-T_2 techniques offer non-invasive, chemically-sensitive and volumetrically-quantitative measurements that are applicable to monitoring petrophysical systems. In recent years the sensitivity of the T_1/T_2 ratio to surface interaction strengths, and hence wettability, has been demonstrated. In this chapter, an Amott-Harvey measurement on a base case strongly water wet sandstone outcrop core has been continuously monitored using global T_1-T_2 measurements – the aim being, to benchmark the T_1/T_2 indicator of wettability against the industry-standard Amott-Harvey wettability index. A low-field 50 mT benchtop NMR spectrometer (2 MHz for ^{1}H nuclei) was used. This is equivalent to the standard NMR systems used in many SCA laboratories and to the upper limit of magnetic field strengths used in downhole NMR well-logging tools (section 2.4.1).

8.1.1 Introducing Wettability

Wettability is the preference for one fluid to adhere to a surface, in the presence of other immiscible fluids. Considering a single-solid two-fluid system, a drop of preferentially-wetting fluid will spread over the surface, displacing any non-wetting fluid originally in place; in contrast, a drop of non-wetting fluid will bead-up, minimising its surface contact. These wetting behaviours are controlled by surface tensions, originating from molecular-level interactions between solids and fluids (Anderson, 1986a,b; Abdallah *et al.*, 2007).

Surface wettability is defined by the contact angle, θ_c, between fluids and a solid surface. Considering a smooth, flat surface in the presence of a liquid and gas, the contact angle and equilibrium surface tensions between the three phases is illustrated in Fig 8.1, where $0° < \theta_c < 180°$.

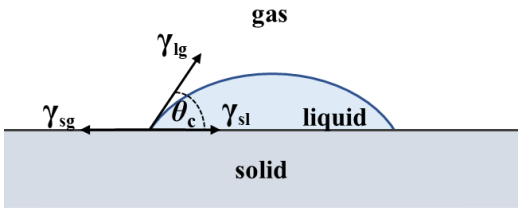

Figure 8.1. Contact angle, θ_c, and surface tensions, γ_T, at the liquid-solid-gas interfaces for a liquid drop wetting a flat, solid surface. Subscripts 'l', 's', 'g' denote liquid-, solid- and gas-phases respectively. Adapted from Anderson (1986b).

As defined by the Young equation (Young, 1805), for the system in Fig. 8.1, the contact angle is defined by:

$$\gamma_{lg}\cos\theta_c = \gamma_{sg} - \gamma_{sl} \tag{8.1}$$

where γ_{lg}, γ_{sg} and γ_{sl} are the surface tensions at the liquid-gas, solid-gas and solid-liquid interfaces, respectively. For an oil/water/rock system in which a water droplet contacts the rock surface and is surrounded by oil, the rock is preferentially water-wetting when $\theta_c < 90°$, and oil-wetting when $\theta_c > 90°$. For $\theta_c = 90°$, neither fluid preferentially wets the surface. This is illustrated in Fig. 8.2.

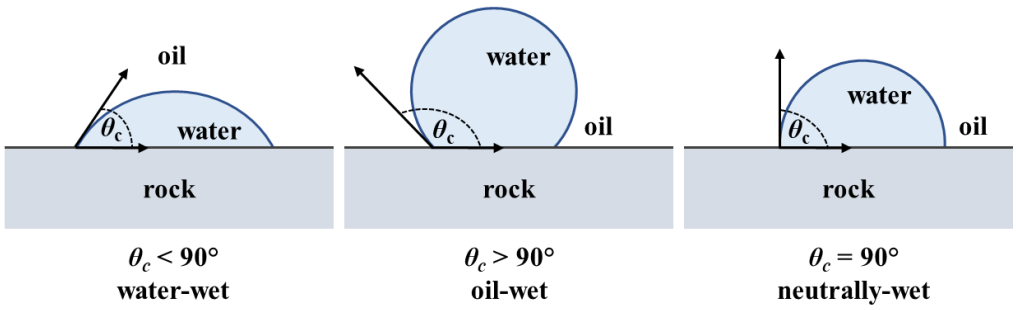

Figure 8.2. Schematic illustrating water-wet, oil-wet and neutrally-wet surfaces, for a water droplet surrounded by oil on a flat, smooth rock surface. Adapted from Anderson (1986b).

The wetting systems illustrated in Fig. 8.2 and defined in Eq. 8.1 are ideal systems; in reality, reservoir rock surfaces are rough, non-rigid and contain chemical inhomogeneities. This results in phenomena such as contact angle hysteresis and mixed wetting conditions. The next subsections briefly introduce the relevance of wettability measurements to oil exploration and production (E&P), together with the factors thought to influence reservoir wettability.

8.1.1.1 Industrial Relevance of Wettability Measurements

Defining the wettability of a reservoir formation is critical to reservoir characterisation. Wettability plays a role in: initial reservoir saturations, the expected reservoir performance; optimising production

strategies (from drilling protocols, to selecting EOR strategies); and reliably interpreting responses from well-logging tools (WLTs). These factors will briefly be considered in turn.

Firstly, rock wettability influences the ease in which an injected fluid invades the pore space, in turn affecting relative permeabilities and the capillary pressure. Fluid saturation, however, varies with capillary pressure, which itself increases with vertical height above the free water level – the highest elevation in a reservoir at which the capillary pressure between the oil- and brine-phases is zero. As capillary pressure increases, so does the saturation of the non-wetting fluid phase. The saturation profile with reservoir depth is thus heavily dependent on the formation wettability (Anderson, 1986b; Abdallah *et al.*, 2007; McPhee *et al.*, 2015). Largely due to its effect on relative permeabilities, wettability strongly influences reservoir productivity and oil recovery (Morrow, 1990). With increasing oil-wetness, k_{rw} increases, leading to earlier oil breakthrough and less efficient recovery (Anderson, 1987b). Incorrectly assuming a reservoir is water-wet can lead to selecting sub-optimal recovery protocols, which can cause irreversible reservoir damage (Abdallah *et al.*, 2007). Together, these factors affect the expected recovery of a prospective field, and hence the economic feasibility of an E&P project.

Characterising reservoir wettability is also critical to optimising other production strategies, from EOR to drilling protocols. In the context of EOR, this enables selecting targeted EOR technologies, such as surfactant-chemical EOR for oil-wet reservoirs. In drilling, selection of an appropriate drilling fluid is also dependent upon reservoir wettability. Incorrect selection, such as an oil-based mud in a water-wet formation, can lead to wettability alteration of the surrounding rock. In turn, this can unknowingly alter well-logging responses, which in themselves require an understanding of reservoir wettability for accurate interpretation. For example, this can influence both the modelling of resistivity logs used for identifying formation saturation and the interpretation of NMR WLT T_2 responses (McPhee *et al.*, 2015).

8.1.1.2 Factors Influencing Wettability

Saturation history is critical in determining the ultimate wetting state of a reservoir. Prior to initial hydrocarbon migration, reservoir rocks are water saturated and thought to be water-wet. Over time their wettability can change due to a number of factors: oil composition, rock mineral surface, brine chemistry (composition, pH, ionic strength), pressure and temperature conditions. Hydrocarbon composition has been shown to be a key factor in the wettability alteration of water-wet rocks, through the adsorption of surfactant polar compounds (resins and asphaltenes) and deposition of organic matter and sulphur compounds, originally in the crude oil, onto the mineral surface (Cuiec, 1984; Anderson, 1986a). A crude oil that is a poor solvent for these surfactants encourages their precipitation and subsequent adsorption onto a mineral surface. Low reservoir pressures and temperature conditions further promote the precipitation of such heavy oil compounds (Abdallah *et al.*, 2007).

The mineralogical composition of the formation also plays a significant role in controlling reservoir wettability. Carbonates tend to be more oil-wet than sandstones, and their wettability is more easily altered (Cuiec, 1984; Anderson, 1986a). This is attributed to their differing surface chemistries which

promote different adsorption responses. Further, high concentrations of certain minerals, such as pyrites and coals, can lead to greater oil-wetting characteristics. Similarly, the brine composition (pH, ionic strength and composition) can strongly affect the rock surface charges, altering the stability of the double electrical layer, wetting films, and the propensity for surfactant adsorption (Anderson, 1986a).

8.1.1.3 Synthetically-Altered Wettabilities

Numerous approaches for obtaining cores of systematically altered wettabilities have previously been employed – primarily through varying core ageing conditions and the use of chemical additives. Controlled modifications to laboratory ageing protocols can deliver systematic wettability alteration by mimicking different reservoir conditions. For example, Graue *et al.* (1999; 2002) demonstrated the influence of ageing time, oil composition and oil flushing protocols on core wettability alteration. Differing initial water saturations (Steinsbø *et al.*, 2014) and brine pH during ageing (Bousseau *et al.*, 1995) have also been demonstrated as methods for controlled wettability alteration.

A more popular approach for systematically altering core sample wettabilities has been the use of surfactant chemical additives. From non-ionic silicone-based surfactants, such as triethoxyoctylsilane (TEOOS) in cyclohexane and polydimethylsiloxane in heptane, applied to: silica catalyst pellets (Weber *et al.*, 2010); compressed sandpacks (Al-Mahrooqi *et al.*, 2006); and sandstone cores (Mungan, 1964), to oil-soluble ionic surfactants, most notably long-chain amines (Mungan, 1964; Zisman, 1964; Alveskog *et al.*, 1998; Tweheyo *et al.*, 1999; Kowalewski *et al.*, 2002; Standnes and Austad, 2003; Chen *et al.*, 2006).

8.1.2 Measuring Wettability

In this section the existing industry-standard methods used for measuring wettability are introduced. In particular, the Amott-Harvey method is focused on, as this is the subject of the work conducted in this chapter.

8.1.2.1 Industry-Standard SCA Wettability Measurements

As introduced in section 8.1, the industry-standard methods for measuring wettability include: the contact-angle measurement (McCaffery and Mungan, 1970), the Amott-Harvey test (Amott, 1959) and the US Bureau of Mines (USBM) test (Donaldson *et al.*, 1969). The contact-angle measurement uses a microscopic optical device to image the contact angle of a fluid wetted on a single, polished mineral surface. Whilst advantageous in that it is not influenced by potentially wettability-altering compounds that contact the rock during coring, such as surfactants and mud filtrates, as a measurement on a single mineral surface it is not representative of the reservoir as a whole. As such, the Amott-Harvey and USBM techniques are widely accepted as being more useful indicators of wettability for core analysis (Anderson, 1986b; McPhee *et al.*, 2015).

The Amott-Harvey and USBM techniques are based upon a series of water imbibition, and oil injection stages on a rock core sample. The Amott-Harvey wettability index is obtained from the difference in the

ratios of produced fluid volumes from spontaneous-versus-forced imbibitions, for both water and oil. The forced stages are conducted using either a centrifuge or a core holder flow cell. The USBM test conducts the forced injections using a centrifuge with incrementally-increased speeds. The USBM wettability index is obtained from the ratio of areas under the capillary pressure-saturation curves for the forced-water and forced-oil injections. While the USBM method offers a comparatively rapid measurement, Amott-Harvey is perceived as being more rigorous. In addition, the Amott-Harvey wettability measurement is more sensitive to neutrally-wet cores and is better-suited to unconsolidated samples, which would not survive the high centrifugation speeds in the USBM test (McPhee *et al.*, 2015).

8.1.2.2 Amott-Harvey Method

Amott-Harvey tests on reservoir core samples are typically conducted on either: 'fresh state cores' – as received from the reservoir; on 'cleaned state cores' – taken to irreducible water saturation (S_{wir}) via primary drainage with reservoir-representative brine and hydrocarbon fluids, following Soxhlet-cleaning protocols; or on 'restored state' cores – wherein 'cleaned state cores' undergo laboratory ageing in reservoir-representative fluids at elevated temperatures and/or pressures, for an extended period of time (days to weeks). Tests on 'restored state' cores are considered most representative of conditions in a reservoir system (McPhee *et al.*, 2015). For a restored-state core sample, the Amott-Harvey cycle is conducted as follows (also illustrated in Fig. 8.3).

1. clean core using hot solvent Soxhlet extraction, to ensure initially water-wet conditions;
2. brine-saturate core (S_w = 1) and take to irreducible water saturation (S_{wir}) through forced injection of the oil-phase (primary drainage) – [stages 1 and 2, Fig. 8.3];
3. age core at elevated temperatures (and/or pressures) to achieve restored-state conditions;
4. spontaneously imbibe core in a brine-filled Amott-Harvey imbibition cell (Fig. 8.4a), record the volume of produced oil, V_{os}, and maintain core in cell for a minimum of 48 h, or until no further oil is produced – [stage 3, Fig. 8.3];
5. forced imbibition – inject brine using a flow cell assembly (or centrifuge) and record the produced oil volume, V_{of} – [stage 4, Fig. 8.3];
6. conduct spontaneous drainage in an oil-filled Amott-Harvey drainage cell (Fig. 8.4b), record the volume of produced brine-phase, V_{ws}, and maintain core in the cell for a minimum of 48 h, or until no further brine-phase is produced – [stage 5, Fig. 8.3];
7. forced drainage – inject oil using a flow cell assembly (or centrifuge) and record the produced water volume, V_{wf} – [stage 6, Fig. 8.3].

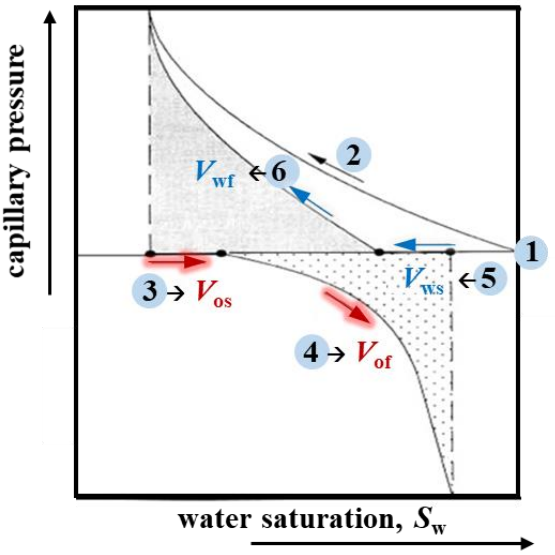

Figure 8.3. The Amott-Harvey cycle: (1) core at $S_w = 1$; (2) primary drainage to S_{wir}; (3) spontaneous imbibition in water, volume of produced oil, V_{os}, is recorded; (4) forced imbibition by injecting water, volume of produced oil V_{of}, is recorded; (5) spontaneous drainage in oil, volume of produced water, V_{ws}, is recorded; (6) forced drainage by injecting oil, volume of produced water, V_{wf}, is recorded. Adapted from McPhee *et al.* (2015).

For the forced stages, constant pressure flooding methods are typically recommended over constant flowrate protocols, in order to minimise capillary end effects. The displacement force used across both forced imbibition and drainage stages should be equivalent, to enable a comparison between the two displacements. Figure 8.4 presents schematic diagrams of the Amott-Harvey spontaneous imbibition and drainage cells.

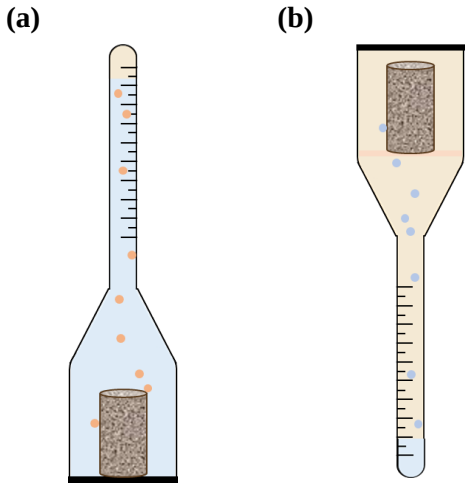

Figure 8.4. Amott-Harvey spontaneous **(a)** imbibition and **(b)** drainage cells. Adapted from McPhee *et al.* (2015).

The Amott-Harvey wettability index (*AHWI*) is calculated by comparing the volumes of oil and water across the imbibition and drainage cycles, respectively – as defined in Eq. 8.2,

$$AHWI = I_w - I_o \tag{8.2}$$

where I_w is the water-wetting index, and I_o is the oil-wetting index, defined by Eqs. 8.3 and 8.4, respectively:

$$I_w = \frac{V_{os}}{V_{os} + V_{of}} \tag{8.3}$$

$$I_o = \frac{V_{ws}}{V_{ws} + V_{wf}} . \tag{8.4}$$

For a water-wet rock, I_w will be close to 1, as most produced oil will occur during the spontaneous imbibition. Likewise, I_o will be close to 1 for an oil-wet rock. By calculating I_w, I_o and *AHWI*, core wettability can be classified using the range of values defined in Table 8.1.

Table 8.1 Amott-Harvey wettability indices. Reproduced from McPhee *et al.* (2015).

Index	water-wet	neutral-wet	oil-wet
I_w	positive	0	0
I_o	0	0	positive
AHWI	+0.3 to +1.0	-0.3 to +0.3	-0.3 to -1.0

Despite offering clear advantages over other industry-standard wettability measurements, there are limitations to the Amott-Harvey technique. Long equilibration times in the spontaneous and forced injection stages result in slow measurement times. Experimentally, Amott-Harvey can suffer from uncertainties in accurately quantifying produced volumes. Firstly, the spontaneous cells typically have trapped droplets of produced fluids, unable to accumulate with the bulk collected fluids. These can result from: water-beads attached to hydrophilic glass walls, oil-beads trapped at ground glass joints (due to the presence of hydrophobic silicone grease), and trapped oil globules at the neck of an imbibition cell. In addition, dead volumes in the flooding system can increase uncertainties in the produced volumes at the forced stages – this error is magnified when samples of comparatively small pore volumes are tested. Finally, as the native saturation of a reservoir core sample is altered, the Amott-Harvey measurement is inherently destructive, and as a bulk measurement it offers no information on localised wettability heterogeneities in a core sample.

8.1.2.3 Alternative Methods for Wettability Measurement

Recent developments in alternative wettability measurements include: atomic force microscopy techniques (Kumar *et al.*, 2005); electrical resistivity approaches (Bona *et al.*, 1999; Moss *et al.*, 2002; Seleznev *et al.*, 2006; Montaron, 2007); combining Cryo Environmental Scanning Electron Microscopy with Energy Dispersive X-ray Spectroscopy (Kowalewski *et al.*, 2003); X-ray photoelectron spectroscopy (Toledo *et al.*, 1996); imaging approaches incorporating microCT (Lebedeva and Fogden, 2011); combining enthalpy of water adsorption measurements with thermogravimetric analysis (Schlangen *et al.*, 1994; Tabrizy *et al*., 2011); and magnetic resonance approaches (Howard, 1994; Zhang *et al.*, 2000; Al-Mahrooqi *et al.*, 2003; 2006; Aspenes *et al.*, 2003; Fleury and Deflandre, 2003;

Chen *et al.*, 2006; Looyestijn and Hofman, 2006; Johannesen *et al.*, 2008; Looyestijn, 2008; Minh and Heaton, 2008; Mitchell *et al.*, 2009a; Al-Muthana *et al.*, 2012; Hürlimann and Song, 2012; Minh *et al.*, 2015; Korb *et al.*, 2017; Valori *et al.*, 2017).

Of particular interest within magnetic resonance approaches, is the use of NMR relaxation time techniques. Not only do these offer rapid, repeatable, non-invasive measurements; they can deliver wettability measures representative across an entire core sample, instead of only across the pore scale – as with microscopy-based approaches. Furthermore, these are not limited to laboratory analyses and as existing techniques used in well-logging, they offer the potential to be used for *in situ* reservoir wettability characterisation.

8.1.3 Using NMR to Measure Wettability

Quantitative NMR wettability indicators have primarily consisted of surface-sensitive 1D NMR T_1 and T_2 relaxometry (Guan *et al.*, 2002; Al-Mahrooqi *et al.*, 2003, 2005, 2006; Fleury and Deflandre, 2003; Chen *et al.*, 2006) and more recently, D-T_2 approaches (Minh and Heaton, 2008; Minh *et al.*, 2015; Nicot *et al.*, 2017). It has been demonstrated that increased wetting behaviours lead to reductions in T_2 relaxation times (Guan *et al.*, 2002; Al-Mahrooqi *et al.*, 2005; Chen *et al.*, 2006; Looyestijn and Hofman, 2006; Johannesen *et al.*, 2007; Looyestijn, 2008; Hürlimann and Song, 2012). NMR wettability indices (WI) based upon 1D T_1 and T_2 approaches have also been proposed and benchmarked against Amott-Harvey and USBM techniques (Fleury and Deflandre, 2003; Al-Mahrooqi *et al.*, 2006; Chen *et al.*, 2006). Whilst these methods can offer useful insights in wettability characterisation, particularly T_2 with its applicability to well-logging tools, there are limitations.

Critically, 1D relaxation times are not solely functions of wettability and their responses are also influenced by the composition of imbibing fluids, saturation, surface relaxivities and pore size distributions (Al-Mahrooqi *et al.*, 2006). Although chemically-sensitive, a distinct separation between hydrocarbon and brine T_2 values can be difficult to achieve. For systems with changing chemical environments, unambiguously attributing deviations in T_2 to either wettability or compositional changes can become challenging. This is a drawback in light of the imbibition and drainage cycles commonly employed in SCAL core ageing and EOR flood testing protocols.

More recently the T_1/T_2 ratio has been demonstrated as a measure of surface interaction strength (McDonald *et al.*, 2005; Mitchell *et al.*, 2009b; D'Agostino *et al.*, 2014) – thus a wettability indicator (Mitchell *et al.*, 2013a; Weber *et al.*, 2009). Using T_1/T_2 as an indicator of interaction strength is superior to 1D T_1 and T_2 measurements alone, due to the independence of T_1/T_2 on pore geometries (see section 2.4.4.2). Furthermore, when measured using a 2D T_1-T_2 measurement, the T_1 dimension can provide additional chemical contrast for hydrocarbon and brine signals, although the level of contrast is system dependent. Together, this allows the T_1-T_2 technique to deliver a species-specific indicator of wettability, applicable to dynamically-changing multicomponent systems.

As noted in section 2.4.4.2, the sensitivity of T_1/T_2 to surface interaction strength is reduced with decreasing magnetic field strengths and decreased surface relaxivities, $\rho_{1,2}$. Interestingly, T_1/T_2 ratios of the hydrocarbon signal in mixed-saturated core plugs at 2 MHz have very recently started being correlated to USBM measures of wettability (Valori *et al.*, 2017). Unfortunately, in that work, the authors chemically doped the aqueous phase to achieve hydrocarbon-brine signal contrast, which negated extracting any T_1/T_2 wettability information on the brine phase.

8.1.4 Aims

The aim of this work is to identify whether the T_1/T_2 ratio can quantitatively measure core sample wettabilities, by using 2D T_1-T_2 acquisition protocols at the low magnetic field strengths common to both standard SCAL NMR measurements and NMR WLTs. The drive behind this is twofold – not only for developing capabilities in dynamically-monitoring wettability changes in SCAL EOR screening floods, but also for enabling *in situ*, downhole measurements of reservoir wettabilities during well-logging protocols.

In this study, the sensitivity of the T_1/T_2 measurement on a core sample of controlled, known wettability was tested at 2 MHz, comparable to the field strengths used in conventional SCAL and WLT NMR measurements. The goal was to benchmark this measurement against the industry-standard Amott-Harvey wettability index. All measurements were conducted non-invasively on undoped systems, to enable the monitoring of wettability trends in both hydrocarbon and aqueous phases. Continuous monitoring of all stages of the AH cycle using T_1-T_2 and L-T_2 measurements was conducted, enabling unambiguous assignment of any changes in NMR response to core saturation and wettability changes.

8.2 Materials and Methods

The experiments conducted in this Chapter are separated into two parts. Firstly, preliminary screening experiments were conducted to identify appropriate base case core samples of synthetically-altered wettabilities, on which to conduct benchmarking analyses. Subsequently, an Amott-Harvey wettability cycle was conducted on one of these base case core samples and continuously monitored using NMR T_1-T_2 measurements.

8.2.1 Materials

This section outlines the sample materials and chemicals for both the preliminary screening and full Amott-Harvey study, together with the equipment set-up used for the Amott-Harvey cycle.

As introduced in section 8.1.1.3, a popular approach for synthetically-altering core wettabilities have been through using long-chain amines. In particular, Kowalewski *et al.* (2002) achieved controlled wettability alterations in Berea sandstone core plugs using n-decane and hexadecylamine (HDA) solutions of varying concentrations. Adsorption of the oil-soluble amine surfactant onto the Berea surface rendered the surface oil-wet, facilitating an interaction with oil molecules in the pore-space.

Therein, the authors completed Amott-Harvey measurements on core plugs treated to a range of amine concentrations, resulting in wettabilities in the range $0.04 < AHWI < 0.73$. These existing Berea-decane-amine systems calibrated to *AHWI*s, form the basis of the sample choice in this chapter.

Preliminary screening tests on a selection of the samples identified by Kowalewski *et al.* (2002) were conducted to both verify the reproducibility of their controlled, altered wetting states, and the likely sensitivity of the T_1-T_2 measurements to these systems – a series of Berea cores, synthetic brine and hexadecylamine/decane solutions were used. Subsequently, a full Amott-Harvey cycle was only conducted on a single Berea core, with synthetic brine and unaltered decane as the hydrocarbon phase.

For all experiments standard 1″ diameter (25.4 mm) by 1.5″ (38.1 mm) long Berea sandstone core plugs were used (Kocurek Technologies, Houston). All cores were Soxhlet cleaned (protocol in section 4.2.1) and subsequently oven dried at 95 °C for 48 h. Their core properties (dimensions, pore volumes and porosities) were determined by gravimetric analyses. Synthetic brine was prepared using sodium chloride (99%, Sigma Aldrich) and deionised water to a concentration of 30.0 ± 0.1 g NaCl litre^{-1}, consistent with typical oilfield water salinities for sandstone oil and gas reservoirs (Oruwori and Ikiensikimama, 2010). For the hydrocarbon phases, decane (≥ 95%, Sigma Aldrich) and hexadecylamine granules (98%, Sigma Aldrich) were used.

Characterisation of bulk liquid responses was conducted in a 2 MHz Oxford Instruments benchtop spectrometer, at 35 ± 0.1 °C, and using a 29 mm r.f. probe. Bulk liquid T_1 and T_2 times of brine and decane were measured as: $T_{1,brine}$ = 2.31 ± 0.01 s; $T_{2,brine}$ = 1.99 ± 0.01 s; $T_{1,decane}$ = 1.12 ± 0.01 s; $T_{2,decane}$ = 1.11 ± 0.01 s, using standard T_1-IR and T_2-CPMG methods. The hydrogen indices (HI) (section 2.4.3) of the fluids were measured as: HI_{decane} = 1.02 ± 0.02 and HI_{brine} = 0.97 ± 0.02, with respect to theoretical HI_{decane} = 1.02 and literature-reported HI_{brine} = 0.975, for the equivalent brine composition (Kleinberg and Vinegar, 1996). These were measured from the total signal intensities for 2D T_1-T_2 experiments on three separate vials of degassed deionised water, decane and 30.0 ± 0.1 g NaCl litre^{-1} brine. The three vials were each prepared to a volume of 15.0 ± 0.2 ml, enabling the calculation of their respective HIs. The HI T_1-T_2 experiments were acquired using the same parameters for all fluids.

For the Amott-Harvey benchmarking experiment, forced injections during primary drainage, imbibition and secondary drainage were conducted in the MRRC core flooding system. The equipment set up is detailed in section 4.3.

8.2.2 Methods

This section outlines the experimental protocols used in both the preliminary screening experiments and in the Amott-Harvey T_1-T_2 benchmarking study (sections 8.2.2.1 and 8.2.2.2, respectively). The NMR experimental parameters used in both studies are discussed in section 8.2.2.3.

8.2.2.1 Preliminary Screening of Synthetically-Altered Wettabilities

As introduced in section 8.2.1.1, the wettabilities of Berea core samples were systematically altered using hexadecylamine/decane solutions of various concentrations. The goal was to test the spontaneous imbibition and NMR responses of three rock cores modified to be 'water-wet', 'intermediate-wet' and 'oil-wet'. A stock solution of 7.22 g ± 0.01 hexadecylamine (HDA)/litre of n-decane was prepared, producing a 0.99 ± 0.01 wt% HDA/decane solution. From this, three solutions were prepared – corresponding to the extreme endpoints and one intermediate concentration, as tested by Kowalewski *et al.* (2002): pure n-decane (most water-wet), 0.20 ± 0.01 wt% HDA/litre n-decane (most oil-wet) and 0.10 ± 0.01 wt% HDA/litre n-decane (intermediate-wet). These were respectively reported to produce wettabilities of *AHWI* = 0.73; *AHWI* = 0.04, and *AHWI* = 0.20 (Kowalewski *et al.*, 2002).

Following Soxhlet-cleaning and oven drying, core dimensions and dry masses were recorded. The cores were then vacuum dried to < 14 mmHg (1.9 kPa) for 12 h, and vacuum saturated in the desired hydrocarbon solution for 24 h. These were then submerged in sealed glass jars, containing their respective degassed hydrocarbon solutions and placed in a laboratory oven to age for six days at 90 °C. After ageing, the cores were cooled to room temperature (20 ± 1 °C) and their wet masses were recorded, removing any excess surface liquid using an oil-dampened tissue. The dry and wet mass recordings were used to determine the sample pore volumes, using a decane density value of ρ_{decane} = 730.4 ± 0.8 kg m^{-3} at 20 ± 1°C (Lemmon *et al.*, 2017). All masses were recorded using a laboratory scale (Precisa 205A), sensitive to 0.001 g.

Rapid wettability screenings of the three core samples were conducted by spontaneous-only Amott imbibition and drainage tests – an indicator of sample wettability (Morrow *et al.* 1994; Zhou *et al.*, 1995). Producing hydrocarbon during spontaneous imbibition in brine suggests water-wetting conditions; producing brine during spontaneous drainage in oil suggests oil-wetting conditions. NMR T_1-T_2 measurements were recorded at each endpoint. Post-ageing, the measurement protocol was conducted as follows:

1. wrapped core in clingfilm (to minimise fluid evaporation from pore space), loaded into NMR magnet, allowed temperature to equilibrate for 30 min, then acquired T_1-T_2 datapoint;
2. spontaneous Amott-Harvey imbibition (AHSI) in brine – allowed 48 h for equilibration in the imbibition cell and recorded produced hydrocarbon volume, V_{os};
3. removed core from imbibition cell, removed excess surface liquid with a brine-wetted tissue, then repeated step 1;
4. spontaneous Amott-Harvey drainage (AHSD) in hydrocarbon fluid – allowed 48 h for equilibration and measured any produced brine volume, V_{ws};
5. removed core from drainage cell, removed excess surface liquid with a hydrocarbon-wetted tissue, then repeated step 1.

8.2.2.2 Full Amott-Harvey Cycle T_1-T_2 Benchmarking Methods

Within the Amott-Harvey cycle T_1-T_2 benchmarking study, NMR measurements were taken at each AH cycle endpoint and during the continuous injection stages. These facilitated obtaining NMR saturations (based upon T_1-T_2 contrast), pore-filling information (based upon T_1, T_2 responses) and wettability information (based upon T_1/T_2 behaviours). The following protocol is described for the first base case – a water-wet Berea core (prepared using only decane as the hydrocarbon fluid, without addition of HDA).

1. **Initial core preparation:**
    a) after Soxhlet-cleaning and oven-drying, recorded the core dry weight and dimensions using a laboratory scale (Precisa 205A, sensitive to 0.001 g) and Vernier callipers (sensitive to 0.02 mm);
    b) vacuum dried core and ceramic disc for 12 h at < 14 mmHg (1.9 kPa), and then vacuum saturated in 30.0 ± 0.1 g NaCl litre^{-1} brine for 24 h. (A 1″ diameter (25.4 mm) ceramic pressure disc (ELE International) rated to 15 bar (218 psi, 1.5 MPa), with effective pore size 0.16 µm, pore volume of 1.2 ml and porosity of 35% was used for achieving S_{wir} via primary drainage).
    c) recorded core wet weight and used the mass difference (from the dry weight measurement) to gravimetrically determine the sample pore volume (using ρ_{brine} = 1033.1 ± 0.2 kg m^{-3} at 20 ± 1°C, (Lemmon *et al.*, 2017)) and porosity, based on the core dimensions;
    d) loaded core and ceramic disc into the RCH probe, with the ceramic disc aligned vertically above the core, to mimic oil-trapping mechanisms in reservoirs;
    e) flushed brine through the CFS to purge out any trapped air in the rig lines;
    f) sealed the core bottom outlet (closed V-12c, Fig. 4.3), filled the RCH inlet line with brine (using a syringe), and connected the injection loop to the top of the RCH under flow conditions – this procedure minimised introducing air to the core.
2. **Initial brine-saturated state (S_w = 1) – [stage (1), Fig. 8.3]:**
    a) pressurised the confining loop to 350 psi (~2.4 MPa) using NMR-silent Fluorinert (Acota, UK);
    b) flushed core with brine from top-to-bottom at linear interstitial velocity u_{int} = 5 ft day^{-1} (equivalent to injectant flowrate, Q_{inj} = 0.05 ml min^{-1}) to ensure all air was purged from the RCH effluent line to CFS (originally unfilled upon initial connection);
    c) acquired reference NMR measurements at S_w = 1: T_1-T_2, L-T_2, with the core isolated and under confining pressure (closed V-12c and V-13c, Fig. 4.3).
3. **Primary drainage – [stage (2), Fig. 8.3]:**
    a) flushed decane through the CFS, purging all lines of brine (isolated from the RCH);

b) injected decane into the core from bottom-to-top, at u_{int} = 0.5 ft day^{-1} (Q_{inj} = 0.011 ml min^{-1}), until the injection pressure approached the ceramic disc pressure limit, as S_{wir} was reached;

c) tracked the primary drainage process continuously with T_1-T_2 and at the endpoint, S_{wir}, ran reference measurements, as in step 2.c).

4. Core ageing (restored state methods):

a) removed core from RCH and submerged in a sealed jar filled with the oil-phase injected during primary drainage, then aged in oven at 90 °C for 6 days;

b) post-ageing – allowed the core to equilibrate to room temperature, wrapped in clingfilm (removing excess liquid on the core surface with oil-soaked tissue), loaded into the magnet, allowed 30 min for temperature equilibration, and then acquired reference measurements, as in step 2.c);

c) detached and cleaned inlet lines to the RCH (lines V-12c-RCH bottom and V-13c-RCH top, Fig. 4.3) – important for accurate quantification of *AH* produced volumes (see section 4.3.5.3).

5. Spontaneous brine imbibition – [stage (3), Fig. 8.3]:

a) core was placed in AH imbibition cell filled with brine and allowed to equilibrate for 6 days – recorded the produced hydrocarbon, V_{os};

b) acquired reference measurements, as in step 2.c), following core wrapping and equilibration procedures as in step 4.b).

6. Forced brine imbibition – [stage (4), Fig. 8.3]:

a) flushed all CFS lines with brine and loaded core into RCH and CFS;

b) operated the forced imbibition as eight pressure steps (from atmospheric pressure to 200 psi (~1.4 MPa), in 25 psi (~0.2 MPa) increments), in constant pressure mode with a maximum limiting flowrate of Q_{inj} = 0.1 ml min^{-1} (equivalent to u_{int} = 4.5 ft day^{-1}), flowing from top-to-bottom (to minimise introduction of air to the core, as in step 1.f)), with a confining pressure of 350 psi (~2.4 MPa):

- at each pressure increment, if the pump was unable to reach set pressure the BPR was incrementally closed (BPR-1, Fig. 4.3) until the set pressure was reached;
- once set pressure was reached the core was left to equilibrate for 1 h, after which, NMR measurements were acquired (as in step 2.c);
- after the final pressure step, a brine volume (equivalent to double the total CFS dead volumes) was flushed through at u_{int} = 1 ft day^{-1} (Q_{inj} = 0.022 ml min^{-1}), to ensure the RCH effluent line (bottom RCH-to-CFS) was cleared of all produced hydrocarbon – important for *AHWI* quantification;
- collected all effluent in a measuring cylinder and recorded produced hydrocarbon volume, V_{of};

c) at S_{or} acquired reference measurements, as in step 2.c).

7. Spontaneous oil drainage – stage (5), Fig. 8.3:

a) removed core from RCH, placed in AH drainage cell filled with decane and allowed to equilibrate for six days – recorded produced brine volume, V_{ws};

b) acquired reference measurements, as in step 2.c), following the core wrapping and equilibration procedures as in step 4.b).

8. Forced decane drainage – stage (6), Fig. 8.3:

a) filled all CFS lines with decane, including the effluent lines from the RCH probe to CFS (important for accurate quantification of *AHWI* volumes), and loaded core into RCH and CFS;

b) operated forced drainage as eight pressure steps – following the same protocol as for forced brine imbibition, step 6.b):

- collected all effluent in a measuring cylinder and record the produced brine volume, V_{wf};

c) acquired reference measurements, as in step 2.c).

8.2.2.3 NMR Methods

This section details the acquisition parameters used in the NMR measurements for both the preliminary screening and full Amott-Harvey studies. All NMR experiments were conducted at 35 ± 0.1 °C temperature-controlled conditions in a 51 mT (2.18 MHz for ^{1}H nuclei) vertical bore permanent magnet (Oxford Instruments Geospec 2-75 Rock Core Analyser), controlled by a DRX HF spectrometer and RINMR software. A 29 mm inner diameter r.f. probe was used for excitation and signal detection. In the Amott-Harvey T_1-T_2 benchmarking study, measurements were acquired using a 29 mm r.f. probe built-in to the RCH (as introduced in section 4.3.5.2). Spatial resolution along the vertical axis (y), the direction of superficial flow in the forced injection stages, was achieved by applying a magnetic field gradient, capable of a maximum gradient strength of 35.1 G cm^{-1}, along the y-direction.

For the preliminary screening study, 2D inversion recovery T_1-T_2 experiments were acquired at the end of each step (see section 8.2.2.1). Hard r.f. pulse durations of t_{90} = 4.55 μs and t_{180} = 9.10 μs were used for all NMR experiments. The 2D T_1-T_2 experiments were acquired with t_E = 2 ms, for 2048 echoes, with a 16-point variable delay list in the range t_{vd} = 1 ms to t_{vd} = 7 s, RD = 7 s and NS = 32, resulting in t_{ACQ} = 1 h 25 min. For the Amott-Harvey benchmarking study, 2D T_1-T_2 and L-T_2 measurements were acquired at the end-point reference states and during the continuous forced injection stages of primary drainage, imbibition and secondary drainage. Hard r.f. pulse durations of t_{90} = 5.8 μs and t_{180} = 11.6 μs were used. The T_1-T_2 experiments were acquired with t_E = 1 ms, for 4096 echoes, with a 32-point variable delay list in the range t_{vd} = 100 μs to t_{vd} = 9 s, RD = 9 s and NS = 64, resulting in t_{ACQ} = 7 h 40 min. Frequency-encoded L-T_2 datasets were acquired at t_E = 3.24 ms and using 64 pixels with FOV = 62.8 mm, giving a slice resolution of 0.98 mm pixel^{-1}. A recycle delay of RD = 16 s with NS = 512 was used, resulting in t_{ACQ} = 2 h 16 min. In both studies, NMR spectra and T_2 one-shot CPMG experiments were

acquired at the start and end of each experiment train – to verify whether any significant signal loss had occurred due to fluid evaporation from sample heating. Different interecho times t_E were used in the spatially-resolved L-T_2 and global relaxation time measurements (T_2 and T_1-T_2) to enable for sufficient points within the imaging FOV of the L-T_2 measurement to be acquired.

The total experimental time for the full Amott-Harvey benchmarking study was ~65 days. This included core flooding system (CFS) set-up, the insertion and removal of the core within the CFS at each Amott-Harvey endpoint, core aging, spontaneous and forced imbibition stages, continuous NMR measurements (during forced imbibition) and the NMR endpoint reference measurements.

Data processing of the measurements of the global and spatially-resolved relaxation time measurements was conducted following the methods outlined in sections 2.4.4.3 and 3.2.2.2.

8.3 Results and Discussion

This section presents the experimental results acquired in both the preliminary screening and the full Amott-Harvey T_1-T_2 benchmarking studies.

8.3.1 Preliminary Screening of Samples with Synthetically-Altered Wettabilities

The measured core sample properties (dimensions, gravimetrically-determined pore volumes and porosities) are summarised in Table 8.2.

Table 8.2. Core sample properties detailing dimensions, masses, pore volumes (P.V.) and porosities (φ_p). Core dimensions reported to sensitivity of ±0.02 mm, masses to ±0.001 g, P.V. to ±0.1 ml, φ to ±0.1%.

Core	Length [mm]	Diameter [mm]	Dry Mass [g]	Wet Mass [g]	P.V. [ml]	φ_p [%]
Berea 1	38.58	25.28	42.607	45.314	3.71	19.1
Berea 2	38.22	25.36	39.426	42.142	3.72	19.3
Berea 3	38.44	25.24	39.858	42.733	3.94	20.5

The produced volumes in the spontaneous imbibition and drainage stages are presented in Table 8.3.

Table 8.3. Produced volumes during spontaneous Amott-Harvey imbibition (AHSI) and drainage (AHSD) stages.
(*) The excepted AHWI denotes the literature reported for cores of equivalent HDA/decane preparation (Kowalewski et al., 2002).

Core	HDA/decane concentration [wt%]	Expected AHWI (*)	AHSI produced volume [ml]	AHSD produced volume [ml]
Berea 1	0.20 ± 0.01	0.04	0.0 ± 0.1	0.0 ± 0.2
Berea 2	0.10 ± 0.01	0.20	0.2 ± 0.1	0.0 ± 0.2
Berea 3	0.0	0.73	1.2 ± 0.1	0.0 ± 0.2

The unaltered core (Berea 3) produced the largest volume of hydrocarbon post-AHSI, whereas the core with the highest amine concentration (Berea 1) produced no hydrocarbon fluid after AHSI. The core at intermediate amine concentrations (Berea 2) produced more hydrocarbon than Berea 1, but significantly less than Berea 3. No cores produced any brine post-AHSD.

Figure 8.5 presents the projected T_1 and T_2 distributions at after each stage (S_o = 1, post-AHSI, post-AHSD), for each core. Figure 8.6 presents the 2D T_1-T_2 distributions at the same saturation endpoints for the three cores. In both, bulk liquid relaxation times for decane and brine are marked for comparison.

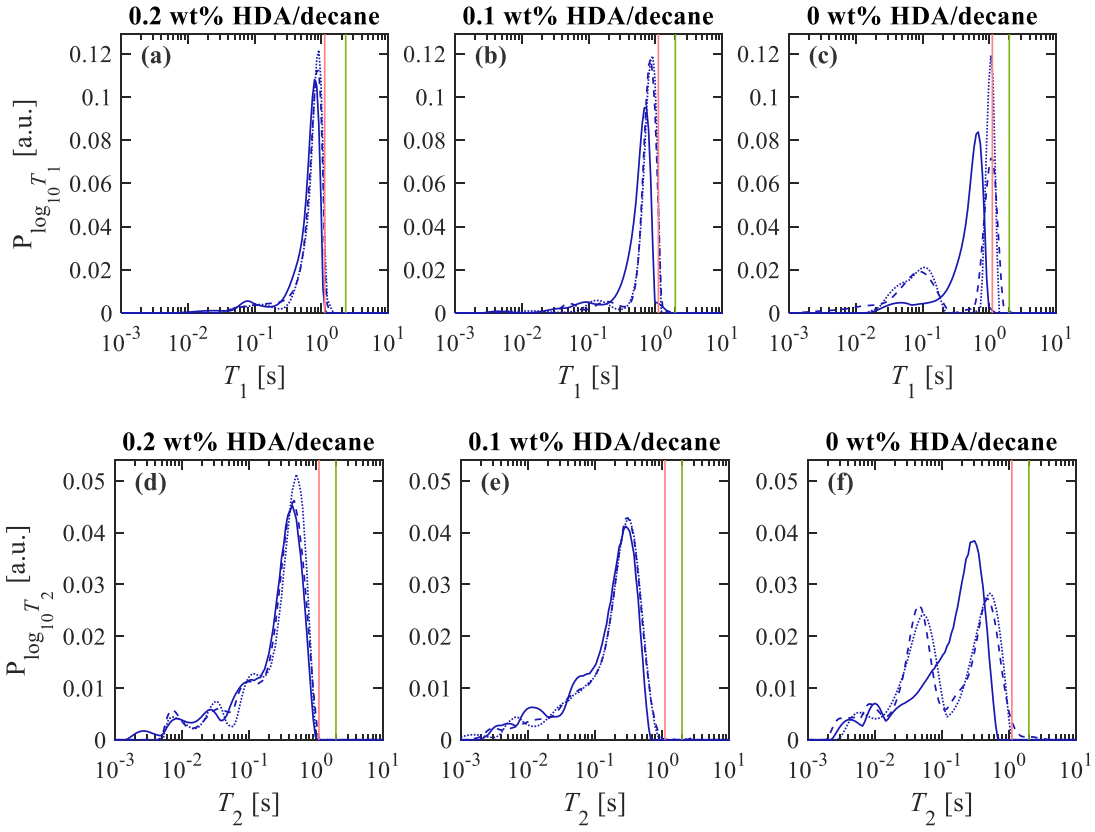

Figure 8.5. (a-c) T_1 and **(d-f)** T_2 distributions, for the three end states: S_o = 1 (—), post-AHSI (--), post-AHSD(⋯), presented separately for the three cores of differing HDA concentration, 0.2 wt% (Berea 1), 0.1 wt% (Berea 2) and 0 wt% (Berea 3). In each figure the bulk T_1 or T_2 values (as appropriate) for decane and brine are indicated with solid red and green lines, respectively.

Figures 8.5 and 8.6 demonstrate that at the initial S_o = 1 state, all rocks display similar relaxation time distributions with a 'tail' in the T_2 dimension. The 0.2 wt% HDA/decane core (Figs. 8.5a,d, 8.6a-c) shows no noticeable change across the three saturation endpoints – consistent with the zero produced volumes in the spontaneous stages. The 0.1 wt% HDA/decane core (Figs. 8.5b,e, 8.6d-f) shows minor change post-AHSI, with a slight lengthening in T_1; no further change is observed post-AHSD. This is again consistent with the produced volumes in the spontaneous stages – small changes in core saturation during AHSI, with no change from AHSD (Table 8.3). Finally, the 0 wt% HDA/decane core (Figs. 8.5c,f, 8.6g-i) shows clear changes in its relaxation time distributions post-AHSI, relative to S_o = 1.

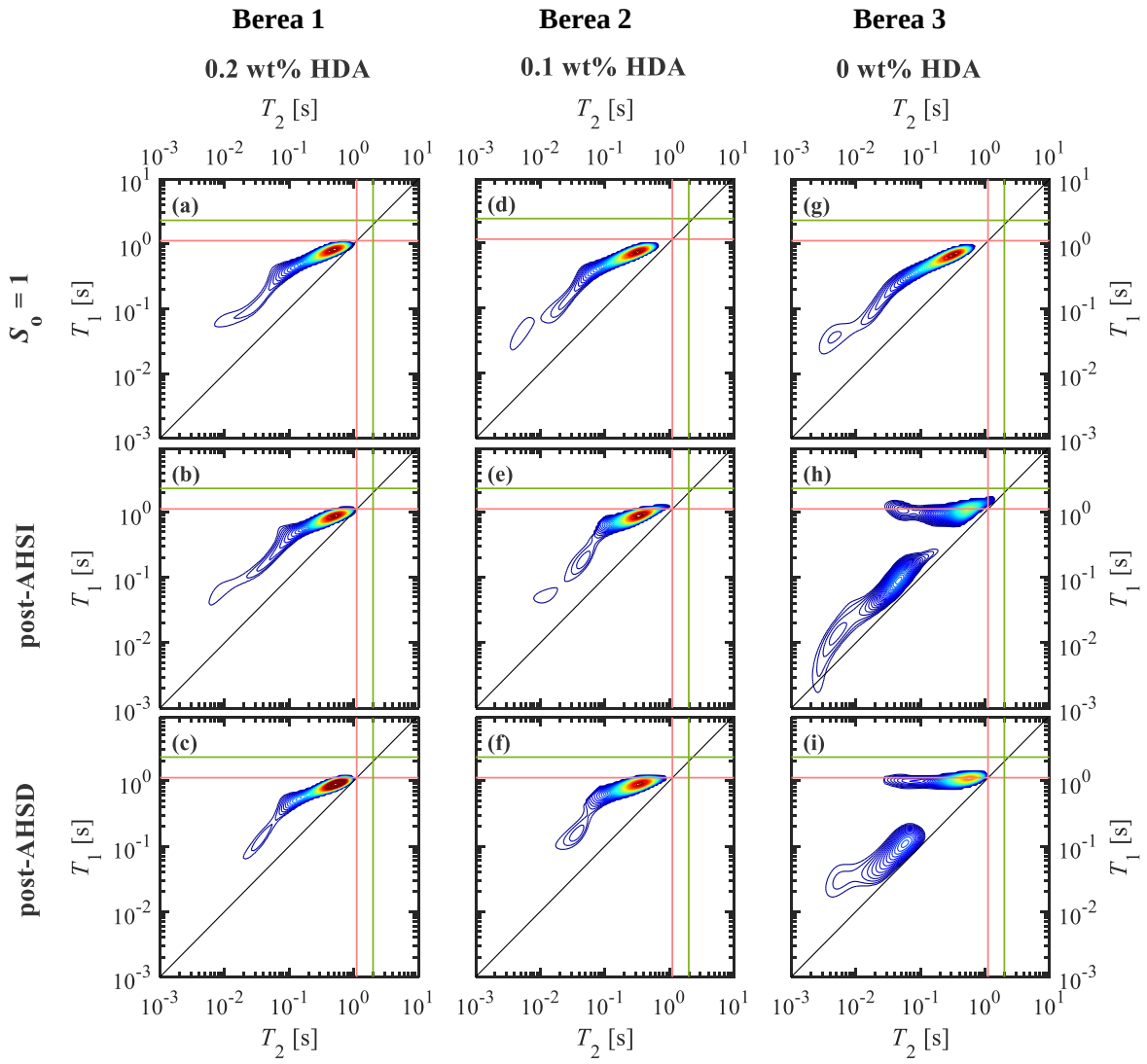

Figure 8.6. 2D T_1-T_2 distributions at the three saturation end points for the three cores. Saturation endpoints (S_o = 1, post-AHSI, post-AHSD) are presented along the rows, the three cores (of 0.2 wt%, 0.1 wt% and 0 wt% HDA/decane saturations) are presented along the columns. For each rock, the 2D correlation maps have been plotted on the same colour scale as their dataset at S_o = 1. Bulk T_1 and T_2 values for decane and brine are indicated with solid red and green lines, respectively.

In both T_1 and T_2 dimensions, the distributions split into two peaks. Both a lengthening and shortening in relaxation time values occur relative to S_o = 1, together with a decrease and increase in signal intensity for the long and short T_1, T_2 regions, respectively. No further changes occur during AHSD. These observations are similarly in agreement with the saturation changes measured volumetrically in the spontaneous imbibition stages (Table 8.3).

The results presented in Table 8.3 and Figs. 8.5-8.6 are hereby discussed and interpreted. It is expected that prior to ageing, the three cores would all initially be strongly water-wetting – as Soxhlet cleaned, Berea sandstone outcrop cores (Worden and Morad, 2000). Based purely on the response in the spontaneous imbibition tests (Table 8.3), it is clear that the addition of hexadecylamine to decane influences the core wettability conditions. Despite having similar pore volumes (a standard deviation of

3.5%, with respect to their mean P.V., Table 8.2), the cores produced considerably different hydrocarbon volumes during AHSI. The 0 wt% HDA/decane core produced 30% of its P.V., the 0.1 wt% HDA/decane core ~5 % of its P.V and the 0.2 wt% HDA/decane core produced none. This suggests that without amine, the cores are water-wet. With amine, the cores become increasingly oil-wet – the extent of oil-wetting increasing with greater amine concentrations. This behaviour agrees with the literature-reported trends and suggests that core samples treated in this way can be used to obtain systems of controlled systematically-altered wettabilities, suitable for conducting benchmarking studies on wettability measurements.

Considering the changes in the relaxation time responses (Figs. 8.5 and 8.6), it is clear that saturation changes occurring in the spontaneous stages (Table 8.3) are reflected in the NMR response. This is observed through: the lack of change in NMR response post-AHSD for all cores; the lack of change in NMR response for the 0.2 wt% core at all points; the small change in T_1 for the 0.1 wt% core post-AHSI; and the significant change for the 0 wt% core post-AHSI. This suggests that such T_1-T_2 measurements are sensitive to saturation changes for the proposed core-oil-brine systems, for use in the T_1-T_2 Amott-Harvey benchmarking study. The lengthened T_2 'tails' present in all datasets are believed to result from internal gradient effects, due to magnetic susceptibilities introduced from clays present in sandstone. Observations of such effects at 2 MHz have previously been observed (Mitchell and Fordham, 2011; Fay *et al.*, 2015).

As the cores were not taken to S_{wir} via a primary drainage from starting conditions of $S_w = 1$, the initial state prior to ageing did not begin with a continuous brine film layer coating the surface of all pores. This negates any assumptions of expected hydraulic continuity of the brine-phase throughout the pore space and hence the short T_1, T_2 signal cannot be unambiguously attributed to surface-wetting brine films – particularly in the 0 wt% HDA/decane case. Unfortunately, it is thus not possible to reliably assign the T_1-T_2 signal to either aqueous or hydrocarbon phases. Likewise, it is not possible to reliably interpret T_1/T_2 trends (assigned to either phase), for probing the comparative system surface interaction strengths. This protocol was selected to rapidly ascertain whether the proposed material system would likely be suitable for conducting the Amott-Harvey T_1-T_2 benchmarking study. The goal was not to obtain quantitative wetting information from the NMR dataset at this stage. Overall, these preliminary tests demonstrate that the decane/amine system material choice facilitates systematic alterations to the wettability of Berea cores, and that T_1-T_2 measurements are sensitive to saturation changes within these systems. This suggested that the materials system was suitable as a base case in the T_1-T_2 Amott-Harvey benchmarking study.

8.3.2 Amott-Harvey Cycle Benchmarking.

The results for the full Amott-Harvey-NMR benchmarking tests are presented as follows: first, the industry-standard, volumetrically-determined *AHWI* is presented; second, the NMR T_1-T_2 measurements

at each Amott-Harvey endpoint are shown. These are subsequently interpreted to obtain saturation, pore residency and wettability information.

8.3.2.1 Industry Standard Amott-Harvey Wettability Index

Table 8.4 presents the core sample properties, Amott-Harvey produced volumes, the gravimetrically-determined saturations following each stage, and the Amott-Harvey wetting indices.

Table 8.4. Summary of initial core properties and Amott-Harvey produced volumes, saturations and calculated wetting indices (see Fig. 8.3 for definitions).

Initial Core Properties		AH Produced Volumes		AH Wetting Indices	
length [mm]	38.52 ± 0.02	V_{os} [ml]	1.7 ± 0.1	I_w	1.00 ± 0.36
diameter [mm]	25.17 ± 0.02	S_w post-V_{os}	0.54 ± 0.04	I_o	0 ± 0
dry mass [g]	39.828 ± 0.001	V_{of} [ml]	0.0 ± 0.6	*AHWI*	1.00 ± 0.36
wet mass [g]	43.826 ± 0.001	S_w post-V_{of}	0.54 ± 0.15		
P.V. [ml]	4.00 ± 0.01	V_{ws} [ml]	0.0 ± 0.1		
φ [%]	20.9 ± 0.1	S_w post-V_{ws}	0.54 ± 0.16		
S_{wir}	0.12 ± 0.02	V_{wf} [ml]	0.5 ± 0.6		
		S_w post-V_{wf}	0.42 ± 0.22		

The produced volumes reported in Table 8.4 show that a significantly greater volume of fluid is displaced in AHSI (V_{os}) rather than AHSD (V_{ws}), suggesting that the core is water-wetting. This is confirmed in the *AHWI* calculation, which gives a value of 1.00 ± 0.36, indicating a strongly water-wetting sample. It is important to note that the errors in produced volumes at the forced stages are considerably higher than for the spontaneous stages. Whilst the latter is governed by the sensitivity of the Amott cells, the former is limited by large CFS dead volumes connecting the RCH outlets to the CFS, (section 4.3.5.3). Consequently, a large fluid volume, relative to the core P.V., must be flushed through the CFS to ensure that all produced core fluids are evacuated. In turn, these flushed volumes require either large measuring cylinders for collection, or multiple readings from smaller collection vessels with more sensitive graduations – both result in greater measurement uncertainties than the spontaneous stage measurements.

8.3.2.2 NMR-Tracked Amott-Harvey Benchmarking Study

In this section, the T_1, T_2 and T_1/T_2 information obtained from the T_1-T_2 datasets at each Amott-Harvey endpoint is presented. This is subsequently interpreted, alongside supporting information obtained from L-T_2 endpoint and dynamically-tracked T_1-T_2 measurements in the primary drainage flood. The 2D T_1-T_2 correlation maps acquired at each Amott-Harvey cycle endpoint are presented in Figure 8.7. Bulk liquid relaxation times for decane and brine are also presented on each correlation map, for reference.

Figure 8.7 shows that at $S_w = 1$ and S_{wir} three regions of T_1, T_2 signal are observed; in all other stages two regions are observed. These regions are defined as “short-”, “mid-” and “long-” range relaxation times,

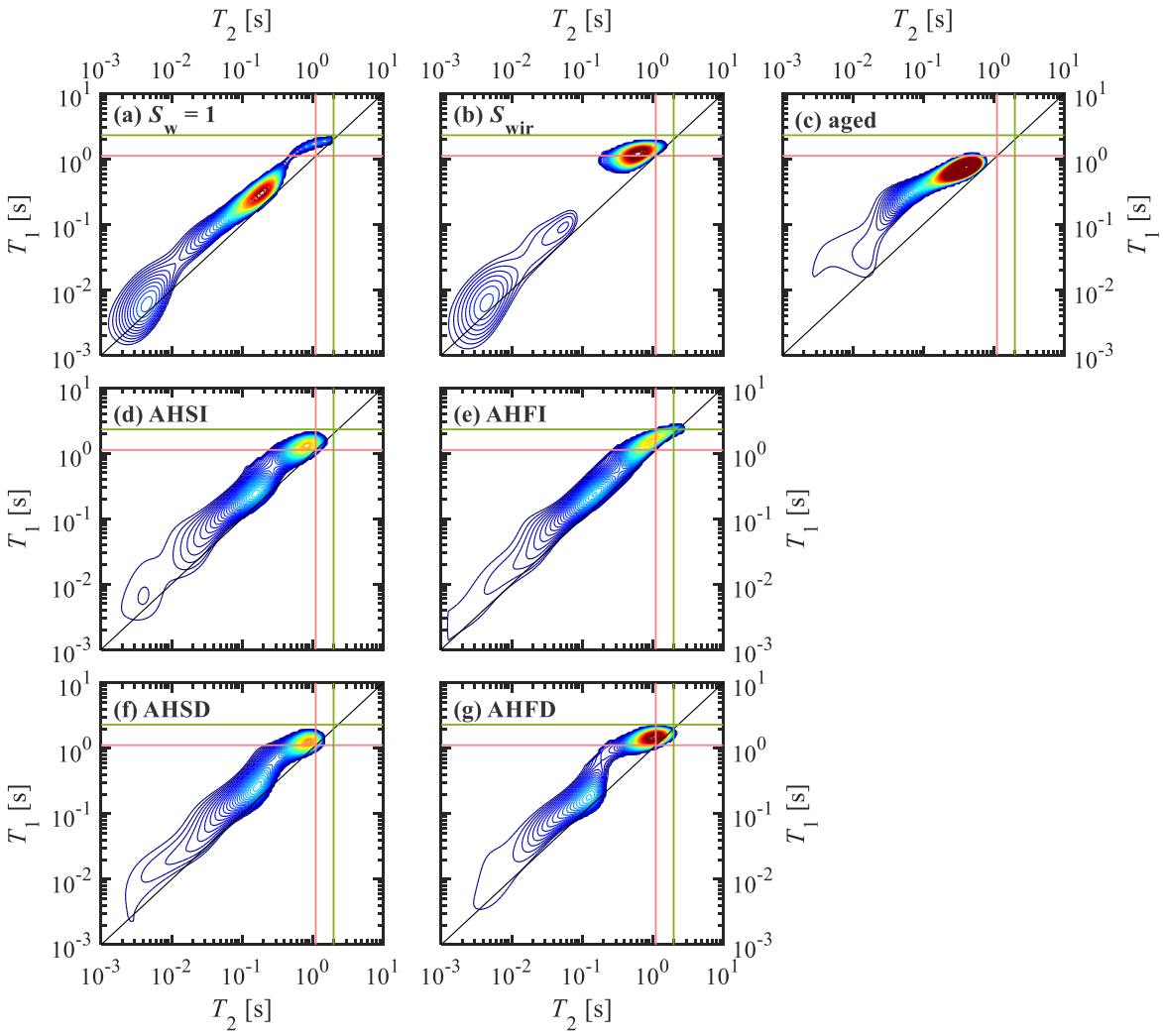

Figure 8.7. 2D T_1-T_2 maps at the core preparatory states and after each Amott-Harvey endpoint. The datasets pertaining to each end stage are labelled (S_w = 1, S_{wir}, aged, AHSI, AHFI, AHSD, AHFD), and all datasets are presented on the same colour scale. Bulk liquid T_1 and T_2 values of decane and brine are demarcated with red and green lines, respectively.

where short-range denotes T_1, T_2 < 10 ms, mid-range denotes 10 ms < T_1, T_2 < ~200 ms and long-range denotes T_1, T_2 > ~200 ms. For each endpoint in Fig. 8.7, the log-mean relaxation times of these signal regions are summarised in Table 8.5. The T_1/T_2 ratio of these log-mean relaxation times are also presented. It is interesting to note that for all endpoints, the T_1/T_2 ratios in the mid-relaxation time region are consistently larger than those recorded in the long-relaxation time region.

At S_w = 1 and S_{wir}, NMR measurements were conducted with the core and ceramic pressure disc. At S_w = 1, the T_1-T_2 distribution consists of a low intensity signal at very short relaxation times ($T_{1,LM}$ = 7 ms, $T_{2,LM}$ = 4 ms), a broad high-intensity distribution in the mid-range, and a low intensity signal, with relaxation times close to those of bulk liquid brine. At S_{wir}, the short T_1, T_2 signal persists and the mid-range signal reduces in intensity whilst its $T_{1,LM}$, $T_{2,LM}$ are shortened. The majority of signal is now in line with the T_1, T_2 of bulk liquid decane. Following primary drainage, the ceramic disc was removed and the core was aged. Post-ageing, the short T_1, T_2 signal disappears and a broad distribution appears,

consisting of a low intensity shoulder at $T_{1,LM}$ = 0.06 s, $T_{2,LM}$ = 0.02 s, and a high intensity peak at $T_{1,LM}$ = 0.57 s, $T_{2,LM}$ = 0.30 s. This long T_1, T_2 signal region has shortened relaxation times relative to S_{wir}.

Table 8.5. Log-mean relaxation times ($T_{1,LM}$ and $T_{2,LM}$) for the regions of signal intensity (short, mid, long) in the T_1-T_2 maps at each endpoint in Fig. 8.7. Region cut-offs were applied based on the minima in the signal projection onto the T_1=T_2 diagonal. The T_1/T_2 ratio, determined from the $T_{1,LM}$ and $T_{2,LM}$ of each region, is also presented.

	$T_{1,LM}$ [s]			$T_{2,LM}$ [s]			$(T_1)_{LM}$ / $(T_2)_{LM}$ [-]		
State	$T_{1,LM}$ SHORT	$T_{1,LM}$ MID	$T_{1,LM}$ LONG	$T_{2,LM}$ SHORT	$T_{2,LM}$ MID	$T_{2,LM}$ LONG	$T_{1,LM}$ / $T_{2,LM}$ SHORT	$T_{1,LM}$ / $T_{2,LM}$ MID	$T_{1,LM}$ / $T_{2,LM}$ LONG
S_w = 1	0.007	0.21	1.76	0.004	0.12	1.47	1.6	1.8	1.2
S_{wir}	0.007	0.07	1.16	0.004	0.03	0.55	1.6	2.1	2.1
aged	-	0.06	0.57	-	0.02	0.30	-	2.5	1.9
AHSI	-	0.12	1.11	-	0.07	0.71	-	1.7	1.6
AHFI	-	0.12	1.31	-	0.07	0.83	-	1.8	1.6
AHSD	-	0.12	1.07	-	0.07	0.72	-	1.6	1.5
AHFD	-	0.12	1.10	-	0.07	0.68	-	1.8	1.6

Post-AHSI, two signal regions are observed – the first occupies similar relaxation times as the mid-range signal at S_w = 1, although with reduced $T_{1,LM}$ and $T_{2,LM}$ values; the second consists of a sharp peak at longer T_1, T_2, in line with bulk liquid decane, as at S_{wir}. Post-AHFI, little further change occurs, however the signal at long T_1, T_2 lengthens, with relaxation times now akin to bulk liquid brine. Following AHSD, this signal region disappears and the T_1-T_2 map closely resembles that post-AHSI. Post-AHFD, the short T_1, T_2 region displays a reduced range of relaxation times and the long T_1, T_2 region increase in intensity. Across each Amott-Harvey endpoint (AHSI to AHFD), little change occurs for signal at mid-range T_1, T_2 values (both in intensity and relaxation times); the greatest changes occur in the long T_1, T_2 regions, following the forced injection stages (AHFI, AHFD).

Considering Fig. 8.7, each T_1-T_2 dataset lies along the T_1 = T_2 diagonal, except for that post-ageing. Therein, the greatest deviation from the diagonal is seen in the mid-range T_1, T_2 region where $T_{1,LM}/T_{2,LM}$ is 2.5. However, the maximum T_1/T_2 ratio attained in this region is significantly larger. This is demonstrated in Fig. 8.8, which presents the distribution of T_1/T_2 ratios for the T_1-T_2 datasets in Fig. 8.7.

The results presented in Figs. 8.7, 8.8 and Table 8.5 are hereby discussed and interpreted, utilising supporting information from L-T_2 endpoint and T_1-T_2 measurements dynamically acquired during primary drainage. The interpretation of the T_1-T_2 datasets is based upon the same essential principles previously outlined in section 5.4, notably: relaxation time values are indicative of sample pore size distributions (under single fluid saturation); long T_1, T_2 values are associated with fluid saturating large pores, and vice versa; the T_1/T_2 ratio is an indicator of wettability, with larger T_1/T_2 values signifying greater surface interaction strengths, and vice versa.

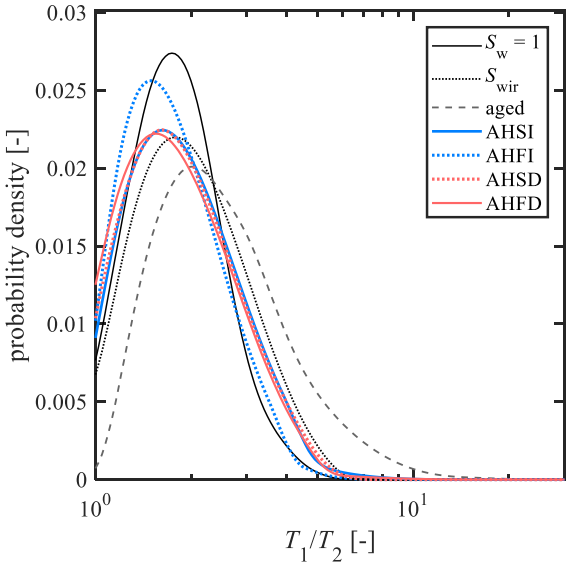

Figure 8.8. Distributions of T_1/T_2 ratios from the T_1-T_2 datasets at each Amott-Harvey cycle end-point.

At S_w = 1 (Fig. 8.7a), the environment measured consists of a brine-saturated core, brine-saturated ceramic disc and remnant injected bulk liquid brine (at the interface between the ceramic disc and the RCH PEEK endplate). The low intensity signal at the shortest relaxation times is interpreted as resulting primarily from the ceramic disc. With an effective pore size of 0.16 µm (two orders of magnitude smaller than the average pore sizes in Berea sandstones), it is expected that the ceramic disc occupies the smallest relaxation times. Likewise, the low intensity signal at long relaxation times is interpreted as remnant bulk liquid brine, following forced brine injection. The broad distribution at mid-range T_1, T_2 is assigned to resulting from the core, thus indicative of its pore size distribution. These assignments are further validated by an L-T_2 measurement at S_w = 1 (Fig. 8.9).

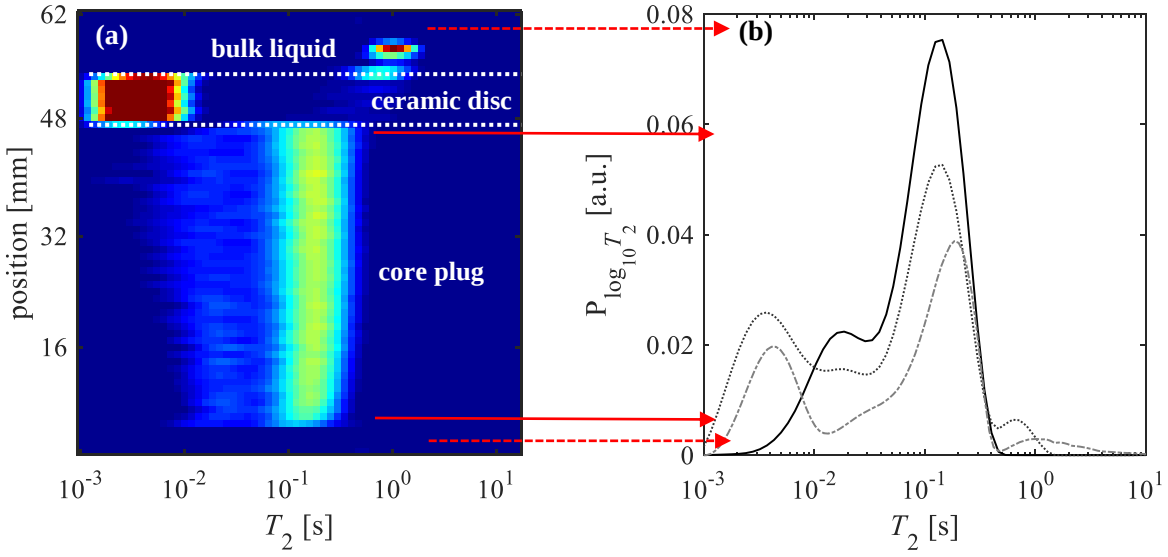

Figure 8.9. (a) L-T_2 dataset of the sample at S_w = 1. **(b)** Comparison of normalised, projected T_2 distributions at S_w = 1, obtained from: the L-T_2 dataset, over the core only (—); the L-T_2 dataset over the entire imaging FOV(···); and projected from the T_1-T_2 dataset in Fig. 8.7a (- - -).

Figure 8.9a presents the variation of T_2 along the sample imaging FOV, validating that the signal with the shortest and longest T_2 values result from the ceramic disc and bulk liquid brine respectively. Figure 8.9b compares the T_2 distributions obtained across only the core region (using L-T_2) and across all regions of the FOV (using both L-T_2 and T_1-T_2 datasets). The L-T_2 and T_1-T_2 global T_2 distributions qualitatively show good agreement in their trends, with some T_2 shortening in the L-T_2 dataset (as expected - see section 3.3.2.2). From the T_2 distributions across the core only (L-T_2), it can be inferred that the core has a broad, largely unimodal pore size distribution. The shoulder peak at shorter T_2 values is believed to result from clay-bound waters (CBW), common to sandstones. In well-logging analysis, a cut-off of $T_2 < 33$ ms is accepted as standard for sandstone CBWs (Coates *et al*., 2001).

At S_{wir} (Fig. 8.7b) the signal at short relaxation times is again interpreted as the ceramic disc. Relative to $S_w = 1$, the reduction in mid-range relaxation times, coupled with the decreased intensity in the region, is interpreted as a lowered brine saturation with brine now filling only the smallest pores and crevices, providing a continuous wetting layer throughout the pore space. The discrete signal at long T_1, T_2 is interpreted as injected decane filling the centres of large pores, in which brine maintains a surface-wetting film. This lack of direct interaction between the decane and pore surface, together with the greater oil globule size achievable in larger pores, results in T_1, T_2 values close to a bulk liquid decane response. This assignment is further validated in Fig. 8.10, which presents T_1-T_2 and L-T_2 measurements dynamically acquired throughout the primary drainage.

Figure 8.10a demonstrates that during primary drainage, the signal originally assigned to brine fully-saturating the pore space at $S_w = 1$ (mid-range T_1, T_2) reduces in intensity and occupies progressively shorter relaxation times, whilst a signal with increasing intensity appears at relaxation times close to bulk liquid decane. These trends continue with sustained decane injection until two discrete signal regions form at S_{wir}. This is similarly observed in the L-T_2 datasets. Figure 8.10b also reveals that from $S_w = 0.33$ to S_{wir}, an increased shortening in T_2 values is observed at the core outlet. This is attributed to pressure effects incurred from the ceramic disc method of achieving S_{wir} – as in section 5.4.

Returning to Fig. 8.7c, post-ageing, the disappearance of signal at short T_1, T_2 is attributed to having removed the ceramic disc, the shift from discrete oil and water signals to a continuous distribution is attributed to a redistribution of pore fluids. The greatest T_1/T_2 is observed in the region associated with brine, suggesting a comparatively stronger surface interaction exists with brine, rather than oil – indicative of a water-wet core. Further, the reduction in relaxation times, most noticeably observed at long T_1, T_2 (signal region attributed to decane), indicates an increased surface interaction with decane after ageing. This is similarly manifested in its T_1/T_2 response – the decane region is further from the $T_1 = T_2$ diagonal, relative to at S_{wir} (Fig. 8.7b). The shortened relaxation times and the shift from discrete oil-water signals to a continuous distribution, post-ageing is consistent with prior observations in the literature (Guan *et al.*, 2002; Al-Mahrooqi *et al.*, 2005).

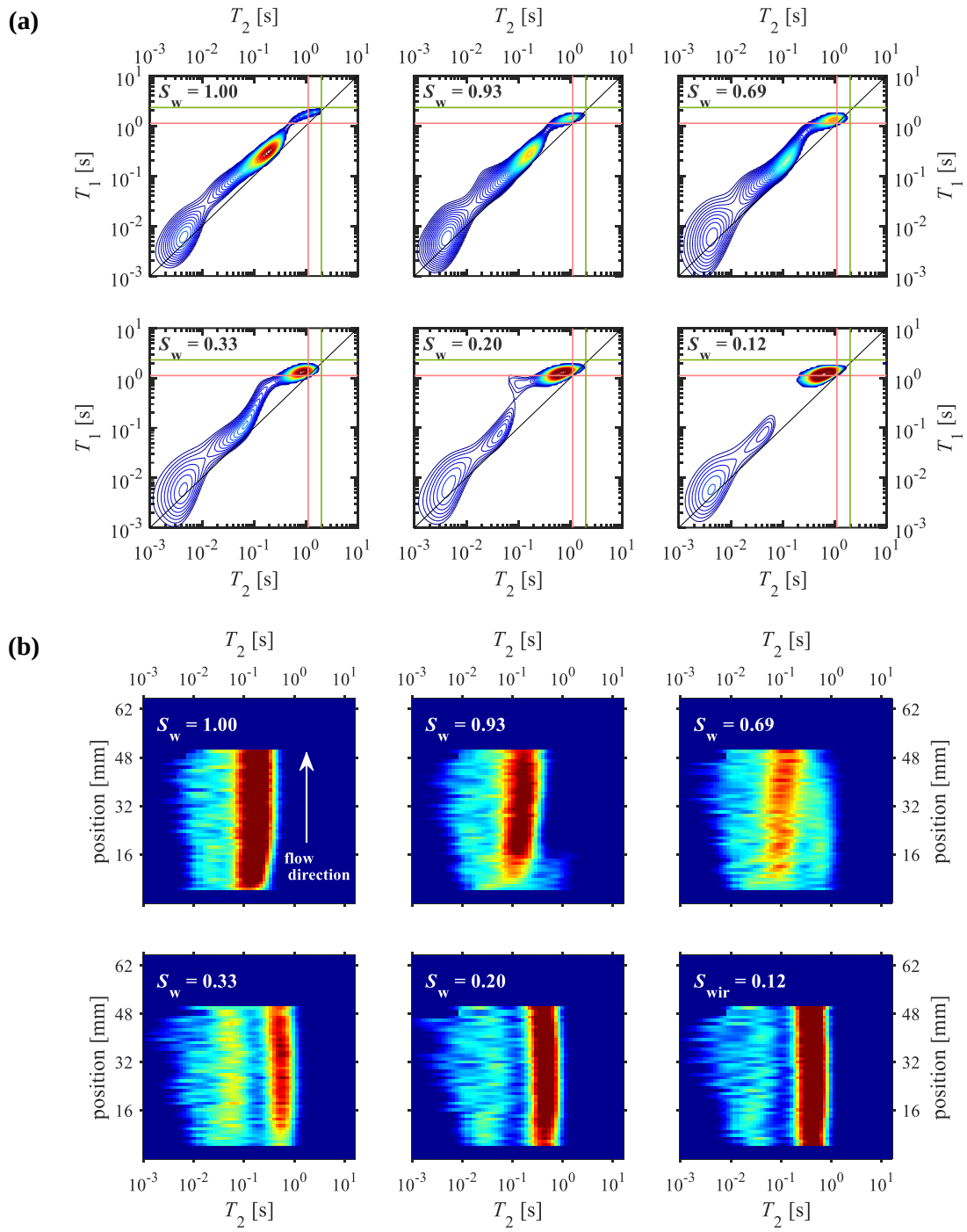

Figure 8.10. (a) T_1-T_2 and **(b)** L-T_2 measurements acquired dynamically throughout the primary drainage at six different saturation conditions, from $S_w = 1$ to S_{wir}. For the L-T_2 datasets, only the signal pertaining to the core is presented.

Such shifts in relaxation times can be used to infer changes in pore residency of the saturating fluids during ageing (Al-Mahrooqi *et al.*, 2005). These changes are more clearly observed through the L-T_2 datasets which facilitate unambiguous comparisons of T_2 changes from ageing, by negating all signal not pertaining to the core – as presented in Fig. 8.11, at $S_w = 1$, S_{wir} and post-ageing. At $S_w = 1$ the brine saturates the full pore size distribution of the core (see discussion for Fig. 8.9). At S_{wir}, the clay-bound water (at $T_2 < 33$ ms) is maintained and the peaks previously assigned to (i) wetting brine in the small

pores and surface film, and (ii) decane in large pore centres, are clearly seen (see discussion for Fig. 8.7b).

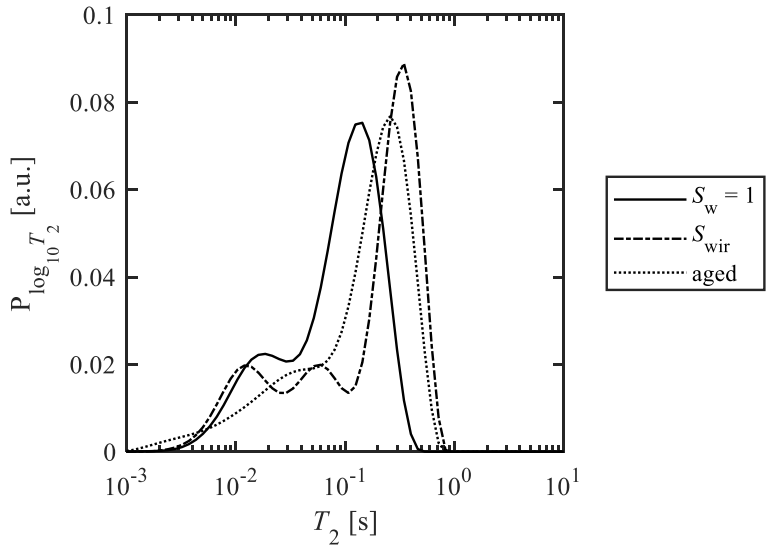

Figure 8.11. T_2 distributions at S_w = 1, S_{wir} and post-ageing, from endpoint L-T_2 measurements, considering signal only pertaining to the core.

Relative to S_{wir}, post-ageing, T_2-shortening is observed across all regions of the distribution and a continuous, poorly-defined distribution replaces the distinct peaks previously observed at T_2 < 100 ms. Al-Mahrooqi *et al.* (2005) reported similar observations on a T_2-monitored ageing study in sandstones cores. The authors attributed both the increased intensity and reduction in relaxation times in short-T_2 regions to a reduction in water-wetting film size, leading to water accumulation in surface crevices. This was believed to result in partial collapse of certain water films, in turn allowing oil ganglia to contact the pore surface and thus explaining the T_2-shortening of the oil peak – reflecting a reduced proportion of oil molecules relaxing with bulk liquid behaviours. It is believed that this interpretation proposed by Al-Mahrooqi *et al.* can explain the changes observed post-ageing in Fig. 8.11.

Considering Fig. 8.7d (post-AHSI), the signal at mid-range relaxation time values occupying a similar region as the core at S_w = 1, is attributed to imbibed brine from AHSI. With shorter $T_{1,LM}$ and $T_{2,LM}$ than at S_w = 1, this suggests that brine does not occupy the full pore size distribution – instead residing in small-to-mid sized pores and a progressively thickening wetting film. This concurs with established mechanisms for brine imbibition in water-wet formations (Dullien, 1992). The signal at long relaxation times is here still attributed to decane in large pore centres, and the low intensity tail at T_1, T_2 < 30 ms is assigned to CBWs and internal gradient effects – the latter of which were demonstrated to be present in this sample using the variable-echo spacing CPMG experiment.

It is interesting to note that post-AHSI, the brine signal no longer displays a strongly elevated T_1/T_2, unlike after ageing. This is similarly observed in Fig. 8.8, for which the greatest T_1/T_2 ratios are only apparent in the aged state. At and beyond AHSI, the T_1/T_2 distributions most closely resemble those

post-primary drainage and at $S_w = 1$. This behaviour is interpreted as follows. Post-ageing, all brine signal would result from the residual water saturation in the small pores, and as hypothesised, the thinning and partially-collapsed wetting film and surface crevices. This would be surface-bound water, for which a high T_1/T_2 is expected. During AHSI, however, a large volume of brine re-entered the pore space – this would be capillary-bound, rather than surface-bound. It is thus expected that whilst the strong surface interaction with the wetting film would still be present, the comparatively large brine volume in this capillary-bound state would dominate the T_1-T_2 response. This would explain why the brine signal is seen to return to the $T_1 = T_2$ diagonal.

Comparing post-AHSI, post-AHFI and post-AHSD (Figs. 8.7d-f), little change is observed in their T_1-T_2 distributions, interpreted as the core undergoing minimal changes in its saturation at these points in the Amott-Harvey cycle – as expected for a strongly water-wet core. The lengthening in relaxation times post-AHFI is attributed to residual liquid brine in the injection lines. Post-AHFD, an increasing intensity in the oil region occurs – suggesting an increased decane saturation. Further, the brine signal occupies a narrower range of relaxation times, suggesting that decane is now filling smaller pores.

Based upon these interpretations and T_1-T_2 signal assignments to the oil- and brine-phases, it is possible to obtain core saturation measurements from the NMR data. The greatest contrast in the assigned oil- and brine- phase signals was achieved by applying a cut-off perpendicular to the $T_1 = T_2$ diagonal. Accordingly, each 2D T_1-T_2 data matrix was projected onto the $T_1 = T_2$ diagonal. Whilst clear minima in the projected distributions were obtained, the signal intensity at these minima did not reach zero. To deconvolve the signals in these regions, Gaussian distributions were fitted to the two peaks about each minimum, using a trust-region algorithm. For the $S_w = 1$ and S_{wir} datasets, the deconvolution was applied for the core brine and ceramic disc signal regions. For the post-AHSI, -AHFI, -AHSD and -AHFD datasets, this was applied at the minimum in the brine-oil signal region. The total signal intensities in each assigned region within the projected distributions were summed, the HI correction for each fluid phase was applied and the brine and oil saturations were subsequently calculated.

The NMR-determined core saturations are reported in Table 8.6. The error bars are based upon the error propagation incurred through the: intensity fitted at each co-ordinate of the 2D T_1-T_2 matrix through the regularisation method (see error analysis discussion in section 3.2.2.3); the random error in the T_1-T_2 measurement; the error in the measured HIs; and the regions of peak overlap in the deconvolutions applied to the projected T_1-T_2 distributions. It is not possible to unambiguously determine the NMR saturation in the post-aged dataset due to the bridging of oil- and brine-phase signals. The saturation would not, however, have been expected to change during ageing as the core was submerged in oil immediately following a high pressure forced injection (see protocol section 8.2.2.2). The *AHWI*s from NMR have been subsequently calculated and are also reported in Table 8.6.

Table 8.6. NMR saturations at each endpoint state, determined based upon interpreted signal assignments in T_1-T_2 datasets. *AHWI*s calculated from these NMR saturations are also presented.

Endpoint NMR Saturations		**AH Wetting Indices**	
$S_w = 1$	1.0 ± 0.0	I_w	1.00 ± 0.14
S_{wir}	0.119 ± 0.006	I_o	0 ± 0
Aged	—	*AHWI*	1.00 ± 0.14
AHSI	0.625 ± 0.035		
AHFI	0.579 ± 0.034		
AHSD	0.644 ± 0.036		
AHFD	0.502 ± 0.019		

The elevated uncertainties in the saturations post-AHSI, -AHFI and -AHSD (Table 8.6), result from the overlaps in the deconvolved fitted peaks, for the signal intensity regions assigned to brine and decane. Post-AHFD, the proportion of signal intensity in the overlapped region is reduced, hence the decrease in the uncertainty.

A significant increase in water saturation following AHSI is observed, in agreement with the volumetric observations. Whilst the saturations post-AHSI through to AHFD show fluctuations, no change is discernible within the uncertainty of the measurements. This is thus interpreted as a zero change in core saturation – likewise in agreement with the volumetric observations. Comparing the NMR T_1-T_2-measured and volumetrically-determined saturations (Table 8.4), it is observed that the T_1-T_2 measurements consistently yield higher water saturations. The error margins in the volumetric measurements are considerably larger than those from NMR. These primarily result from the uncertainties in quantifying produced volumes in the forced injection stages. These errors are then further propagated in the saturations at subsequent stages of the AH cycle, for which their calculation is dependent on preceding saturation measurements. Nonetheless, within the uncertainties of both measurements, the NMR-determined and volumetrically-determined saturations are in agreement. Likewise, the *AHWI*s determined using both techniques are in agreement – both indicating that the core is strongly water-wet.

The original goal of the study was to test the sensitivity of the T_1/T_2 measurement at 2 MHz on a base case core sample of controlled, known wettability, and to benchmark this against the industry-standard Amott-Harvey measurement. Two key observations can be drawn from the trends in T_1/T_2 responses in Fig. 8.7 and Table 8.5: (i) for most endpoint datasets, only small differences exist in the T_1/T_2 ratios of the wetting brine and non-wetting hydrocarbon phases; (ii) across all datasets, T_1/T_2 is consistently greater in the T_1-T_2 signal associated with brine, than that associated with hydrocarbon (Table 8.5).

The small differences in T_1/T_2 responses are interpreted as resulting from the reduced sensitivity of T_1/T_2 to surface interactions at low magnetic field strengths. As discussed in section 2.4.4.2, the ratio of surface relaxivities ρ_2/ρ_1, and thus the sensitivity to T_{1s}/T_{2s} increases with field strength. For Berea

sandstones, surface relaxivity ratios have been reported as: $1.6 < \rho_2/\rho_1 < 2.1$ (Zhang *et al.*, 1998), $\rho_2/\rho_1 = 1.5$ (Tinni *et al.*, 2014; Washburn *et al.*, 2017) and 1.74 (Kleinberg *et al.*, 1993). These values suggest that differences in T_1/T_2 between the wetting and non-wetting species would be expected to occur, but at lower sensitivities relative to that possible at higher field strengths, such as the reported $\rho_2/\rho_1 = 3.4$ for Berea sandstones at 12 MHz (Mitchell and Fordham, 2014).

The consistently greater T_1/T_2 ratio of the brine signal indicates that the core is water-wet. This was apparent in all T_1-T_2 measurements conducted at mixed saturations and is in agreement with the benchmarked Amott-Harvey measurement. However as noted in section 2.4.4.2, the observed T_1/T_2 is not only dependent on surface interaction strengths, but also on the bulk relaxation times, such that the sensitivity of T_1/T_2 can reduce at larger pore sizes:

$$\frac{T_1}{T_2} = \frac{T_1^{(\text{surface})}\left(T_2^{(\text{surface})} + T^{(\text{bulk})}\right)}{T_2^{(\text{surface})}\left(T_1^{(\text{surface})} + T^{(\text{bulk})}\right)} \tag{8.5}$$

where T_1/T_2 is the observed T_1/T_2 ratio, $T_1^{(\text{surface})}/T_2^{(\text{surface})}$ is the ratio of surface relaxivities, equivalent to ρ_2/ρ_1, and T^{bulk} is the bulk liquid $T_{1,2}$, assuming that $T_{1,\text{bulk}} \equiv T_{2,\text{bulk}}$.

Accordingly, it is important to verify that the reduced T_1/T_2 ratios observed in the hydrocarbon region of the T_1-T_2 datasets do not lie within this sensitivity limit and can indeed be interpreted as reduced interaction strengths, rather than reduced sensitivities at larger pore sizes. Using the method outlined in Valori *et al.* (2017), the limiting regions of sensitivity in the observed T_1/T_2 at differing relaxation times can thus be simulated. This was conducted using the expected range of $1.5 < \rho_2/\rho_1 < 2.1$ quoted in the literature, and for mean bulk relaxation time values of $T_{\text{bulk,decane}} = 1.11$ s and $T_{\text{bulk,brine}} = 2.15$ s, as presented in Fig. 8.12.

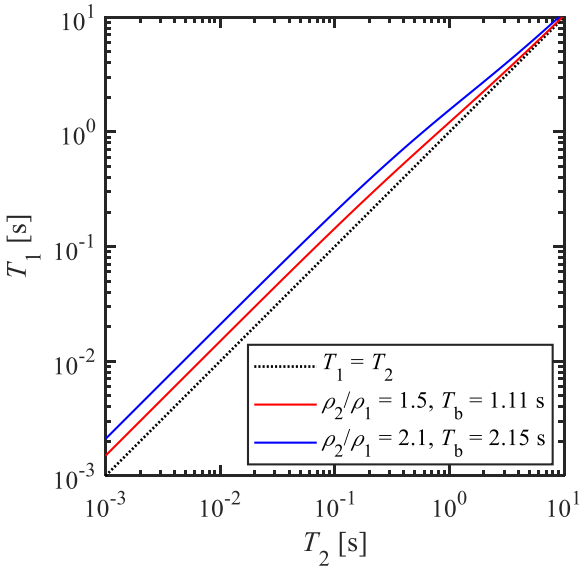

Figure 8.12. Simulated T_1/T_2 ratios for fixed bulk liquid relaxation time values, T_b, and fixed surface components of relaxation ($T_{1s}/T_{2s} \equiv \rho_2/\rho_1$). Expected upper (blue) and lower (red) limiting bounds for the Berea-decane-brine system at 2 MHz are presented. Bounds calculated based upon T_b values of decane and brine, and literature-reported range of ρ_2/ρ_1 values for Berea sandstone at 2 MHz.

Figure 8.12 demonstrates that for the expected limiting bounds in the Berea-decane-brine system at 2 MHz, the observed T_1/T_2 is sensitive to surface interaction strengths within the range of relaxation time values $10^{-2} < T_{1,2} < 10^{0}$ observed in the Berea sample (see Fig. 8.7). Loss of sensitivity in obtaining surface information is expected to occur beyond relaxation times circa 10^{0} s, beyond which T_1/T_2 tends towards unity. Below this cut-off the sensitivity of the observed T_1/T_2 does not noticeably change, suggesting that the T_1/T_2 of brine and decane signals, as indicators of wettability, are indeed comparable.

8.4 Conclusions and Future Work

In this work, the industry-standard Amott-Harvey wettability measurement was applied to a base case water-wet Berea sandstone core sample. This was monitored using the global 2D NMR T_1-T_2 and the spatially-resolved L-T_2 measurement. The goal was to test the sensitivity of the T_1/T_2 ratio at 2 MHz, and to benchmark this against the AHWI. A field strength of 2 MHz was selected as this is directly comparable to those used in conventional SCAL and well-logging tool NMR measurements. All measurements were conducted non-invasively on undoped systems, to enable the monitoring of wettability trends in both hydrocarbon and aqueous phases. Continuous NMR monitoring of all stages of the AH cycle was employed, facilitating unambiguous assignment of any changes in NMR response to core saturation and wettability changes.

The results demonstrate that NMR relaxation time measurements deliver a wealth of additional information beyond that which can be obtained through standard SCAL AH wettability measurement protocols. Firstly, T_1-T_2 measurements have been used to probe pore filling environments – not only at the Amott-Harvey cycle endpoint states, but also to continuously monitor dynamic changes in the pore-filling environments under forced injection protocols. Secondly, utilising the chemical contrast achievable through 2D T_1-T_2 measurements, the core saturations and NMR-determined AHWIs were quantified. These were benchmarked against standard volumetric AH approaches, and provided independent measures of saturation at each AH endpoint. This contrasts with the standard volumetrically-determined saturations, whose quantification is dependent upon measurements at prior stages in the cycle. In addition, the L-T_2 measurement was also used to provide additional information for signal assignment in the T_1-T_2 datasets, otherwise undiscernible through bulk measurements alone.

The results of this study suggest that the T_1/T_2 ratio at 2 MHz is sensitive, albeit weakly, to the core sample wettability – here, the T_1/T_2 measurement yielded results in line with the industry-standard Amott-Harvey wettability index. It is particularly interesting to note that the T_1/T_2 ratio can be used to infer the core wetting state at premature stages within the Amott-Harvey cycle – in this case, at the restored state post-ageing and following AHSI. This holds the potential for providing a wettability measurement without the requirement for completing the full Amott-Harvey cycle – if feasible, an incredibly valuable tool for both downhole WLT *in situ* measurements of reservoir wettability, and rapid wettability measurements in SCAL applications. Further work however needs to be completed through

repeating this study on an oil-wet base case core. It is suggested that the hexadecylamine in decane method for synthetically-altering the wettability of Berea cores, as identified in the preliminary screening tests within this work, should be followed. This would offer the same bulk T_1, T_2 relaxation properties in the hydrocarbon phase, enabling direct comparisons to the water-wet base case tested herein.

Furthermore, it has been demonstrated that at 2 MHz the T_1/T_2 ratio suffers from limited sensitivity and could benefit from being taken to higher fields. It is thus proposed that a systematic study exploring the sensitivity of the T_1/T_2 wettability measurement be conducted in samples of controlled wettabilities at different magnetic field strengths. Conducting measurements at high fields would still be of relevance to SCAL studies, wherein the field strength applied would not be limited by the low-fields commanded in WLTs.

Finally, whilst in this particular system the T_1-T_2 method was able to achieve sufficient chemical contrast, the addition of enhanced contrast would be beneficial – particularly for application to more complex samples, such as those encountered with crude oils, in which such clear cut T_1, T_2 responses may not be so easily achievable. The inclusion of D-T_2 measurements in future iterations of this work are thus recommended. In addition, if measurements are to be conducted at higher fields, the inclusion of spectral resolution in the T_1 and T_2 measurements would also become feasible and may be a desirable option. Caution would have to be taken to ensure that any elevated field strengths do not present significant increases in internal gradient effects, that compromise the quality of the T_1/T_2 data (D'Agostino *et al.*, 2014).

Chapter 9

Summary of Conclusions and Future Work

9.1 Summary of Conclusions

Chapter 1 introduced the industrial relevance of studying oil recovery processes. In this context, the aims of this thesis were to use NMR to non-invasively, quantitatively and dynamically study EOR core floods and standard SCAL procedures at reservoir-representative conditions, to: (i) develop a deeper understanding of core- and pore-level mechanisms by which oil recovery processes take place; and (ii) assess standard SCAL procedures for sample preparation and characterisation, with a view to benchmarking NMR alternatives.

Chapters 2, 3 and 4 introduced the techniques and equipment used throughout this thesis. Chapter 2 provided a background to NMR and MRI theory. Chapter 3 focused on the implementation, development and validation of spatially-resolved NMR relaxometry L-T_1-T_2 and L-T_2 sequences on 85 MHz and 2 MHz magnet systems. Chapter 4 detailed the MRRC core flooding system, which facilitated conducting core floods at reservoir-representative conditions.

Chapter 5 continuously monitored the primary drainage of oil into a brine-saturated Bentheimer core using the semi-permeable ceramic disc method. Simultaneous measurement of pore pressures and spatially-resolved NMR relaxometry allowed for characteristic features in the capillary pressure curve to be related to internal core fluid distributions. Axial heterogeneities in pore filling processes were revealed, with oil saturation increasing preferentially at the core outlet, closest to the ceramic disc. At the onset of capillary pressure rise, and as irreducible water saturation conditions were approached, a continuous brine-wetting film formed throughout the core. Thinning of the brine-wetting film with increasing pressure was also observed. Whilst previously noted in the literature within optically-transparent glass micromodels, this work provided direct experimental evidence of wetting film-thinning during capillary pressure rise in a reservoir-representative system.

Chapter 6 continuously monitored a xanthan gum polymer-EOR flood in a Bentheimer sandstone using L-T_1-T_2. Core saturation measurements (obtained from T_1-T_2 chemical contrast) indicated a total recovery of 56.1% of the OOIP, of which 4.9% was from polymer EOR – in agreement with both effluent volumetrics, and typical literature-reported recoveries. L-T_1-T_2 measurements suggested that xanthan achieved macroscopic improvements to sweep efficiency via deposition of polymer debris in small pores. This resulted in blocking of the smallest pores, diverting brine flow to larger pores and enabling greater oil displacement therein. This pore blocking effect was reduced during the EOR waterflood, attributed to both polymer dilution and the flushing out of some xanthan debris.

Chapter 7 studied an HPAM-EOR polymer flood in a water-wet Bentheimer. Spectrally-tracked saturations indicated a total recovery of 62.4% of OOIP, 4.3% from polymer-EOR – agreeing with effluent volumetrics and literature-reported recoveries. PFG T_2-propagators demonstrated that post-waterflooding and post-EOR, stagnant fluid primarily consisted of oil whereas moveable fluid was primarily brine. A small fraction of moveable fluid was attributed to oil (despite no further oil production), suggesting agreement with the literature-reported elastic turbulence mechanism. The influence of HPAM-EOR on oil ganglia size was also studied, using PFG diffusion measurements at no-flow. Larger oil ganglia were noted, suggesting HPAM encourages oil ganglion coalescence and stabilisation – supporting the "oil thread stabilisation" mechanism observed in glass micromodels. As far as is known, this effect has not previously been demonstrated in reservoir-representative samples.

Chapter 8 monitored an industry-standard SCAL Amott-Harvey wettability measurement on a water-wet Berea sandstone using T_1-T_2 and L-T_2 measurements at 2 MHz – comparable to conventional SCAL and reservoir well-logging tool NMR system field strengths. The goal was to conduct preliminary tests on the sensitivity of the T_1/T_2 NMR wettability ratio at 2 MHz, and to benchmark this against the Amott-Harvey wettability index (AHWI). It was demonstrated that at 2 MHz, T_1/T_2 was weakly sensitive to the core sample wettability, agreeing with the Amott-Harvey wettability measurement. The T_1/T_2 ratio yielded information on the core wettability at early stages within the AH cycle. This suggests the potential for delivering faster wettability measurements – both for SCAL applications and downhole WLT *in situ* reservoir measurements. Further work in oil-wet and intermediate-wet cores are required to validate the technique.

9.2 Suggestions for Future Work

Further studies of HPAM-EOR influence on oil ganglia

Chapter 7 demonstrated that HPAM promoted increased oil ganglia sizes, suggesting oil ganglia coalescence and stabilisation. This supported the "oil thread stabilisation" mechanism previously observed in glass micromodels. However, the magnetic field gradients on the 85 MHz system (maximum 10.7 G cm^{-1}) limited the resolution of these measurements. Further studies in NMR systems capable of delivering larger magnetic field gradients would enable improved resolution for probing changes in oil ganglion size. Chemical contrast techniques would be required to separate oil- and brine-phase PFG diffusion signals. This would enable unambiguously detecting restricted diffusion effects from oil ganglia alone, excluding any restriction effects from wetting-brine contacting the pore walls within the tortuous pore network.

Further studies on Amott-Harvey-NMR T_1/T_2 wettability benchmarking

Chapter 8 demonstrated that at 2 MHz T_1/T_2 was weakly sensitive to core wettability, yielding a result that agrees with industry-standard Amott-Harvey wettability measurements. This study was however only conducted on a water-wet system and should be extended to an oil-wet system, to complete the

preliminary benchmarking. A hexadecylamine/decane system for delivering altered oil-wetting systems is recommended – with equivalent oil-phase bulk relaxation time properties, this would enable direct dataset comparison with this study. Systematic studies benchmarking T_1/T_2 in core systems of controlled wettabilities at higher magnetic field strengths (known to exhibit greater sensitivity to surface interactions) would also be of interest.

Development of preliminary core screening protocol and core sample library

Challenges were faced in unambiguously attaining relaxation time contrast in the systems studied in this thesis. Of notable difficulty was the unexpected, differing T_1-T_2 responses within near-equivalent systems of: identical hydrocarbon and brine-phase compositions, identical magnetic field strengths, and identical core type. This was attributed to differences in internal pore structure. It is expected that similar effects would likely occur for other NMR contrast mechanisms influenced by internal pore structures, such as diffusion or D-T_2 responses. It would thus be useful to develop a core screening protocol and/or core sample library for future studies. Characterisation of core samples, together with identification of their optimal NMR contrast mechanisms and fluid samples to be used, would be beneficial.

Extension of EOR flooding studies to more challenging systems

Of great commercial relevance is the combination of polymer-EOR with chemical surfactants. These technologies have demonstrated further improvements in oil recoveries within reservoir pilot field studies, thought to result from alterations in reservoir wettabilities and oil-water interfacial tensions. The L-T_1-T_2 technique would be well-suited to detecting axial variabilities in surface interactions during a surfactant-EOR flood. Mapping localised changes in microemulsion saturation and size during a surfactant-EOR flood could also be of interest.

Lastly, only simple, homogeneous core samples were used in this thesis. Extension to studying EOR floods within cores of heterogeneous structures and wettabilities (representative of the variation in reservoir properties) would also be of interest. The capacity for delivering spatial-resolution on a core-scale, together with its sensitivity to pore-scale effects, uniquely position NMR techniques to study such systems non-invasively.

References

Abdallah, W., Buckley, J.S., Carnegie, A., Edwards, J., Herold, B., Fordham, E. *et al.*, 2007. Fundamentals of Wettability. *Schlumberger Oilfield Review Summer 2007*.

Abidin, A.Z., Puspasari, T. and Nugroho, W.A., 2012. *Procedia Chem.,* **4***,* 11-16.

Ahmadi, P., Riazi, M. and Malayeri, M.R., 2017. SCA Paper 2017-012. In proc: International Symposium of the Society of Core Analysts, Vienna, Austria, 27 August-1 September, 2017.

Ahola, S., Perlo, J., Casanova, F., Stapf, S., Blümich, B., 2006. *J. Magn. Reson.*, **182**, 143-151.

Ait-Kadi, A. and Carreau, P.J., 1987. *J. Rheol.*, **31**, 537-561.

Al-Fossail, K. and Handy, L.L., 1989. *J. Colloid Interface Sci.*, **134**(1), 256-263.

Alhammadi, A.M., AlRatrout, A., Bijlejic, B. and Blunt, M.J., 2018. *J. Vis. Exp.*, **140**, e57915.

Al-Gharbi, M.S. and Blunt, M.J., 2005. *Phys. Rev. E*, **71**, 016308.

Al-Mahrooqi, S.H., Grattoni, C.A., Moss, A.K. and Jing, X.D., 2003. *J. Pet. Sci. Eng.*, **39**, 389-398.

Al-Mahrooqi, S.H., Grattoni, C.A., Muggerdige, A.H. and Jing, X.D., 2005. SCA Paper 2005-10. In proc: International Symposium of the Society of Core Analysts, Toronto, Canada, 21-25 August 2005.

Al-Mahrooqi, S.H., Grattoni, C.A., Muggeridge, A.H., Zimmerman, R.W. and Jing, X.D., 2006. *J. Pet. Sci. Eng.*, **52**, 172-186.

Almansour, A.O., AlQuraishi, A.A., AlHussinan, S.N. and AlYami, H.Q., 2017. *J. Petrol. Explor. Prod. Technol.*, **7**(4), 1149-1158.

Al-Muthana, A.S., Hursan, G.G., Ma, S.M., Valori, A., Nicot, B., Singer, P.M., 2012. SCA Paper 2012-31. In proc: International Symposium of the Society of Core Analysts, Aberdeen, Scotland, 27-30 August 2012.

Al-Sharji, H.H., Grattoni, C.A., Dawe, R.A. and Zimmerman, R.W., 2001. SPE Paper 68972. In proc: SPE European Formation Damage Conference, 21-22 May, The Hague, The Netherlands, 2001.

Alveskog, P.L., Holt, T., Torsæter, O., 1998. *J. Pet. Sci. Eng.*, **20**, 247-252.

Amott, E., 1959. *Petroleum Transactions AIME*, **216**, 156-162.

Anderson, W.G., 1986a. *JPT*, **38**(10), 1124-1144.

Anderson, W.G., 1986b. *JPT*, **38**(11), 1246-1262.

Anderson, W.G., 1987a. *JPT*, **39**(10), 1283-1300.

Anderson, W.G., 1987b. *JPT*, **39**(12), 1605-1622.

Andrew, M., Bijeljic, B. and Blunt, M.J., 2014. *Adv. Water Resour.*, **68**, 24-31.

Andrianov, A., Farajzadeh, R., Mahmoodi, M., Talanana, M. and Zitha, P.L.J., 2012. *Ind. Chem. Eng Res.*, **51**, 2214-2226.

Appel, M., 2004. *Petrophysics*, **45**(3), 296-307.

Archer, J.S. and Wong, S.W., 1973. SPE paper 3551. In proc: SPE-AIME 46th Annual Full Meeting, New Orleans, 3-6 Oct 1973.

Arora, S., Horstmann, D. and Cherukupalli, P., 2010. SPE paper 129069. In proc: SPE EOR Conference at Oil & Gas West Africa. Muscat, Oman, 11-13 April 2010.

Aspenes, E., Graue, A. and Ramsdal, J., 2003. *J. Pet. Sci. Eng.*, **39**, 337-350.

Aspenes, E., Ersland, E., Graue, A., Stevens, J. and Baldwin, B.A., 2008. *Transport Porous Med.*, **74**, 35-47.

ASTM Standard D4404-84, 1998. *Standard Test Method for Determination of Pore Volume and Pore Volume Distribution of Soil and Rock by Mercury Intrusion Porosimetry.* West Conshohocken, PA: ASTM International.

Baldwin, B.A., Stevens, J., Howard, J.J., Graue, A., Kvamme, B., Aspenes, E. *et al.*, 2009. *Magn. Reson. Imaging*, **27**, 720-726.

Baldwin, B.A. and King, R.L., 1998. Why Would an Oil Company Use MRI? In: Blümler, P., Blümich, B., Botto, R. and Fukushima, E., 1998. *Spatially Resolved Magnetic Resonance Methods, Materials, Medicine, Biology, Rheology, Geology, Ecology, Hardware: Ch 55.* Wiley-VCH.

Baldwin, B.A. and Yamanashi, W.S., 1988. *Magn. Reson. Imaging*, **6**, 493-500.

Baldwin, B.A. and Yamanashi, W.S., 1991. NMR Imaging of Fluid Saturation Distributions in Cores. *The Log Analyst.* September-October, 1991. Society of Core Analysts.

Ball, R.C., Blunt, M. and Barford, W., 1989. *J. Phys. A: Math. Gen.*, **22**, 2587-2595.

Baraka-Lokmane, S., Teutsch, G. and Main, I.G., 2001. *Geo. J. Int.*, **147**, 263-271.

Barrie, P.J., 2000. *Annu. Rep. NMR Spectrosc.*, **41**, 265-278.

Bartels, W.-B., Rücker, Boone, M., Bultreys, T., Mahani, H., Berg, S. *et al.*, 2017. SCA Paper 2017-005. In proc: International Symposium of the Society of Core Analysts, Vienna, Austria, 27 August-1 September, 2017.

Baumgaertner, A. and Muthukumar, M., 1991. *J. Chem. Phys.*, **94**, 4062.

Berg, S., Ott, H., Klapp, S.A., Schwing, A., Neiteler, R., Brussee, N. *et al.*, 2013. *Proc. Natl. Acad. Sci. U.S.A.*, **110**(10), 3755-3759.

Beyea, S.D., Balcom, B.A., Mastikhin, I.V., Bremner, T.W., Armstrong, R.L. and Grattan-Bellew, P.E., 2000. *J. Magn. Reson.*, **144**, 255-265.

Bjørlykke, K., 2015. *Petroleum Geoscience: From Sedimentary Environments to Rock Physics*. Berlin Heidelberg: Springer-Verlag.

Blackband, S., Mansfield, P., Barnes, J.R., Clague, A.D.H. and Rice, S.A., 1986. *SPE Formation Evaluation*, February 1986.

Blunt, M.J., 2001. *Curr. Opin. Colloid & Interface Sci.*, **6**, 197-207.

Blunt, M.J., Jackson, M.D., Piri, M. and Valvatne, P.H., 2002. *Adv. Water Resour.*, **25**, 1069-1089.

Blunt, M.J., Bijeljic, B., Dong, H., Gharbi, O., Iglauer, S., Mostaghii, P. *et al.*, 2013. *Adv. Water Resour.*, **51**, 197-216.

Bona, N., Rossi, E. and Capaccioli, S., 1999. SPE Paper 50720. In proc: SPE International Symposium on Oilfield Chemistry, Houston, Texas, 16-19 February 1999.

Bousseau, C., Liu, Y. and Buckley, J.S., 1995. SCA Paper 9532. In proc: International Symposium of the Society of Core Analysts, San Francisco, California, 12-14 September 1995.

Brautaset, A., Ersland, G., Graue, A., Stevens, J. and Howard, J., 2008. SCA paper 2008-41. In proc: International Symposium of the Society of Core Analysts, Abu Dhabi, UAE, 29 October-2 November 2008.

Brownstein, K.R. and Tarr, C.E., 1987. *Phys. Rev. A.*, **19**, 2446-2453.

Callaghan, P.T., 1991. *Principles of Nuclear Magnetic Resonance Microscopy*. New York: Oxford University Press.

Callaghan, P.T., 2011. *Translational Dynamics and Magnetic Resonance: Principles of Pulsed Gradient Spin Echo NMR*. Oxford: OUP.

Calvetti, D., Golub, G.H. and Reichel, L., 1999. *BIT*, **39**(4), 603-619.

Carr, H.Y. and Purcell, E.M., 1954. *Phys. Rev.*, ***94***, 630-638.

Cense, A.W. and Berg, S., 2009. SCA Paper 2009-13. In proc: International Symposium of the Society of Core Analysts, Noordwijk, The Netherlands, 27-30 September, 2009.

Chatzis, I and Morrow, N., 1984. *SPE J*, **25**(5), 555-562.

Chen, Y.Y., 2010. *Quantitative Fast MRI Studies of Controlled Release Drug Delivery Systems*. Ph.D. University of Cambridge, UK.

Chen, Q., Gingras, M.K. and Balcom, B.J., 2003. *J. Chem. Phys.*, **119**(18), 9609-9616.

Chen, J., Hirasaki, G.J., and Flaum, M., 2006. *J. Pet. Sci. Eng.*, **52**, 161-171.

Chen, Y.Y., Hughes, L.P., Gladden, L.F. and Mantle, M.D., 2010. *J. Pharm. Sci.*, **99**(8), 3462-3472.

Clark, N.J., 1969. *Elements of Petroleum Reservoirs.* Dallas, Texas: AIME.

Clarke, A., Howe, A.M., Mitchell, J., Staniland, J. and Hawkes, L.A., 2015. SPE Paper 174654. In proc: SPE Asia Pacific Enhanced Oil Recovery Conference, Kuala Lumpur, Malaysia, 11-13 August 2015.

Coates, G.R., Xiao, L. and Prammer, M.G., 2001. *NMR Logging Principles and Applications.* Oxford: Elsevier Science and Technology.

Colbourne, A.A., Sederman, A.J., Mantle, M.D. and Gladden, L.F., 2016. *J. Magn. Reson.*, **272**, 68-72.

Cole, W.F., 1969. *Reservoir Engineering Manual.* 2nd ed. Houston, Texas: Gulf Publishing Company.

Cotts, R.M., Hoch, M.J.R, Sun, T. and Markert, J.T., 1989. *J. Magn. Reson.*, **83**, 252-266.

Cuiec, L., 1984. SPE Paper 13211. In proc: SPE Annual Technical Conference and Exhibition, Houston, Texas, 16-19 September 1984.

D'Agostino, C., Mitchell, J., Mantle, M.D. and Gladden, L.F., 2014. *Chem. Eur. J.*, **20**, 13009-13015.

Darby, R., 2001. *Chemical Engineering Fluid Mechanics*. 2nd ed. New York: Marcel Dekker.

Datta, S.S., Ramakrishnan, T.S. and Weitz, D.A., 2014. *Phys. Fluids*, **26**, 022002.

Davies, S., Packer, K.J., Roberts, D.R. and Zelaya, F.O., 1991. *Magn. Reson. Imaging*, **9**, 681-685.

Davies, S. and Packer, K.J., 1990. *J. Appl. Phys.*, **67**(6), 3163-3170.

Dehner, A. and Kessler, H., 2005. *ChemBioChem*, **6**(9), 1550-1565.

Denys, K., Fichen, C and Zaitoun, A., 2001. SPE Paper 64984. In proc: SPE International Symposium on Oilfield Chemistry, Houston, Texas, 13-16 February 2001.

Donaldson, E.C., Thomas, R.D. and Lorenz, P.B., 1969. *SPE Journal*, **9**(1), 13-20.

Douglas, J.F., 1989. *Macromolecules*, **22**, 3707-3716.

Dullien, F.A.L., 1992. *Porous Media: Fluid Transport and Pore Structure*. 2nd ed. San Diego; London: Academic Press.

Dullien, F.A.L., Lai, F.S.Y. and Macdonald, I.F., 1986. *J. Colloid Interface Sci.*, **109**(1), 201-218.

Dupuis, D., Lewandowski, F.Y., Steiert, P. and Wolff, C., 1994. *J. Nonnewton. Fluid Mech.*, **54**, 11-32.

Dyes, A.B., Caudle, B.H. and Erickson, R.H., 1954. *JPT*, **6**(4), SPE 309-G.

Edelstein, W.A., Hutchison, J.M.S., Johnson, G. and Redpath, T., 1980. *Phys. Med. Biol.*, **25**, 751-756.

English, A.E., Whittall, K.P., Joy, M.L.G. and Henkelman, R.M., 1991. *Magn. Reson. Med.*, **22**, 425-434.

Enwere, M.P. and Archer, J.S., 1992. NMR SPE paper 24166. In Proc: *SPE Eighth Symposium on Enhanced Oil Recovery*, Tulsa, Oklahoma, 22-24 April 1992.

Ersland, G., Husebø, J., Graue, A and Kvamme, B., 2009. *Energy Procedia*, ***1(1)***, 3477-3484.

Ersland, G., Fernø, M.A., Graue, A., Baldwin, B.A. and Stevens, J., 2010a. *Chem. Eng. J.*, **158**, 32-38

Ersland, G., Husebø, J., Graue, A., Baldwin, B.A., Howard, J. and Stevens, J., 2010b. *Chem. Eng. J.l*, **158**, 25-31.

Fay, E., Knight, R.J. and Song, Y.-Q., 2015. *Geophysics*, **80**(3), D281-D294.

Feng, G. and Yu, M., 2015. *Petroleum*, **1**, 158-163.

Fernø, M.A., Ersland, G., Haugen, Å, Johannesen, E, Graue, E., Stevens, J. *et al*., 2007. SPE paper 108699. In proc: *2007 International Oil Conference and Exhibition*, Veracruz, Mexico, 27-30 June 2007.

Fishbein, K.W., McGowan, J.C. and Spencer, R.G., 2005. Hardware for Magnetic Resonance Imaging. In: Filippi, M., de Stefano, N., Dousset, V. and McGowan, J.C., ed. 2005. *MR Imaging in White Matter Diseases of the Brain and Spinal Cord.* Berlin, Heidelberg: Springer-Verlag. Ch. 2.

Fleury, M. and Deflandre, F., 2003. *MRI*, **21**, 385-387.

Fogden, A., 2012. *Colloids Surf. A Physicochem. Eng. Asp.*, **402**, 13-23.

Freedman, R., 2006. Advances in NMR Logging. *Journal of Petroleum Technology*, January 2006. Society of Petroleum Engineers.

Freire, J.M., Domingues, M.M., Matos, J., Melo, M.N., Veiga, A.S., Santos, N.C. *et al.*, 2011. *Eur. Biophys. J.*, **40**, 481-487.

Fukushima, E. and Roeder, S.B.W., 1981. *Experimental Pulse NMR: A Nuts and Bolts Approach*. Reading, Massachusetts: Addison-Wesley.

Gallegos, D.P., Munn, K., Smith, D.M. and Stermer, D.L., 1987. *J. Colloid Interface Sci.*, **119**(1), 127-140.

Gao, Y., Lin, Q., Bijeljic, B. and Blunt, M.J., 2017. *Water Resour. Res.*, **53**(12), 10,274-10,292.

Gaymard, R. and Poupon, A., 1968. *The Log Analyst*, **9**(5), 3-12.

Ghannam, M.T., Abu-Jdayil, B. and Esmail, N., 2014. *JPSR*, **3**(1), 1-15.

Gladden, L.F., 1994. Chem. Eng. Sci., **49**(20), 3339-3408.

Gladden, L.F. and Sederman, A.J., 2017. *Annu. Rev. Chem. Biomol. Eng.*, **8**, 227-247.

Godefroy, S., Jorb, J.P., Fleury, M. and Bryant, R.G., 2001. *Phys. Rev. E.*, **64**, 021605.

Grattoni, C.A., Luckham, P.F., Jing, X.D., Norman, L. and Zimmerman, R.W., 2004. *J. Pet. Sci. Eng.*, **45**, 233-245.

Graue, A., Viksund, B.G., Eilertsen, T., Moe, R., 1999. *J. Pet. Sci. Eng.*, **24**, 85-97.

Graue, A., Aspenes, E., Bognø, T., Moe, R.W. and Ramsdal, J., 2002. *J. Pet. Sci. Eng.*, **33**, 3-17.

Gray, R., Trewin, B., Pallatt, N. and Mitchell, P., 1992. SCA Paper 1992-15. In proc: International Symposium of the Society of Core Analysts, Oklahoma City, Oklahoma, 15-17 June 1992.

Guan, H., Brougham, D., Sorbie, K.S. and Packer, K.J., 2002. *J. Pet. Sci. Eng.*, **34**, 35-54.

Guo, X.H., Li, W.D., Tian, J., Liu, Y.Z., 1999. SPE Paper 57294. In proc: SPE Asia Pacific Improved Oil Recovery Conference, Kuala Lumpur, Malaysia, 25-26 October 1999.

Habermann, B., 1960. *Petrol. Trans. AIME*, **219**, 264-272. SPE 1540-G.

Haines, W.B., 1930. *J. Agric. Sci.*, **20**(1), 97-116.

Harris, C.C. and Morrow, N.R., 1964. *Nature*, **203**, 706-708.

Hassenkam, T., Pedersen, C.S., Dalby, K., Austad, D. and Stipp, S.L.S., 2011. *Colloids Surf A Physicochem Eng. Asp.*, **390** (1-3), 179-178.

Hassenkam, T., Mitchell, A.C., Pedersen, C.S., Skovbjerg, L.L., Bovet, N. and Stipp, S.L.S, 2012. *Colloids Surf. A Physicochem. Eng. Asp.*, **403**, 79-86.

Hassler, G.L. and Brunner, E., 1945. *Trans. AIME*, **160**, 114-123.

Haugen, Å, Mani, N., Svenningsen, S., Brattekås, B., Graue, A., Ersland, G.*et al.*, 2014. *Transport Porous Med.*, **104**, 109-131.

Hennig, J., Nauerth, A., and Friedburg, H., 1986. *Magn. Reson. Med.*, **3**, 823-833.

Hilner, E., Andersson, M.P., Hassenkam, T., Mathiesen, J., Salino, P.A. and Stipp, S.L.S., 2015. *Sci. Rep.*, **5**: 9933.

Hiorth, A., Cathles, L.M. and Madland, M.V., 2010. *Transport Porous Med.*, **85**, 1-21.

Holland, D.J., Mitchell, J., Blake, A. and Gladden, L.F., 2013. *PRL*, **110**, 018001.

Hone, D., Ji, J. and Pincus, P.A., 1987. *Macromolecules*, **20**, 2543-2549.

Hou, J., Li, Z., Zhang, S., Cao, X., Du, Q. and Song, X., 2009. *Transport Porous Med.*, **79**, 407-418.

Howard, J.J., 1994. *MRI***,** **12**(2), 197-200.

Howe, A.M., Clarke, A. and Giernalczyk, D., 2015. *Soft Matter*, **11**, 6419.

Huang, Y.-W. and Gupta, V.K., 2001. *Macromolecules*, **34**, 3757-3764.

Huang, D.D. and Honarpour, M.M., 1996. SCA Paper 9634. In proc: International Symposium for the Society of Core Analysts, Montpellier, France, 8-10 September 1996.

Huh, C. Lange, E.A. and Cannella, W.J., 1990. SPE Conference 20235. In proc: SPE/DOE Enhanced Oil Recovery Symposium, Tulsa, Oklahoma, 22-25 April 1990.

Huh, C. and Pope, G.A., 2008. SPE Paper 113417. In proc: SPE Symposium on Improved Oil Recovery, Tulsa, Oklahoma, 20-23 April 2008.

Hürlimann, M.D., 1998. *J. Magn. Reson.*, **131**, 232-240.

Hürlimann, M.D., Helmer, K.G., Latour, L.L. and Sotak, C.H., 1994. *J. Magn. Reson A*, **111**, 169-178.

Hürlimann, M.D. and Song, Y.-Q., Schlumberger Technology Corporation, 2012. *Continuous Wettability Logging Based on NMR Measurements*. U.S. Pat. 8,278,922 B2.

Hussain, R., Pintelon, T.R.R., Mitchell, J. and Johns, M.L., 2011. *AIChE J.*, **57**(7), 1700-1709.

Jerauld, G.R. and Salter, S.J., 1990. *Transport Porous Med.*, **5**, 103-151.

Johannesen, E.B., Riskedal, H., Tipura, L., Howard, J.J. and Graue, A., 2007. SCA Paper 2007-02. In proc: International Symposium of the Society of Core Analysts, Calgary, Canada, 10-12 September 2007.

Johannesen, E., Howard, J., Graue, A., 2008. SCA Paper 2008-17. In proc: International Symposium of the Society of Core Analysts, Abu Dhabi, UAE, 29 October-2 November 2008.

Johannessen, A.M. and Spildo, K., 2014. *Energy Fuels*, **28**, 6723-6734.

Johns, M.L., Sederman, A.J., Gladden L.F., Wilson, A. and Davies, S., 2003. *AIChE J.*, **49**(5), 1076-1084.

Johns, M.L. and Hollingsworth, K.G., 2007. *Prog. Nucl. Magn. Reson. Spec.*, **50**, 51-70.

Kamal, M.S., Sultan, A.S., Al-Mubaiyedh, U.A., Hussein, I.A., 2015. *Polym. Rev.*, **55**, 491-530.

Kim, K.-H., Chen, S., Qin, F. and Watson, A.T., 1992. SCA paper 9219. In proc: International Symposium of the Society of Core Analysts, Oklahoma City, Oklahoma, 15-17 June 1992.

Kleinberg, R.L., 1994. *Magn. Reson. Imaging*, **12**(2), 271-274.

Kleinberg, R.L., 2001. *Concepts Magn. Reson.*, **13**(6), 342-343.

Kleinberg, R.L., Farooqui, S.A. and Horsfield, M.A., 1993. *J. Colloid Interface Sci.*, **158**, 195-198.

Kleinberg, R.L. and Horsfield, M.A., 1990. *J. Magn. Reson.*, **88**, 9-19.

Kleinberg, R.L. and Jackson, J.A., 2001. *Concepts Magn. Reson.*, **13**(6), 340-342.

Kleinberg, R.L. and Vinegar, H.J., 1996. *Log Analyst*, **37**(6), 20-32.

Knapstad, B., Skjølsvik, P. A. and Øye, H.A., 1989. *J. Chem. Eng. Data*, **34**(1), 37-43.

Kokkedee, J.A. and Boutkan, V.K., 1995. Towards measurement of capillary pressure and relative permeability of representative wettability. In: de Haan, H.J., 1995. *New Developments in Improved Oil Recovery*. Geological Society, London, Special Publications, **84**, 43-50.

Korb, J.-P., Nicot, B. and Jolivet, I., 2017. *Microporous Mesoporous Mater.*, 2017 (in press), 1-5.

de Kort, D.W., Reci, A., Ramskill, N.P., Appel, M., de Jong, H., Mantle, M.D. *et al.*, 2018. *J. Magn. Reson*, **295**, 45-56.

Kowalewski, E., Holt, T. and Torsaeter, O., 2002. *J. Pet. Sci. Eng.*, **33**, 19-28.

Kowalewski, E., Boassen, T. and Torsaeter, O., 2003. *J. Pet. Sci. Eng.*, **39**, 377-388.

Kumar, K., Dao, E. and Mohanty, K.K., 2005. *J. Colloid Interface Sci.*, **289**, 206-217.

Kumar, M., Senden, T.J., Sheppard, A.P., Middleton, J.P. and Knackstedt, M.A., 2009. SCA paper 2009-16. In proc: International Symposium of the Society of Core Analysts, Noordwijk, The Netherlands, 27-30 September 2009.

Lake, L.W., 1989. *Enhanced Oil Recovery.* Prentice-Hall, Englewood Cliffs, New Jersey, USA.

Langnes, G.L., *et al.*, 1985. Waterflooding. In: Donaldson, E.C., Chilingarian, G.V. and Yen, T.F., 1985. *Enhanced Oil Recovery I: Fundamentals and Analyses.* Elsevier. Ch. 8.

Latour, L.L., Kleinberg, R.L. and Sezginer, A., 1992. *J. Colloid Interface Sci.*, **150**(2), 535-548.

Lebedeva, E.V. and Fogden, A., 2011. *Energy Fuels*, **25**, 5683-5694.

Lemmon, E.W., McLinden, M.O. and Friend, D.G., 2017. Thermophysical Properties of Fluid Systems. In: Linstrom, P.J. and Mallard, W.G., ed. 2017. *NIST Chemistry WebBook, NIST Standard Reference Database Number 69*, National Institute of Standards and Technology, Gaithersburg MD, 20899.

Lenormand, R., Zarcone, C. and Sarr, A., 1983. *J. Fluid Mech.*, **135**, 337-353.

Leu, G., Fordham, E.J., Hürlimann, M.D. and Frulla, P., 2005. *Magn. Reson. Imaging*, **23**, 305-309.

Li, L., Han, H. and Balcom, B.J., 2009. *J. Magn. Reson.*, **198**, 252-260.

Li, M., Vashaee, S., Romero-Zerón, L., Marica, F. and Balcom, B.J., 2017. *Energy Fuels*, **31**, 10802-10811.

Liu, G., Li, Y. and Jonas, J., 1991. *J. Chem. Phys.*, **95**, 6892-6901.

Liu, Y., Song, Y., Zhao, Y., Wang, T. and Jiang, L. 2011. *Procedia Environ. Sci.*, **11**, 650-654.

Liu, H., Hunter, M., Obruchkov, S., McCarney, E., Robison, M., Dykstra, R. and Galvosas, P., 2015. SCA Paper 2015-13. In proc: International Symposium of the Society of Core Analysts, St John's Newfoundland, Canada, 16-21 August 2015.

Liu, Z.H., Li, Y.Q., Cui, M.H., Wang, F.Y. and Prasiddhianti, A.G., 2016. *Pet. Sci.*, **13**, 91-99.

Loahardjo, N. and Morrow, N.R., 2010. SCA paper 2010-16. In proc: International Symposium of the Society of Core Analysts, Halifax, Nova Scotia, Canada, 4-7 October 2010.

Looyestijn, W.J., 2008. *Petrophysics*, **49**(2), 130-145.

Looyestijn, W. and Hofman, J., 2006. Wettability-Index Determination by Nuclear Magnetic Resonance. *SPE Reservoir Evaluation & Engineering*, **9**(2), 146-152.

Mahani, H., Keya, A.L., Berg, S. and Nasralla, R., 2015. SPE paper 175568-MS. In proc: SPE Reservoir Characterisation and Simulation Conference and Exhibition, Abu Dhabi, UAE, 14-16 September 2015.

Majors, P.D., Smith, J.L., Kovarik, F.S. and Fukushima, E., 1990. *J. Magn. Reson.*, **89**, 470-478.

Majors, P.D., Ping, L. and Smith, J.L., 1997. *SPE Formation Evaluation*, September 1997. SPE Paper 30557.

Mantle, M.D. and Sederman, A.J., 2003. *Prog. Nucl. Magn. Reson. Spectrosc.*, **43**, 3-60.

Martel, K.E., Martel, R., Lefebvre, R. and Gélinas, P.J., 1998. *GWMR*, Summer 1998, 103-113.

McCaffery, F.G. and Mungan, N., 1970. *Journal of Canadian Petroleum Technology*, **9**(3), 185-196.

McCullough, J.J., Albaugh, F.W. and Jones, P.H., 1944. Determination of the Insterstitial-Water Content of Oil and Gas Sand by Laboratory Tests of Core Samples. *American Petroleum Institute: Drilling and Production Practice.* New York, New York, U.S.A., 1 January 1994. American Petroleum Institute.

McDonald, P.J., Korb, J.P., Mitchell, J. and Monteilhet, L., 2005. *Phys. Rev. E*, **72**¸ 011409.

McPhee, C., Reed, J. and Zubizarreta, I., 2015. Core Analysis: A Best Practice Guide. In: Cubitt, J., *Developments in Petroleum Science* (Vol. 64). Amsterdam: Elsevier.

Meiboom, S. and Gill, D., 1958. *Rev. Sci. Instrum.*, **29**, 688-691.

Meybodi, H.E., Kharrat, R. and Wang, X., 2011. *Transport Porous Med.*, **89**, 97-120.

Mills, R., 1973. *J. Phys. Chem.*, **77**(5), 685-688.

Minh, C.C. and Heaton, N.J., Schlumberger Technology Corporation, 2008. *Interpretation Methods for NMR Diffusion-T_2 Maps*. U.S. Pat. 7,388,374 B2.

Minh, C.C., Crary, S. Singer, P.M., Valori, A., Bachman, N., Hursan, G. *et al.*, 2015. In proc: SPWLA 56th Annual Well Logging Conference, Long Beach, California, 18-22 July, 2015.

Mitchell, J., Sederman, A.J., Fordham, E.J., Johns, M.L. and Gladden, L.F., 2008. *J. Magn. Reson.*, **191**(2), 267-272.

Mitchell, J., Chandresekera, T.C., Fordham, E.J., Crawshaw, J., Staniland, J., Johns, M.L. and Gladden L.F., 2009a. *Diffusion Fundamentals*, **10**, 24.1-24.3.

Mitchell, J., Hürlimann, M.D. and Fordham, E.J., 2009b. *J. Magn. Reson.*, **200**, 198-206.

Mitchell, J., Chandrasekera, T.C. and Gladden, L.F., 2010a. *J. Chem. Phys.*, **132**, 244705.

Mitchell, J., Chandrasekera, T.C., Johns, M.L., Gladden, L.F. and Fordham, E.J., 2010b. *Phys. Rev. E.*, **81**, 026101.

Mitchell, J., Chandrasekera, T.C. and Gladden, L.F., 2012a. *Prog. Nucl. Magn. Reson. Spectrosc.*, **62**, 34-50.

Mitchell, J., Edwards, J., Fordham, E., Staniland, J., Chassagne, R., Cherukupalli, P. *et al.*, 2012b. SPE Paper 154704. SPE EOR Conference at Oil and Gas West Asia, Muscat, Oman, 16-18 April 2012.

Mitchell, J., Staniland, J., Chassagne, R. and Fordham, E.J., 2012c. *Transp. Porous Med.*, **94**, 683-706.

Mitchell, J., Staniland, J., Wilson, A., Howe, A., Clarke, A., Fordham, E.J. *et al.*, 2012d. SCA Paper 2012-30. In proc: International Symposium of the Society of Core Analysts, Aberdeen, Scotland, 27-30 August 2012.

Mitchell, J., Broche, L.M., Chandrasekera, T.C., Lurie, D.J. and Gladden, L.F., 2013a. *J. Phys. Chem. C*, **117**(34), 17,699-17,706.

Mitchell, J., Chandrasekera, T.C. and Gladden, L.F., 2013b. *J. Chem. Phys.*, **139**, 074205.

Mitchell, J., Chandrasekera, T.C., Holland, D.J., Gladden, L.F. and Fordham, E.J., 2013c. *Phys. Rep.*, **526**, 165-225.

Mitchell, J., Staniland, J., Chassagne, R., Mogensen, K., Frank, S., and Fordham, E.J., 2013d. *J. Pet. Sci. Eng.*, **108**, 14-21.

Mitchell, J. and Fordham, E.J., 2011. *J. Magn. Reson.*, **212**, 394-401.

Mitchell, J. and Fordham, E.J., 2014. *Rev. Sci. Instrum.*, **85**, 111502.

Mitchell, J., Lyons, K., Howe, A.M. and Clarke, A., 2016. *Soft Matter*, **12**, 460.

Mitra, P.P., Sen, P.N. and Schwartz, L.M., 1993. *Phys. Rev. B.*, **47**(14), 8565-8574.

Mo, H., Harwood, J., Zhang, S., Xue, Y., Santini, R. and Raftery, D., 2009. *J. Magn. Reson.*, **200**(2), 239-244.

Montaron, B., 2007. SPE Paper 105041. In proc: SPE Middle East Oil and Gas Show and Conference, Manama, Bahrain, 11-14 March.

Morrow, N.R., 1970. *Chem. Eng. Sci.*, **25**, 1799-1815.

Morrow, N.R., 1990. *JPT*, **42**(12), 1476-1484.

Morrow, N.R., Ma, S., Zhou, X. and Zhang, X., 1994. In Proc: Petroleum Society of Canada Annual Technical Meeting. Calgary, Alberta, 12-15 June 1994.

Moss, A.K., Jing, X.D. and Archer, J.S., 2002. *J. Pet. Sci. Eng.*, **33**, 75-85.

Muggeridge, A., Cockin, A., Webb, K., Frampton, H., Collins, I., Moulds, T. and Salino, P., 2014. *Philos. Trans. Royal Soc. A*, **372**: 20120320.

Mungan, N., 1964. *SPEJ*, **4**(2), 115-123.

Newsham, K.E., Rushing, J.A., Lasswell, P.M., Cox, J.C. and Blasingame, T.A., 2004. SPE Paper 89866. In proc: SPE Annual Technical Conference and Exhibition, Houston, Texas, 26-29 September 2004.

Nicot, B., Ibrahim, G. and Dubes, G., 2017. SCA Paper 2017-036. In proc: International Symposium of the Society of Core Analysts, Vienna, Austria, 27 August-1 September 2017.

Nilsson, S., Stavland, A. and Jonsbråten, H.C., 1998. SPE Paper 39635. In proc: SPE/DOE Improved Oil Recovery Symposium, Tulsa, Oklahoma, 19-22 April 1998.

Norris, D.G., Börnert, P., Reese, T. and Leibfritz, D., 1992. *Magn. Reson. Med.*, **27**, 142-164.

North, F.K., 1985. *Petroleum Geology*. 2nd ed. London: Allen & Unwin.

Ogunberu, A.L. and Ashgari, K., 2005. *J. Can. Petrol. Technol.*, **44**(11), 56-61.

Olatunde, S., 2013. *The Effect of Disproportionate Permeability Reducers on Spontaneous Imbibition of Water into Wallace Sandstone*. MEng. Dalhousie University.

Oruwori, A.E. and Ikiensikimama, S.S., 2010. SPE Paper 136997-MS. In Proc: Nigeria Annual International Conference and Exhibition, Tinapa-Calabar, Nigeria, 31 July-7 August 2010.

Petrov, O.V., Ersland, G., Balcom, B.J., 2011. *J. Magn. Reson.*, **209**, 39-46.

Plug, W.J. and Bruining, J., 2007. *Adv. Water Resour.*, **30**, 2339-2353.

Pomerantz, A.E., Sigmund, E.E. and Song, Y.-Q., 2007. *Appl. Magn. Reson.*, **32**, 221-231.

Pomerantz, A.E., Tilke, P. and Song, Y.-Q., 2008. *J. Magn. Reson.*, **193**, 243-250.

Purcell, W.R., 1949. *Petrol. Trans. AIME*, **186**, 39-48.

Ramskill, N.P., Bush, I., Sederman, A.J., Mantle, M.D., Benning, M., Anger, B.C. *et al.*, 2016. *J. Magn. Reson.*, **270**, 187-197.

Ramskill, N.P., Sederman, A.J., Mantle, M.D., Appel, M., de Jong, J. and Gladden L.F., 2018. *Transp. Porous Med.*, **121**, 15-35.

Rangel, I.R., Thompson, R.L., Pereira, R.G. and de Abreu, F.L.B., 2012. *J. of the Braz. Soc. Of Mech. Sci. & Eng.*, **34**(3), 285-293.

Reci, A., 2016. *NMR Relaxation analysis and the application on rock pore size distribution*. NOTAF. University of Cambridge.

Rezghi, M. and Hosseini, S.M., 2009. *J. Comput. Appl. Math.*, **231**, 914-924.

Roland, O.E., Akinlolu, W., Siddiqui, S., Alquraishi, A. and Okpelu, O., 2013. In proc: AIChE 2013 Annual Meeting: Global Challenges for Engineering a Sustainable Future. San Francisco, California, 2-8 November 2013.

Romero-Zerón, L.B., Li, L., Ongsurakul, S. and Balcom, B., 2009. *Pet. Sci. Tech.*, **27**, 1993-2009.

Romero-Zerón, L.B., Ongsurakul, S. and Balcom, B., 2010. *Pet. Sci. Tech.*, **28**, 52-67.

Rothwell, W.P. and Vinegar, H.J., 1985. *Appl. Opt.*, **24**(23), 3969-3972.

Salter, S.J. and Mohanty, K.K., 1982. SPE Paper 11017. In proc: SPE Annual Technical Conference and Exhibition, New Orleans, Louisiana, 26-29 September 1982.

Scheenen, T.W.J., van Dusschoten, D., de Jager, P.A. and Van As, H., 2000. *J. Exp. Bot.*, **51**(351), 1751-1759.

Scheven, U.M., Seland, J.G. and Cory, D.G., 2005. *Magn. Reson. Imaging*, **23**(2), 363-365.

Schlangen, L.M., Koopal, L.K., Cohen Stuart, M.A. and Lyklema, J., 1994. *Colloids Surf. A.*, **89**, 157-167.

Schön, J.H., 2011. Physical Properties of Rocks: A Workbook. In: Cubitt, J., ed. 2011. *Handbook of Petroleum Exploration and Production: Vol. 8*. Oxford: Elsevier.

Sedaghat, M.S., Ghazanfari, M.H., Parvazdavani, M. and Morshedi, S., 2013. *J. Energy Resour. Technol.*, **135**, 032901.

Seleznev, N.V., Habashy, T.M., Boyd, A.J. and Hizem, M., 2006. In proc: SPWLA 47th Annual Logging Symposium. Veracruz, Mexico, 4-7 June 2006.

Sharma, M.M. and Wunderlich, R.W., 1987. *J. Pet. Sci. Eng.*, **1**, 127-143.

Shiran, B.S. and Skauge, A., 2013. *Energy Fuels*, **27**, 1223-1235.

Shu, S., Husain, S. and Koros, W.J., 2007. *J. Phys. Chem. C.*, **111**, 652-657.

Slijkerman, W.F.J. and Hofman, J.P., 1998. *MRI*, **16**(5-6), 541-544.

Slobod, R.L., Chambers, A. and Prehn Jr., W.L., 1951. *JPT*, **3**(4), 127-134.

Smith, W.O., 1933. *Physics*, **4**(425), 425-438.

Song, Y.-Q., Venkataramanan, L., Hürlimann, M.D., Flaum, M., Frulla, P. and Straley, C., 2002. *J. Magn. Reson.*, **154**, 261-238.

Song, K.M., Mitchell, J., Jaffel, J. and Gladden, L.F., 2010. *J. Mater. Sci.*, **45**, 5282-5290.

Song, Y., Zhu, N., Zhao, Y., Liu, Y., Jiang, L. and Wang, T., 2013. *Phys. Fluids*, **25**, 053301.

Soxhlet, F., 1879. Die gewichtsanalytische Bestimmug des Milchfettes. *Dingler's Polytechnisches Journal*, **232**, 461-465.

Sparlin, D.D., 1976. *JPT*, **28**(8), 906-914.

Standnes, D.C. and Austad, T., 2003. *J. Pet. Sci. Eng.*, **39**, 431-446.

Stavland, A. and Nilsson, S., 2001. SPE Paper 71510. In proc: SPE Annual Technical Conference and Exhibition, New Orleans, Louisiana, 30 September-3 October 2001.

Steinsbø, M., Graue, A. and Fernø, M.A., 2014. SCA Paper 2014-037. In proc: International Symposium of the Society of Core Analysts, Avignon, France, 8-12 September 2014.

Stejskal, E.O. and Tanner, J.E., 1965. *J. Chem. Phys.*, **42**, 288-292.

Suekane, T., Furukawa, N., Tsushima, S., Hirai, S. and Kiyota, M., 2009. *JPM*, **12**(2), 143-154.

Sulpizi, M., Gaigeot, M.-P. and Sprik, M., 2012. *J. Chem. Theory Comput.*, **8**, 1037-1047.

Sun, Y., Saleh, L. and Bai, B., 2012. Measurement and Impact Factors of Polymer Rheology in Porous Media. In: De Vicente, J., 2012. *Rheology*. InTech., 187-202.

Tabrizy, V.A., Denoyel, R. and Hamouda, A.A., 2011. *Colloids Surf. A.*, **384**, 98-108.

Takeda, M., Hallenga, K., Shigezane, M., Waelchli, M., Löhr, F., Markley, J.L. and Kainosho, M., 2011. *J. Magn. Reson.*, **209**(2), 167-173.

Tanner, J.E., 1970. *J. Chem. Phys.*, **52**, 2523-2526.

Terpstra, M., Andersen, P.M. and Gruetter, R., 1998. *J. Magn. Reson.*, **131**(1), 139-143.

Terry, R.E., 2001. Enhanced Oil Recovery. In: Meyers, R.E., ed. 2001. *Encyclopaedia of Physical Science and Technology*. 3rd ed., vol 18. Academic Press. 502-518.

Tiab, D. and Donaldson, E.C., 2016. *Petrophysics*. 4th ed. Gulf Professional Publishing.

Tinni, A., Sondergeld, C. and Rai, C., 2014. SCA Paper 2014-091. In proc: International Symposium of the Society of Core Analysts, Avignon, France, 8-12 September 2014.

Toledo, P.G., Araujo, Y.C. and Leon, V., 1996. *J. Colloid Interface Sci.*, **183**, 301-308.

Tweheyo, M.T., Holt, T. and Torsæter, O., 1999. *J. Pet. Sci. Eng.*, **24**, 179-188.

Valori, A., Hursan, G. and Ma, S.M., 2017. *SPWLA*, **58**(4), 352-365.

Venkatakrishnan, A. and Kuppa, V.K., 2018. *Curr. Opin. Chem. Eng.*, **19**, 170-177.

Venkataramanan, L., 2002. *IEEE Trans. Signal Process.*, **50**(5), 1017-1026.

Vilgis, T.A. and Heinrich, G., 1994. *Macromolecules*, **27**, 7846-7854.

Vinegar, H.J., 1986. X-ray CT and NMR Imaging of Rocks. *JPT*, (March), 257-259.

Vinogradov, J. and Jackson, M.D., 2015. *Geophys. Res. Lett.*, **42**, 6287-6294.

de Waal, J.A., Smits, R.M.M., de Graaf, J.D. and Schipper, B.A., 1989. SPWLA Conference Paper 1989-II. In proc: SPWLA 30th Annual Logging Symposium, Denver Colorado, 11-14 June 1989.

Waggoner, R.A. and Fukushima, E., 1996. *Magn. Reson. Imaging*, **14**(9), 1085-1091.

Wahba, G., 1977. *SINUM*, **14**(4), 651-667.

Wang, D., Cheng, J., Wu, J. and Wang, G., 2002. SPE Paper 77693. In proc: SPE Annual Technical Conference and Exhibition, San Antonio, Texas, 29 September-2 October, 2002.

Wang, D., Wang, G., Wu, W., Xia, H. and Yin, H., 2007. SPE Paper 109016. In proc: SPE Annual Technical Conference and Exhibition, Anaheim, California, 11-14 November 2007.

Wang, Y., Luce, T., Ishizawa, C., Shuck, M., Smith, K., Ott, H. *et al.*, 2010. SCA paper 2010-18. In proc: International Symposium of the Society of Core Analysts, Halifax, Nova Scotia, Canada, 4-7 October 2010.

Wang, D., Wang, G. and Xia, H., 2011. SPE Paper 144294. In proc: SPE Enhanced Oil Recovery Conference, Kuala Lumpur, Malaysia, 19-21 July.

Wang, Z., Le, X., Feng, Y. and Zhang, C., 2013a. *J. Pet. Sci. Eng.*, **111**, 139-143.

Wang, W., Yue, X. and Chen, Y., 2013b. *J. Dispers. Sci. Technol.*, **34**, 639-643.

Washburn, K.E., Sandor, M. and Cheng, Y., 2017. *J. Magn. Reson.*, **275**, 80-89.

Washburn, K.E. and Madelin, G., 2010. *J. Magn. Reson.*, **202**, 122-126.

Webb, K., Lager, A. and Black, C., 2008. SCA Paper 2008-39. In proc: International Symposium of the Society of Core Analysts, Abu Dhabi, UAE, 29 October-2 November 2008.

Weber, D., Mitchell, J., McGregor, J. and Gladden, L.F., 2009. *J. Phys. Chem. C*, **113**, 6610-6615.

Weber, D., Sederman, A.J., Mantle, M.D., Mitchell, J. and Gladden, L.F., 2010. *Phys. Chem. Chem. Phys.*, **12**, 2619-2624.

Wei, B., Romero-Zerón and Rodrigue, D., 2014. *J. Pet. Explor. Prod. Technol.*, **4**, 113-121.

Wever, D.A.Z., Picchioni, F. and Broekhuis, A.A., 2011. *Prog. Polym. Sci.*, **36**, 1558-1628.

Wever, D.A.Z., Picchioni, F. and Broekhuis, A.A., 2013. *I&EC Research*, **52**, 16352-16363.

Williams, J.L.A., Taylor, D.G., Maddinelli, G., Enwere, P. and Archer, J.S., 1991. *Magn. Reson. Imaging*, **9**, 767-773.

Williams, J.L.A., Maddinelli, D.G. and Taylor, D.G., 1994. *J. Magn. Reson. A*, **109**, 124-128.

Williams, C.F.M., Redpath, T.W. and Norris, D.G., 1999. *Magn. Reson. Med.*, **41**, 734-742.

Wilson, J.D., 1992. *J. Mater. Sci.*, **27**(14), 3911-3924.

Windt, C.W., Vergeldt, F.J. and Van As, H., 2007. *J. Magn. Res.*, **185**, 230-239.

Winn, E.B., 1950. *Phys. Rev.*, **80**(6), 1024-1027.

Worden, R. and Morad, S., 2000. *Quartz Cementation in Sandstones*. Oxford, United Kingdom: Blackwell Sciences.

Yadav, G.D., Chatzis, I. and Dullien, F.A.L., 1985. *Chem. Eng. Sci.*, **40**(8), 1618-1619.

Yadav, G.D., Dullien, F.A.L., Chatzis, I. and Macdonald, I.F., 1987. *SPE Reservoir Engineering*, **2**(2), 137-147.

Young, T., 1805. *Phil. Trans. R. Soc. Lond.*, **95**, 65-87.

Youssef, S., Rosenberg, E., Deschamps, H., Oughanem, R., Maire, E. and Mokso, R., 2014. SCA paper 2014-023. In proc: International Symposium of the Society of Core Analysts, Avignon, France, 11-18 September 2014.

Yuechao, Z., Yongchen, S., Yu, L., Lanlan, J. and Ningjun, Z., 2011. *Petroleum Science*. **8**(2), 183-193.

Zeelenberg, H.P.W. and Schipper, B.A., 1991. Developments in *I-*S_w Measurements. In: Worthington, P.F. and Longeron, D., 1991. *Advances in Core Evaluation II Reservoir Appraisal – Reviewed*

Proceedings of the Second Society of Core Analysts European Core Analysis Symposium. Philadelphia, U.S.: Gordon and Breach Science Publishers.

Zeppieri, S., Rodríguez, J. and López de Ramos, A.L., 2001. *J. Chem. Eng. Data*, **46**, 1086-1088.

Zhang, Q., Lo, S.-L., Huang, C.C., Hirasaki, G.J., Kobayashi, R. and House, W.V., 1998. SPWLA-1998-FF. In proc: SPWLA 39th Annual Logging Symposium, Keystone, Colorado, 26-28 May 1998.

Zhang, G., Huang, C.-C. and Hirasaki, G., 2000. *Log Analyst*, **41**(3). SCA-9921.

Zhang, J.C., Song, K.P., Liu, L. and Yang, E.L., 2008. *Chin. Phys. Lett.*, **25**(5), 1750-1753.

Zheng, C.G., Gall, B.L., Gao, H.W., Miller, A.E. and Bryant, R.S., 2000. *SPE Reservoir Evaluation and Engineering*, **3**(3), SPE Paper 64270.

Zhong, L. and Oostrom, M., 2013. *J. Hazard. Mater.*, **244-245**, 160-170.

Zhou, X.M., Torsæter, O., Xie, X. and Morrow, N.R., 1995. *SPE Formation Evaluation*, **10**(4), 259-265.

Zisman, W.A., 1964. Relation of the Equilibrium Contact Angle to Liquid and Solid Constitution. In: Fowkes, F.M., ed. 1964. *Contact Angle, Wettability, and Adhesion, Vol. 43.* ACS. Ch.1.